

université
de **BORDEAUX**

Joint Thesis

Approved by:

Department of Material and Geosciences of the Technical University of Darmstadt
submitted in fulfilment of the requirements for the Degree of Doktor Ingenieurs
The Doctoral School of Chemical Sciences of the University of Bordeaux in fulfilment of
the requirements for the degree of Doctor with specialty in Physical Chemistry of
Condensed Matter

Charged defects in BaTiO₃ thin films

Christopher Castro Chavarría

Born in Mexico City, Mexico

Defended on 09/11/2021 before a jury composed of:

President	Dr. Prellier, Wilfrid	(ENSI Caen)
PhD supervisor	Dr. Maglione, Mario	(U Bordeaux)
PhD supervisor, Reviewer	Prof. Dr. Klein, Andreas	(TU Darmstadt)
Reviewer	Prof. Dr. Donner, Wolfgang	(TU Darmstadt)
Examiner	Prof. Dr. Rödel, Jürgen	(TU Darmstadt)
Examiner	Prof. Dr. Béchou, Laurent	(U Bordeaux)
Examiner	Dr. Besland, Marie-Paule	(Université de Nantes)
Examiner	Prof. Dr. Remiens, Denis	(UPHF)
Examiner	Dr. Bouyssou, Emilien	(ST-Microelectronics)

Charged defects in BaTiO₃ thin films

Approved dissertation by Christopher Castro Chavarría from Mexico City, Mexico

Darmstadt, Technische Universität Darmstadt

Year thesis published in TUPrints 2022

URN : urn:nbn:de:tuda-tuprints-213925

URL : <https://tuprints.ulb.tu-darmstadt.de/id/eprint/21392>

Day of the viva voce: 09.11.2021

Published under CC BY 4.0 International
<https://creativecommons.org/licenses/by/4.0/>



Declaration of Authorship

I hereby confirm that I have written the present thesis independently and without illicit aid from third parties, using solely the aids mentioned. All passages from other sources are marked as such. This work has not been presented to an examination office before in this or a similar form.

Déclaration sur la Dissertation

Je déclare par la présente que la thèse a été rédigée sans l'aide d'un tiers et que toutes les aides et supports ont été mentionnés. Toutes les sources ont été indiquées. Ce travail n'a pas été présenté antérieurement devant un comité d'examen, que ce soit en totalité ou en partie.

Erklärung zur Dissertation

Hiermit versichere ich, die vorliegende Dissertation ohne Hilfe Dritter nur mit den angegebenen Quellen und Hilfsmitteln angefertigt zu haben. Alle Stellen, die aus Quellen entnommen wurden, sind als solche kenntlich gemacht. Diese Arbeit hat in gleicher oder ähnlicher Form noch keiner Prüfungsbehörde vorgelegen.

Darmstadt, August 19th 2021

Christopher Castro Chavarria

Acknowledgements

"The smallest act of kindness is worth more than the grandest intention"
Oscar Wilde

First of all, I would like to thank Marie-Paule Besland, research directress at IMN in Nantes and Denis Remiens, professor at IEMN-DOAF at UPHF, for accepting to examine this thesis. I would like to express my gratitude to the president of the jury, Wilfrid Prellier, research director at CRISMAT in Caen, and Emilien Bouyssou, Laurent Bechou, Jürgen Rödel and Wolfgang Donner for participating in the jury.

I would like to express my special thanks of gratitude to the people who made this work possible, my Ph.D. advisors Dr. Mario Maglione and Prof. Dr. Andreas Klein. Thank you for your patience and resilience, without them I wouldn't have been able to finish. I have learned so much and with your guidance, I have seen that I still have a lot to learn. I would like to express as well special thanks to Sandrine Payan, the person that recruited me, trusted me and introduced me to many people at ICMCB.

I would like to thank as well the people that helped me with some of the experiments that are presented here. Alla Artemenko, for the EPR measurements, thank you for your time and the many explanations you gave me to really understand this (very) complex measurement. Jean-Paul Salvétat, for the ToF-SIMS experiments, thank you for your time and thanks for contributing so much with the paper we have written. And last but not least, Lionel Teulé-Gay, thank you for the many hours we spent discussing, they were really enlightening, for the banter and mostly for contributing with many ideas that lead to a very interesting result (O₂ plasma co-sputtering).

In addition, I want to thank the group researchers and common services: Sebastien Fourcade, Cathérine Elissalde, Michäel Josse, Eric Lebraud, Edgar, Sandrine at ICMCB and Erich at TU-Darmstadt, and those who contributed at some point to this thesis or simply helped me getting around both laboratories. Additionally, my special thanks to Quentin Simon, the post-doc, professor and many other (non recognized) professions of our dear group at ICMCB, without your knowledge

and help with the theory and experiments I would have passed many more hours trying to figure out things. And at TU-Darmstadt, Andy, Hans, Christian and Philipp (the big 4), for teaching me how to use our big machine (XPS).

I would also like to thank my family, specially my parents and my brother, you are my motivation and I think of you every day.

These years also allowed me to meet so many people at both laboratories. I would like to start with my Italian friends Alice and Lorenzo, not only I was able to continue to speak Italian with you but I made really good friends. I want to continue with the people that were not from group 1, but that were part of my group of friends: Clio, Marie, Iñaki and Juan, thanks for all the good moments. I want to thank, obviously, the people that were part of my group. At ICMCB, Clément, a skater that proved me that appearances are deceiving, Sergey, a Siberian who never left home but discovered a world in Bordeaux, David, a very loud Basque with a very big heart, Quentin (again), a Breton with many capacities, specially drinking beer and of course, Thomas, a person with a huge heart that first was a stranger, then my office-mate and then my friend for life. At TU-Darmstadt, Andy, a quiet but very fun person, Christian, a person with whom you can always have a good time, Priya a very thoughtful person and a really good cooker, Yannick, a very competitive yet kind person, Hans, a very big and strong man in appearance but very soft inside, Raphaël, my French friend with whom I found a fellow countryman, and last but not least, Philipp, my office mate and my friend, you helped me so much; I wish our friendship will last long.

Lastly, I would like to thank all the people I knew during these years outside the labs. In Germany, Raphael and my flatmates, Robin, Paulina and Ina, thank you for the really good times and showing me around. In France, my "flatmates", Anaïs, Prune, Thomas, Thibaut, Sol and Suzie, my little family in Bordeaux. Of course Mathieu, a person that I thought I would never talk again after the first time I met, but then I knew you better and now you are my best friend.

To those I forget, please forgive me. Nonetheless, I had a wonderful time with you during these years.

Finally, I want to thank one of the most important people to me, my dear Chloé, without you I would have never finished this thesis, you pushed me and put me back on track, and for that, you have my eternal gratitude.

Zusammenfassung

In dieser Arbeit werden die Eigenschaften dotierter BaTiO₃ Dünnschichten behandelt, die mittels Magnetron-Kathodenzerstäubung hergestellt wurden. Durch die ferroelektrischen Eigenschaften des BaTiO₃ können diese für steuerbare Kondensatoren sowie in nicht-flüchtigen Speichern verwendet werden. Die Eigenschaften der mit Kathodenzerstäubung hergestellten Schichten sind jedoch wesentlich schlechter als die von keramischen Volumenmaterialien. Diese Arbeit verfolgte das Ziel die dielektrischen Eigenschaften der Schichten zu verbessern, indem Multilagengestrukturen mit unterschiedlich geladenen Defekten (Mn, Nb, La) hergestellt wurden. Der Vergleich der Multilagengestrukturen zu den dotierten Einzelschichten ergab, dass die Permittivität durch das Einbringen der Grenzflächen erhöht werden kann. Dies steht dem allgemeinen Verständnis entgegen, dass Grenzflächen inaktive Schichten, sogenannte „dead-layers“ bilden. Die Schichten wurden mittels Röntgenbeugung (XRD), Photoelektronenspektroskopie (XPS, UPS), Elektronen-Spin-Resonanz (EPR), Impedanz-Spektroskopie, sowie Flugzeit-Massenspektrometrie (TOF-SIMS) untersucht. Dadurch konnten verschiedene physikalische und chemische Größen, wie die Fermi-Energie und die Defekteigenschaften an den Grenzflächen untersucht werden. Insbesondere wurde die Lage des Fermi-Niveaus in den Mn-dotierten Schichten, die auf unterschiedlichen Substraten abgeschieden wurden, im Detail untersucht, um den Einfluss des Substrats auf Aufladungen und eventuelle Beeinflussungen der Messungen durch Photospannungen aufzuklären. Um die Grenzen des Fermi-Niveaus besser zu verstehen wurden auch Mn-dotierte Schichten mittels zusätzlicher Anwendung eines Sauerstoffplasmas abgeschieden. Dieses Verfahren wurde speziell für diese Arbeit entwickelt.

Stichworte: Bariumtitanat, Dünnschichten, Dotierung, Defekte, dielektrische Eigenschaften, Elektronenspektroskopie, Elektronen-Spin-Resonanz, Massenspektrometrie

Résumé

Les travaux ici présents portent sur l'étude des couches minces BaTiO₃ (BTO) dopées et déposées par pulvérisation cathodique. Grâce à ses propriétés ferroélectriques et à sa forte permittivité diélectrique, le BTO est utilisé comme un condensateur accordable ou encore dans des mémoires non-volatiles (FeRAM). Néanmoins, ces propriétés sont fortement dégradées lors de sa déposition sous forme de couche mince à cause des effets extrinsèques d'interface. La stratégie adoptée dans cette étude pour améliorer ces propriétés diélectriques est de contrôler les défauts chargés à l'interface par des multicouches de couches minces de BTO dopé au Mn, Nb et La. Des études sur les couches monodopées et les multicouches ont montré que les interfaces soigneusement conçues conduisent à augmenter la permittivité relative des couches minces de BTO, en contradiction avec la croyance commune selon laquelle les interfaces se comportent comme des couches mortes. L'utilisation des différentes techniques comme la Résonance Paramagnétique Electronique (RPE), l'impédance diélectrique et notamment la Spectrométrie de Photoélectrons X (XPS en anglais) et la Spectrométrie de Masse à Ions Secondaires à Temps de Vol (ToF-SIMS en anglais) nous a permis de relier les différents aspects physiques et chimiques comme le niveau de Fermi et la chimie de défauts aux interfaces des multicouches de BTO. De plus, nous avons étudié les particularités du niveau de Fermi des couches dopées au Mn. Des phénomènes de charge ou même du photovoltage de surface induisent un changement artificiel du niveau de Fermi du BTO dopé Mn déposé sur différents substrats. Enfin, nous avons mis en place une technique de dépôt à l'aide du plasma d'oxygène qui a permis de baisser le niveau de Fermi vers la bande de valence du BTO dopé Mn.

Mots-clés : Titanate de barium, couches minces, diélectrique, XPS, ToF-SIMS, défauts chargés, dopage, courants de fuite, RPE

Abstract

The work presented here focuses on the study of doped BaTiO₃ (BTO) thin films deposited by magnetron sputtering. Due to its ferroelectric properties and its high dielectric permittivity, BTO is used as a tunable capacitor or also in non-volatile memories (FeRAM). Nevertheless, these properties are strongly degraded when deposited as thin films as a result of the extrinsic interface effects. The strategy adopted in this study to improve these dielectric properties was to control the charged defects at the interface by multilayered doped BTO thin films (Mn, Nb and La). Studies on monodoped thin films and multilayers have shown that the carefully designed interfaces lead to increasing relative permittivity of BTO thin films, contradicting the common belief that interfaces behave like dead layers. The use of different techniques such as Electron Paramagnetic Resonance (EPR), dielectric impedance and in particular X-ray Photoelectron Spectroscopy (XPS) and Time-of-Flight Secondary Ion Mass Spectroscopy (ToF-SIMS) have enabled us to relate the different physical and chemical aspects such as the Fermi level position and the defect chemistry at the interfaces of BTO multilayers. In addition, we have studied the particularities of the Fermi level position of Mn-doped layers. Charging phenomena or even surface photovoltage induce an artificial change in the Fermi level of the Mn-doped BTO when deposited on various substrates. Finally, we implemented a deposition technique using oxygen plasma which made it possible to lower the Fermi level position towards the valence band of Mn doped BTO.

Keywords: Barium titanate, thin films, dielectric, XPS, ToF-SIMS, charged defects, doping, leakage currents, EPR

Resumen

El presente trabajo se refiere al estudio de películas delgadas de BaTiO₃ (BTO) dopadas y depositadas por pulverización catódica. Gracias a sus propiedades ferroeléctricas y su alta permitividad dieléctrica, el BTO se utiliza como condensador de sintonización o en memorias no volátiles (FeRAM). Sin embargo, estas propiedades se degradan fuertemente durante su deposición de película delgada debido a los efectos de la interfaz extrínseca. La estrategia adoptada en este estudio para mejorar estas propiedades dieléctricas es, controlar los defectos cargados en la interfaz por multicapas de películas delgadas de BTO dopadas con Mn, Nb y La. Los estudios sobre las capas monodopadas y las multicapas han demostrado que las interfaces cuidadosamente diseñadas conducen a una mayor permitividad dieléctrica relativa de las películas delgadas de BTO, lo que contradice la creencia común de que las interfaces se comportan como capas muertas. El uso de diferentes técnicas como la Resonancia Paramagnética Electrónica (RPE), la impedancia dieléctrica y en particular la Espectroscopia de fotoelectrones emitidos por rayos X (XPS en inglés) y la Espectroscopia de masa de electrones secundarios (ToF-SIMS en inglés) nos permitió vincular los diferentes aspectos físicos y químicos como el nivel de Fermi y la química de defectos en las interfaces de multicapas de BTO. Además, estudiamos las peculiaridades del nivel de Fermi de las películas dopadas con Mn. Los fenómenos de carga o incluso el fotovoltaje de superficie inducen un cambio artificial en el nivel de Fermi del BTO dopado con Mn depositado en diferentes sustratos. Finalmente, implementamos una técnica de deposición usando plasma de oxígeno que permitió bajar el nivel de Fermi hacia la banda de valencia del BTO dopado con Mn.

Palabras clave: Titanato de bario, películas delgadas, dieléctrico, XPS, ToF-SIMS, defectos cargados, dopaje, corrientes de fuga, RPE

Contents

Introduction	5
1 Fundamentals	9
1.1 Bulk Ferroelectricity	9
1.1.1 Dielectric polarization	10
1.1.2 Polarization mechanisms	11
1.1.3 Dielectric loss mechanisms	12
1.1.4 Ferroelectricity in BaTiO ₃	13
1.2 Ferroelectric thin film	15
1.2.1 Deposition methods	15
1.2.2 Interface effects	22
1.3 Space charges	25
1.4 Fermi level position in semiconducting oxides	27
1.4.1 Electronic structure	27
1.4.2 Ionization defect levels	31
1.5 Conduction mechanisms	34
1.5.1 Richardson-Schottky conduction model	34
1.5.2 Thermionic field emission models	35
1.5.3 Poole-Frenkel emission model	35
1.5.4 Tunneling Effect	36
1.6 Enhancement of the dielectric permittivity	37
1.6.1 Defect chemistry in ferroelectrics	37
1.6.2 Heterovalent substitution	40
1.6.3 Mn, Nb, Fe and La BaTiO ₃ doping	43
1.6.4 Doped BaTiO ₃ multilayer thin films	45
2 Experimental characterization	49
2.1 Magnetron sputtering	49
2.2 X-Ray Diffraction	52
2.3 Impedance spectroscopy	53
2.3.1 Temperature dependence	54

2.4	X-Ray Photoelectron Spectroscopy	56
2.4.1	Valence band in ATiO ₃ compounds	58
2.4.2	Fermi level determination, interface experiment	59
2.5	Leakage Currents	62
2.5.1	Temperature dependence	63
2.6	Electron Paramagnetic Resonance	65
2.7	ToF-SIMS	67
3	Results and discussion	69
3.1	Introduction	69
3.2	Thin film deposition and structural analysis	70
3.3	Impedance spectroscopy	73
3.3.1	Single doped BaTiO ₃ thin films	73
3.3.2	Heterostructures	77
3.3.3	Summary	82
3.4	X-Ray Photoelectron Spectroscopy	84
3.4.1	Single doped films	88
3.4.2	Oxygen atomic source post-deposition treatment	93
3.4.3	Heterostructures	94
3.4.4	Summary	99
3.5	Leakage Currents	100
3.5.1	Single doped BaTiO ₃	101
3.5.2	Heterostructures	102
3.5.3	Summary	104
3.6	Electron Paramagnetic Resonance	107
3.6.1	Powder analysis	107
3.6.2	Single doped BaTiO ₃ films	109
3.6.3	Heterostructures	110
3.6.4	Summary	114
3.7	Discussion	115
3.7.1	Single doped films	115
3.7.2	Relative permittivity enhancement	117
3.8	TOF-SIMS analysis	121
3.9	Fermi level engineering	125
4	General conclusion and perspectives	139
Annex		163
4.1	Annex 1: Literature	163
4.2	Annex 2: Leakage currents	168
4.3	Annex 3: Ellipsometry	170

CONTENTS

3

4.3.1 Principle	170
4.3.2 Main results	170

Introduction

Ferroelectric materials were only a curiosity for the scientific community after the first decades of their discovery by Valasek in 1920 [1]. Only a few pioneers were interested in these materials at this time, as they exhibit a hysteresis of polarization under the effect of an electric field [2]. A first upsurge took place since the 1940's, with the discovery of BaTiO₃, then many new ferroelectric materials were discovered. This major period has given us a glimpse of a strong interest in industrial applications. During the last twenty-five years, major advances have been made in the understanding of these materials, both theoretically and experimentally. The emergence of the first ferroelectric thin films in the 1980's and their integration into electronic chips allowed these materials to enter the semiconductor industry. Intensive research was then carried out, and new applications emerged in microelectronics [3], such as ferroelectric FeRAM memories, temperature sensors, transistor gate oxides, or recently reconfigurable microwave devices for the telecommunications market. Finally, the ability (called tunability) of some ferroelectric materials such as barium titanate to see their dielectric permittivity reversibly modified by an electric field gives them a great interest in the development of agile components for uses at high frequencies.

To perform their function properly, these thin layers of ferroelectric materials must have a stoichiometric composition, a dense and crystallized microstructure and good uniformity. In addition, certain properties in terms of dielectric characteristics must be conserved. However, the properties of thin films are often very different from those of the bulk material from which they are derived [4]. The substrate on which they are deposited indeed has a strong impact on their microstructure [5]. In addition, their two-dimensionality limits the size of the grains and confers a very important role on the interfaces. Thus, one of the barriers of the thin films integration of ferroelectric films is the importance of its dielectric losses and leakage currents, which are governed by the quality of the interfaces between the dielectric material and the electrodes.

The most common methods to analyse the electric properties of these ferroelectric materials are current-voltage characteristics and impedance spectroscopy. However, these methods are limited in the identification of interface properties

due to their macroscopic approach. One method that has been widely used to study interface formation of semiconductors is the X-Ray Photoelectron Spectroscopy (XPS).

In order to more explore the physical and chemical properties of ferroelectric films more comprehensively, a simultaneous effort is needed. That is why a collaboration has been established between the Institut de Chimie de la Matière Condensée de Bordeaux (ICMCB), which specializes in the chemistry aspect of material sciences and ferroelectric oxides and Technische Universität Darmstadt (TU-Darmstadt), which specializes in the physics aspect of material sciences and the XPS measurements.

The potential of BaTiO₃ is no longer needed to be demonstrated, as proven in many publications and thesis [5-9]. As mentioned before, interface control in ferroelectric materials is a long-standing issue needing a deeper understanding, mostly about the interplay between point charge defects and interfaces. Our main case study will be BaTiO₃ thin films, which will be chemically substituted and processed as to generate and control space charges at the interfaces and hopefully to increase the dielectric permittivity. The objective of this work is to prepare and characterize ferroelectric thin films and multilayers at ICMCB and study the interfaces at TU-Darmstadt.

This thesis dissertation is divided into four chapters.

The first part defines the main useful concepts for the study of ferroelectric materials, then details the different synthesis methods, the peculiarities and the problematic of ferroelectric thin films. The importance of the Fermi level position on the electronic properties as well as the relationship of this to the leakage currents are highlighted. The impact of different dopants on the dielectric properties already studied are presented and the strategy adopted for this study is finally presented.

The description of magnetron sputtering, the deposition technique used, and the presentation of the main physico-chemical characterization methods of thin films are the subject of the second chapter. The techniques that make possible to determine the dependence in frequency, in electric field and in temperature of their permittivity, implemented during this work, are detailed. Moreover, we describe the typical informations which can be extracted from the XPS spectra.

Chapter 3 is devoted to the study of BaTiO₃ thin films and the effects of dopants. Moreover, we show that carefully designed internal interfaces through multilayered structures lead to increasing the relative permittivity of the BaTiO₃ thin films, in contradiction with the common belief that interfaces behave as dead layers [7, 10, 11]. This chapter is divided in three parts. The first part of this chapter contains the major results of the thesis. The description of the thin film and multilayer deposition, their dielectric properties as a function of temperature and electric field are first reported. The main result, which is central to this work,

is a strong increase of the dielectric permittivity up to more than 1000 of 300 nm thick trilayers made of a Nb-doped BaTiO₃ films sandwiched in-between two thin La-doped BaTiO₃. This high permittivity is nearly temperature independent, which signs its extrinsic origin, and the associated losses stay below 2%. The electronic properties of individual layers and of stacks investigated by in-situ XPS are then described. The first outcome of these investigations is that, provided the oxygen vacancy content is controlled as much as possible, the Fermi level position can be tuned from close to the conduction band to deeper in the band gap. In the case of the already mentioned trilayers an unusual band bending is observed at internal interfaces. This establishes a first link between the large effective permittivity and the electronic structure of these trilayers. The leakage currents versus temperature and the study of point defects via Electron Paramagnetic Resonance (EPR) are further evidences of the specific contributions of La, Nb, Mn point defects to the BaTiO₃ thin films conductivity. The second part of chapter 3 is a discussion about the above mentioned results converging towards localisation of charges at internal interfaces as a way to increase the dielectric permittivity in multilayers. To support this model Time-Of-Flight Secondary Ion Mass Spectroscopy (ToF-SIMS) experiment have been carried out. An extended cross diffusion of Nb and La at interfaces between layers is evidenced which could explain the electronic bands bending at these interfaces and the increased dielectric permittivity. The last part explores the particular case of Mn doping in BaTiO₃ and its variation of Fermi level position.

The fourth chapter closes this manuscript with a general conclusion of this dissertation and the many perspectives generated by this work.

Chapter 1

Fundamentals

1.1 Bulk Ferroelectricity

Ferroelectric materials are a sub-division class of dielectrics. In fact, ferroelectrics have dielectric, pyroelectric and piezoelectric properties. Dielectrics are insulating materials that are used because of their polarizability enabling increased charge storage in capacitors. They do not conduct electricity due to the very low density of free charge carriers and a large band gap. In particular, ferroelectric materials present spontaneous polarization that results from the separation of the barycentres of positive and negative charges. The distinctive feature of ferroelectric materials is the ability of their spontaneous polarization to be switched by an electric field, resulting in a polarization-electric field hysteresis loop. The first ferroelectric material, namely Rochelle salt, was discovered by Valasek in 1921 [1], then in the 1930's the thermodynamic and atomistic models of ferroelectricity were developed by the discovery of the potassium dihydrogen phosphate family (KDP) [12]. Unfortunately, this property was not exploitable for these compounds due to the instability and complexity in the case of the Rochelle salt and the working temperatures for the KDP family (below -150°C) as traced back by Cross and Newnham [2]. Shortly after, in the 1940's, barium titanate (BaTiO_3) was investigated. Showing a ferroelectric transition at 130°C and high stability; the associated large dielectric permittivity at room temperature range enabled the development of high k capacitors. From this period more and more ferroelectric materials were discovered and these materials began to proliferate and diversify in many technologies. Recently, these materials have been tried to be integrated in different electronic systems as they have been deposited as thin films. Unfortunately, polycrystalline BaTiO_3 usually loses its main properties when deposited as thin film [13-16]. Much lower permittivity than in bulk and no clear phase transition are often observed as a result of random internal strain

induced by the deposition process, lattice expansion mismatch, or (local) variation of stoichiometry [17]. Since the mid-nineties deep investigations have shown that restoring the polarization and dielectric properties in BaTiO₃ thin films requires advanced processes [18].

1.1.1 Dielectric polarization

Permittivity (often found as dielectric constant) characterizes the ability of a material to accumulate charges [19]. For a linear, homogeneous and isotropic material, the macroscopic polarization is written:

$$\vec{P} = \varepsilon_0 \chi_e \vec{E}$$

where χ_e is the electrical susceptibility and ε_0 the permittivity of vacuum (8.85×10^{-12} F/m). Maxwell's equations make it possible to relate the polarization and the electric field to the electric induction vector:

$$\vec{D} = \varepsilon_0 \vec{E} + \vec{P} = (1 + \chi_e) \varepsilon_0 \vec{E} = \varepsilon_r \varepsilon_0 \vec{E}$$

where $\varepsilon_r = \chi_e + 1$ is the relative permittivity of the material.

Let $\vec{E} \cdot \vec{E}_0 \cdot e^{i\omega t}$ be a sinusoidal electric field. The polarization it induces in the material is the result of several mechanisms of movement and orientation of charges that take some time to establish. Due to this polarization establishment time, a phase shift δ may appear between the applied electric field and the induced polarization. The permittivity is then defined as a complex quantity, which depends on the frequency of the field:

$$\varepsilon(\omega) = \varepsilon'(\omega) + i\varepsilon''(\omega)$$

Then we can write:

$$\tan \delta(\omega) = \left| \frac{\varepsilon''(\omega)}{\varepsilon'(\omega)} \right|$$

This magnitude (in %) is called the coefficient of dielectric losses or losses and reflects the electrical energy absorption by the material, or the difference that this material presents compared to a perfect insulator. Certain loss mechanisms results from leakage currents: free electrons, "holes" and/or ionic vacancies (mainly oxygen) can migrate through the material. The electrical conductivity σ is related to the imaginary part of the permittivity and depends on the frequency:

$$\sigma = \varepsilon'' \omega \varepsilon_0$$

Permittivity and dielectric losses can be determined by electrical measurements. The capacity of a planar capacitor is proportional to dielectric permittivity, to the area of the electrodes and inversely proportional to the thickness of the material:

$$C = \frac{\varepsilon_r \varepsilon_0 S}{t}$$

where S is the surface of the conducting electrodes and t the thickness of the insulator between the plates of the capacitor.

1.1.2 Polarization mechanisms

The different polarization mechanisms that appear inside a material under the impulse of an electric field and as a function of its frequency are: the deformation of electronic clouds, the orientation of the dipoles in the direction of the field, the appearance of space charges and the relative displacement of ionic charges. Each of these phenomena contributes to the total polarization of the material and takes a certain time to establish, mainly due to the inertia of the entities involved. They therefore have a critical frequency beyond which they fade. Figure 1.1 shows the frequency spectrum of the real and imaginary parts of the permittivity for a polar dielectric containing space charges.

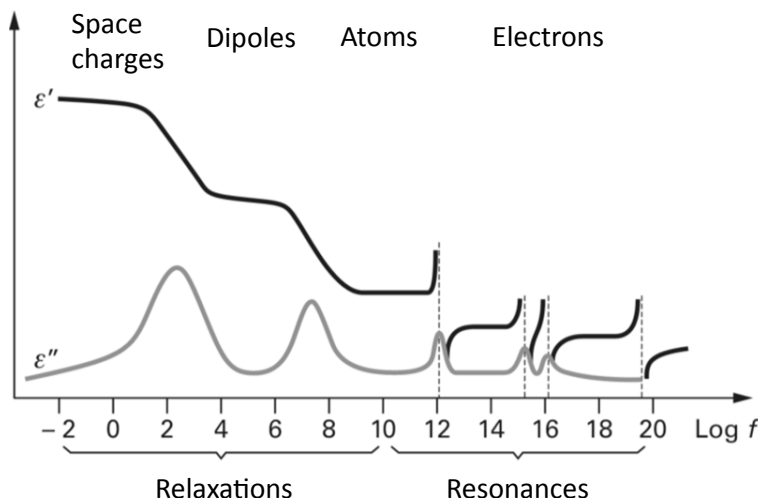


Figure 1.1: Dielectric dispersion phenomena (at room temperature) linked to the different polarization mechanisms. Real and imaginary parts of permittivity as a function of frequency [20]

As the frequency of the electric field decreases, more and more charges can follow changes in this field. At high frequencies, the vibrational processes to

which these loads are subjected are of the same type as those of a harmonic oscillator and therefore have a resonant shape. When the excitation frequency becomes lower than that of the lattice vibrations, the restoring forces are no longer elastic and a friction term leads to relaxation. The resulting low frequency processes for the dielectric permittivity are no more resonances but follow the Debye law.

1.1.3 Dielectric loss mechanisms

As presented in 1.1.1, a capacitor has dielectric losses, which origin can be traced from the material properties. These losses, noted $\tan \delta$, are defined as the ratio of the imaginary part to the real part of the permittivity and they translate the difference between the material and the perfect insulator. Dielectric losses are the dissipation of energy through the movement of charges in an alternating electromagnetic field as polarisation switches direction. Dielectric loss is especially high around the relaxation or resonance frequencies (c.f. figure [1.1](#)) of the polarisation mechanisms as the polarisation lags behind the applied field, causing an interaction between the field and the dielectric's polarisation that results in heating. We can attribute these losses to intrinsic or extrinsic contributions.

The first ones, their fundamental origin comes from the absorption of the material's electromagnetic field.

A maximum is also observed as a function of the frequency, depending on the nature of the material, and being around one hundred GHz. The contribution of these intrinsic losses can therefore not be negligible in radiofrequency applications.

On the other hand, an extrinsic contribution to dielectric losses can be observed, depending on the quality of the material. It comes mainly from the presence of charged defects in the material, entering into oscillation with the applied alternating electric field, and thus generating waves [\[21\]](#). According to the model then formulated by Vendik and Platonova, then developed by Garin [\[22, 23\]](#), the $\tan \delta_{charged\ defects}$ losses can be approximated as:

$$\tan \delta_{charged\ defects} \propto \varepsilon n_d Z^2$$

With n_d and Z respectively the atomic concentration and the charge of the defects. An essential characteristic of these losses is that they are proportional to the dielectric permittivity.

In addition, the presence of ferroelectric domains can contribute to increasing dielectric losses [\[24, 25\]](#). All of these contributions add up to the global dielectric

losses of the material translated as:

$$\tan \delta = \sum_{i \in \Omega} \tan \delta_i$$

In summary, at zero bias field superimposed to the oscillating one, the intrinsic contributions will dominate the dielectric losses of the material, which will decrease during the application of an electric field. A transition will therefore take place beyond a certain field where the extrinsic contributions will this time be decisive. We will see later that the control of these losses will be a key step for the feasibility of tunable capacitors with ferroelectric materials.

1.1.4 Ferroelectricity in BaTiO₃

It was in the mid-1940s that Wul and Goldman [26] demonstrated the very high dielectric permittivity (several thousand) of BaTiO₃, the ferroelectric properties of which were studied by Von Hippel [27]. The phenomenological study of Devonshire, based on the thermodynamic model of Landau, allowed to account in detail of the temperature dependence of the properties of this perovskite [28].

The BaTiO₃ compound has a perovskite ABO_3 - type structure, the prototype phase of which is cubic symmetry: the Ti⁴⁺ cations, small in size, occupy the center of the unit cell, the Ba²⁺ cations, much larger, are located at the vertices of the cube. and the O²⁻ anions are in the center of the faces. The titanium ions are thus found in an octahedral environment formed by the oxygen ions (cf. Figure 1.2).

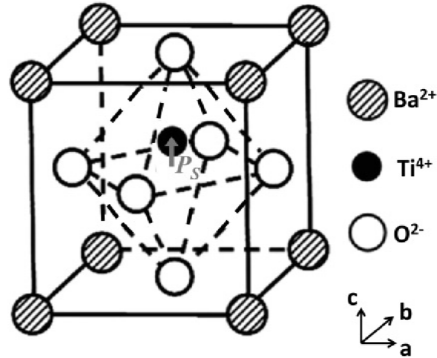


Figure 1.2: Structure of BaTiO₃ in its tetragonal structure. A spontaneous polarisation P_S is created due to the off-centering of Ti⁴⁺ [29]

This structure corresponds to the so-called high temperature phase, the unit cell of which has a center of symmetry, which prohibits any spontaneous polarization. BaTiO₃ at high temperature is therefore a paraelectric material, with a lattice

parameter of approximately 4\AA . Cooling results in the appearance of a phase of lower symmetry, obtained by deformation of the crystal lattice. At the transition temperature, called the Curie temperature and close to 130°C for BaTiO_3 , spontaneous polarization appears. Below this temperature, the material that has become ferroelectric has a tetragonal structure and exhibits a hysteresis loop. By further reducing the temperature, two other phase transitions are observed (tetragonal to orthorhombic around 0°C and orthorhombic to rhombohedral around -90°C), the material then retaining its ferroelectric properties.

During a transition, the lattice elongates in a particular direction, several directions being crystallographically equivalent. Several polar axes are therefore possible, which results in a structure in domains. The direction of the polarization vector varies from domain to domain, and is modifiable by the application of an electric field. Each phase transition implies a modification of the value of the polarization, which results in a maximum of the permittivity [30].

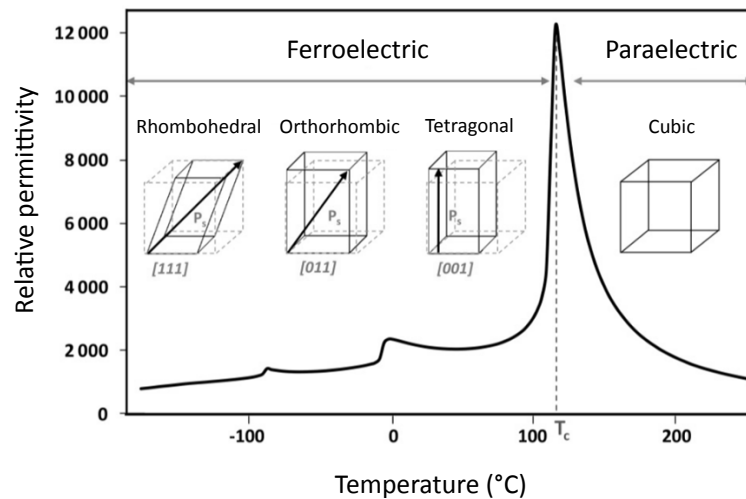


Figure 1.3: Evolution of relative permittivity of BaTiO_3 in temperature showing a phase transition at each peak of permittivity. [30]

1.2 Ferroelectric thin film

A thin film is a layer of a determined material where the thickness is massively reduced from that of a bulk. The range of thickness can vary from a fraction of a nanometer (nm) to several micrometers (μm). This reduction in thickness carries a perturbation in the majority of the material's bulk properties. The deposition technique, the choice of the substrate and the temperature at which the thin film is deposited, have the biggest influence on the material's properties.

1.2.1 Deposition methods

The synthesis of thin films always demands the deposition of a precursor material on a substrate. The state in which the precursor is found and the way it is transferred to the substrate allow to differentiate the different processes.

The physical methods involve solid precursors which are transferred in the vapour phase to the substrate. The main techniques are the pulsed laser deposition (PLD), the magnetron sputtering and the molecular beam epitaxy (MBE).

The atomic layer deposition (ALD), metalorganic chemical vapour deposition (MOCVD), the solution-gelation (sol-gel) technique and hydrothermal reaction are chemical processes in which liquid or vapour phase reactions are involved. Some techniques have modifications that can improve their characteristics. The main criteria to be evaluated in the choice of the method are the ability to produce films of controlled stoichiometry and structure, the speed and the surface homogeneity of the deposit, its adhesion to the substrate, the cost and finally, the reproducibility of the technique.

Physical Methods

These more or less high vacuum methods allow a solid film to be deposited on the surface of a substrate by the vapour phase transfer of the precursor material. They require high substrate temperatures to obtain a crystalline deposit.

Pulsed Laser Deposition

Pulsed Laser Deposition (PLD) is a technique that uses high power laser pulses (typically 10^8 Wcm^{-2}) to melt, evaporate and ionize material from the surface of a target. This "ablation" event produces a transient, highly luminous plasma plume that expands rapidly away from the target surface. The ablated material is collected on an appropriately placed substrate upon which it condenses and the thin film grows. The vaporized material, containing neutrals, ions, electrons etc., is known as a laser-produced plasma plume and expands rapidly away from the

target surface. Film growth occurs on a substrate upon which some of the plume material recondenses as shown in figure 1.4. This technique offers advantages for

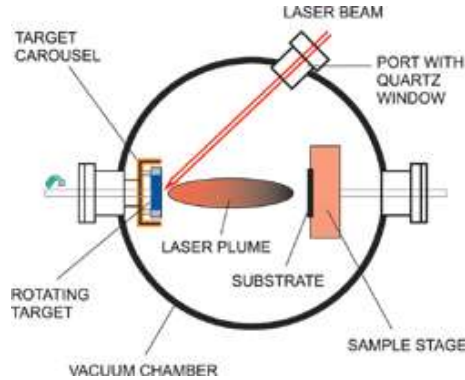


Figure 1.4: Pulsed Laser Deposition principle. [31]

BaTiO₃ film growth, including epitaxial growth at low substrate temperatures [32–34] and congruent deposition of materials with complex stoichiometries [32, 35]. Moreover, high dielectric permittivities above 1000 are achieved [32, 35, 36]. Nonetheless, high stress is observed in such films and to remove it, an amorphous BaTiO₃ buffer layer is deposited, as strain relieved films are more suitable for the development of tunable microwave devices.

Magnetron sputtering

Magnetron Sputtering is the most used Physical Vapor Deposition technique in industry for depositing metal and oxide films by controlling the crystalline structure and surface roughness. The simple form of the sputtering system consists of an evacuated chamber containing metallic anode and cathode in order to obtain a glow discharge in the residual gas in the chamber. The sputtering process depends on the bombardment of the ions released from the discharge to the molecules in the cathode leading to the liberation of the molecules from the cathode with higher kinetic energy. These molecules move in straight lines and strike on the anode or on the substrate to form a dense thin film. A more detailed principle will be explained in section 2.1. The diagram of the sputtering system is shown in Figure 1.5. Moreover, we have also deposited some films at ICMCB with an off-axis configuration integrated in the sputtering deposition chamber. This technique, which has been developed at Stanford University [37], places the target at 90° to the substrates plane reducing thus the effect of the ion resputtering as seen in Figure 1.6. The resputtering effect occurs particularly when volatile elements are deposited like Pb in Pb(Zr,Ti)O₃ compositions [38]. This technique has been used by a number of groups to process perovskite films [38, 39].

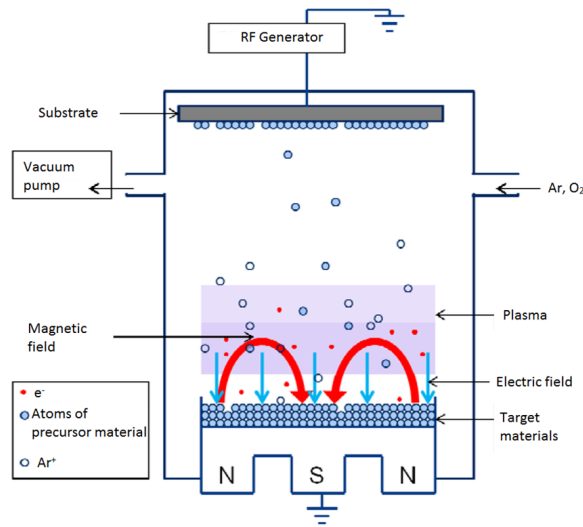


Figure 1.5: Radio-Frequency sputtering principle

BaTiO_3 grown by magnetron sputtering requests a high temperature (above 500°C) on the substrate to present a high relative permittivity and low dielectric losses [40]. Epitaxial films are only achieved on STO substrates or STO buffered substrates [41, 42], otherwise polycrystalline films are achieved [40, 43, 44]. Due to its simplicity, this technique has been adopted widely by the industry [45]. Nonetheless, it has a rather low deposition rates and as a result of the resputtering effect, non-stoichiometric films are produced [39].

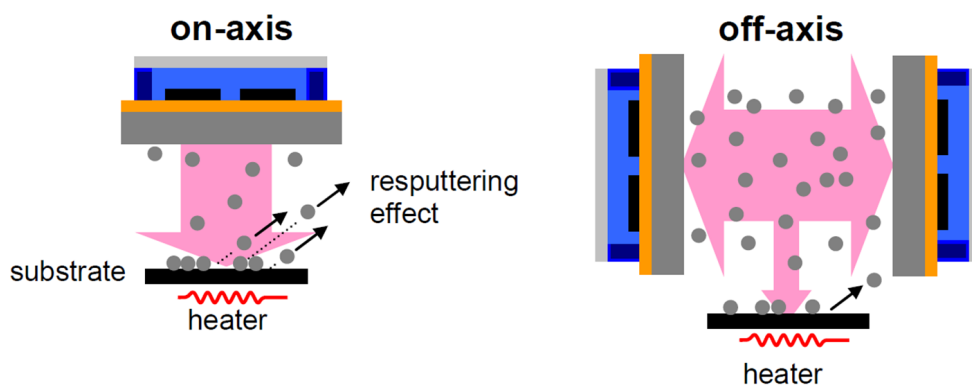


Figure 1.6: Left: on-axis sputtering configuration. Due to fast ions collisions, resputtering occurs. Right: off-axis geometry reducing the growth rate and thus the energy transfer collision on the substrate. [39]

Molecular Beam Epitaxy

Molecular Beam Epitaxy (MBE) is an epitaxial growth technique based on the interaction of species adsorbed from molecular beams of thermal energy on a heated crystalline substrate under ultra-high vacuum conditions (UHV), producing high quality epitaxial structures with monolayer control. Molecular beams are generated by the so-called effusion cells by evaporating or sublimating high purity materials contained in radiatively heated crucibles. Atoms or clusters of atoms, which are produced by heating up a solid source, migrate in an UHV environment and impinge on a hot substrate surface, where they can diffuse and eventually incorporate into the growing film as shown in figure 1.7.

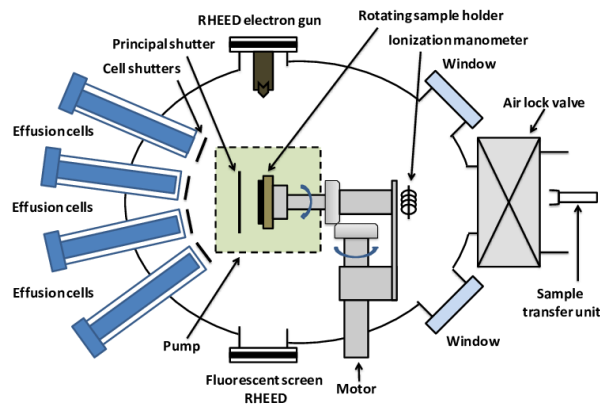


Figure 1.7: Molecular Beam Epitaxy principle. From [46]

BaTiO_3 grown by MBE needs high temperature on TiO_2 cycles (1400°C) and 500°C on BaO cycles. Thanks to the UHV environment, epitaxial films are possible to grow on SrTiO_3 [47–49] and MgO [50] (with a buffer layer) substrates. Due to the monolayer growth, surface can be controlled, therefore it is possible to have BaTiO_3 with TiO_2 or BaO terminated surfaces [48]. Because of the monolayer growth process, it is a substantially slow. In consequence, very thin films are produced and the analysis of their dielectric properties is "hard". Nonetheless, Tsurumi have measured a butterfly shape on the C-V characteristic with a maximum ϵ of around 100 [49].

Chemical Methods

These methods allow the deposition of a solid film on the surface of a heated substrate via one or more gas phase chemical reactions. The vaporized precursors (which can initially be in the solid, liquid or gas phase) are injected into a reactor

where the material transport is always carried out in the vapour phase. For the deposition of ferroelectric thin films, the most common CVD technique is MOCVD (Metal-Organic Chemical Vapour Deposition) [51]: the precursors are organometallic compounds in liquid or solid form (and dissolved in an appropriate solvent). CVD can also be assisted by plasma (PECVD for Plasma Enhanced), which by supplying energy to incident species allows the temperature of the substrate to be lowered [52, 53]. One of the advantages of CVD is that it allows films to be deposited on uneven and big surfaces at fairly high speeds.

Atomic Layer Deposition

ALD is a variant of the CVD technique that relies on saturated, self-limiting, separate gas-solid reactions between typically two compounds. A characteristic feature of ALD is that the precursors are pulsed alternately, one at a time, and separated by inert gas purging in order to avoid gas phase reactions (Figure 1.8). The successive, self-terminated surface reactions of the reactants enable controlled growth of the desired material. The unique self-limiting growth mechanism results in perfect conformality and thickness uniformity of the film even on complicated 3D structures.

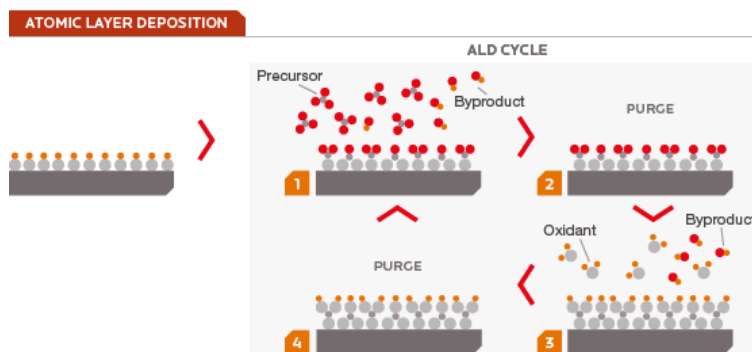


Figure 1.8: Atomic layer deposition principle [54]

For BaTiO_3 thin films deposited by ALD, it is essential to have volatile and thermally stable precursor compounds. The diversity of volatile and thermally stable compounds of the larger alkaline-earth metals is still rather limited. The ALD method has advantages such as self-limited reaction that makes it possible to deposit thin films of uniform thickness. The low processing temperatures of ALD perovskites are generally not sufficient to crystallize the film. Therefore, it is necessary to develop an appropriate crystallization treatment to achieve high dielectric permittivity. ALD perovskites can be easily contaminated by carbonates and hydroxides, which can increase the leakage current of the film

[55]. Contamination during the ALD process is possible owing to incomplete removal of the precursor ligand. Though dielectric constants as high as 200 were achievable for BaTiO₃, these films which exhibited relatively high leakage currents [56, 57] due to the inclusion of cracks induced by large crystalline grains. Studies on compositional variations revealed that a relative enrichment of A-site cations (Ba, Sr) allows high permittivity values while preserving low leakage currents [54]. This strongly influences the crystallization temperature and texture of the crystallized samples. Plasma treatments have also been addressed as a solution to achieve the desired crystal phase and dielectric properties, overcoming crack formation and related drawbacks in leakage currents and film damage.

Metalorganic Chemical Vapour Deposition

The metal-organic chemical vapour deposition (MOCVD) is a CVD technique using organo-metallic precursors. The principle of MOCVD is to realise the contact between volatile compound material to be deposited and a substrate heated under vacuum. Precursors are transported to the substrate by the carrier gas (Ar or N₂) and then are adsorbed on the substrate surface (Figure 1.9). The reactive species thus diffuse at the surface to preferential sites and react in heterogeneous phase to give rise to the formation of the film. The volatile products of the reaction are discharged through the gas flow vector. The aerosol thus formed is vaporised in a flash evaporator. The vapours obtained are transported via a gas mixture consisting of a neutral carrier gas (N₂ or Ar) and a reactive gas in the deposition chamber where they decompose to form a layer on the substrate.

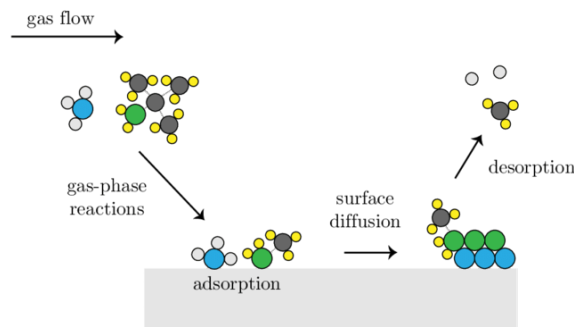


Figure 1.9: Metal-organic chemical vapour deposition principle. [58]

This deposition technique is very promising because it allows good control of the chemical composition, high deposition speed, over large surfaces, and homogeneity of the film for complex topographies. However, the implementation of this method can be complex due to the toxic nature of the precursors for BaTiO₃.

It can be achieved textured [59, 60] or even epitaxial films [61] depending on the substrate. Moreover, very low leakage currents were obtained by Dietz, Ehrhart and Gilbert [60–62].

Sol-gel

Sol-gel (short for solution-gelation) is a technique where the reagents of the material to be deposited are in the form of a solution and when it is spread on the substrate, a gelation reaction will occur. Several types of sol-gel exist such as dip-coating, aerosol-gel, or spin-coating. The latter is the most common, its process follows the following steps, summarized in Figure 1.10.

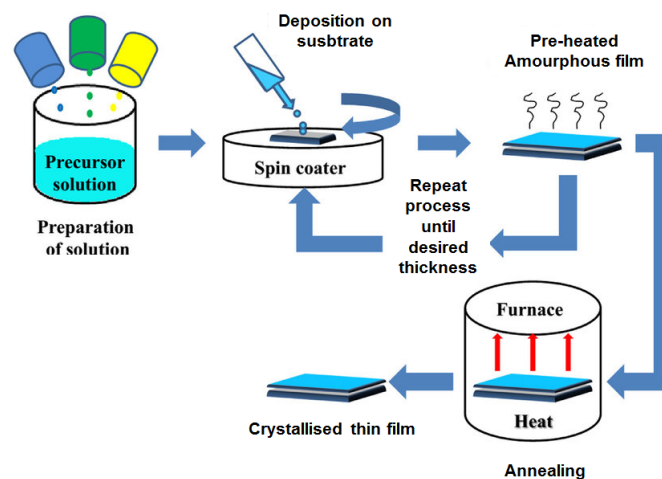


Figure 1.10: Sol-gel principle. [63]

One of the main advantages of sol-gel deposits is their low cost, which makes them very competitive for industrial integration of ferroelectric thin films for the realization of tunable capacitors. They also allow good control of chemical composition and residual stresses to be obtained for large deposition surfaces [64, 65]. Moreover, low loss and low leakage currents are attainable [66, 67]. However, it's a slow process, as an annealing is necessary for crystallisation, and due to its nature, impurities are commonly found.

Hydrothermal reaction

Hydrothermal synthesis is a wet-chemistry technique that produces complex inorganic oxide powders in supercritical state and/or sub-critical state. By changing the reaction variables such as reaction temperature, reaction pressure, mineralizer

concentration and additive concentration, nucleation and/or crystal growth rates can be controlled easily in the hydrothermal process [68]. A diagram of the hydrothermal synthesis process is resumed in figure 1.11.

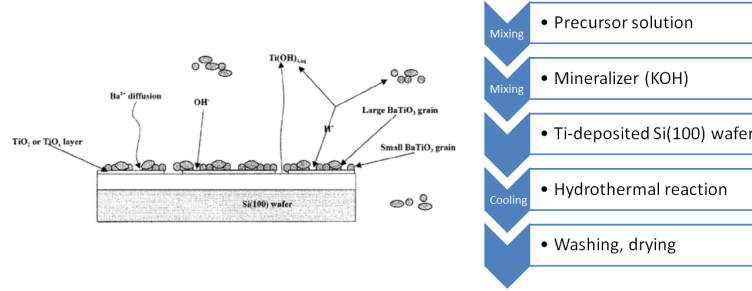


Figure 1.11: Hydrothermal reaction principle [69, 70]

Hydrothermal processing is able to synthesize BaTiO₃ crystalline structures at significantly lower temperatures in strong alkaline solutions. In all studies, planar Ti films were deposited and utilized as a precursor. The Ti template must be thick enough so that it does not enable full consumption, as complete dissolution will occur and a continuous BaTiO₃ film will not deposit on the underlying substrate. Nonetheless, moderate dielectric permittivities with fairly low dielectric losses are achieved with this technique [69, 71, 72].

1.2.2 Interface effects

One of the main purposes in the electronic industry is to reduce the size of capacitors while keeping high permittivity of insulators to provide a high capacitance per unit area. Unsuccessfully, most of the lead-free high dielectric materials, such as SrTiO₃, BaTiO₃ or (Ba,Sr)TiO₃, have smaller permittivity than expected.

Dead layer

One of the main reasons of this, it is the presence of a low permittivity layer at the interface with the electrodes, the so called "dead layer" [73]. Experimental literature have found that the "dead layer" have a thickness of around 5-10 nm [74–78], while first principle calculations consider a smaller thickness of 1nm [79–81]. Nevertheless, the addition of a low permittivity layer to the capacitor reduce substantially the global permittivity. Such a system can be described by capacitors in series corresponding to the different layers:

$$\frac{1}{C_t} = \frac{2}{C_d} + \frac{1}{C_b} \quad (1.1)$$

where C_t is the total capacitance, C_d the capacitance of a dead layer created at the interfaces metal/insulator and C_b the bulk BaTiO₃ capacitance.

The origin of this dead layer is still not fully understood, and different views have been the subject of hot debate in the literature. For some, the origin of this dead layer is entirely extrinsic, taking its origin from defects and imperfections linked to the deposition or integration process, such as oxygen vacancies, dislocations or secondary phases [82–86]. Several experimental results in literature [87, 88] point out that epitaxial growth can indeed significantly sharpen the form of the peak in dielectric permittivity versus temperature, and raise the peak of the dielectric permittivity closer to single crystal values. Moreover, Scott et al. showed that a thin layer of a BaTiO₃ single crystal of the order of a hundred nanometers exhibits a dielectric response similar to that of a bulk [3].

Moreover, it is clear that the choice of the electrode plays a role on the defects created at the interface with the insulator. Spaldin et al. [89] carried out ab initio calculations of the dielectric properties of SrRuO₃/SrTiO₃/SrRuO₃ and Pt/SrTiO₃/Pt nanocapacitors and found that the dead layer effect is reduced by a factor of four for electrodes made of elemental metals (such as Pt) as electrodes. These results suggest that electrodes with shorter electronic screening length, e.g. Pt or Au, are the best candidates for reducing the dead layer.

Grain size

Another parameter that can explain the modification of the dielectric properties of the thin film insulator is the size of the grains. In a polycrystalline ferroelectric material, the grains, considered as crystallites with a crystalline order at a large distance, have a high permittivity ϵ_G , while the grain boundaries that surround them, which have many defects or variations in composition, have a much lower permittivity.

In thin polycrystalline films, the grain size varies from tens to hundreds of nanometers, significantly smaller than that of ceramics, which can range from a few microns to hundreds of microns. Thus in the case of thin films, the ratio of grain volume to grain boundary volume will be much lower. The effect of this volume ratio on the overall permittivity of the layer will depend on the morphology of the grains, and can be described by different models of two-component composites [7].

In the case of columnar grains, the system can be described by an equivalent model with two capacitors in parallel [90], one of high permittivity corresponding to the grains, and the other of low permittivity corresponding to the grain boundaries. The total permittivity of the ϵ_t layer is expressed by the following equation:

$$\varepsilon_t(v) = (1 - v)\varepsilon_G + v\varepsilon_{GB} \quad (1.2)$$

where v is the volume fraction of the grain boundaries and ε_{GB} the mean permittivity of these. The decrease in grain size leads to an increase in v , and therefore a drop in the apparent permittivity of the material. This grain size effect has been explored by many authors in ferroelectric thin films, and Sinnamon et al. notably raised the possibility that the effect of the dead layer, observed on the permittivity by varying the thickness of the layers, was in fact only a grain size effect [91]. Gervorgian's group showed that the size of the grains had a direct effect on the decrease in the transition temperature [88].

Stoichiometry

One of the difficulties when transferring the ceramic to a thin film is to maintain the material stoichiometry. This factor is even more important for ferroelectric materials whose properties are highly temperature dependent. Therefore inhomogeneities of compositions, or gradients of compositions can affect the dielectric properties of the layers, by widening the ferroelectric transition peak or by shifting the Curie temperature [7].

Strain

The thin film is mechanically connected to a substrate, which can exert stress on the thin film. This stress can vary the lattice parameters, and stabilize the material in a certain phase. In some cases, it can be such that it can cause large shifts in Curie temperature, as shown by Haeni et al. which made an epitaxial layer of SrTiO_3 on DyScO_3 highly strained making it ferroelectric at room temperature [92]. Today, this stress, induced by the difference in lattice parameters and thermal expansion coefficients of the substrate and the layer, is considered to be the main source of modification of the dielectric properties between the same layers deposited on different substrates [93, 94].

1.3 Space charges

In the interface regions, electrochemical interactions between the conductive electrodes and the charge carriers of the thin film can take place. A decrease in electron density can occur in this area, called depletion, creating charged regions called space charge region. This phenomenon can originate from the presence of surface states, induced in particular by the presence of oxygen vacancies [95], or in analogy to semiconductor models, to the difference in work function between the ferroelectric material, a high gap material, and the metal of the electrode [96].

This space charge zone can influence the dielectric and ferroelectric properties of films [97–99]. Indeed, an internal electric field results from this charged zone, creating a local polarization at the interface and thus influencing the permittivity of the material. Using a model of series capacitors identical to the one in section 1.2.2 it is possible to see the impact of this layer on the permittivity [7].

A similar effect is seen in the case of giant-dielectric phenomenon. Subramanian et al [100] found a high permittivity of around 12000 in $\text{CaCu}_3\text{Ti}_4\text{O}_{12}$ (CCTO) ceramics which, when measured at 1 kHz, remained constant between 100K and room temperature. The authors also reported a drastic decrease in the room temperature permittivity with increasing measuring frequency or decreasing temperature. These results are shown in Figure 1.12.

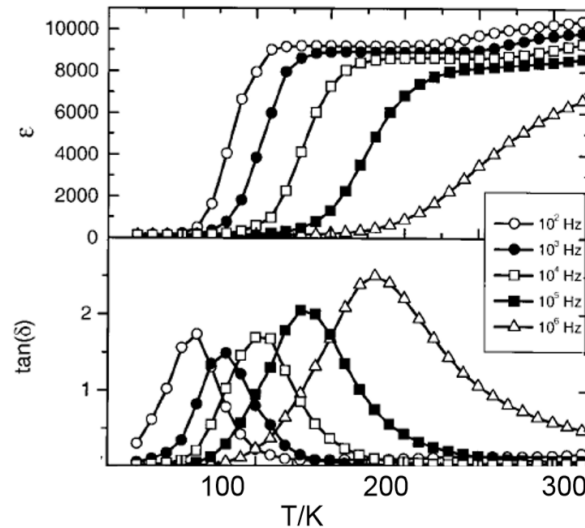


Figure 1.12: Frequency dependence of the dielectric permittivity of CCTO. The dielectric loss is also reported. Colossal permittivity is clearly measured with large loss (>1). [100]

Although the origin of the large permittivity of the CCTO system is well known to be due to extrinsic mechanism, such as grain boundaries, twinning

boundaries (domain walls) and interfaces with electrodes, the physical origin of this interfacial polarisation is not fully established. Nonetheless, we can say that interfaces (grain boundaries, domain walls or electrodes) play again a major role in the dielectric properties of the CCTO system. However, applications of CCTO in modern electronics seem to be limited due to large loss and weak permittivity at frequency beyond megahertz.

In the BaTiO₃ thin films, it has already been reported the existence of space charges at the electrodes interfaces. Trithaveesak et al found out a frequency dependent dielectric properties when measuring in a wide range of temperatures [101]. They pointed out that BaTiO₃ capacitors are strongly influenced by the interaction with the interfaces to the electrodes. Moreover, Qiao and Bi found a high frequency dependence of the Curie Temperature on highly oriented BaTiO₃ films, indicating a diffusive characteristic, probably due to oxygen vacancies induced structural disorders and compositional fluctuations in the film during the sputtering [72].

Even though these results are unpromising for space charge related films, these space charges are either created at the interface of the electrodes. Our main goal is to restore or induce large (artificial) dielectric permittivity without increasing losses in BaTiO₃ thin films electronically, that is to say, using n-p junctions. Indeed, it is possible to induce space charge regions using doping of different nature. As BaTiO₃ can be considered a large band gap semiconductor, it is possible to dope it to modify its conductivity. To better understand this, we need to recall the main properties of semiconductors.

1.4 Fermi level position in semiconducting oxides

1.4.1 Electronic structure

A band gap, also called an energy gap, is an energy range in a solid where no electronic states can exist. The band gap is often displayed in graphs of the electronic band structure of solids, and it generally refers to the energy difference (in electron volts) between the top of the valence band and the bottom of the conduction band in insulators and semiconductors. In other words, it is the energy required to promote a valence electron bound to an atom to become a conduction electron, which is free to move within the crystal lattice and serve as a charge carrier to conduct electric current. Materials with large band gaps are generally insulators, those with smaller band gaps are semiconductors, while conductors either have very small band gaps or none, because the valence and conduction bands overlap.

The band gap of a semiconductor can be of two basic types, a direct band gap or an indirect band gap (see figure 1.13). The minimal-energy state in the conduction band and the maximal-energy state in the valence band are each characterized by a certain crystal momentum (k -vector) in the Brillouin zone. If the k -vectors are different, the material has an "indirect gap". The band gap is called "direct" if the crystal momentum of electrons and holes is the same in both the conduction band and the valence band. The nature of the band gap is mostly important for the optical properties of semiconductors [102].

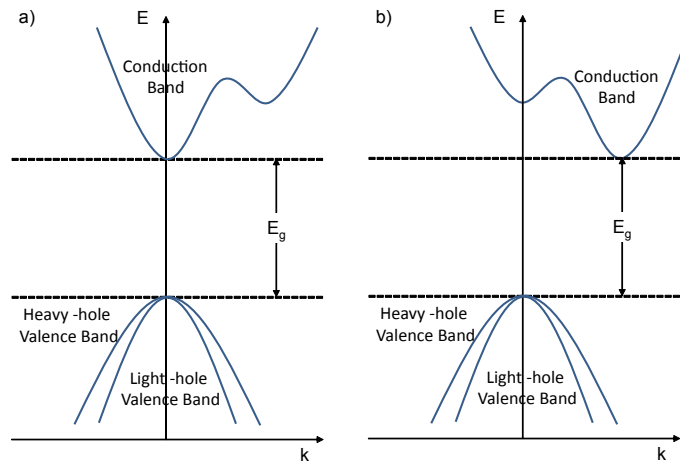


Figure 1.13: a) Direct bandgap material. b) Indirect bandgap material [102]

Examples of direct bandgap materials include amorphous silicon and some III-V materials such as InAs, GaAs. Indirect bandgap materials include crystalline silicon and Ge. The electronic structure of a material is often described by the

position of the energy bands such as the conduction and valence band and the energy gap. Moreover, for better understanding of the electric nature of a material, the position of its Fermi level is given. The Fermi energy of a material is the term used to describe the top of the collection of electron energy levels at absolute zero temperature (see Figure 1.14).

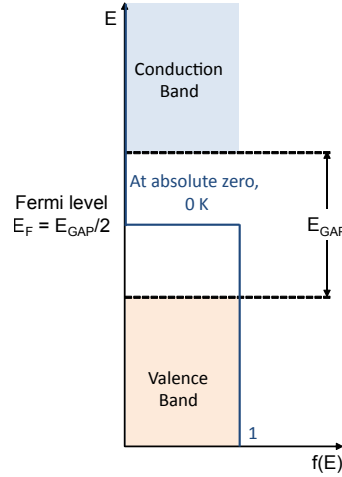


Figure 1.14: Fermi Dirac distribution at absolute zero 0 K.

This concept comes from Fermi-Dirac statistics. Since electrons are fermions and by the Pauli exclusion principle they cannot exist in identical energy states. So at absolute zero, they pack into the lowest available energy states and build up a "Fermi sea" of electron energy states. The Fermi energy is the top energy level of that sea at absolute zero where no electrons will have enough energy to rise above.

$$f(E_i) = \frac{1}{1 + e^{(E_i - E_f)/k_B T}} \quad (1.3)$$

where T is the absolute temperature and k_B is the Boltzmann constant. This function gives the probability $f(E_i)$ of an electron to occupy an energy state E_i . The Fermi level determines the probability of electron occupancy at different energy levels. For solids, the probability of occupancy with the energy level determines the ease of conductivity; whether a material is an insulator, semiconductor, or conductor. The Fermi level is referred to as the electron chemical potential. The conductivity can also be affected by factors such as temperature and purity. From the distribution, the temperature has a direct effect on how the energy states are populated. When temperature increases the tail of the exponential gets longer and wider, thus making the conduction band level population more accessible, as seen in Figure 1.15.

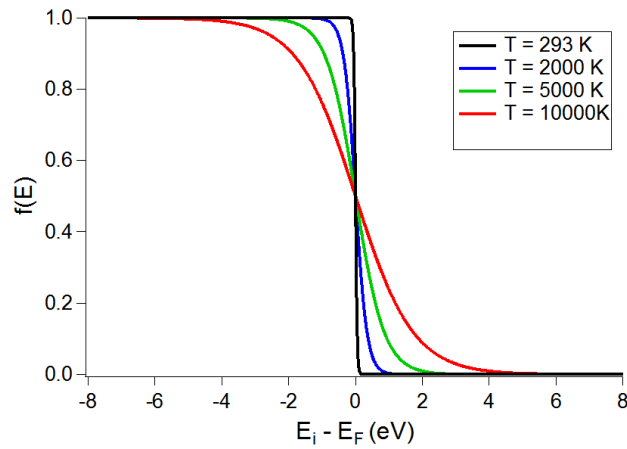


Figure 1.15: Fermi Dirac distribution at different temperatures.

The ability of semiconductors to conduct electricity can be greatly improved by introducing donor or acceptor atoms to the crystalline structure, either producing more free electrons or more holes. This process is called "doping" and as the semiconductor material is no longer pure, these donor and acceptor atoms are collectively referred to as "impurities". By carefully designing the doping process, semiconductor crystals can be modified into one of two distinct types of semiconductors: N-type or P-type (see Figure 1.16).

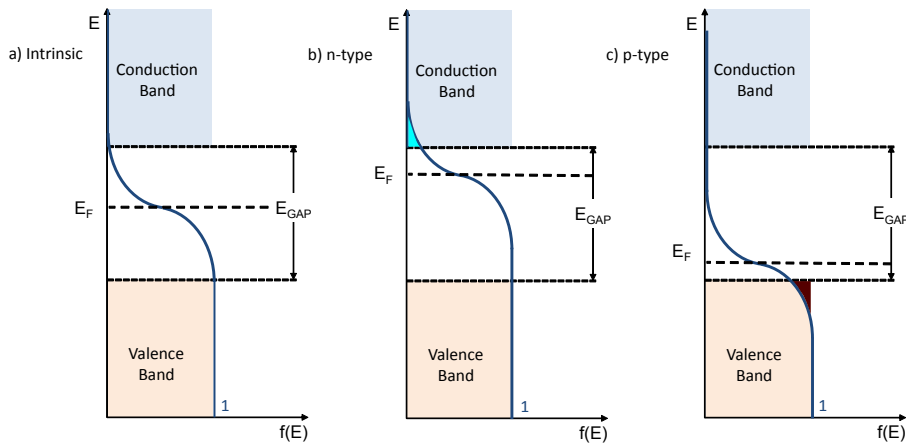


Figure 1.16: Fermi Dirac distribution and Fermi level position for different doping types: a) Intrinsic, b) n-type and c) p-type

In both semiconductor types, the position of the Fermi level relative to the band structure can be controlled to a significant degree by doping. Introducing donor impurities will bring the Fermi level up and when it is brought high enough,

part of the tail of the energy distribution will go over to the conduction band (c.f. Figure 1.16). This makes it easier for electrons or holes to travel to the conduction or valence band, respectively, and thus conductivity will improve.

In experimental study, the band gap of tetragonal BaTiO_3 has been reported around 3.20 eV and can be categorized as an indirect band gap.

Figure 1.17 shows the full potential-linearized augmented plane wave (FP-LAPW) method in the framework of the density functional theory (DFT) to calculate the electronic structure of BaTiO_3 [103]. This DFT method yielded an indirect band gap of 2.30 eV which is lower than the experimental value of 3.2 eV. The electronic structure was calculated using the experimental lattice constant ($a_0 = 3.9945 \text{ \AA}$ and $c_0 = 4.0335 \text{ \AA}$).

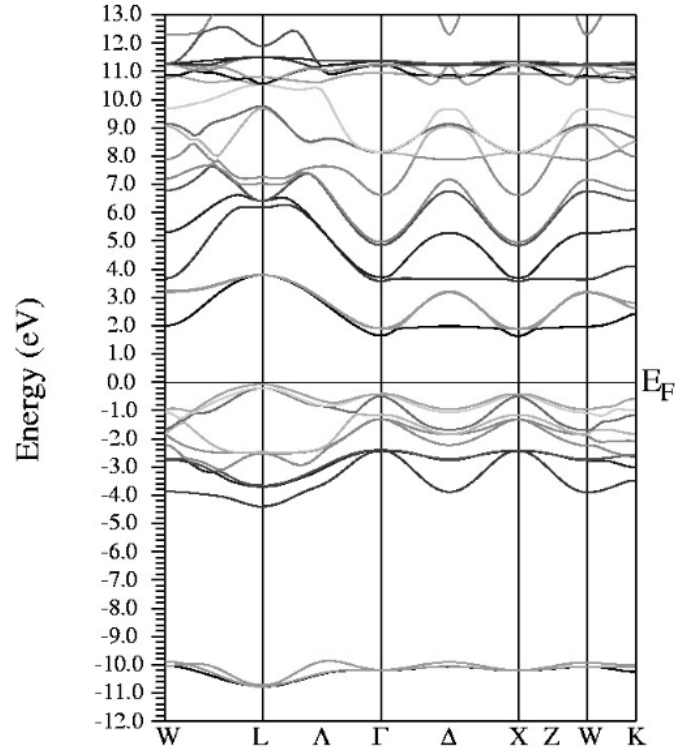


Figure 1.17: Electronic structure of BaTiO_3 calculated with density functional theory (DFT) with the generalized gradient approximation (GGA). Taken from [103]

We can clearly see an indirect bandgap between the bottom of the conduction band at the Γ point and the top of the valence band at the L point.

1.4.2 Ionization defect levels

As stated before, the Fermi level position can be adjusted by doping, imposed electric fields, photostimulation, and other factors. Thus, the ionization state of the defect can often be controlled. If the defect possesses significant capacity to store excess charge within its structure, the range of ionization states can be quite large. Some defects have eigenstates close to the edges of the valence band or conduction band; For defects having eigenstates deeper within the band gap of the semiconductor, a more detailed quantum mechanical treatment is needed. For many purposes, the concentration of defects in a given charge state must be known. This concentration requires use of Fermi statistics. In an ideal intrinsic (undoped) semiconductor, the Fermi energy E_F takes the value

$$E_F = \frac{E_C + E_V}{2} + \frac{kT}{2} \ln \left(\frac{N_V}{N_C} \right) \quad (1.4)$$

where E_C is the energy at the bottom of the conduction band, E_V is the energy at the top of the valence band, and N_V (N_C) is the effective density of states in the valence (conduction) band. For intrinsic material, the Fermi level lies approximately in the middle of the band gap. The product of the two charge-carrier concentrations is independent of the Fermi level and obeys:

$$n_i^2 = n \times p \quad (1.5)$$

where n_i (p_i) is the intrinsic concentration of electrons (holes). Clearly, in undoped material, the concentrations of electrons and holes are equal.

In doped material, the electron and hole concentrations are no longer identical. Boltzmann statistics can be used under most conditions to approximate Fermi statistics and obtain a probability that a state is occupied by an electron. The electron and hole concentrations can also be approximated by:

$$n = N_C \times e^{\frac{E_F - E_C}{kT}} \quad (1.6)$$

$$p = N_V \times e^{\frac{E_V - E_F}{kT}} \quad (1.7)$$

When n and p are varied by doping, the Fermi level either rises toward the conduction band (made more n-type) or falls toward the valence band (made more p-type). This variation in Fermi energy must be taken into account when calculating the concentration of charged defects in the bulk.

Fermi-Dirac statistics apply to the calculation of charged defect concentrations as follows. Take, for instance, the ionization of an acceptor defect "X" to X^{-1} , which can be represented by the reaction:



In particular, the ionization level equals the value of the Fermi energy at which the concentrations of the two charge states are identical (to within a degeneracy factor).

Clearly the charged defect concentrations vary with T .

The fact that the concentration of a charged defect depends upon its charge state and the position of the Fermi energy implies related dependencies in the defect's formation energy. After all, there is work involved in moving an electron from the Fermi energy into the energy state associated with the defect. When considering a surface defect as opposed to a bulk defect, all the same basic principles apply except that the value of the Fermi energy at the surface (which often differs from that in the bulk) determines the concentrations of various ionization states.

Semiconductors often contain intentionally introduced dopant atoms or accidentally introduced impurity species that alter the type and amount of charged defects in the bulk. Doping can change the predominant charge state of intrinsic bulk defects or introduce new extrinsic defects. The location of these new defects within the semiconductor depends on dopant or impurity atomic radius, charge, and bulk crystal structure. While some atoms prefer to reside in substitutional sites, replacing atoms on the crystal lattice, others assume interstitial configurations. Dopant and impurity atoms can remain as isolated point defects or join with each other (or intrinsic defects) to form defect complexes.

Dopants are frequently characterized as either "shallow" or "deep." A shallow donor implies a (+1/0) ionization level that lies very close to the conduction band. A deep donor implies a (+1/0) ionization level lying within the band gap much further from the conduction band minimum. These expressions translate for acceptor defects except that shallow and deep, instead, refer to the distance between the defect ionization level and the valence band maximum.

Fermi level pinning

Fermi level pinning refers to a situation where the band bending in a semiconductor contacting a metal is essentially independent of the metal even for large variation in the work function of the metal [104]. Fermi level pinning is a well-known phenomenon, which indicates the independence of Schottky barrier heights at semiconductor/metal interfaces. The degree of Fermi level pinning is often characterized in terms of an index of interface behaviour S , which is defined by:

$$\Phi_B = S \times X_m$$

where X_m is the electronegativity of the metal forming the barrier. The electronegativity of the metal is used here, as it reflects the local charge transfer related to the chemical bonds at the semiconductor/metal interface and does not depend on particular surface properties of the metal. The index of interface behavior S is small for strong Fermi level pinning, which is particularly pronounced for semiconductors with strong covalent bonding character [105]. Prominent examples are the elemental (C, Si, Ge) and the group III-V (GaAs and others) semiconductors, for which $S = 0.1$. Only weak Fermi level pinning $S = 1$ has originally been observed for semiconductors with more ionic bonds, including the oxides of interest here. The different magnitude of the interface index S has been related by Cowley and Sze to a different density of interface states [104]. The interface states are electronic states in the band gap of the semiconductor, which are separated from the crystallographic interface by a distance d_i . The calculation of Cowley and Sze provided the well-known dependence of the barrier height given by:

$$\Phi_{B,n} = S \cdot (\Phi_{met} - X_{sc}) + (1 - S) \cdot (E_{CB} - E_{CNL})$$

where $\Phi_{B,n}$, Φ_{met} , X_{SC} and E_{CNL} are the barrier height for electrons, the work function of the given metal, the electron affinity of the semiconductor and the charge neutrality level respectively. E_{CNL} is associated with the interface states, which are intrinsic to the semiconductor/metal interface, can be considered as a fundamental material parameter in the Schottky barrier determination [106].

1.5 Conduction mechanisms in semiconducting oxides

Various models and transport mechanisms have been proposed to explain the current-voltage characteristics of metal-ferroelectric oxide-metal junctions [107–113]. Nonetheless we can group these models in 2 types of conduction: 1) bulk controlled mechanisms such as space charge limited currents, Poole-Frenkel emissions, ionic conduction, ohmic conduction, grain boundary limited conduction, hopping conduction; and 2) interface controlled mechanisms such as Fowler-Nordheim tunneling, direct tunneling, Schottky emission, thermionic-field emissions or any combination of these. Among all of these conduction mechanisms, the most common found in literature for ferroelectric oxides are: for bulk, Poole-Frenkel emission and for interface controlled mechanisms, Schottky emission and thermionic field emission [107–113].

It is worth noting that doping in BaTiO₃ and the nature of the dopant may change the conduction mechanisms. The next models that are presented are the general conduction mechanisms in ferroelectric materials. This is a non-exhaustive list of models, which are the most cited in literature as these conduction models were the first developed as they were created first for the classical semiconducting industry (Si, Ge, etc).

1.5.1 Richardson-Schottky conduction model

The Richardson-Schottky's model is arguably the most widely found in the literature for ferroelectric materials, in which the current is due to the thermionic injection of electrons from the electrode into the thin insulating layer. A potential barrier Φ_0 is formed at the interface between the ferroelectric layer and the electrode, representing the difference between the Fermi level of the metal and the conduction band minimum of the insulator. When a potential is applied to the electrode, the barrier is lowered by the electrostatic force of the applied field, which will allow a flow of carriers to pass through the barrier. In the case of the Richardson-Schottky mechanism, conduction is governed by charges thermally injected at the interface. The evolution of the current is described by the equation:

$$J = A^* T^2 \exp\left(\frac{-q\phi_B}{k_B T}\right) \exp\left(\frac{q \sqrt{\frac{qE_{ext}}{4\pi\epsilon_0\epsilon_r}}}{k_B T}\right) \quad (1.9)$$

with $A^* = \frac{4\pi q k^2 m^*}{h^3} = \frac{120 m_e}{m_0} \text{Am}^{-2}\text{K}^{-2}$

where A^* , q , ϵ_0 , k_B , m^* , m_0 and h correspond respectively to the Richardson constant, the charge of the electron, the vacuum permittivity, the Boltzmann

constant, the effective electron mass, the rest electron mass and the Planck's constant, T is the temperature and E_{ext} the external electric field. The two physical quantities that will need to be determined are ϕ_0 the barrier height and ε_r the dielectric permittivity at optical frequencies [102].

1.5.2 Thermionic field emission models

This model was developed by Simmons [114] by pointing out that in insulators the electron energy is not conserved across the interspace between electrodes, that is to say, the electronic mean free path in the insulator is not very long, i.e., less than the insulator thickness. For this configuration, the electron mobility is necessary to describe the J-E characteristic as shown in equation 1.10

$$J = A^* \sqrt{\frac{2\pi m^*}{k_B}} T^{3/2} \mu E_{ext} \exp\left(\frac{-q\phi_B}{k_B T}\right) \exp\left(\frac{q\sqrt{\frac{qE_{ext}}{4\pi\varepsilon_0\varepsilon_r}}}{k_B T}\right) \quad (1.10)$$

$$\text{With } A^* = \frac{4\pi q k^2 m^*}{h^3} = \frac{120m_e}{m_0} \text{Am}^{-2}\text{K}^{-2}$$

(same as in Schottky emission) where μ is the mobility of the insulator and all other characters remain the same.

It is noted that there is no clear distinction in this case between the bulk-limited and electrode-limited processes, because each part plays a role in the conduction process. The density of the free carriers at the interface is electrode limited, while the mobility is a bulk property.

1.5.3 Poole-Frenkel emission model

The Poole Frenkel emission is a volume controlled conduction mechanism. The charges are emitted by discrete donor levels of the band gap, associated with defects. These defect levels are called traps. This emission is of the thermionic type, where the height of the crossed barrier, called the height of the trap, corresponds to the energy difference between the localized state and the conduction band. The emitted electron then migrates briefly through the material before being trapped again at a localized energy level. The current density is a function of temperature and electric field as it follows:

$$J = q\mu N_c E_{ext} \exp\left(\frac{-q\phi_t}{k_B T}\right) \exp\left(\frac{q\sqrt{\frac{qE_{ext}}{\pi\varepsilon_0\varepsilon_r}}}{k_B T}\right) \quad (1.11)$$

where μ and N_c are the mobility and density of carriers in the conduction band, respectively. The physical parameters to be determined are ϕ_t the height of the barrier between two traps, and ε_r .

1.5.4 Tunneling Effect

There are two types of tunneling effect, the indirect tunneling effect also called Fowler-Nordheim and the direct effect in the case of very thin films. In the case of Fowler-Nordheim tunneling, the charges from the electrode are injected into the conduction band of the oxide by crossing the potential barrier. They therefore need a significant amount of energy and the current density depends on the height of the barrier and the applied field, but is independent of the temperature as shown in equation [1.12](#)

$$J = \frac{q^2 E_{ext}^2}{8\pi h \phi_0} \exp\left(\frac{-8\pi\sqrt{2m^*}q\phi_0^{3/2}}{3hE_{ext}}\right) \quad (1.12)$$

In summary, when a potential is applied to the electrode, the barrier is lowered by the electrostatic force of the applied electric field, which will allow a flow of carrier to pass through the barrier (Richardson-Schottky), over the barrier (Thermionic field emission), crossing the potential barrier (Tunneling) or by carriers which are thermally emitted from trap levels (Poole-Frenkel). These conduction models are resumed in figure [1.18](#)

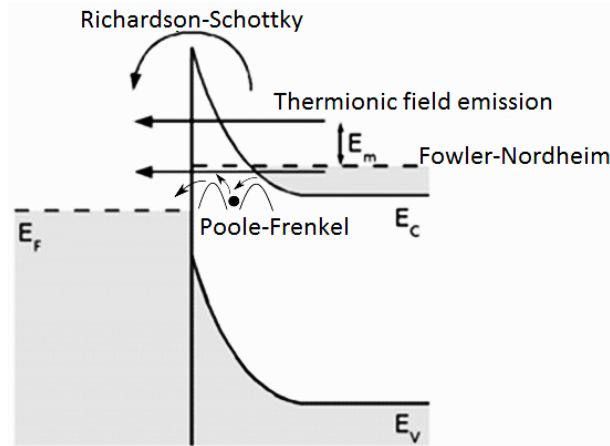


Figure 1.18: Schematic band diagram of a Metal / Insulator structure under the effect of an electric field illustrating various conduction mechanisms

1.6 Enhancement of the dielectric permittivity in BaTiO₃

There are many strategies to improve the dielectric properties of BaTiO₃ films such as the addition of simple oxides such as MgO, ZrO₂, MnO₂, La₂O₃, TiO₂ or SiO₂, the addition of an interfacial layer, the reoxidation by annealing at different oxygen partial pressure and lastly, doping.

The first method was developed by introducing a secondary phase of MgO, TiO₂, ZrO₂ or Al₂O₃ [115-119], and while this method decreases effectively the dielectric losses, it also decreases the relative permittivity. An interfacial layer have been used to decrease the dielectric loss by introducing a layer of a low-loss material, such as SiO₂ [120], MgO [121], TiO₂ [122], CeO₂ [123] or Ta₂O₅ [124, 125], between the ferroelectric thin film and the electrode. However, this will heavily decrease the relative permittivity of our thin film.

Compensating the oxygen vacancies of our ferroelectric film would drastically improve its properties, especially its conductivity and its dielectric losses. Depositing BaTiO₃ by magnetron sputtering under different partial pressures of oxygen have shown that this parameter makes it possible to optimize the properties, with in particular a reduction in leakage currents for the higher O₂ / Ar ratio and lower Fermi level positions [39].

The most commonly used method to improve dielectric properties and leakage currents is by the doping of the material. This consists of the substitution of the A-site (Ba²⁺) or B-site (Ti⁴⁺) of the perovskite by another element (heterovalent substitution). The doping site is primarily determined by the ionic radius of the doping element. Two types of doping can be distinguished: donor doping or acceptor doping. Since this will be our main strategy to improve the properties of our films, this will be further developed in section 1.6.2.

Firstly, we will discuss how these doping elements will affect the chemistry of BaTiO₃.

1.6.1 Defect chemistry in ferroelectrics

If an ion is replaced by a different ion of different valence, it is called aliovalent which it can be separated in two groups: acceptors, which their charge is less than that of the cation they replace (Mn³⁺/Ti⁴⁺) and donors, in the contrary case (Nb⁵⁺/Ti⁴⁺). After replacement, charge neutrality is conserved by either oxygen vacancies (V_O) or generation of free electrons/holes.

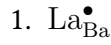
Isovalent ions are such that when introduced to the lattice they substitute a different ion of the same valence (Sr²⁺/Ba²⁺).

Aliovalent cation impurities and their effects on the defect chemistry of fer-

roelectric materials, specially on the generation of free charges, are the most common in literature. Nonetheless, isovalent cation are mostly common for substitution as they have no first order effect on the generation of free charges (charge neutrality is conserved).

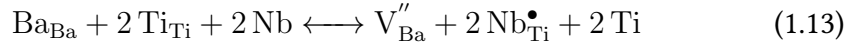
If the amount of impurities introduced in the perovskite structure is less than 1% atomic concentration, it is commonly known as doping. For higher content, the term substitution is more frequently used.

For writing chemical equations for charge neutrality when different ions are introduced to the lattice, the Kröger and Vink notation have been accepted as the most useful [126]. The next examples are used to clarify this notation.

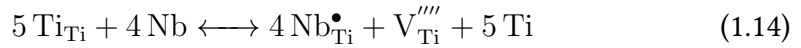


Example (1) denotes the ion La substituting a Ba ion with a positive charge denoted with a dot. Example (2) shows a titanium vacancy, denoted by the letter V with Ti as a subscript, leading to four extra negative charges.

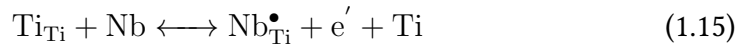
Therefore if we dope, for instance, BaTiO_3 with Nb, the following equations would arise:



Equation 1.13 indicates that Ba vacancies (ionic compensation) act as the charge compensating defect

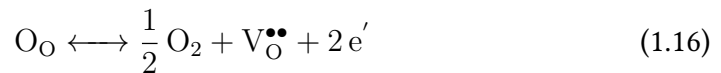


1.14 express that Ti vacancies serve as the charge compensating defect (ionic compensation)



Furthermore, equation 1.15 show that injection of extra electrons could counter balance the valence mismatch between Ti^{4+} and Nb^{5+} (electronic compensation). Thus, the conductivity is greatly increased, where the number of charge carriers is equal to the effective Nb concentration.

Lastly, equation 1.16 shows another reaction that could happen without the need of doping. This reduction reaction produces oxygen vacancies and free electrons that can contribute to the conductivity as well. Indeed, Chan et al [127], have shown that doubly charged oxygen vacancies are accountable for n-type conduction under oxygen poor conditions.



One of our goals is to improve the insulation of BaTiO₃ by doping with Mn. Indeed, thanks to the polyvalency of Mn, this dopant is able to accept both electrons from equation 1.16 giving the following equation:



Taking this into consideration, if we try to dope BaTiO₃ with an ion of different valence as to accept or give electrons, it is important to investigate the effects of the dopants on the dielectric, structure and conductivity properties on BaTiO₃.

Moreover, depending on the doping concentration, donor-doped BaTiO₃ resistivity can vary, as portrayed in Figure 1.19. Indeed, the dependence of room temperature resistivity versus dopant concentration has been largely demonstrated [128-130] but poorly understood. However, it is usually explained by a change of compensation mode from electronic compensation to ionic compensation, that is to say, from equation 1.15 to equations 1.13 and 1.14.

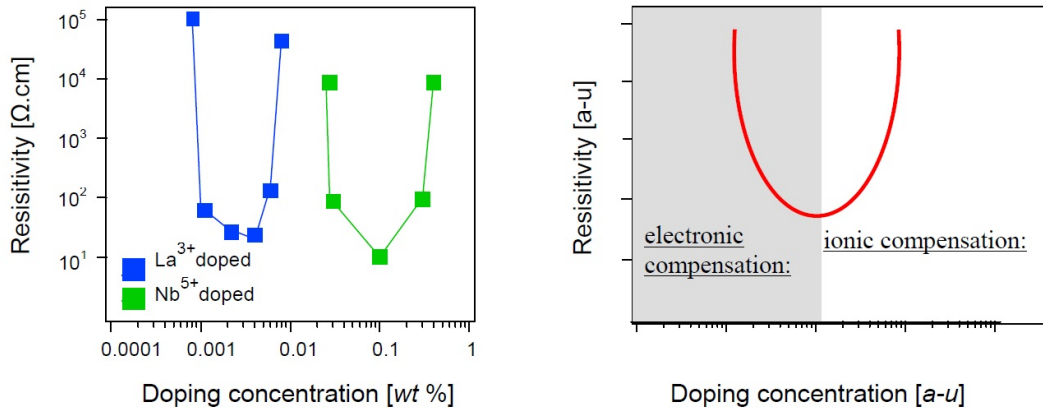


Figure 1.19: Left: Resistivity of BaTiO₃ ceramics as a function of La/Nb concentration. A resistance minimum is observed with increasing the amount of dopant [131, 132]. Right: Schematic diagram showing the change of resistivity vs. doping content and possible mechanism of compensation involve in each region of semiconductivity. From [39]

1.6.2 Heterovalent substitution

In the case of donor doping, the cations are substituted by ions of higher charge. This is the case, for example, with La^{3+} or Y^{3+} at the Ba^{2+} site or with Nb^{5+} at the Ti^{4+} site. Rather, this type of doping tends to deteriorate the desired properties, since it allows free charges to be released in the material, resulting in reduction of the titanium. This is the principle behind the PTCR (Positive Thermal Coefficient of Resistivity) effect where a drastic change in resistivity is observed with temperature [131, 133, 134]. However, a certain number of authors have shown a reduction in dielectric losses with lanthanum [135] or yttrium [136], considering that the dopant is inserted in the titanium site thus acting as acceptors, accompanied by an effect of strain for yttrium. According to some authors, donor insertion would decrease the oxygen vacancy concentration during crystallization annealing of the material [137].

In the case of acceptor doping, the cations are this time substituted by ions with a lower valence state. The idea this time is to capture a free electron, released for example during the ionization of an oxygen gap. Although a few elements such as K^+ make it possible to substitute the A site of the cell [138], a very large majority of the published studies relate to the substitution of the B site. The literature on this subject is very dense, and different categories of Elements of the periodic table have been studied. For example, noble metals have been used, with Ag [139] and Au [140] making it possible to reduce losses or leakage currents of the components studied. Rare earths have also been used, as shown in the ceramic study by Zhang et al. which compares the effect of 8 elements [141]. Finally, other metals have been investigated, such as copper [142] or aluminum [143] also showing a reduction of leakage currents.

Not all cations are able to substitute neither Ba nor Ti. In order to substitute either of these cations, it is necessary that the ionic radius of the substituting element match the Ba^{2+} or the Ti^{4+} ions. Ions of two different elements can replace one another only if their ionic radii differ by approximately 15 percent or less. Limited substitution can occur if the radii differ by 15 to 30 percent, and a difference of more than 30 percent makes substitution unlikely. These limits, calculated from empirical data [144], are only approximate. Having this into consideration, we will only look at cations with coordination XII or VI with at most 30 percent mismatch for Ba^{2+} or Ti^{4+} radii correspondingly, that is to say $1.61 \pm .48$ for cations substituting Ba^{2+} and 0.605 ± 0.18 for cations substituting Ti^{4+} .

In our first approach, we refer to the literature done in bulk ceramic BaTiO_3 , as we try to narrow down the pure effect of dopants in BaTiO_3 since it is well known that effects of impurities can be shadowed by other effects such as grain size, internal strain induced by the thin film deposition process, lattice expansion

mismatch, or local variation of stoichiometry (see full table in Annex 1).

Prominently, literature refers to La, Nb, Mn, Fe and Y. These cations will be discussed in the next section. Secondly, Sr, Ca and Zn can be classified as substitution cations, since these are mostly present in BaTiO₃ in more than 10 at. %. These won't be discussed as our goal is to dope BaTiO₃ with small amounts (less than 1 at. %) and these materials have on their own different properties than pure BaTiO₃. For the rest of the dopants (on this list), Ni, Co, Al, Bi, Mg, Nd and Ce were the most cited to this date.

Next, we will look at literature for which these dopants have been transferred to thin films. The technique used to deposit the films have an effect on the results. That is why we tried to do a list for which we covered a considerable range of methods to judge better the influence of the dopants in BaTiO₃ based films. In Table 1.1, we resumed the major results of literature of several dopants that were discerned to choose our case of study. These were principally, the leakage currents, resistivity, dielectric permittivity and dielectric losses.

Table 1.1: Literature. ϵ_r : Relative permittivity at 100kHz room temperature. Dielectric losses $\tan(\delta)$ @100kHz RT. Leakage currents J [A/cm²] at 100 kV/cm. ρ Resistivity at room temperature.

Dopant	At. %	J [A/cm ²]	ρ [Ω cm]	ϵ_r	$\tan(\delta)$	Structure	Deposition
Mn							
[145]	5	$1 \cdot 10^{-9}$		600	0.02	Poly.	PLD
[146]	0.1-1	$1 \cdot 10^{-10}$		180	0.0054	Poly	r-f
[147]	0.5			700	0.013	nano.	sol-gel
[148]	0.1-1	$2 \cdot 10^{-6}$		400	0.015	Poly	sol-gel
La							
[149]	3-10			650		poly	sol-gel
[61]	0.6		55				mocvd
[150]	1	$1 \cdot 10^{-7}$	$8 \cdot 10^6$				pld
[151]	<1		$1 \cdot 10^6$			epitax	mocvd
[152]	0.5				0.02		pld
[153]	0.1-3	$1 \cdot 10^{-4}$		500		poly	r-f
[154]	5-40		10-0.01			epitax	PLD
[155]	1-5			210-150		poly	solgel
Nb							
[151]	1.5		$1 \cdot 10^6$			epitax	
[156]	0.05		$1 \cdot 10^{11}$	200	0.03	poly	r-f
[157]	30					epitax	mbe
[155]	1			200			sol-gel

[143]	1.5	$1 \cdot 10^{-7}$					r-f
[158]	1.5		$1 \cdot 10^7$			epitax	mocvd
Fe							
[159]				280	0.5		sol-gel
[160]	1			300	0.25		sol-gel
[161]	50-75						PLD
[162]	0-1			1000-4000			sol-gel
[163]	3-20						sol-gel
Y							
[164]	0.2			1100	0.3	Poly	PLD
[165]	0.2			1300	0.03	Poly	PLD
Ni							
[166]	0.3-2			175-400		poly	sol-gel
Bi							
[167]	3-10						
[168]	2-4			100	60		
Ca							
[169]	10-30	10-100					
[170]	2-20	$8 \cdot 2 \cdot 10^{-6}$		300-250	0.018-0.014	poly	sol-gel
Ce							
[171]	50	$1 \cdot 10^{-1}$		200			
[152]	5.5			100	6		RF
[36]				7nF			PLD
[155]	1-5	$1 \cdot 10^{-3}$		240-300	0.03	poly	solgel
Co							
[172]	0,25-1			200	0.04	poly	CSD
[173]	2-10			230	0.013	poly	CSD
[174]	.5-10			450 to 250	0.1 to 0.03	poly	sol-gel

Looking at the main results from literature in Table 1.1, Mn doping offers the lowest leakage currents with fair values of permittivity. La [61, 153, 154], Nb [155, 157, 158] and Fe [162] doping is able to increase greatly the conductivity if the doping is in a window of doping concentration. Indeed, Nb and La doping may be electronically compensated or ionically compensated (see section 1.6.1). Y is also known for its PTCR effect, but in literature it has only been reported with high concentration which displays high

permittivity. Lastly, Bi, Ca, Ce, Ni and Co displayed mid-range values of permittivity and fairly low dielectric losses without any particular effect.

Many criteria influenced the choice of dopants used in this work: feasibility on the incorporation of dopant in BaTiO₃ (no secondary phases), low leakage currents, low resistivity, high permittivity and low dielectric losses. High values of permittivity found in literature may be attributed to the quality of the film (crystallinity/space charges). These values can be discarded when looking at dielectric losses. If the dielectric loss is high (more than 0.1), the value of the given permittivity is an extrinsic effect and should not be attributed to the effect of doping nor as an intrinsic property [see section 1.3].

1.6.3 Mn, Nb, Fe and La BaTiO₃ doping

As already mentioned the number of possible substitutions in BaTiO₃ is extensive. As our scope is to use interfacial effects to increase the effective permittivity of BaTiO₃-based multilayers, we will focus on heterovalent substitutions to provide free charges and/or create a space charge region. A survey of the available literature in the field of heterovalent substitution in ceramics is given in Annex 1. In the present part, we will restrict the discussion on a limited number of cases. This choice has been guided by various reasons: the long-term knowledge about particular dopants and the feasibility of magnetron sputtering deposition of films and multilayers and the electronic properties (such as the ionization defect level). The obvious restriction was also to be able to process a large number of films and multilayers and to characterize the interface electronic states. The first dopants that could fit these restrictions is Fe, which could act as an acceptor dopant electronically. Indeed, it has long been used as a substitution to Ti⁴⁺ in single crystals to enhance the photo induced electronic charges among the multivalency states of Fe: Fe⁴⁺, Fe³⁺, Fe²⁺ [175]. High purity single crystals were produced with a very low amount of residual point defects and controlled Fe doping up to about 0.2 at.%. Electronic space charges could be generated in such single crystals using laser interferences patterns whose modulated intensity could localise electronic charges. Fe is thus a candidate for the generation of space charges at interfaces in BaTiO₃- based multilayers. Moreover, in Fe-doped BaTiO₃ based ceramics, the presence of this dopant reduces the Curie temperature to 320 K, the maximum permittivity ϵ_m and the dielectric loss [162]. Furthermore, samples highly substituted (content above 1 atomic percent) exhibit paramagnetic behaviour and over 30 atomic percent a clear ferromagnetic transition has been observed and an effective paramagnetic moment of 6.1 μ_B [176]. We however decided not to use this dopant because of the existence of several and very close ionisation states between 2+, 3+ and 4+. In our conditions of deposition (oxygen-poor film deposition and the use of Pt electrodes), it is difficult to stabilize well-defined ionisation states. Indeed, two ionization states are possible: Fe^{3+/4+} with a defect level calculated at 0.8 eV and Fe^{2+/3+} with a defect level of 2.4 eV has been calculated [177]. The use of Pt electrodes make it difficult to stabilize the first ionization state as the Fermi level will be pinning at around 2.0 eV. The second one can be stabilized with Pt electrodes, however, if we wish to create an effective space charge region and trap electrons with Fe ions, this task will be rather difficult as the Fermi

level would be higher than it is desired. The next candidate to be an acceptor dopant is Manganese, having ionization states 4+, 3+, 2+ and ionic sizes fully compatible with the octahedral Ti^{4+} site. Mn has long been used in BaTiO_3 ceramics and reached the mass production of Multilayer Ceramic Capacitors (MLCC) to decrease the intrinsic dielectric losses of BaTiO_3 mainly resulting from native oxygen vacancies [178–181]. The trapping of free electrons by Mn level located deep in the BaTiO_3 band gap is thus very well documented and the amount of such dopants is usually less than 0.5 at.% for an efficient decrease of losses and leakage currents. Indeed, Moretti [182] and Hagemann [177] have shown that the transition levels $\text{Mn}^{2+/3+}$ and $\text{Mn}^{3+/4+}$ in BaTiO_3 are situated at $E_F - E_{\text{VB}} = 1.9$ eV and 1.3 eV respectively. Such beneficial effects have been extended to thin films processed by sol-gel [147, 148], PVD [146] or PLD [145]. We thus choose Mn as an acceptor with atomic content less than 1% in our multilayers. Donor dopants are very well known in BaTiO_3 and are commonly used in Positive Temperature Coefficient of Resistance (PTCR) that shows orders of magnitude increase of the resistance over a very restricted temperature range in the vicinity of the BaTiO_3 ferroelectric transition temperature [131]. The origin of this overheating protecting effect lies in interfacial electronic band structure at grain boundaries that is strongly affected by the structural changes of the grain bulk [131]. Among all the possible n-doping ions, a lot of rare earth can be substituted to Ba^{2+} , the charge imbalance resulting from the 3+ ionization state of the rare earth cation. The most popular and well investigated dopants for this purpose are Y^{3+} and La^{3+} from which we selected La^{3+} . The optimal dopant concentration for observing the PTCR effect is below 0.5 at.%; we thus selected this concentration range because we want to increase as much as possible the interfacial contribution to the overall dielectric properties of our multilayers. Beyond PTCR ceramics, $\text{BaTiO}_3:\text{La}$ thin films were already investigated [61, 149–152, 183]. Moreover, [184] has calculated the La^{3+} defect in SrTiO_3 to be 2.4 eV above the valence band. Another n-type dopant is Nb^{5+} whose ionic radius and preferred coordination are fully compatible with the Ti^{4+} site in BaTiO_3 . This dopant is as well leading to a PTCR effect even though it is usually of smaller amplitude than for the previously described rare earth doping in the Ba site. This may be resulting from the rather high probability of stabilizing a 4+ ionization state of Nb [39] which do not require electronic compensation. The occurrence of oxygen vacancies is one of the driving forces for the stabilization of such unusual ionization [185]. The availability of single crystals make it possible to investigate deeply the optical and conductivity behaviour of $\text{BaTiO}_3:\text{Nb}$. In particular, well-defined conductivity steps were observed at each of the phase transition temperature of BaTiO_3 , demonstrating that the electron mobility and the lattice structure are well connected [186]. Another evidence of the strong coupling between electronic conductivity and lattice comes out from $\text{SrTiO}_3:\text{Nb}$ in which the compensation mechanism of Nb^{5+} is exactly the same as in BaTiO_3 [39]. High quality single crystals of both SrTiO_3 and 0.2 at.% Nb-doped SrTiO_3 are commercially available and they are used as substrate for thin films. As seen on Figure 1.20, the optical absorption is much increased by the Nb doping. Moreover, such $\text{SrTiO}_3:\text{Nb}$ materials are superconducting at low temperatures, which indicates a strong coupling between electronic states and the lattice dynamics. Indeed, [187] have calculated

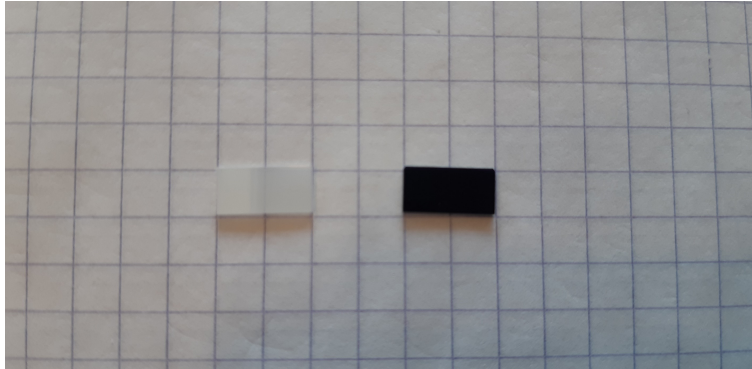


Figure 1.20: Undoped (left) and 0.2 at. % Nb-doped (right) SrTiO_3 single crystals showing the optical absorption resulting from the n-doping of Nb^{5+} on the Ti^{4+} site of BaTiO_3 .

that Nb^{4+} has a donor level localized about 0.1 - 0.2 eV below the conduction band, while Nb^{5+} lies just below the conduction band.

Coming back to $\text{BaTiO}_3:\text{Nb}$, thin films have been processed using various routes: MOCVD [188], sol-gel [155], PLD [189], PVD [143, 156]. Unlike ceramics, PTCR behaviour is hardly observed in such thin films, the main reason being that they are composed of grains of submicronic size. In ceramics, it is known that grains of larger size are needed for the balance between internal grain and grain boundaries conductivities to be efficient [190]. In PVD $\text{BaTiO}_3:\text{Nb}$ films, large interfacial band bending was evidenced by in-situ XPS as well as outward Nb diffusion [156].

To sum this part, among a wealth of possible substitution, we decided to select Mn substituted for Ti as an acceptor dopant and La (Ba site) and Nb (Ti site) as donor centres. For all cases, the substitution rate will stay well below 1 at. % to follow the observed trends in ceramics.

1.6.4 Doped BaTiO_3 multilayer thin films

Our main goal is to increase artificially the dielectric properties by using interfacial space charges in a BaTiO_3 based multilayer system. To do so, we have looked at all possibilities in the literature and by assessing their effects on the properties of BaTiO_3 and our limitations of processing, we have selected 3 different aliovalents to dope our BaTiO_3 films that is Mn, Nb and La.

Now that we have selected 3 different aliovalents, first, we will investigate their effects on the structure, dielectric and electronic properties (see section 3). It is critical to understand what are the specific properties of each dopant so that we can discern its effect on a multilayer configuration. Once we have determined this, we will proceed to deposit different type of stacks.

The very first stack will be a classic n-p junction. From literature we know that La and Nb will play the role of n-type semiconduction and Mn as p-type. They will be investigated by depositing on a MIM structure and determine which are the best ratios of

thickness as we want to conserve a constant thickness throughout the whole study (i.e 300 nm)

Next, we will investigate the 3-stack multilayers: n-p-n, p-n-p and n-n-n as shown in Figure 1.21. These stacks will be our main cases of study as symmetry will allow us to determine the effects of dopants in the internal interfacial space charges.

Lastly, we will investigate whether this property is conserved in 5-stack BaTiO_3 based multilayer such as n-p-n-p-n or n-n-n-n-n. If the interfaces are indeed increasing artificially the dielectric permittivity, this effect will be enhanced by adding more layers. Nevertheless, we need to conserve the volume fraction of each element and the total thickness of the multilayer to really understand the effect to the number of interfaces and not the dopants themselves.

Once we have analyzed the dielectric properties of these multilayers, we will proceed to investigate the role of each interface by measuring each stack by Electron Paramagnetic Resonance (EPR). First, the single doped BaTiO_3 layers (undoped, Mn, Nb and La) will give us a base of which defects are present "naturally" in BaTiO_3 . Then, we will analyse what are the differences and the potential addition of defects when interfaces are introduced to BaTiO_3 .

Finally, once we have understood the different defects associated with each multilayer, we will investigate our multilayers by TOF-SIMS. This will allow us to understand the diffusion and the chemistry during the processing of our films. Indeed, defects may or not be created by the presence of a dopant. If this dopant has a tendency to diffuse, when deposited as a multilayer, each stack will be a purely doped layer but in a very short range there will be an overlap of both dopants, hence it will create different type of defects, found by EPR, and create artificially a highly insulating material at the interfaces and therefore modify the dielectric and electric properties of our BaTiO_3 films.

As mentioned before, to study the physico-chemical properties of thin films, different characterization techniques were used in this thesis work. Certain analyses were carried out in a systematic way on all the samples, they will be explained on the following

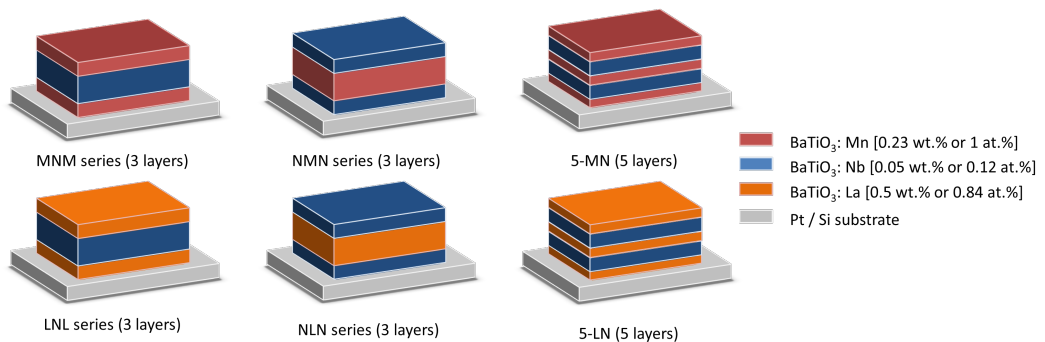


Figure 1.21: Heterostructures layers diagram. Correspondance of colors and materials are written in the legend. Thickness of layers and substrate are not to scale. Overall thickness of all heterostructures is around 300 nm

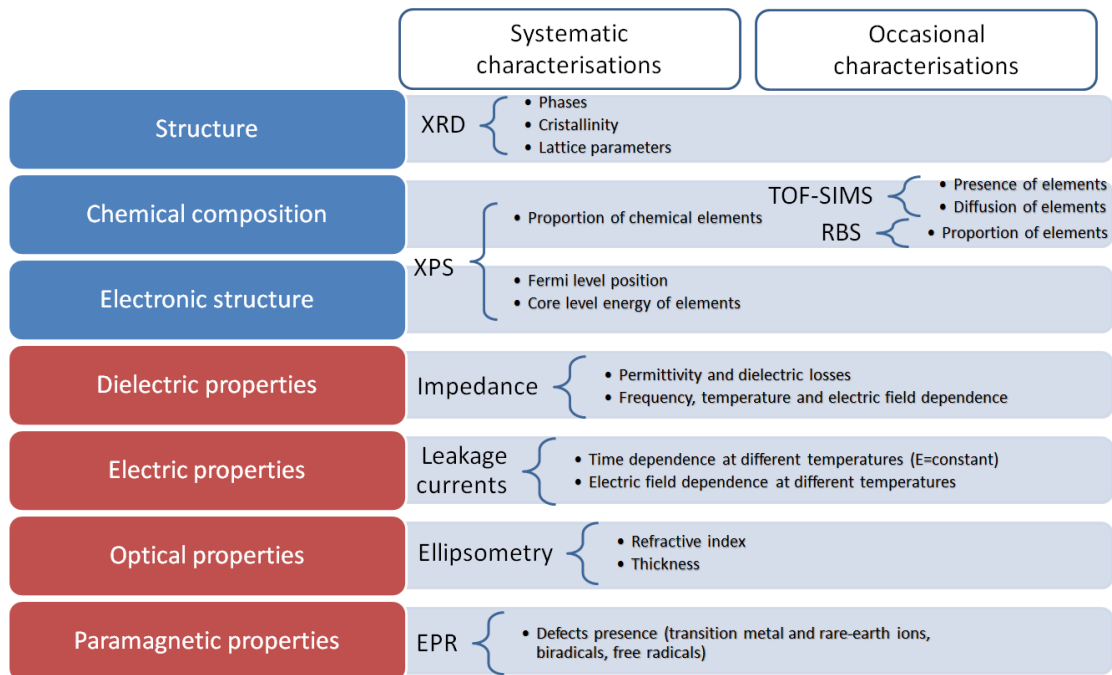


Figure 1.22: Block diagram of the different characterization techniques used on thin films. On the left, the analyses carried out systematically on each sample, on the right the occasional analyses. XRD: X-ray diffraction; TOF-SIMS: Time-of-Flight Secondary Ion Mass Spectrometry; RBS: Rutherford Backscattering Spectrometry; XPS: X-ray Photoelectron Spectroscopy; EPR: Electron Paramagnetic Resonance.

chapter. All of these analytical techniques used and the information derived from them are summarized in Figure [1.22](#). Only the techniques of XRD, EPR and TOF-SIMS have been executed by others, however, the exploitation of the results has been carried out by the author.

Chapter 2

Thin film synthesis and experimental characterization methods

In this chapter, we will present a more detailed description of the thin film deposition technique and the various experimental techniques used to characterize the properties of the studied materials. We will accentuate on the X-Ray Photoelectron Spectroscopy technique description as this characterization was the main technique and link between other experiments.

2.1 Magnetron sputtering

Throughout the work, all films were deposited by RF magnetron sputtering. RF magnetron sputtering is a deposition technique where ions or neutral particles are accelerated by a RF electric field hitting the surface of a target of the material desired to be deposited as film. Such target is then sputtered in all directions reaching the substrate. A magnetic field is used to fold the ions and electrons trajectories. The electrons follow helical paths around the magnetic field lines undergoing more ionizing collisions with neutral molecules near the target than would otherwise occur. This increases the mean free path and the sputtering yield. Sputtered atoms are electrically neutral, which are unaffected by the magnetic field. A conventional planar magnetron is used, obtaining a looping magnetic field round the internal and outer magnet pole that confines the plasma in a closed loop on the target surface. In order to achieve a proper target sputtering, a high vacuum (10^{-5} Pa) is required to control impurities and quality control. Following this, since BaTiO₃ targets are easily reduced, a mixture of Argon and Oxygen is introduced into the chamber (1-10 Pa) to ensure stoichiometric films. The quality of the films is affected by several factors such as the sputtering power, the work pressure, the composition of the gas (Ar/O₂), the position of the substrate with respect to the target and mainly the substrate temperature [40]. These factors depend on each other and the set of deposition parameters has been

determined in previous works [39, 40] and are shown in section 3.1. Once the power is supplied to the magnetron, it leads to a negative voltage (typically 50-100 V) applied to the target. This negative voltage attracts high speed positive ions (e.g. argon) to the target surface. Usually when a positive ion collides with atoms at the surface of a solid an energy transfer occurs. If the energy transferred to a lattice site is greater than the binding energy, primary recoil atoms can be created, which can collide with others atoms and distribute their energy via collision cascades. Figure 2.1 summarizes the process and the system.

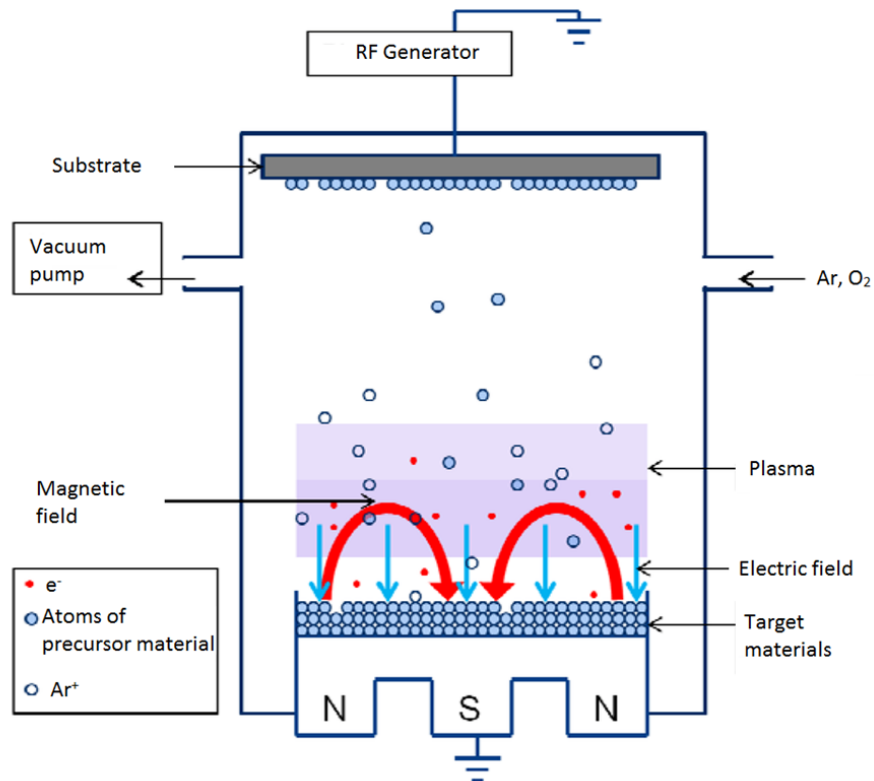


Figure 2.1: Schematic diagram of a Radio Frequency Magnetron Sputtering. Ar^+ are accelerated by a electric field and focused by a magnetic field leading to the sputtering of a target (cathode) and afterwards deposited onto a substrate (anode)

Throughout this thesis, most films have been deposited under on-axis configuration, that is to say, the substrate is facing the sputtered target. With such geometry, resputtering can happen from fast ions collisions causing an unlikely faithful composition transfer from the target to the film. An off-axis sputtering configuration (see Figure 2.2) can be used at ICMCB to reduce resputtering that can affect microstructure and stoichiometry of the films. A comparison between microstructure and dielectric properties of on/off-axis sputtered films is discussed in sections 3.2 and 3.2.

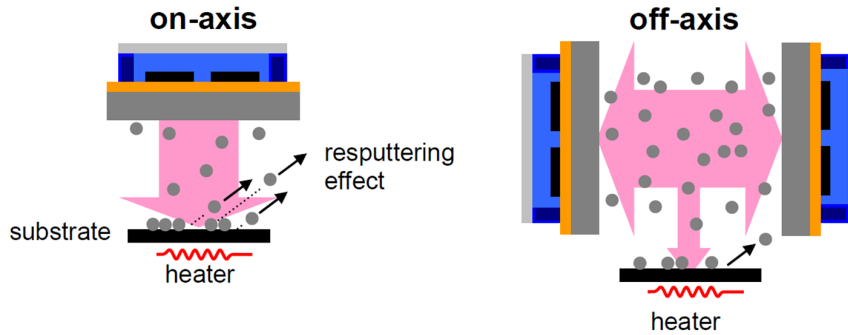


Figure 2.2: Left: on-axis sputtering configuration. Due to fast ions collisions, resputtering occurs. Right: off-axis geometry reducing the growth rate and thus the energy transfer collision on the substrate. [39]

Due to chamber geometries being different at ICMCB and TUD, we tried to setup all sputtering parameters as close as possible. Table 2.1 summarizes the thin film deposition conditions.

Table 2.1: RF magnetron sputtering parameters for BaTiO₃ thin film deposition

Power density [W/cm ²]	2.5
Pressure [Pa]	5
Ar/O ₂ gas content [sccm]	99/1 [1% O ₂]
Temperature [°C]	650
Substrate distance [cm]	8
Deposition rate [nm/min]	2.5

2.2 X-Ray Diffraction

Several properties of thin films can be analyzed by X-ray diffraction, crystallinity, crystal phases, crystal lattice constant, grain size, grain orientation and strain due to substrate clamping. All this information and its estimation depends strongly on the quality of the film, thickness and substrate. Nonetheless, this analysis is crucial after the film deposition and before any other characterisation is done on it, as it allows us to control the present phases as any parasitic phase would indicate that the synthesis need to be redone. The principle of XRD is as it follows: an X-ray beam emitted by a copper anode is sent to the sample, the beam is then diffracted by the atomic planes of the crystallized material as shown in Figure 2.3

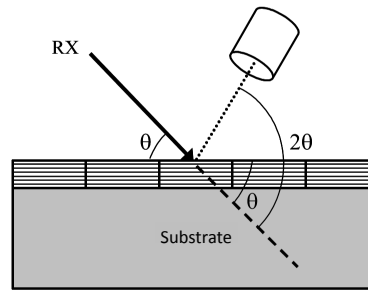


Figure 2.3: Graphic representation of the configuration $\theta - 2\theta$ for a thin film. [39]

Depending on the angle of the incident beam θ relative to the sample, the diffracted rays have different positions. Indeed, due to the regular organization of the crystalline planes, in some places in space the waves cancel each other out by destructive interference, and in others they add up by constructive interference. Thus, considering λ , the wavelength of the radiation, and d , the interreticular distance of the diffracting crystal plane, then there are 2θ directions of space for which there will be peaks of intensity, verifying the following equation :

$$2d \sin \theta = n\lambda \quad (2.1)$$

with n the diffraction order. This relationship, called Bragg's law, is illustrated in Figure 2.3. The additional optical path traveled by the rays is $2d \sin \theta$. The interferences are then constructive if the path introduces a phase shift, which is multiple a of 2π , that is to say if the additional path is a multiple of λ . Throughout this work we used the Bragg-Brentano analysis geometry ($\theta - 2\theta$). The sample moves from θ while the detector moves 2θ from the fixed incident beam. This technique allows only the observation of the diffraction lines corresponding to atomic planes parallel to the substrate (see Figure 2.3), without providing information on the orientation of the grains in the thickness of the layer. The routine experiments were carried out for $8 < 2\theta < 80^\circ$, with a step of 0.1° and a counting time of 1s, using a Philips copper anode spectrogoniometer of wavelength $\lambda = 1.5406$. Each acquisition lasted for 34 minutes. The Cu-K_α radiation was generated at 45 kV and 40 mA ($\lambda = 0.15418\text{nm}$).

2.3 Impedance spectroscopy

An HP 4194-A impedance analyzer was used to determine the dielectric properties of our samples as a function of the frequency and the applied electric field. This device is connected to a probe assembly (Prober PM5 from Süss Microtec, tungsten probes with radius $20\mu\text{m}$). The 4-wire connection is made using coaxial cables of the BNC (British Naval Connector) type, which allow interference signals to be overcome thanks to their shielding (see Figure 2.4).

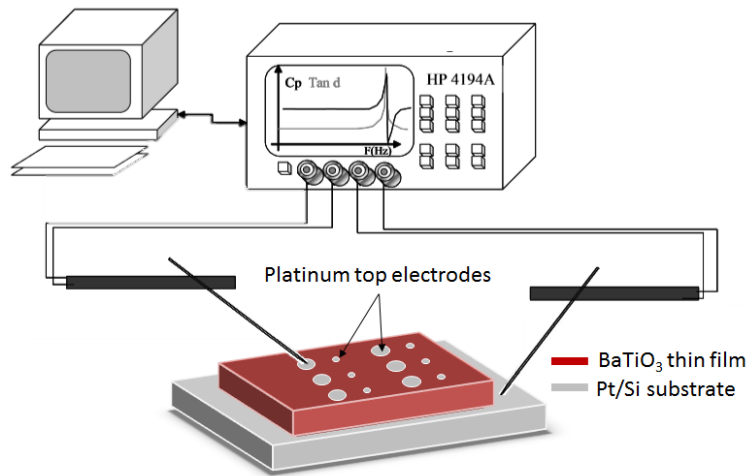


Figure 2.4: Impedance analyser set-up with sample

Thin film samples with Pt electrodes can be modelled by an RLC circuit, whose electric response when applying an alternating electric field of frequency f is measured by the impedance Z . The impedance of a sample (in Ohms) reflects its opposition to passage of an alternating current. The complex impedance Z is written: $Z = R + jX$, where R is the resistance and X is the electrical reactance. The total reactance has 2 contributions, a capacitive and an inductive one: $X_T = X_L + X_C = \omega L - \frac{1}{\omega C}$; where ω is the angular frequency equal to $2\pi f$, L and C are the inductance and the capacitance of the sample. Generally, the inductance of the sample is negligible and the sample is considered as a RC circuit. The projection of the complex impedance on the real and imaginary axes makes it possible to deduce the values of capacitance and dielectric losses $\tan \delta$, as shown in equation 2.2. These two quantities can then be expressed with the following formulas:

$$\tan \delta = \frac{R}{X} \text{ and } C = \frac{X}{2\pi f(R^2 + X^2)} \quad (2.2)$$

A thin film of a dielectric material is never purely capacitive, and the deviation from a pure reactance is given by $\tan \delta$, which reflects the dielectric losses in the sample. In the case of a planar capacitor, the permittivity is given by: $\varepsilon = \frac{C * t}{\varepsilon_0 * S}$, where t is the

thickness of the thin film and S the surface of the electrode. The plane capacitor structure was adopted in our case as it is the simplest to fabricate, by depositing platinum dots by sputtering through a stainless steel mask under 0.5 Pa and $2.5\text{W}/\text{cm}^2$ for 10 minutes so as to obtain a thickness around 200 nm. Due to the presence of grain boundaries and other defects in our layers, short circuits can occur between the 2 electrodes, this being more likely as the size of the dots is large. In our case, we opted for 2 diameters for our top electrodes: $300\mu\text{m}$ and $600\mu\text{m}$. Thickness and diameter were checked with a profilometer.

For the frequency dependent measurements at room temperature, an alternating electric field of amplitude 0.5 V is applied to the sample and its response is recorded from 100 Hz to 1 MHz (see Figure 2.5). Static electric field tunability measurements are performed from -5 to +5 V at 100 kHz.

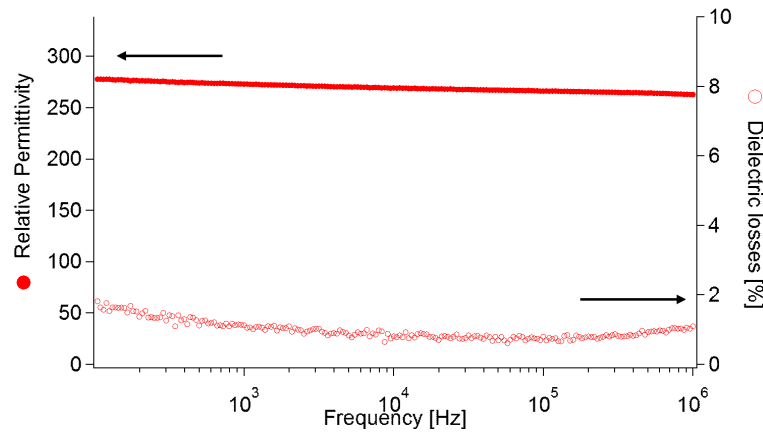


Figure 2.5: Frequency dependent dielectric properties of a Mn-doped BaTiO_3 film at room temperature

2.3.1 Temperature dependence

The influence of temperature on the dielectric properties of our ferroelectric thin films was measured using a metallic cell (see Figure 2.6) developed at the University of Dijon, which allows the temperature to be precisely regulated next to the sample. The heating coil is in fact located inside the measuring cell and screws onto a brass cylinder, which carries the sample. The thermal contact between the oven and the sample is therefore metallic. Two temperature sensors (Pt-100 probes) are located in the brass cylinder, one for controlling the oven, the other for reading the temperature as close as possible to the sample. Once closed, the cell is impervious and can be placed under vacuum (connection to an oil-free pump using a tombak) or under helium. The assembly is placed in a cryogenic storage dewar, which can be filled with liquid nitrogen so as to take measurements from 80 to 440 K.

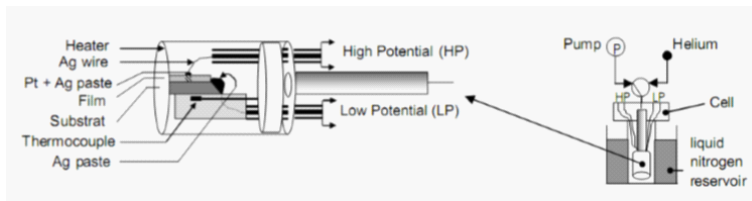


Figure 2.6: Metallic cell for temperature dependent dielectric measurements. From [39]

The connections between the thin film bottom Pt electrode and the electrodes of the cell are done (see Figure 2.6) by using a spot of silver lacquer which connects the layer of platinum from the substrate to one of the electrodes of the cell. The top Pt contact is made using a silver wire ($\phi = 100 \mu\text{m}$) glued with silver lacquer on one of the Pt dots ($\phi = 300$ and $600 \mu\text{m}$) and glued to the other electrode of the cell. For each sample, before the first temperature measurement cycle, the contacts are annealed under vacuum at 440 K for 30 minutes, in order to completely stabilize the silver lacquer and then cool down to room temperature to fill the cell with He so as to no water vapour enter can the cell. Finally, the cell is cooled down with liquid nitrogen until 80 K. A ramp speed of 0.5 K/min was used up to 400 K. A Keithley 195 A multimeter allows the acquisition of temperature at the sample level. Electrical data is measured by an HP 4192 A impedance bridge.

2.4 X-Ray Photoelectron Spectroscopy

X-ray Photoelectron Spectroscopy (XPS) is based on the photoelectric effect, in which electrons are emitted from matter after absorption of energy. The required energy to extract the electron from the matter has to be higher than the work function of the material. In addition, the kinetic energy of the collected electron must remain unaffected during the photoemission process. Thus, photoemission experiments are typically performed in ultra-high-vacuum (UHV) system, that is below 10^{-7} Pa. The mean free path of the emitted electron is large enough for them to travel through an energy analyzer to a detector without scattering. In fact, the analyzer collects two kinds of electrons from the sample: (i) the primary electrons contributing to the chemical and electronic information and (ii) inelastically scattered electrons contributing to the background intensity (secondary electrons). Both contributions can be appreciated in Figure 2.7. For the primary electrons, the measured kinetic energy is directly coupled to their inelastic mean free path as sketched in Figure 2.7.

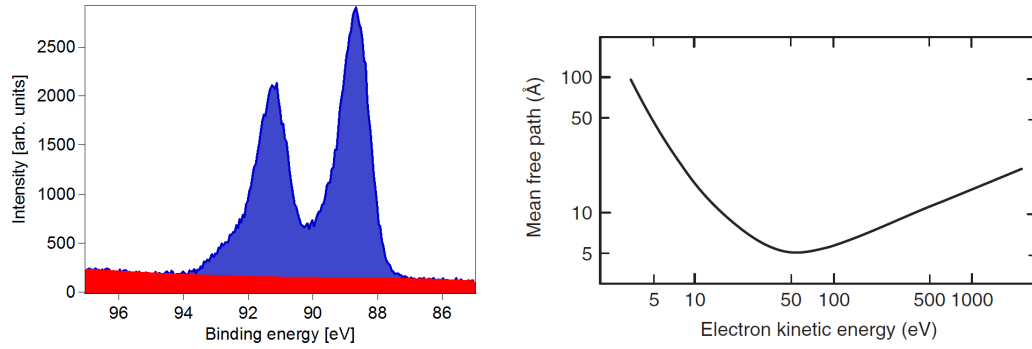


Figure 2.7: Right: Typical Sr 3d XPS spectra recorded on SrTiO₃ material. The background line (red) is the result of secondary electrons collection. Left: Inelastic mean free path of electrons in solids. This relation is also called “bathtub curve”. From [191]

The electron binding energy (BE) of each of the emitted electrons can be determined as in the following equation:

$$E_{binding} = h\nu - E_{kinetic} - \phi_{sp} \quad (2.3)$$

where $E_{binding}$ is the binding energy of the electron, $h\nu$ is the energy of the X-ray photons being used, $E_{kinetic}$ is the kinetic energy of the electron measured by the instrument and ϕ_{sp} is an instrumental parameter (work function of the spectrometer). As an electrical contact is established between the sample and the spectrometer during the measurement, their respective Fermi energies (E_F) are aligned. Therefore, all the recorded binding energies are referenced to this Fermi level (the same between the sample and the spectrometer). This is particularly useful to know the position of the Fermi level since any chemical and electronic change will be quantifiable thanks to this reference ($E_F = 0$ eV).

Typically, three kinds of measurements are performed during the surface analysis: (i) the survey spectrum, which is used to identify all the chemical elements present at the surface, (ii) the recording of core levels at their characteristics binding energies available in the XPS handbook [192] and (iii) the valence band spectrum, which provides important information on the Fermi level position, particularly useful to quantify the semiconducting character (p-type, n-type). Typical survey, core levels and valence band (VB) spectra are reported in Figure 2.8 for BaTiO₃ thin films.

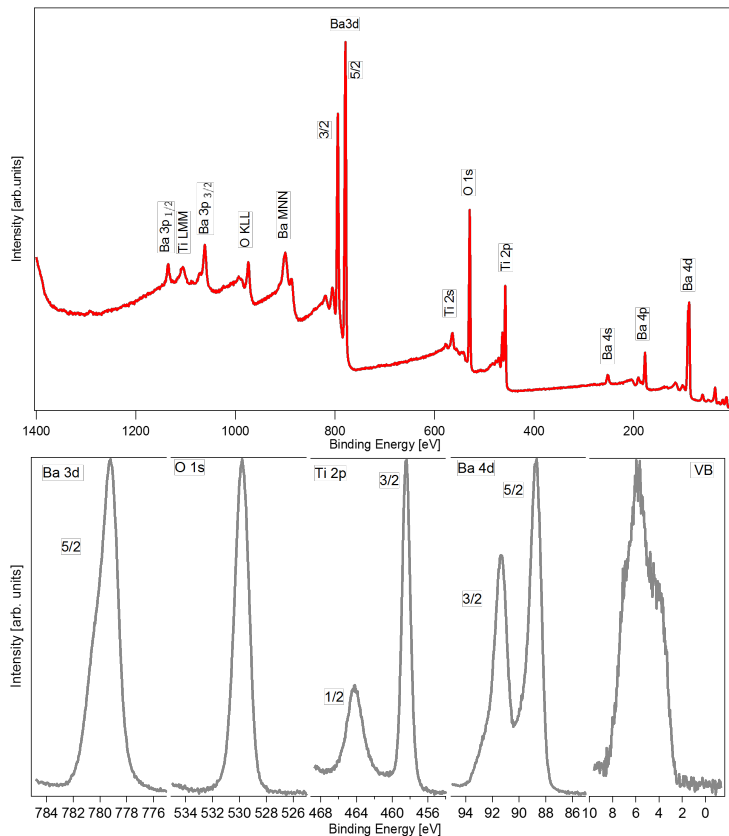


Figure 2.8: XPS survey (top) and core-levels (bottom) of an undoped BaTiO₃ thin film recorded with monochromatized Al K α radiation.

With the core levels presented above, one can quantify the chemical compositions of the observed surface. The relative composition (e.g. Ba vs. Ti) can be determined after background subtraction of the secondary electrons (see Figure 2.7). Different mathematical approaches can be used for the subtraction (line, polynomial). The method of Shirley [26] and Tougaard [27] can be also be used in some cases. After background subtraction, since the integrated intensity of a photoemission line depends on the atomic concentration of the respective elements, the stoichiometry can be determined. It is also important to note that the intensity of a photoemission line depends (i) on the geometry of the spectrometer and (ii) the measured element. Atomic Sensitivity Factors (ASF) have been

defined to include (i) and (ii) [192]. Therefore, each element possesses its own ASF, related to the spectrometer being used. ASF are usually given by the manufacturer of the surface analytic system. For homogeneously distributed elements A and B, the relative concentrations are given by equation:

$$\frac{n_a}{n_b} = \frac{I_a ASF_b}{I_b ASF_a} \quad (2.4)$$

where n is the concentration of the respective element and I the integrated intensity of the photoemission line. Schafranek et al. have shown that stoichiometry calculation from XPS measurements can differ from those measured with RBS due to low oxygen sensibility in RBS [193]. In fact, stoichiometry calculated by photoemission is not a quantitative determination but rather a good technique to provide the relative composition ratio from one element in comparison to another, for instance in dependence on sample treatment or deposition conditions.

2.4.1 Valence band in ATiO₃ compounds

The valence band (VB) emission displayed in Figure 2.9 shows a well-defined two peak structure extending up to 8 eV below the Fermi level (E_F) position ($E_F = 0$ eV). This emission has been observed in ceramic and single crystal of BaTiO₃ [194-196], thin films of (Ba,Sr)TiO₃ [193, 197, 198], SrTiO₃ [199, 200] single crystal and single crystal of KNbO₃ [196]. The valence band (VB) emission of Nb-doped SrTiO₃ single crystal and BaTiO₃ thin films are reported in Figure 2.9 with the annotations A, B, C, D and VBM.

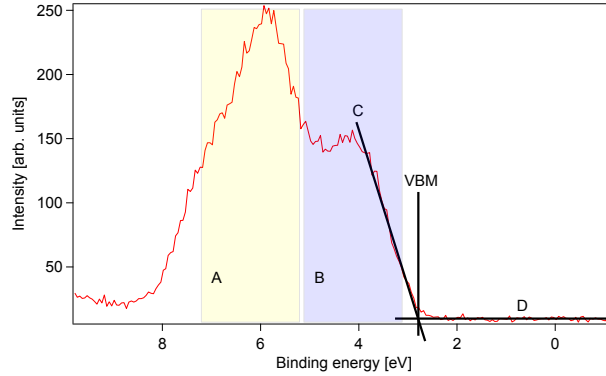


Figure 2.9: XPS valence band spectra of BaTiO₃ thin film. Two well-defined structures are denoted A and B and lines C and D are discussed in the text. The VBM positions are also reported.

The B band corresponds to the O2p non-bonding states, while the A band denotes the bonding between the O2p and Ti3d states [194]. We thus clearly see that the valence band is mainly of oxygen 2p character and shows a significant degree of covalent character in the Ti3d – O2p bonding, which is expected in ATiO₃ compounds [201]. Since Nb-doped

is more crystalline than polycrystalline BaTiO_3 , the $\text{O}2p$ non-bonding states (B) is more pronounced for SrTiO_3 .

The valence band maxima (VBM) of the spectra are determined by linear extrapolation of the leading edge of the valence band emission (C line) as the zero of binding energy corresponds to the Fermi level position. Since the optical band gap in BaTiO_3 is about 3.2 eV [202], a VBM value recorded around 2.8 eV, indicate a n-type semiconducting character (Fermi level position close to the conduction band). The VBM value recorded with the presented BaTiO_3 sample exhibits a value of 2.8 eV.

2.4.2 Fermi level determination, interface experiment

During this PhD thesis, in-situ experiments have been performed, the deposition chamber was directly connected to the analysis chamber by an ultra-high vacuum system. The layout of this system, which is used in the surface science group at TU-Darmstadt is sketched in figure 2.10.

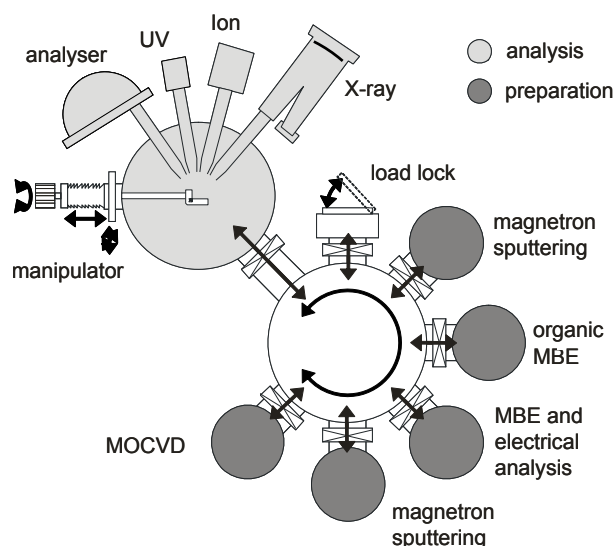


Figure 2.10: Layout of the integrated ultra-high vacuum system combining a multi-technique surface analysis system including a photoelectron spectrometer for XPS and UPS. Several chambers for thin films deposition are connected to the system, like magnetron sputtering deposition used during this thesis. From [39]

Thanks to this configuration, it is possible to determine the electronic properties of samples coming from ICMCB (ex-situ) and also deposit our films and analyse them without breaking the UHV (in-situ). Moreover, we are capable of analysing the electronic structure of a growing film on a substrate and therefore determinate the band bending of two materials in contact. Indeed, by measuring the XPS spectra in between layers of the deposited material, it is possible to examine the evolution of the binding energies of the core levels of each material. To do this, it is necessary to have previously acquainted with

precision the distance $E_{\text{VBM}}-E_{\text{core}}$ of each element of the growing material so that we can recover the Fermi level position as the valence band of the analysed surface will be a convolution of the individual valence band spectra of the two materials in contact [203].

For XPS analysis, samples can be prepared ex-situ, i.e., prepared outside the vacuum system and then inserted in the analysis chamber. Therefore, a surface treatment is required to clean the surface. Typically, we can use an Ar-ion gun to etch the surface and clean the common carbonate adsorbates (see Figure 2.11-A). Unfortunately, this method is not suggested for oxide compounds as the O will be primarily ejected from the sample as compared to other elements. This selective etching will lead to a non-stoichiometric surface and a shift in the binding energies of the original surface as shown in figure Figure 2.11-B. To avoid this, it is possible to use an O-ion gun to etch the surface or simply heat in a vacuum chamber, under low oxygen partial pressure, above the decomposition of such carbonates (400°C). In Figure 2.11-C, we compare the different methods to clean BaTiO_3 surfaces and their impact on the composition and electronic structure.

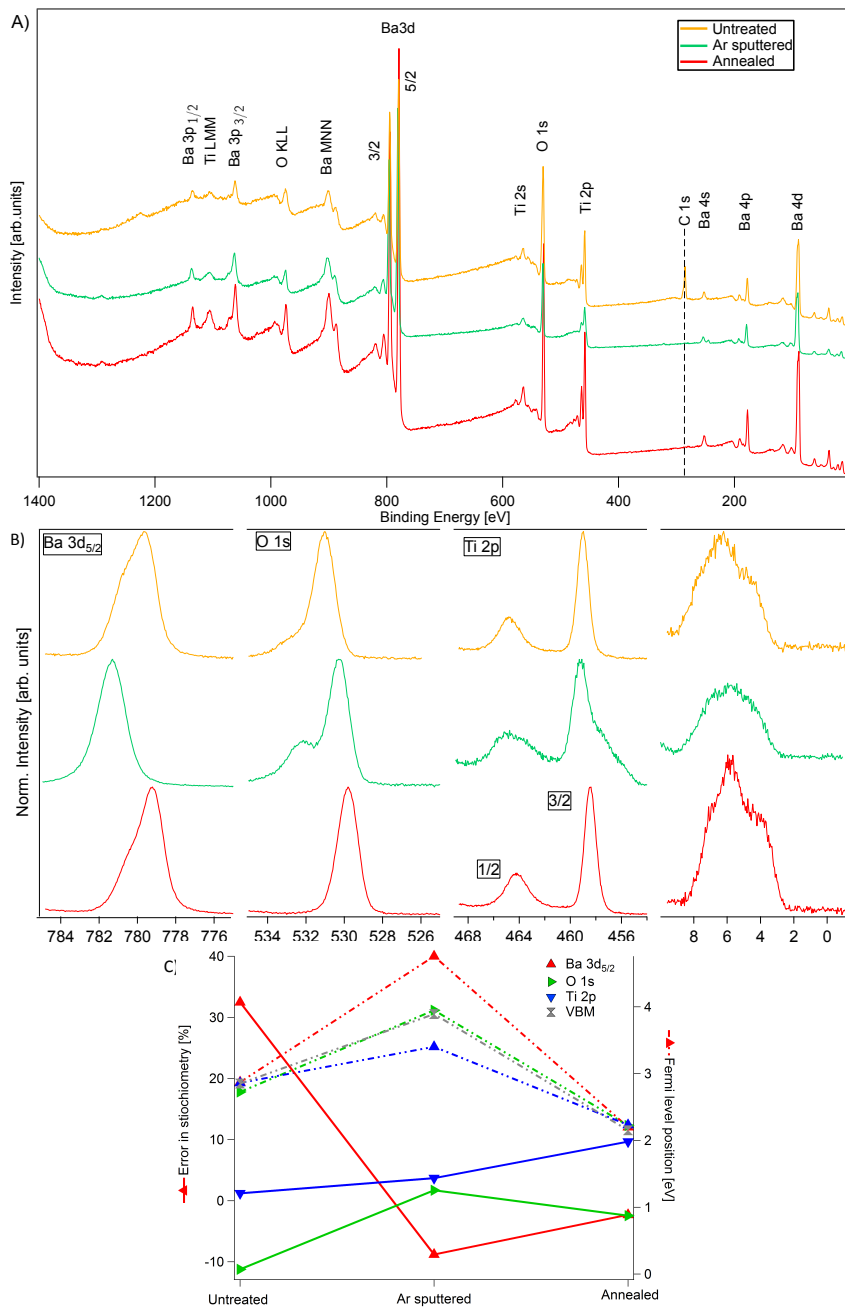


Figure 2.11: XPS survey (A), core-levels (B) and composition and Fermi level position (C) of untreated, Ar sputtered and annealed Mn-doped BaTiO₃ thin films. The error in stoichiometry of each film is displayed in comparison with a stoichiometric BaTiO₃, that is 20% Ba, 20% Ti and 60% O.

2.5 Leakage Currents

A good performance on a tunable capacitor is achieved when the properties of the dielectric are stable in temperature and electric field. As a matter of fact, when a voltage is used to tune the permittivity of the dielectric thin films, for nanometric films a small voltage can induce high electric fields in the order of kV/cm. Even if the material is supposed to be an insulator, inside the material there are defects that induce a certain conductivity. These defects will contribute to the propagation of a current through the material under these high electric fields, most often called leakage currents. When these high electric fields are applied for a long period of time they can generate a breakdown of the device.

To measure these currents on this type of capacitors is not an easy task as the I-V response of ferroelectric materials [110] tends to evolve over time. Therefore, before measuring the I-V characteristic, a previous study of the leakage currents versus time is necessary to determine the conditions for the measurement of I-V characteristics.

Four zones of the I-t characteristic of ferroelectric materials have been defined by E. Bouyssou [110]: dielectric relaxation (A), true leakage current (B), resistance degradation (C) and current decrease (D) as shown in Figure 2.12.

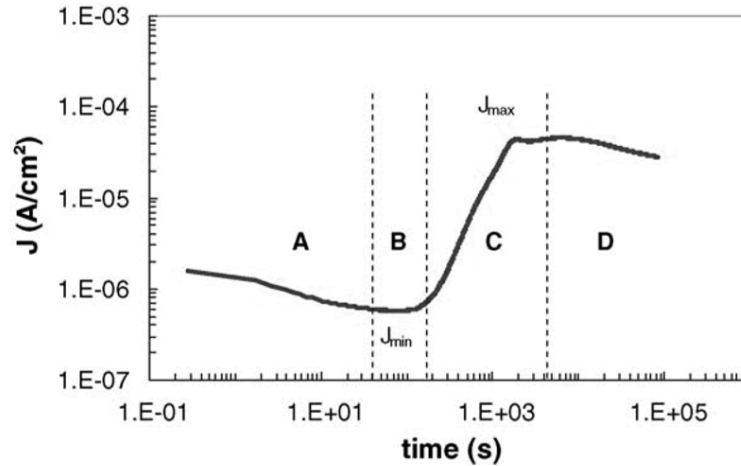


Figure 2.12: Current density versus time characteristic of PZT capacitors at 105° for an applied voltage of 5 V. From [110]

Region A is characterized by a decrease in current density due to dielectric relaxation attributed to a Maxwell Wagner polarization with several relaxation times. In region B the current reaches its minimum J_{min} so called "true leakage current" of the capacitor. After this, a significant increase in current is attained reaching a maximum J_{max} in region C attributed to a degradation of the resistance of the capacitor. After this maximum J_{max} , the current starts to decrease in region D, so-called reversibility of resistance degradation.

At first, we measured the leakage currents over time at room temperature stressed with 100 kV/cm over $4 \times 10^4 \text{ s}$. At this temperature, the relaxation of the current begins

around 100 s and the degradation of the resistance begins around 1000 s. Since the true leakage current needs a long time to be measured at room temperature, it is possible to increase the temperature in order to avoid region A and start the measurement in the B region as shown by E. Bouyssou [110]. Figure 2.13 displays a time dependent measurement of a Mn-doped sample at different temperatures.

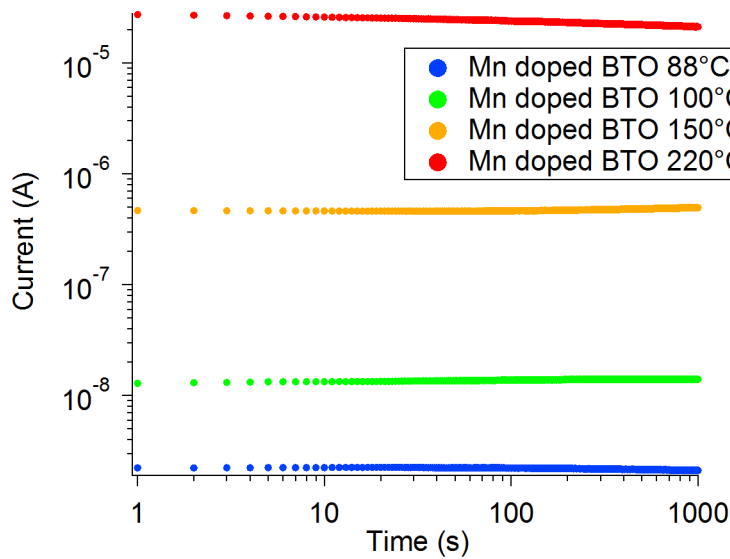


Figure 2.13: Current density versus time characteristic of Mn-doped BaTiO₃ films capacitors at different temperatures for an applied voltage of 3 V

From figure 2.13, the current still decreases at 88°C and stops around 100 seconds. After 100°C we can observe that the current only increases after 100 seconds of measurements. Therefore our leakage current measurements will only start at 100°C and above to avoid the dielectric relaxation and stop after 100 seconds to avoid the resistance degradation.

In order to measure the "true leakage currents" as a function of the electric field, various procedures can be carried out. The most common are, the Staircase mode for which the voltage is increased in steps, and the Pulse mode for which successive voltage steps are applied, separated by short-circuiting intervals. In this work, the Staircase mode was used, the temporal profile of which is presented in Figure 2.14. For each step, the voltage is applied for a certain time before taking the measurement (t_p). In this work, $\Delta V = 0.01$ V from 0 V up to 3 V and $t_p = 1$ s so as to avoid the resistance degradation.

2.5.1 Temperature dependence

The leakage currents measurements were carried on an Agilent 4156c precision semiconductor parameter analyzer coupled with Pt thermocouples that were in contact with the ceramic heating plate and the edge of the Si/Pt substrate. After a calibration of the

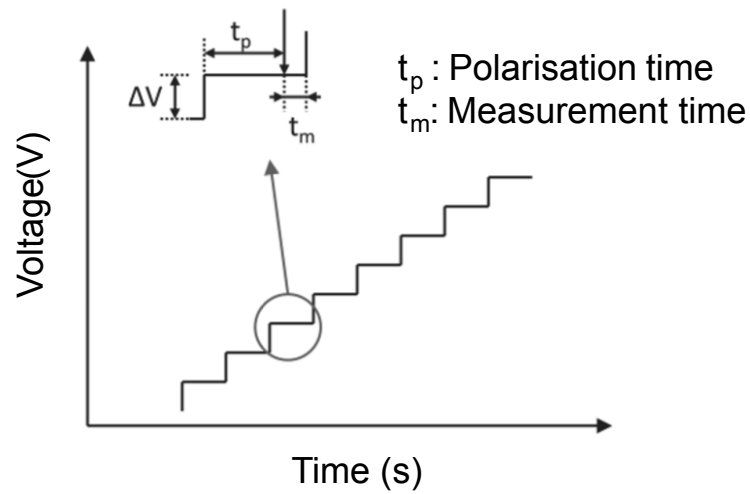


Figure 2.14: Voltage staircase measurement set-up

temperature was done on a clean sample, measurements were carried out with a 25 degrees step with a waiting time of 20 minutes for a better temperature stabilization. Measurements started at 100 degrees and stopped at 200 degrees. For the current density measurements, the same protocol was carried out as mentioned in section 2.5. Moreover, the films were stressed at For the current density measurements, the same protocol was carried out as mentioned in section 2.5. Moreover, the films were stressed at 200°C at 100 kV/cm for 60s and then quenched in air to room temperature prior to the leakage current measurements.

200°C at 100 kV/cm for 60s and then quenched in air to room temperature prior to the leakage current measurements.

2.6 Electron Paramagnetic Resonance

This technique allows us to study many point defects in solids such as:

- local damages of the crystalline lattice (F-centers, vacancies, “positive holes”, “broken” bounds...);
- free radicals in solid, liquid and gas phases (free radicals- molecule which contains one unpaired electron...);
- biradicals (molecules with 2 unpaired electrons at large enough distance to consider that the interaction between them is negligible);
- systems in triplet state (systems with 2 unpaired electrons);
- transition-metal and rare-earth ions, lanthanides and actinides;

The principle of EPR is as it follows. Microwave irradiation excites an electron to an upper energy level when the applied magnetic field is equal to the field for resonance as shown in Figure 2.15. The motion of the charged electrons from the hole in the anode to the reflector and back to the anode generates an oscillating electric field and thus electromagnetic radiation. [204]

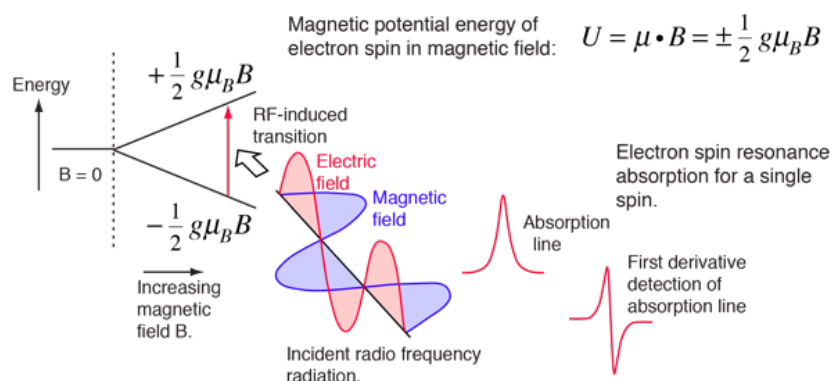


Figure 2.15: EPR principle. Magnetic field strength better apparent resolution than absorption spectra. [204]

From EPR spectra it is possible to determine the charge of the paramagnetic ion, symmetry of local environment and together with data obtained from XRD estimate the position of the paramagnetic ion in the lattice. The knowledge of the energy levels of the paramagnetic ion allows compare EPR results with the data from optical spectra and to calculate the magnetic susceptibility of the ferroelectrics.

EPR spectra were carried out in the temperature interval of 4 K and 300 K recorded on an X-band Bruker spectrometer operating at $\nu = 9.4\text{GHz}$ (X-band) including a TE 102 rectangular microwave cavity with 100 kHz magnetic field modulation, in a magnetic field measurement range from 5 to 5000 Oe.

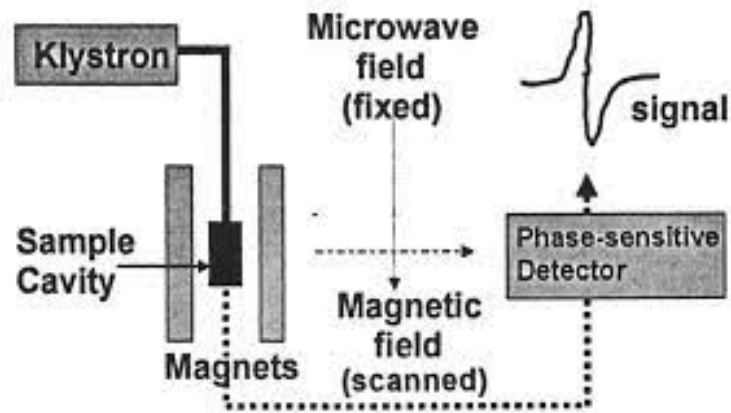


Figure 2.16: EPR set-up. [204]

The surface of the samples used were approximately $6 \times 3 \text{ mm}^2$. The samples were introduced in a quartz tube and placed in an Oxford Instruments ESR 900 continuous-flow helium cryostat inside the microwave cavity that allow performing the temperature dependence study.

EPR measurements were done on BaTiO_3 powders (around 0.4 mg) and BaTiO_3 thin films deposited onto Si substrates ($3 \times 5 \text{ mm}^2$ and 300 nm thickness). Powders samples were taken from sintered BaTiO_3 samples, which followed the same treatments as for the BaTiO_3 targets used for RF-sputtering.

2.7 Time-Of-Flight Secondary Ion Mass Spectrometry

Time-of-Flight Secondary Ion Mass Spectrometry (ToF-SIMS) is an analytical method for surfaces that uses a pulsed ion beam (Cs) to remove molecules from the first layers of the sample's surface. The particles are removed from atomic monolayers on the surface (secondary ions). These particles are then accelerated into a "flight" tube and their mass is determined by measuring the exact time at which they reach the detector (time-of-flight). Three operational modes are available using ToF-SIMS: depth profiling, surface spectroscopy and surface imaging [205-207]. This technique allows us to study analytical capabilities, such as:

- Distinction of different particles with same nominal mass. Indeed particles with the same nominal mass (e.g. Si and C₂H₄, both with AMU = 28) are easily distinguished from one another because there is a slight mass shift as atoms enter a bound state.
- Mass range of 0-10,000 amu; ions (positive or negative), isotopes, and molecular compounds (including polymers, organic compounds, and up to amino acids) can be detected.
- Trace element detection limits in the ppm range.
- Sub-micron imaging to map any mass number of interest.
- Depth profiling capabilities; sequential sputtering of surfaces allow analysis of the chemical stratigraphy on material surfaces (typical sputtering rates are 100 Å/minute).
- Retrospective analysis. Every pixel of a ToF-SIMS map represents a full mass spectrum. This allows an analyst to retrospectively produce maps for any mass of interest, and to interrogate regions of interest (ROI) for their chemical composition via computer processing after the dataset has been instrumentally acquired.

ToF-SIMS uses a focused, pulsed particle beam (typically Cs or Ga) to dislodge chemical species on a materials surface. Particles produced closer to the site of impact tend to be dissociated ions (positive or negative). Secondary particles generated farther from the impact site tend to be molecular compounds, typically fragments of much larger organic macromolecules. The particles are then accelerated into a flight path on their way towards a detector. Because it is possible to measure the "time-of-flight" of the particles from the time of impact to detector on a scale of nano-seconds, it is possible to produce a mass resolution as fine as 0.001 atomic mass units (i.e. one part in a thousand of the mass of a proton). Under typical operating conditions, the results of ToF-SIMS analysis include: a mass spectrum that surveys all atomic masses over a range of 0-10,000 amu, the rastered beam produces maps of any mass of interest on a sub-micron scale and depth profiles are produced by removal of surface layers by sputtering under the ion beam.

Chapter 3

Results and discussion

3.1 Introduction

The objectives of this chapter are both to present the work done to improve the dielectric properties of thin films of barium titanate by interfacial effects and discuss the mechanism of the different effects that have been observed.

- The deposition of BaTiO₃ films can be carried out by different methods as discussed in chapter 1. In the case of this thesis, the rf sputtering route was chosen. The films were deposited both at ICMCB and at TU-Darmstadt.
- Impedance spectroscopy in function of frequency was carried out as well both at ICMCB and at TU-Darmstadt. However, only the temperature dependence was done at ICMCB.
- XPS measurement and analysis were performed at TU-Darmstadt along with leakage current measurements.
- EPR was carried out at ICMCB with the help of Dr. Alla Artemenko who performed the experiments and the data analysis.
- Lastly, TOF-SIMS have been realized with the help of Dr. Jean-Paul Salvétat who performed the experiments. Data analysis was done by the author.

3.2 Thin film deposition and structural analysis

All films depositions have been carried out by radio-frequency magnetron sputtering using bulk ceramic targets of either 2 inches or 3 inches in diameter, synthesized and sintered by solid state chemistry. Only nominally undoped BaTiO₃ and Mn-doped BaTiO₃ targets have been fabricated at ICMCB as described in chapter 2. The films fabricated at ICMCB were deposited with 3 in. diameter targets and those at TU-Darmstadt were deposited with 2 in. diameter targets. All films were deposited onto platinized (111) Si substrates (Si/SiO₂/TiO_x/Pt). In order to reduce the variance between both deposition chambers, we decided to deposit the films with the same power density, temperature, oxygen content, pressure and substrate distance to obtain a constant deposition rate. To control this, we systematically measured the films thicknesses by X-Ray Reflectivity (thin thickness) and ellipsometry (thick thickness). The deposition conditions are summarized in table 3.1

Table 3.1: Thin film deposition conditions

Power density [W/cm ²]	2.5
Pressure [Pa]	5
Ar/O ₂ gas content [sccm]	99/1 [1% O ₂]
Temperature [°C]	650
Substrate distance [cm]	8
Deposition rate [nm/min]	2.5

The films' structure and crystallinity were studied by XRD. Figure 3.1 shows the diffractograms of undoped, Mn-, Nb- and La-doped BaTiO₃ films. From these results, the films do not show secondary phases, in the resolution limits of the machine. The films presented a pseudo-cubic structure determined from the lattice constants resumed in Figure 3.2. The films are polycrystalline with a "preferential" [111] orientation excluding Mn- and La-doped films which most intense peak still corresponds to the [111] orientation direction. In contrast to the powder samples, all films fitted the best with a cubic structure suggesting that the BaTiO₃ thin films are in a paraelectric phase at room temperature.

From Figure 3.1 we can observe a slight shift on 2θ on BaTiO₃ peaks. After a fitting the spectra following a Rietveld profile refinement, it was possible to obtain the lattice parameters. This method works by reconstitution of the diffractogram by theoretical calculation and minimizing the difference between this one and the measured one. In Figure 3.2 we resume the fitted lattice volume V calculated for a cubic structure Pm-3m and the intensities ratio between planes (111) and (110).

From the ratio of intensities I_{111} and I_{110} , it is clear that the Mn- and La-doped films have almost no preferential orientation whereas Nb- and undoped films have a strong difference between the (110) and (111) directions. Moreover, knowing the ionic radii of all possible ions that can be substituted and can enter in BaTiO₃ lattice, namely Ba²⁺, Ti⁴⁺, Mn²⁺, Mn³⁺ and Mn⁴⁺, Nb⁵⁺ and La³⁺, we verified the difference on the lattice

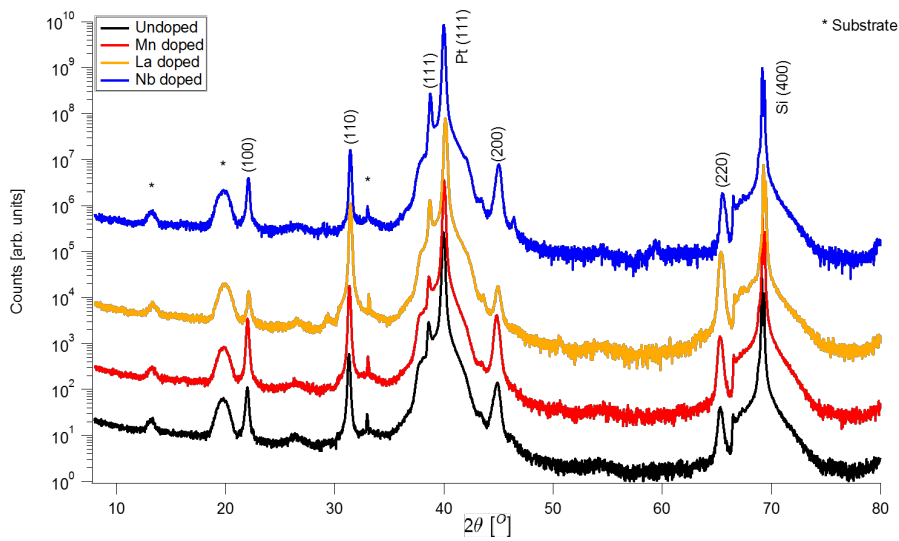


Figure 3.1: Diffractograms of undoped, Mn-, La- and Nb-doped BaTiO₃ thin films deposited on Si platinized (111) substrates

volume V . Taking the result from the undoped sample as reference, we see that Mn-doped sample has a higher parameter V , indicating that Mn is entering the lattice as a $2+$ ion since Mn can only enter on the B site (if stoichiometry is respected) and $\text{Mn}^{2+} = 67 \text{ pm}$ and $\text{Ti}^{4+} = 60.5 \text{ pm}$ and all higher valences of Mn have a lower ionic radii than Ti^{4+} , if we consider that Mn stays in the low spin state. For the La-doped sample, we see that V_{La} is slightly lower than V_{undoped} , even if La^{3+} has a much lower ionic radius (136 pm) than Ba^{2+} (161 pm), which is the only site it can enter by only looking at the ionic radii. For Nb-doped sample, this does not fit with the difference of ionic radii since $r_{\text{Nb}^{5+}} > r_{\text{Ti}^{4+}}$ (65 pm), but one can argue that there is also a big difference on the orientations (111) and (110) and this would affect the Rietveld refinement calculations.

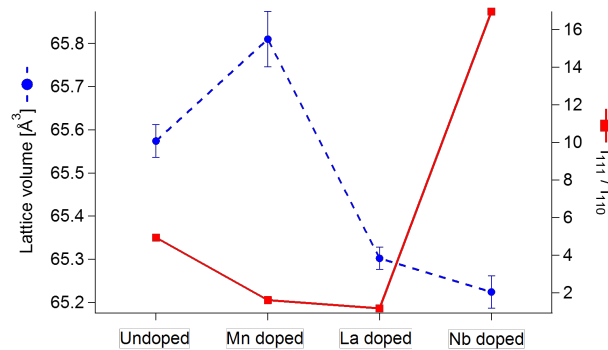


Figure 3.2: Fitted lattice volume V and I_{111}/I_{110} of undoped, Mn-, La- and Nb-doped thin films

3.3 Impedance spectroscopy

Dielectric properties of MIM capacitors of around 300 nm thickness (see Table 3.2) were measured within a range of frequencies between 100Hz to 1MHz to determine the relative permittivity and dielectric losses in function of temperature and electric field. An HP 4194-A impedance analyzer was employed to determine the dielectric properties of our samples. To determine the value of the permittivity of a sample, we measured multiple replicates of such sample and to avoid variance of the measuring spot, several Pt top electrodes were deposited on each sample (see section 2.3). Once the room temperature measurement gave the first results, a sample representing the average among all other replicates was analyzed on the temperature dependence impedance set-up (see section 2.6).

Table 3.2: Thin films thicknesses measured by ellipsometry (see Annex 3). Sample names are coded as it follows: CC-Christopher Castro. CCB: Si/Pt substrate deposited at Bordeaux (ICMCB). CCBS: Sapphire/Pt substrate deposited at Bordeaux. CCT: Si/Pt substrate deposited at TU-Darmstadt.

Sample	Doping	Thickness	Sample	Doping	Thickness
CCB02	Nb	320	CCB21	Nb/La/Nb	288
CCB03	Nb	450	CCB22	La/Nb/La/Nb/La	388
CCB03-1	Nb	420	CCB25	Nb/Mn	266
CCB04	Mn	298	CCB26	La/Mn	238
CCB05	Undoped	342	CCB32	Mn/Nb	265
CCB06-2	Mn/Nb/Mn	293	CCB34	La	304
CCB07	Undoped	178	CCB35	Nb	280
CCB09	Mn	300	CCB37	La/Nb/La	340
CCB10	Mn	300	CCB38	Mn	318
CCB11	Mn/Nb/Mn/Nb/Mn	335	CCB39	Mn	319
CCB12	Mn/Nb/Mn	250	CCB40	Mn	319
CCB12-2	Mn/Nb/Mn	331	CCB42	La/Nb/La	340
CCB14	Nb/Mn/Nb	310	CCB43	La	311
CCB15	La	289	CCB44	Mn	319
CCB16	Nb	307	CCBS06	Mn	338
CCB17	La/Nb/La	341	CCT04	Undoped	234
CCB20	La/Nb/La	288	CCT19	Mn	970

3.3.1 Single doped BaTiO₃ thin films

Temperature dependence

Dielectric properties of BaTiO₃ capacitors were measured within a range of frequencies between 100Hz to 1MHz to determine the relative permittivity and dielectric losses in

function of temperature from 90K to 400K. In Figure 3.3 the variation of relative permittivity a) and dielectric losses b) of undoped, Mn-doped, Nb-doped and La-doped BaTiO₃ is shown. In the relative permittivity curves, a diffuse transition from the ferroelectric to

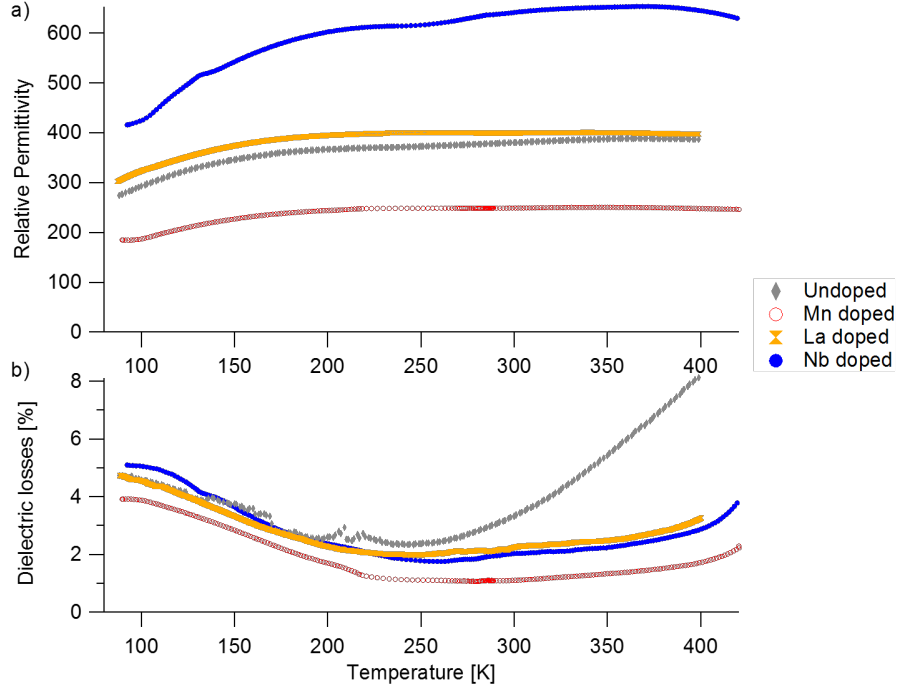


Figure 3.3: a) Relative permittivity and b) dielectric losses of undoped, Nb-, La- and Mn-doped BaTiO₃ thin films determined at 100kHz

the paraelectric state can be observed for all films, a common feature for BaTiO₃ sputtered thin films. For the sputtered thin films, a maximum of the permittivity ϵ_M can be determined at 100kHz and at a corresponding temperature T_M . For the undoped sample, ϵ_M is 388 at a T_M of 367K. In ceramics and thin films an enhancement of permittivity is reported when BaTiO₃ is doped with low concentrations of either Nb [151, 156, 158] or La [149, 151, 208] and a loss in permittivity upon doping with Mn [145-147, 178, 209] or Mg [210, 211]. We observed an increase of ϵ_M to 650 for Nb-doped sample and 400 for La-doped BaTiO₃ and a decrease to 250 for the Mn-doped sample. It appears that the La doping has little to no effect on the permittivity, indicating the non inclusion of La into BaTiO₃ structure. This could be also explained by a slight inclusion of La in the BaTiO₃ lattice (high ϵ_r) and a segregation of La to the grain boundaries, creating a lower permittivity material, thus, neutralizing the previous inclusion, resulting in an overall null effect of La on the permittivity. A slight change of T_m has also been observed: Nb-doped sample to a higher temperature and to lower temperatures for La- and Mn-doped samples. We emphasize that T_m values are difficult to determine due to the diffuse transition, so T_m values obtained here shouldn't be taken as absolutes.

In the dielectric loss curves, an increase of these are visible at high temperatures, indicating an increase of the conductivity. This increasing feature is more visible at lower

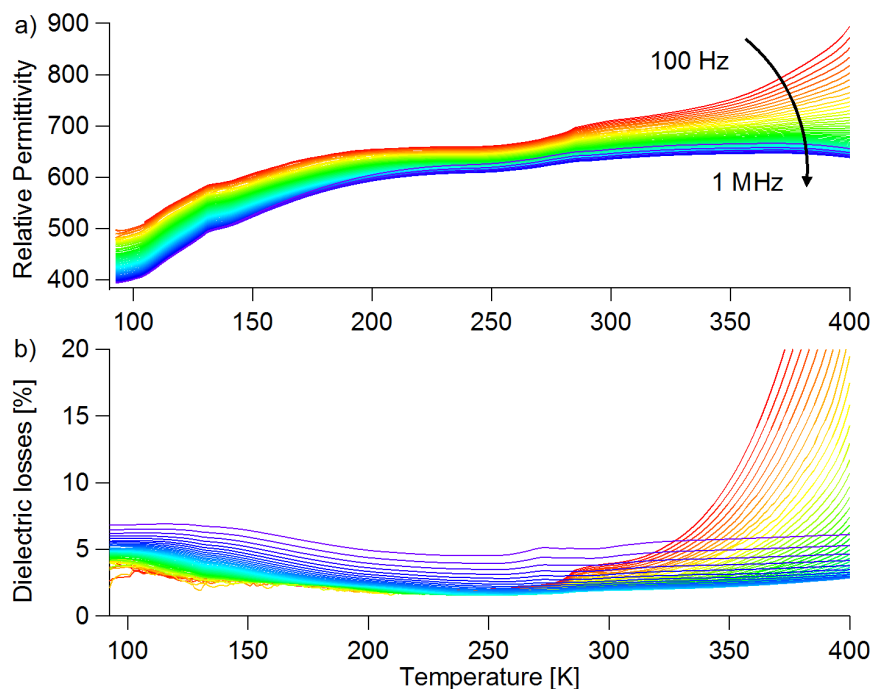


Figure 3.4: Frequency and temperature dependence of a) relative permittivity and b) dielectric losses of Nb-doped BaTiO₃ thin films

frequencies due to thermally activated conduction mechanisms as shown in Figure 3.4. For comparison, Nb-doped BaTiO₃ displays dielectric losses up to 51% at 400K and 100 Hz, nominally undoped BaTiO₃ reaches 89%, La-doped samples show 34% and Mn-doped BaTiO₃ 17%. At high temperatures, all doped samples show significantly lower dielectric losses compared to the undoped film, suggesting that all doped films are better insulators than the undoped one, especially the Mn-doped samples. Nevertheless, when we look at the Nyquist diagrams, as shown in figure 3.5, we first observe that all films have a high resistance since it is impossible to determine the exact radius of the semicircles. Furthermore, all arcs decrease in slope when increasing the temperature indicating a decrease in radius, thus confirming the increase of conductivity.

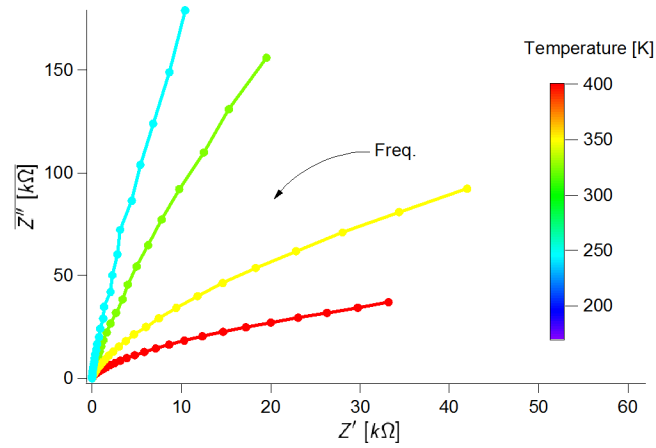


Figure 3.5: Nyquist plots of an undoped BaTiO₃ sample at different temperatures

Electric field dependence

Tunability properties have been measured at room temperature for all doped samples up to 5 V at 100 kHz. We calculated the tunability of films for 100 kV/cm, as shown in Figure 3.6. We observed the highest tunability at 100 kHz and 100 kV/cm for the Nb-doped BaTiO₃ with 38.4%, followed by the undoped one with 19.3%, then 7.2% for the Mn-doped BaTiO₃ and finally 6.16% for the La-doped BaTiO₃. By looking at the shape of these curves, we notice the typical "butterfly" shape for the Nb-doped and undoped BaTiO₃ thin films indicating a ferroelectric state, due to the hysteresis of the polarisation [212]. In contrast, Mn-doped and La-doped BaTiO₃ behave more as a tunable dielectric since they lack both a "butterfly" shaped hysteresis loop, both in permittivity and dielectric losses curves.

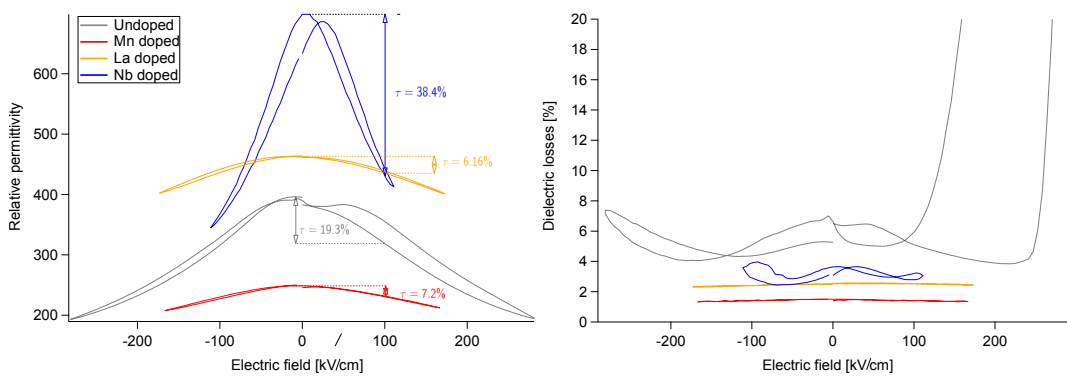


Figure 3.6: a) Relative permittivity and b) dielectric losses versus applied electric field of undoped, Nb-, La- and Mn-doped BaTiO₃ thin films determined at 100 kHz and room temperature. Tunability (τ) values were determined at 100 kV/cm

3.3.2 Heterostructures

In order to enhance the dielectric properties of BaTiO_3 thin films through interfacial effects, it was decided to deposit stacked layers of these different doped materials. One of the strategies was to decrease the dielectric losses without decreasing the permittivity by depositing a thinner film of a low dielectric loss material between the electrodes and a thicker thin film core of a high permittivity material. This was based on the fact that it is considered that most of the dielectric losses comes from the interface between a dielectric thin film and the electrode [45]. Since we are using Pt electrodes, it is commonly known that after Pt depositing on top of BaTiO_3 thin films by magnetron sputtering, a high amount of oxygen vacancies are created, increasing the dielectric losses as consequence [213]. Therefore, we need to deposit a p-doped material next to the Pt electrodes in order to decrease the dielectric losses. Based on the previous results, we decided to deposit a 300 nm film composed of 3 and 5 layers heterojunctions of Mn-doped BaTiO_3 and Nb-doped BaTiO_3 , placing the Mn-doped films in contact with the electrodes and a core of Nb-doped BaTiO_3 (3 layers) and alternating Mn- and Nb-doped films (5 layers) with thinner Mn-doped films at the sides and in the middle and thicker Nb-doped BaTiO_3 films in between. For comparison, we deposited the inverted 3 layer heterostructure, that is to say, Nb-doped films in contact with the electrodes and a Mn-doped core (see Figure 3.7). The second strategy was to obtain the highest permittivity regardless of the dielectric losses. In order to obtain this, we need to generate space charges inside the BaTiO_3 layers. From a previous study, it was observed that in Nb-doped BaTiO_3 films (deposited by magnetron sputtering) there was a segregation of Nb towards the surface, increasing the doping content in BaTiO_3 at the surface [156]. We used this result as a starting point and coupled it with La-doped BaTiO_3 thin films, creating a second type of heterojunctions, using either 3 or 5 structured layers. In this case, we tried both configurations, that is to say Nb-doped films in contact with the electrodes and a La-doped BaTiO_3 core; and La-doped films in contact with the electrodes and a Nb-doped film as a core (see Figure 3.7).

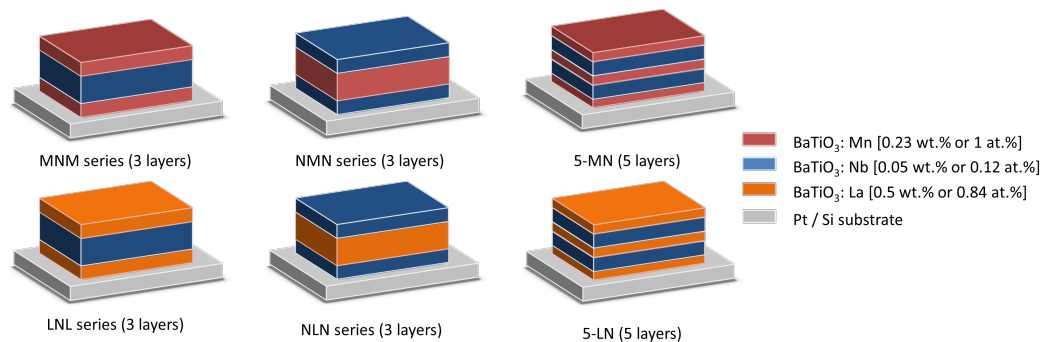


Figure 3.7: Heterostructures layers diagram. Correspondence of colors and materials are written in the legend. Thickness of layers and substrate are not to scale. Overall thickness of all heterostructures is around 300 nm

Mn/Nb based heterostructures

In order to assess the minimum thickness of Mn-doped films needed to observe a change in dielectric properties we chose 5, 10 and 20 nm of Mn-doped samples on both sides and 290, 280 and 260 of a Nb core correspondingly, in order to conserve a total thickness of 300 nm for each sample. These heterostructures will be referred as MNM5, MNM10 and MNM20. To confirm our hypothesis that Mn-doped BaTiO₃ layers at the interface with the Pt electrodes decreases the dielectric losses, we chose to deposit a thin film inverting the order of the layers, that is to say, a Mn-doped film at the core and 2 Nb-doped layers of 20nm at the flanks (sample referred as NMN20). We chose to analyse samples in temperature that fitted this hypothesis. When measuring samples at room temperature (as seen in figure 3.9) we observe that only samples MNM10 and MNM20 have low dielectric losses. In figure 3.8 we observe in the relative permittivity curves that MNM10 and MNM20 samples present a lower permittivity compared to a single Nb-doped BaTiO₃. Furthermore, in the dielectric loss response, it is clear that 20 nm of Mn-doped BaTiO₃ heterostructure displays similar losses than a single Mn-doped BaTiO₃, and decreasing the thickness of the Mn-doped layer, increases progressively the dielectric losses, from 2% to 4% with 20 nm and 10 nm of Mn-doped BaTiO₃ correspondingly.

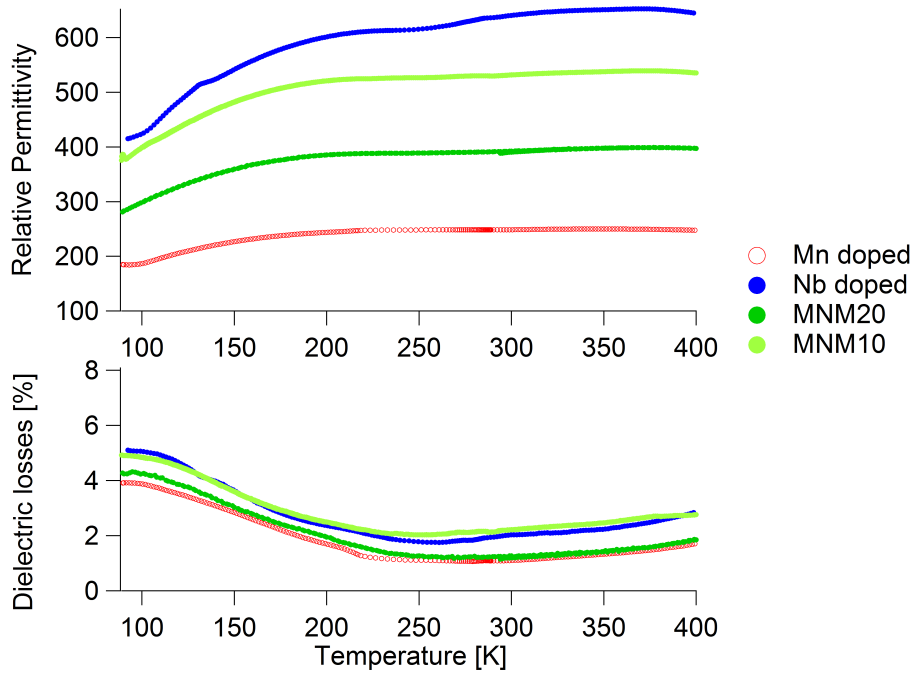


Figure 3.8: a) Relative permittivity and b) dielectric losses versus temperature at 100 kHz of MNM10 and MNM20 heterostructures. Nb- and Mn-doped BaTiO₃ are plotted for comparison

The electric field dependence of permittivity and dielectric losses of these p-n-p

heterostructures are shown in Figure 3.9. We clearly see the tunability of the films is inversely proportional to the amount of Mn-doped BaTiO₃ films, as for MNM20 we only have 18.9%, followed by MNM10 with 23.9% and the highest value of 39.9% corresponding to MNM5. The addition of 5 nm of Mn-doped BaTiO₃ in between the Pt electrodes and the Nb-doped BaTiO₃ core film not only increased the relative permittivity value at 100kHz it also increased the tunability of the film. Nevertheless, we observe again that the dielectric losses are also increasing inversely proportionally to the substituted thickness of Mn-doped BaTiO₃. We point out that MNM20, at higher fields than 100kV/cm, the dielectric losses reach a higher value than those of MNM10, despite the fact that the relative permittivity of MNM20 is still lower than MNM10. This can be explained with the electric field dependence of the relative permittivity in the paraelectric phase. In addition to these Mn substrate heterostructures, we included the electric field dependence of the dielectric properties of a n-p-n heterostructure: NMN20 (20nm Nb-doped / 260nm Mn-doped / 20nm Nb-doped). Sample NMN20 shows a relative permittivity higher than a single Mn-doped film but lower than MNM20 (which has the lowest value of permittivity amongst the p-n-p heterostructures) and a slightly higher dielectric losses than MNM20.

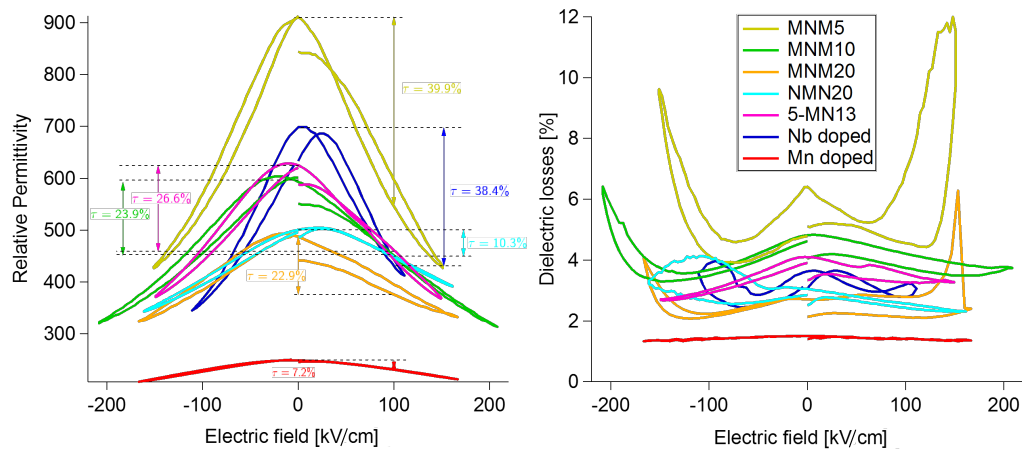


Figure 3.9: a) Relative permittivity and b) dielectric losses versus applied electric field of MNM10 and MNM20 heterostructures determined at 100 kHz and room temperature. Nb- and Mn-doped BaTiO₃ are plotted for comparison. Tunability (τ) values were determined at 100 kV/cm

La/Nb based heterostructures

For this type of heterostructure both dopants are reported to increase the relative permittivity and none of those are meant to decrease the dielectric losses. That is why we choose to deposit 10 nm for the thinner layer and 280 nm of the thicker core layer to achieve a total thickness of 300 nm in order to be able to compare with all other films. We tried both type of trilayered heterostructures, that is to say Nb/La/Nb (NLN10) and

La/Nb/La (LNL10), in order to artificially increase the dielectric constant by creating a space charge layer in between the layers of the ferroelectric film. In Figure 3.10 it is plotted the temperature dependence of the relative permittivity and dielectric losses of LNL10 and in addition single Nb- and La-doped BaTiO₃ for comparison.

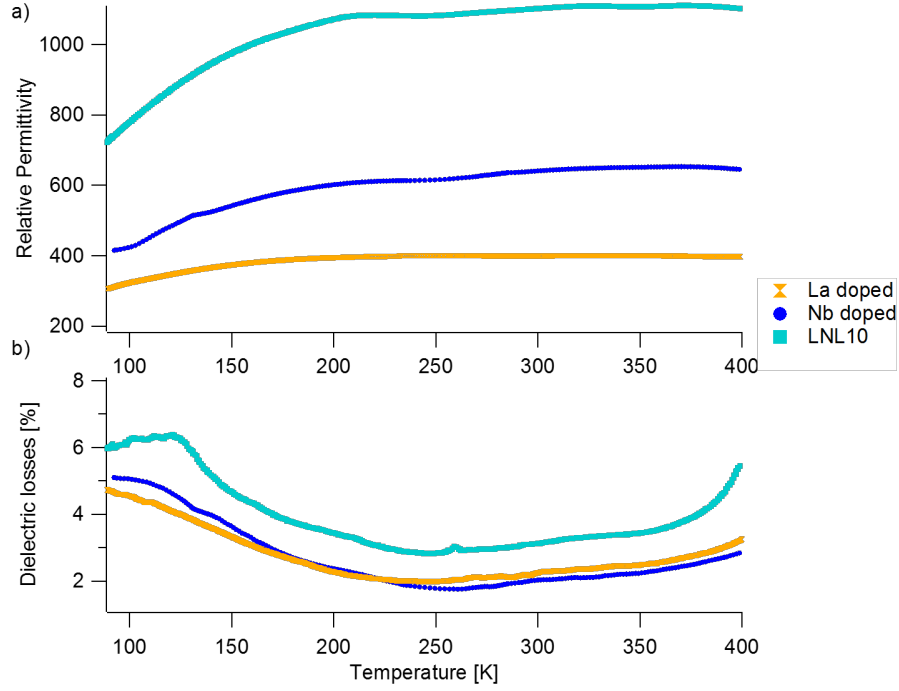


Figure 3.10: a) Relative permittivity and b) dielectric losses versus temperature at 100 kHz of LNL10. Nb- and La-doped BaTiO₃ are plotted for comparison

At first glance we observe the enhancement of the relative permittivity, as any linear combination of capacitors in series would always give an in-between value of the single doped films. Also we observe an increase of the dielectric losses (see Figure 3.10), especially at lower frequencies, suggesting that the enhancement of dielectric constant comes from space charges as dielectric losses at temperatures higher than 350K and frequencies lower than 1kHz can reach values from 0.2 up to 4. In effect, if we calculate the relative permittivity that would arise from 3 capacitors in series we will have:

$$\frac{1}{C_T} = \sum_i \frac{1}{C_i} \quad (3.1)$$

with $i=1$ to 3 and C_T the total capacitance resulting from the series of capacitors C_i . Considering that we have the same surface and that the first and the last capacitor have the same thickness and relative permittivity, equation 3.1 can be simplified to:

$$\frac{t_{total}}{\varepsilon_{total}} = \frac{t_1}{\varepsilon_{r1}} + \frac{2t_2}{\varepsilon_{r2}} \quad (3.2)$$

with t_{total} the total thickness of the layer, $t_{1,2}$ the corresponding thickness of each film, ε_{r_1} the relative permittivity of the core thin film and ε_{r_2} the dielectric permittivity of the outer thin films. Rearranging and substituting equation 3.2 for LNL10 at 100kHz and room temperature we obtain:

$$\varepsilon_{total} = \frac{\varepsilon_{r_1}\varepsilon_{r_2}t_{total}}{\varepsilon_{r_2}t_1 + 2\varepsilon_{r_1}t_2} = \frac{640 \times 400 \times 300\text{nm}}{400 \times 280\text{nm} + 2 \times 640 \times 10\text{nm}} \simeq 615 \quad (3.3)$$

As seen on Figure 3.10 (a), the experiment gives $\varepsilon_{total} > 1000$ thus indicating that an extra contribution is to be taken into account. This discrepancy certainly results from the main assumption behind equation 3.1 which is that if the interfaces are supposed to be abrupt, that is to say, there is no diffusion of any species, in this case La and Nb. This matter will be addressed and further developed in the discussion section, after having investigated the interfacial electronic states using XPS as described just below.

Electric field dependence of the dielectric permittivity and losses of these heterostructures are plotted in Figure 3.11.

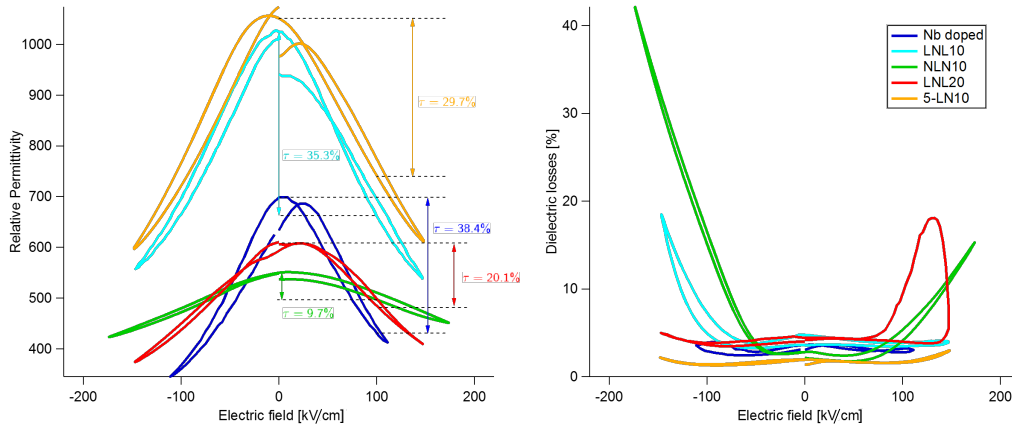


Figure 3.11: a) Relative permittivity and b) dielectric losses versus applied electric field of trilayer LNL10, NLN10, LNL20 and 5 layer 5-LN10 heterostructures determined at 100 kHz and room temperature. Nb- and La-doped BaTiO₃ are plotted for comparison. Tunability (τ) values were determined at 100 kV/cm

We first see the clear disappearance of the "butterfly" shape of LNL10, suggesting that the enhanced value of permittivity achieved for this heterostructure is not originating from a ferroelectric contribution. In the plot b) it is evident that there is a huge difference between the bottom interface and the top interface since at -100kV/cm , $\tan(\delta) > 18\%$, whereas at 100kV/cm , $\tan(\delta) \approx 4\%$. Such asymmetry can be ascribed to the different thermal history of the bottom layers as compared to the top ones.

3.3.3 Summary

Undoped, Mn-, Nb- and La-doped BaTiO₃ thin films were deposited in a MIM structure with Pt as electrodes. Temperature, frequency and electric field dependence of the relative permittivity and dielectric losses were characterized. In order to improve these dielectric properties, we deposited different heterostructures using these doped films with a thick core and thinner films at the sides. Figure 3.12 recapitulates the dielectric properties of all BaTiO₃ thin films.

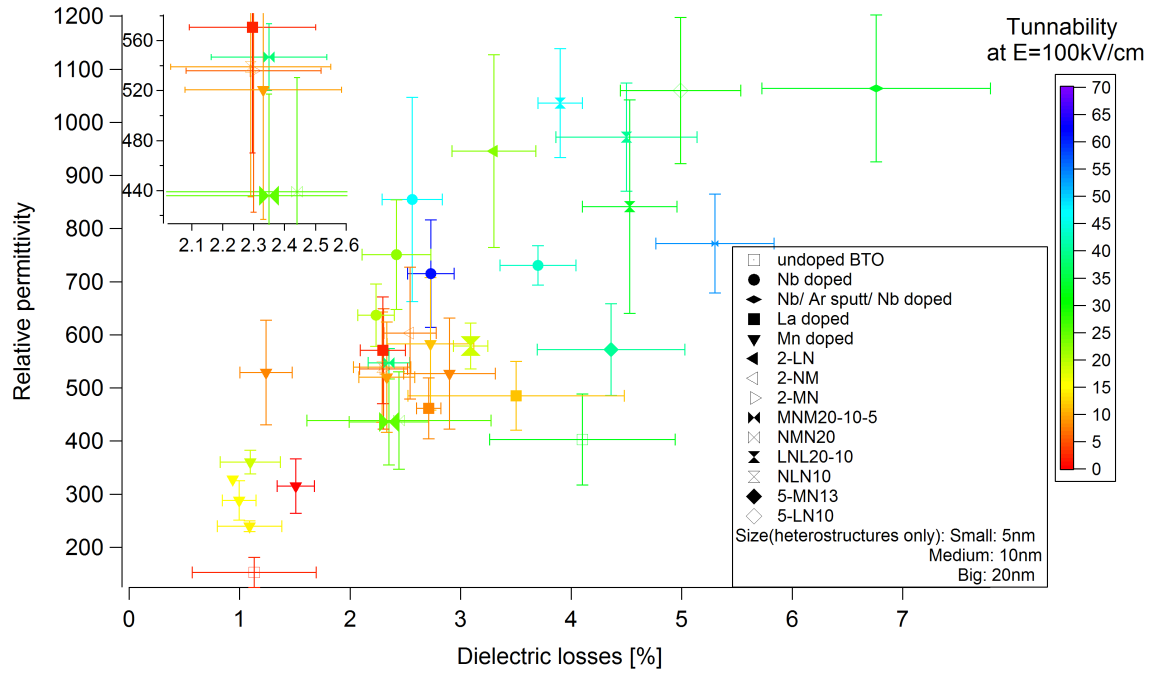
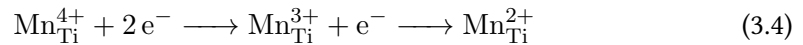


Figure 3.12: Relative permittivity versus dielectric losses of BaTiO₃ single doped and heterostructures thin films determined at 100 kHz and room temperature. Tunability (τ) values were determined at 100 kV/cm. Error bars calculated for a confidence interval of 95%

The lowest dielectric losses are obtained with samples doped with Mn and the highest permittivity is achieved by La/Nb based heterostructures. Mn-doped BaTiO₃ decrease the dielectric losses by trapping electrons originated from oxygen vacancies (see eq. 3.4) in the ion form Mn²⁺ or Mn³⁺ [178, 214].



N-type doped BaTiO₃ increases dielectric permittivity displaying a Positive Temperature Coefficient of Resistivity (PTCR) effect [131, 133, 134]. Furthermore, our heterostructures show high permittivity, which is in addition stable in temperature. This striking result could not be explained by a simple model of capacitors in series, which leads to the

hypothesis that this enhancement comes from interfacial space charges. These space charges may be visible as a relaxation peak in the impedance measurements. However, this hypothetical relaxation can only be visible at very low temperatures, and such experiment was not available at ICMCB due to timing problems. Nonetheless, space charge regions and defects in a material can be seen by looking at the electronic bands curvature and Fermi level position, respectively. Both of these parameters can be analyzed by X-Ray Photoelectron Spectroscopy. This has been done using the DArmstadt's Integated SYstem for MATerial Science (DAISY-MAT) at Technische Universität Darmstadt (TUD).

3.4 X-Ray Photoelectron Spectroscopy

X-Ray Photoelectron Spectroscopy (XPS) was performed using a Physical Electronics PHI 5700 spectrometer. Core level and valence band spectra were measured using a monochromatized Al K_α radiation with an energy resolution of approximately 400 meV. In order to get absolute values of the BaTiO₃ core level binding energies, the system was calibrated by using a sputter cleaned Ag foil and measuring the Ag $3d_{5/2}$ core level and the Gaussian broadening of the Fermi Edge on the same day of each measurement. In-situ XPS was carried out on samples freshly deposited by RF-magnetron sputtering in the Darmstadt Integrated System for Materials Research (DAISY-MAT) and then transferred to the analysis chamber without breaking the ultra-high vacuum (UHV). Ex-situ XPS analysis were carried out on samples deposited at ICMCB. In order to eliminate the common surface contaminations (i.e. carbonate adsorbates), a heat treatment was performed (400°C / 0.5 Pa / 2 sccm O₂ / 2 hours) inside one of the deposition chambers and then transferred to the XPS chamber.

A routine XPS analysis consists on 3 types of measurements. First, a survey spectrum which is used to determine the composing chemical elements present at the surface and identify possible contaminations. Second, a thorough measurement of the core levels of each element on their most intense peaks, for instance, in BaTiO₃ we will look at Ba $3d_{5/2}$, Ti $2p$, O $1s$ and Ba $4d$ in order to analyse the oxidation states, surface composition and electronic structure. Finally, a detailed spectrum of the valence band, as its position in binding energy will provide the position of the Fermi level, indicating the electrical nature of our semiconducting films. Figure 3.13 resumes a typical in-situ XPS routine analysis of an undoped BaTiO₃ thin film.

Foremost, after examination of the XPS survey spectrum, we do not detect any impurities (on the limit of resolution detection of XPS) and we proceed to examine the core-levels. On the Ba $3d_{5/2}$ spectrum, the peak asymmetry is related to a convolution of two components, a high-binding energy component often attributed to under-coordinated barium located at the surface (Ba_{surf}) for BaO termination and a lower energy component resulting from bulk-coordinated barium (Ba_{bulk}). Arveux et al. have shown this phenomenon as there is a change of Ba $3d_{5/2}$ spectra while measuring at different take-off angles. In fact, measuring at smaller take-off angles will lead to a higher surface sensitive measurement, and they have observed an increment of the Ba_{surf} signal while decreasing the take-off angle. This change in Ba-coordination between surface and bulk was attributed to a BaO surface segregation which was further confirmed by a shoulder on O $1s$ peak, which decreases while reducing the take-off angle. In our case, after deconvolution of the Ba $3d_{5/2}$ peak, we found out an energy difference between Ba_{bulk} and Ba_{surf} of 1.0 eV \pm 0.1eV for an undoped BaTiO₃ film.

It is well known that deposition of titanate based thin films by rf-sputtering produces oxygen vacancies due to the low oxygen content atmosphere [39, 40, 215], and it is often published that these V_O induce Ti³⁺ species [128, 130, 216–218]. However, as shown on the Ti $2p$ doublet, we observe no Ti³⁺ in our films as the Ti $2p_{3/2}$ peak does not show a shoulder at lower binding energies associated to Ti³⁺.

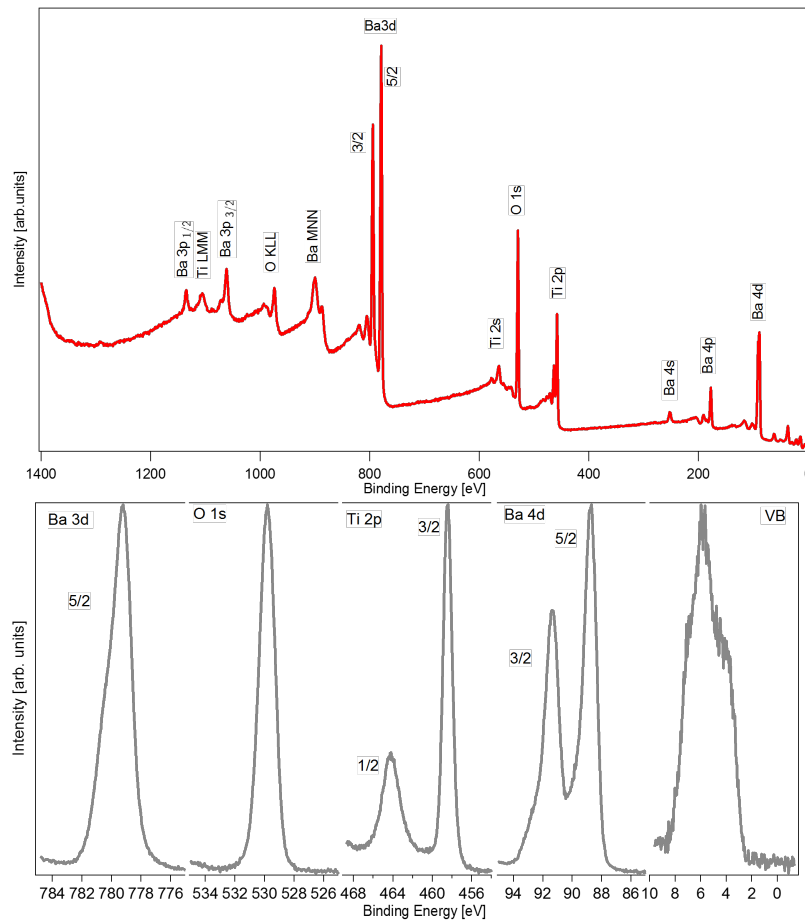


Figure 3.13: XPS survey (top) and core-levels (bottom) of an undoped BaTiO₃ thin film recorded with monochromatized Al K α radiation.

As for the Ba 4d spectrum a doublet arises ($4d_{5/2}$ and $4d_{3/2}$) due to spin-orbit splitting. This doublet presents as for Ba 3d two components, a low binding energy pair as result of Ba atoms in the perovskite and a higher energy pair attributed to Ba atoms in a relaxed surface [39]. After deconvolution of the Ba 4d peak we find a difference in energy between the two components of $0.9 \text{ eV} \pm 0.1 \text{ eV}$.

The valence band (VB) emission extends up to 8 eV below the Fermi energy, presenting a two-peak structure coming predominantly from O 2p states with a higher binding energy component of Ti 3d - O 2p bonding states [194], a well-known structure characteristic of ATiO₃ compounds (SrTiO₃, Ba[Sr]TiO₃, KNbO₃) [193-196, 196-200]. Moreover, one can directly determine the Fermi level position relative to the valence band maximum, $E_F - E_{VB}$, by looking at the intersection between the base line and the linear extrapolation of the leading edge of the valence band emission. In the case of the sample presented this value corresponds to $2.7 \pm 0.1 \text{ eV}$. Knowing that the band gap for BaTiO₃ is 3.2 eV [202], it is obvious that the Fermi energy is close to the conduction band minimum, indicating

that our nominally undoped film exhibits a n-type doping character. Most probably, such unwanted doping may result from oxygen sub-stoichiometry.

In addition to this, $E_F - E_{VB}$ can be obtained by measuring the core level binding energy of any BaTiO_3 core level as the difference $E_{VB} - E_{CL}$ is a material constant. In the case of this work, the value for $E_{VB} - E_{CL}$ has been determined by XPS in-situ measurements of the binding energies of the core levels Ba $3d$, O $1s$, Ti $2p$ and Ba $4d$ of several doped and undoped BaTiO_3 thin films.

As several samples have been prepared outside DAISY-MAT, it is relevant to indicate the differences between ex-situ and in-situ samples. In Figure 3.14, we compare several BaTiO_3 thin films, the samples prepared at ICMCB (ex-situ) and those prepared at DAISY-MAT (in-situ).

In addition to these spectra, we can observe an extra emission around 205 eV for the in-situ Nb-doped BaTiO_3 films, attributed to Nb $3d$ emission. None of the other dopants are observable on XPS as their low concentration and their main line positions on XPS make them inaccessible.

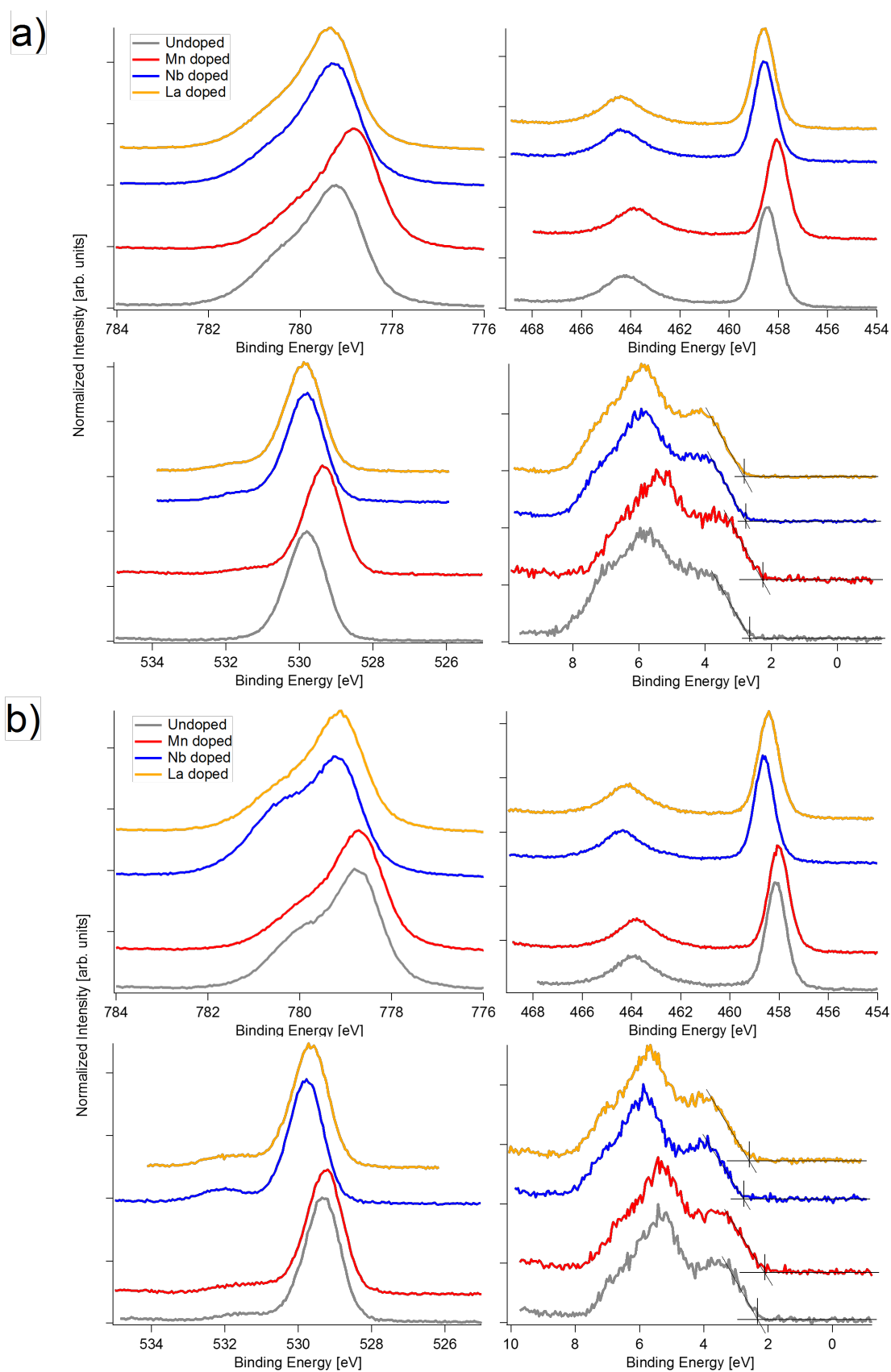


Figure 3.14: Ba 3*d*, O 1*s*, Ti 2*p* and VB XPS emissions of undoped and doped BaTiO₃ thin films deposited on Pt/Si substrates. a) In situ, b) Ex-situ

3.4.1 Single doped films

When comparing spectra coming from an in-situ or an ex-situ film of its corresponding dopant, the binding energy peaks of the different core levels are almost identical (see Figure 3.15). As stated before, $E_{VB} - E_{CL}$ is a material constant, by using this method, Figure 3.15 resumes the Fermi Energy of the different doped BaTiO₃ films analyzed ex and in-situ.

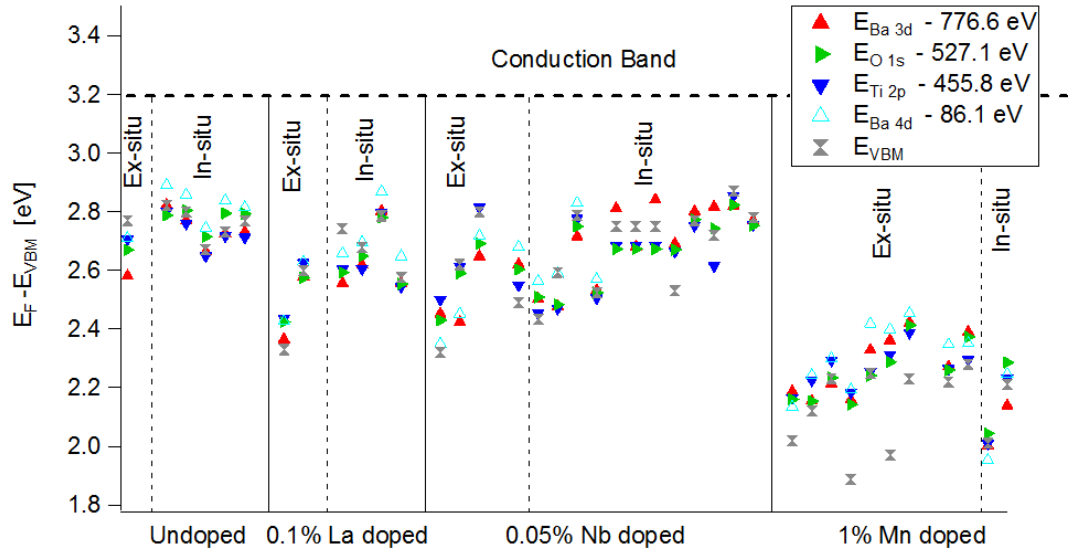


Figure 3.15: Fermi level position with respect to the Valence Band Maximum of different doped BaTiO₃ thin films analyzed by in/ex-situ XPS. The energies subtracted from each core level were obtained by several in-situ XPS measurements. Conduction band position is placed by using the optical bandgap of BaTiO₃ (3.2 eV).

The binding energies coming from the core levels of the in-situ films converge to a precision of the Fermi level of around 0.05eV whereas the ex-situ films have a wider error (0.12 eV). This difference is most likely coming from the surface modification due to the oxidation (cleaning procedure) prior to the measurement.

The biggest impact of the cleaning procedure is on the XPS emissions of Ba 3d and O 1s, as the peaks present an increasing shoulder at higher binding energies, leading to the speculation that this annealing to eliminate the carbonate adsorbates induces a further segregation of Ba to the surface in the form of BaO, as observed in the take-off angle experiment [39], as the intensity ratio between Ba_{surf} and Ba_{bulk} increases when decreasing take-off angle.

If we only consider the in-situ samples, after deconvolution of the Ba 3d peak by using two Gauss-Laurentz singlets, we observe that all doped films have similar Ba_{surf}/Ba_{bulk} intensity ratio. On the other hand, we detect a slightly higher Ba_{surf} component on the undoped BaTiO₃ thin film as seen in Figure 3.16

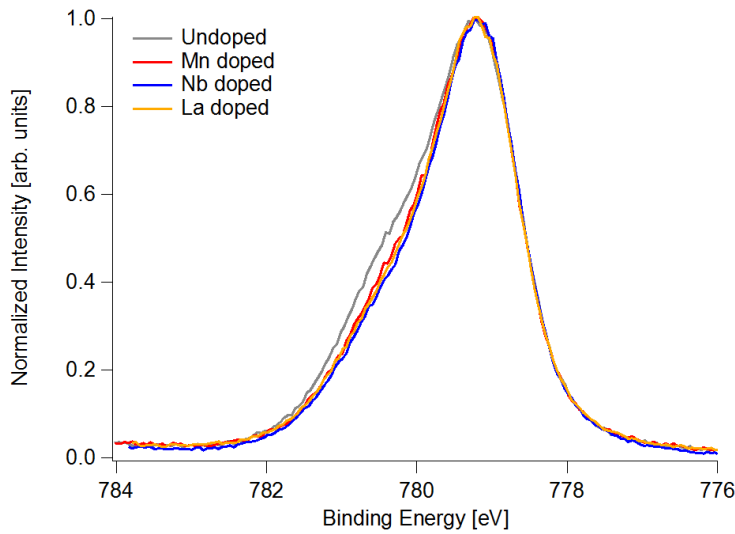


Figure 3.16: Ba3d XPS emission of doped and undoped BaTiO₃ thin films. The peaks were normalized and shifted in binding energies for better comparison of the Ba_{surf} and Ba_{bulk} components

When comparing the dopant effect on BaTiO₃, the Fermi level positions of each dopant are consistent whether it was analysed in or ex situ.

It is widely known that a Fermi level close to the conduction band will lead to a higher (electron) conductivity material and as it gets away from it the material will become more insulating. In the case of these films, the microstructure plays a bigger effect on the conductivity, as the columnar structure of the PVD will increase the leakage currents compared to ceramics or single crystals (see section 3.4). Nonetheless, we can compare our results with the theoretical values of the defect impurity levels and identify the valence state of our dopants via the defect transition levels, as some of the dopants inserted in our films are not detected on XPS due to the low concentrations used. In Figure 3.17 we compare the experimental in-situ Fermi level position of the single doped films deposited on Pt and the impurity transition levels of the corresponding dopants.

It is clear that all the dopants and deposition conditions have an effect on the E_F of BaTiO₃ thin films. Nonetheless, the theoretical values for each sample are still not at the position that it is expected. For the undoped sample, the E_F is far from the conventional understanding of an insulator, that is to say, a mid-gap fermi level position (1.6 eV). As discussed before, this can be explained by the oxygen poor atmosphere during deposition, creating a high concentration of oxygen vacancies that are compensated electronically, rising the E_F closer to the conduction band in consequence. For the Mn-doped sample, we observe that E_F obtained in this work is in accordance with the value found in literature for the impurity transition level of Mn^{2+/3+}. Thanks to the paramagnetic character of Mn ions, we can verify this by EPR measurements (see section 3.6). It is worth mentioning that due to the deposition conditions, we should be able to reach the second transition

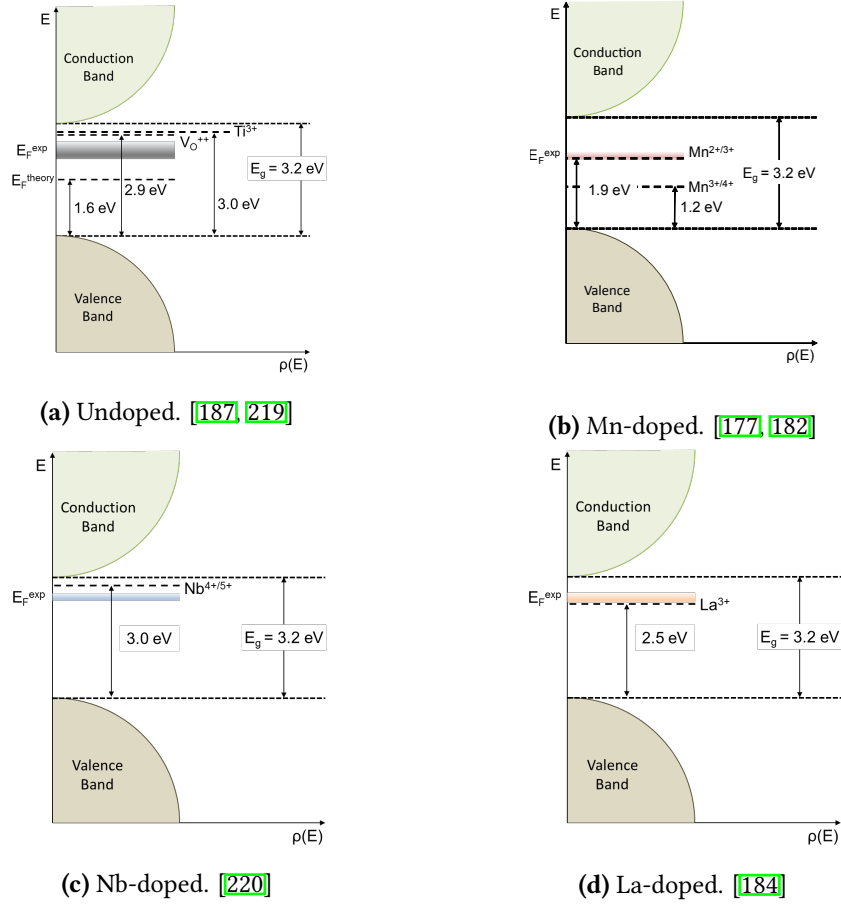


Figure 3.17: Experimental E_F of undoped and doped BaTiO₃ thin films. For each sample, the corresponding main theoretical impurity levels are shown for comparison. V_O [177, 221], Ti^{3+} [187], Mn [177, 182, 221], Nb [187] and La [184]

level, $Mn^{3+/4+}$, by oxidizing treatments (cf fermi level engineering). This decrease of the Fermi level position within the band gap under Mn doping is consistent with previous reports on sol-gel films [209]. In regards to the Nb- and La-doped samples, both dopants rise the E_F closer to the CB, but it appears that the Nb doping is not sufficient to bring the E_F to the theoretical value of $Nb^{4+/5+}$. We can observe the same phenomenon with the evolution of resistivity in function of Nb concentration (see Figure 1.19), as Nb-doped BaTiO₃ reaches a minimum of resistivity for a Nb concentration of 0.1% implying that E_F reaches a maximum value closer to the CB. Moreover, if the theoretical value of La doping is as deep as 2.5 eV, this dopant can hardly be used to make n-type semiconducting BaTiO₃. Experimentally, it is known that a low amount of La in BaTiO₃ can increase highly the conductivity [131, 132], meaning that this theoretical level should be closer to the conduction band.

Composition analysis

In order to assess with precision the surface composition of our films it is necessary to subtract the background coming from the secondary electrons (c.f. section 2.4). In the case of BaTiO₃, 2 functions were used for background subtraction: a quartic polynomial (polynomial of degree four) for the core-levels of Ba 3d_{5/2} and O 1s, and a Shirley function for Ti 2p. Once this step is done, it is possible to determine the chemical composition of our films by integrating the background-corrected peak areas and then correcting them by using the corresponding atomic sensitivity factors for X-ray sources. As mentioned before, among all dopants, only Nb is visible in the XPS spectra. Because of this, we compare the cation ratio between samples as the ratio between A and B site concentration. In Figure 3.18 we resume the overall B/(A+B) sites ratio. Moreover, the Nb content found by this composition analysis is significantly higher than the target's doping concentration (0.05% wt. = 0.12% at.) as the calculation gives a concentration of 4.84% at. suggesting 3 possibilities, a surface segregation of Nb from the bulk or a higher sputtering rate of Nb with respect to the other elements, with a depletion of the target as a consequence or a lower resputtering effect of Nb from the film. This will be addressed in detail on the discussion section.

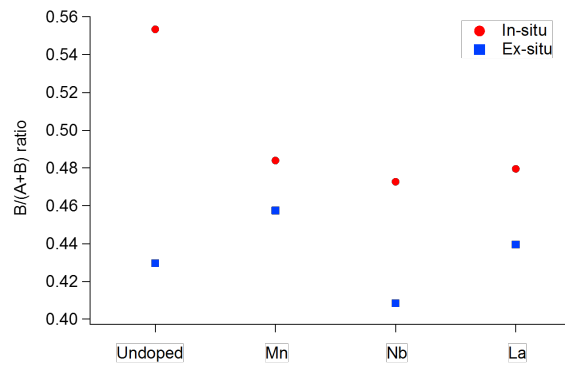


Figure 3.18: Cationic ratio ($B/[A+B]$) of in and ex situ doped BaTiO₃ thin films

In regard to the overall cationic ratio, we find out that films produced in DAISY-MAT are close to stoichiometry whereas films deposited at ICMCB (ex-situ) have an excess of Ba. This can be due to the Ba segregation to the surface, producing a secondary phase that will increase the overall Ba surface concentration. It is worth mentioning that for an undoped in situ film (DAISY-MAT), a Ti-rich BaTiO₃ is produced, but for an ex-situ film (ICMCB) we found the same trend as for single doped samples deposited at ICMCB. For undoped ATiO₃ compounds, it is commonly observed a Ti excess in thin films as a resputtering effect of the A-site is involved during deposition [39, 40]. The relatively high deposition speed (2.5 nm/min) and the sputtering yield of each species prevent having the same Ba/Ti ratio in the target and the films [222]. In our case, Ba resputtering can cause a Ti excess of 5-10%, most likely located at the grain boundaries [40]. This has also an effect on the E_F as described by Arveux [39], where they observe and evolution

of E_F associated with the excess of Ti in BaTiO_3 as Ti-rich films display high E_F (2.7 eV) in low oxygen content (1%) and decrease down to 2.35 eV when the films are closer to stoichiometry obtained in high oxygen content (20%). Concerning the undoped samples produced at ICMCB, we observed a lower Fermi level and higher Ba content. One could argue that this result is the consequence of the annealing cleaning process prior to the XPS measurement. In order to prove (or disprove) this hypothesis, we took the in-situ samples out of the system (DAISY-MAT) and perform the same cleaning procedure (annealing at 400 degrees at 0.5 Pa O_2 for 2h) as a sample coming from ICMCB. We observed roughly the same Fermi level position (2.75 ± 0.05 eV) and 0.01 lower value on the cationic ratio. This results indicates that the cleaning procedure has little to none effect on the Fermi level position and the overall surface composition of the BaTiO_3 thin films. We can only say that undoped films deposited at ICMCB have lower Fermi level and a small excess of Ba. This difference is therefore related to the deposition conditions. At ICMCB the targets are 3 inches in diameter and the power chosen to deposit the films is around 100 W, so, the dc "autopolarization" voltage is quite high. In order to match the deposition rate and power per surface area at DAISY-MAT, as the target used is 2 inches in diameter, the power used is lower (25 W) and therefore the voltage is also lower.

Once a dopant is introduced in the lattice, we observed close to stoichiometry thin films regardless of the nature or location (A or B site) of the dopant.

Nevertheless, it is clear that ex-situ films show a Ti deficiency compared to in situ films. This does not affect the leading edge of the valence band (Fermi level position) for the doped samples, as seen in Figure 3.15, but it does seem to have an effect on the higher binding energy component of the valence band, that is to say, the Ti $3d - \text{O } 2p$ bonding states, as we note a more intense shoulder around 7 eV for the in-situ samples (see Figure 3.14). This inequality can be seen again in the difference between Ti $2p$ and O $1s$ binding energies in function of the Ti content as presented in Figure 3.19.

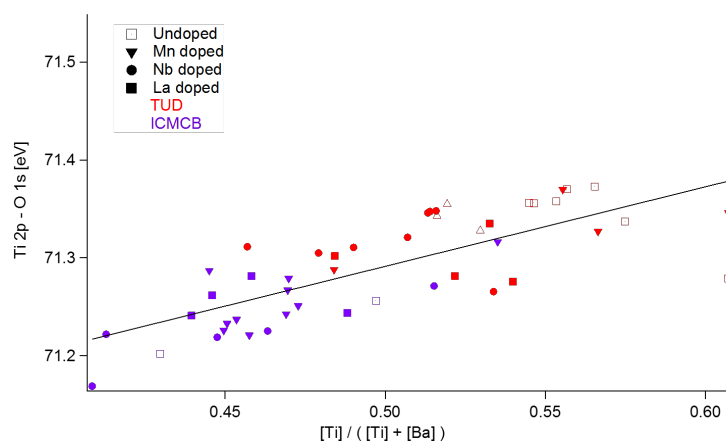


Figure 3.19: Ti $2p$, O $1s$ binding energies difference versus cationic ratio ($\text{Ti}/[\text{Ba}+\text{Ti}]$) of in and ex situ doped BaTiO_3 thin films.

As the Ti content increases, the Ti $2p$ and O $1s$ difference in binding energy increases

as well, showing an evolution of the chemical bonding causing a broader valence band.

As stated before, these results are in correlation with the oxygen poor atmosphere along with the resputtering of the surface during deposition, creating a high concentration of oxygen vacancies and non stoichiometric films. To explore the effects of the oxygen content in our films, we decided to do a post-treatment on the surface of the films with an oxygen atomic source which aims to increase the oxygen concentration at the surface, decreasing the oxygen vacancies concentration and therefore lowering the Fermi level position towards to the valence band.

3.4.2 Oxygen atomic source post-deposition treatment

Oxygen plasma treatment is known for surface cleaning for oxide films, reactive sputtering, etching and as oxidation treatment [55, 223]. After thin films deposition (same sputtering conditions as described in section 2.1), we first analyzed the chemical and electronic properties by XPS, then transferred to the chamber where our atomic source is located. We used a GEN II-TPIS Plasma Source (Atom/Ion Hybrid source) from Tectra. This source allows reactive neutrals (O_2) to escape and form the dominant beam fraction by using a BN aperture plate that inhibits ions from escaping from the plasma.

We inserted our samples in the chamber far from where the oxygen plasma beam is directed, increased the pressure to 10^{-4} mbar with 2 sccm of O_2 , then turned on the plasma by increasing the intensity slowly to 40 mA and waited for 15 minutes before putting our samples in front of the plasma as to reduce the impurities coming from ionized particles during the plasma ignition (typically N and/or B coming from aperture or Mo from the extraction grid). After this delay, we brought the samples in front of the oxygen plasma for 20 minutes and re-analyzed them by XPS.

In Figure 3.20, we show the Fermi level position of single doped samples before and after oxygen plasma treatment determined by the position of the valence band and the core levels.

In general, the oxygen plasma treatment decreased effectively the Fermi level position of our films by around 0.2 eV. In the case of Mn doping, this shift was only about 0.1 eV. This difference will be discussed in section 3.7

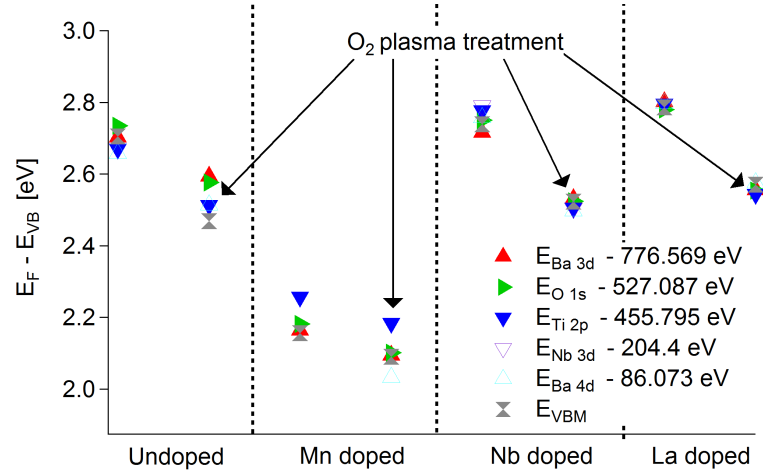


Figure 3.20: Fermi level position with respect to the Valence band of single doped samples. O_2 plasma post deposition treated samples are indicated with an arrow

Composition analysis

In order to better understand the effect of the oxygen plasma treatment, it is necessary to analyse the effect on the stoichiometry at the surface of our films. In Figure 3.21 we resume the overall $B/(A+B)$ sites ratio.

The O_2 plasma treatment did increase the oxygen content for all of films. The only case where the oxygen content was not greatly increased, it was for the Mn-doped film. This means that the lowering of the Fermi level position for the La- and Nb-doped films is regulated by the concentration of oxygen at the film's surface. Moreover, looking at the overall stoichiometry of the films, as shown in the inset of Figure 3.21, no significant change of the cationic ratio of BaTiO_3 films is observed after the oxygen treatment was applied.

The mechanisms of the change of Fermi level will be discussed in section 3.7

3.4.3 Heterostructures

Following the strategy of creating space charges, either to enhance the relative permittivity or to decrease the dielectric losses, we analysed both type of heterostructures and their symmetrical arrangement. We determined the electronic bands curvature and the composition by a series of interface experiments by following the evolution of core level binding energies as a function of film thickness (Kraut method [224]). To achieve this goal, we analysed by XPS after each deposition step. The first step consisted of a deposition of a base sample (i.e. 20 nm) of a determined doped BaTiO_3 sample (i.e. Mn), followed by several deposition steps of a differently doped BaTiO_3 (i.e. Nb). The choice of the first layer thickness was based on the thickness of the films analysed by impedance spectroscopy. Film thicknesses are calculated assuming that the deposition rate of each

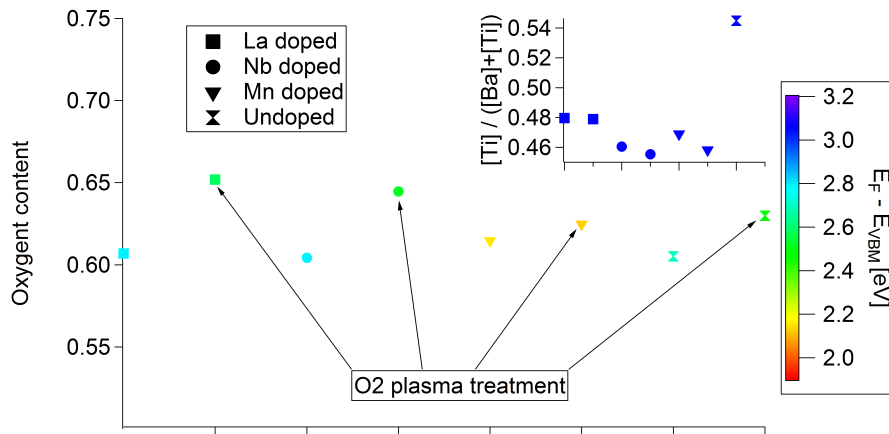


Figure 3.21: Oxygen concentration ratio $[O]/([Ba]+Ti+[O])$ of untreated and oxygen plasma treated (un)doped $BaTiO_3$ thin films. Inset: Cationic ratio $Ti / (Ba + Ti)$ of (un)treated (un)doped $BaTiO_3$ thin films

doped target remains constant (see section 3.2).

Mn/Nb doped based heterostructures

First, a Nb-doped $BaTiO_3$ thin film was deposited with a thickness of 20 nm in order to reproduce the core of sample MNM20 (see section 3.2). Next, the film was analysed by XPS, recording the core levels of Ba 3d, O 1s, Ti 2p, Nb 3d, Ba 4d and the valence band. Subsequently, Mn-doped $BaTiO_3$ was sputtered on the base Nb-doped $BaTiO_3$ film in a 6 steps deposition from a calculated deposition rate of 2.5 nm/min, from 0.5 nm up to 20 nm. Figure 3.22 shows the evolution of the previously mentioned core levels and valence band throughout the Mn-doped $BaTiO_3$ increasing film thickness.

The Ba 3d, O 1s, Ti 2p and VB shift progressively to lower binding energies as the thickness of Mn-doped $BaTiO_3$ increases. Interestingly, the Nb 3d doublet continues to appear after 120 seconds.

In Figure 3.23 we plot the evolution of the Fermi level determined from Kraut method, in function of the thickness calculated from the deposition time and the average deposition rate. The Nb-doped $BaTiO_3$ substrate displays a $E_F = 2.6$ eV and reaches a minimum of 2.2 eV after 10 nm of Mn-doped $BaTiO_3$, which can be taken as the thickness of the space charge region (SCR) of this n-p junction. We also note that the stable Fermi level which is reached after 10 nm thickness is in perfect agreement with the observed position for the single layer Mn-doped $BaTiO_3$ (see Figure 3.17). It is worth mentioning that due to the high Mn concentration of the deposited film one would expect to have a sharper and thinner SCR, but we have to consider the eventual Nb diffusion from the substrate to the Mn-doped film and the effective carrier concentration. This will be described in detail in the discussion section.

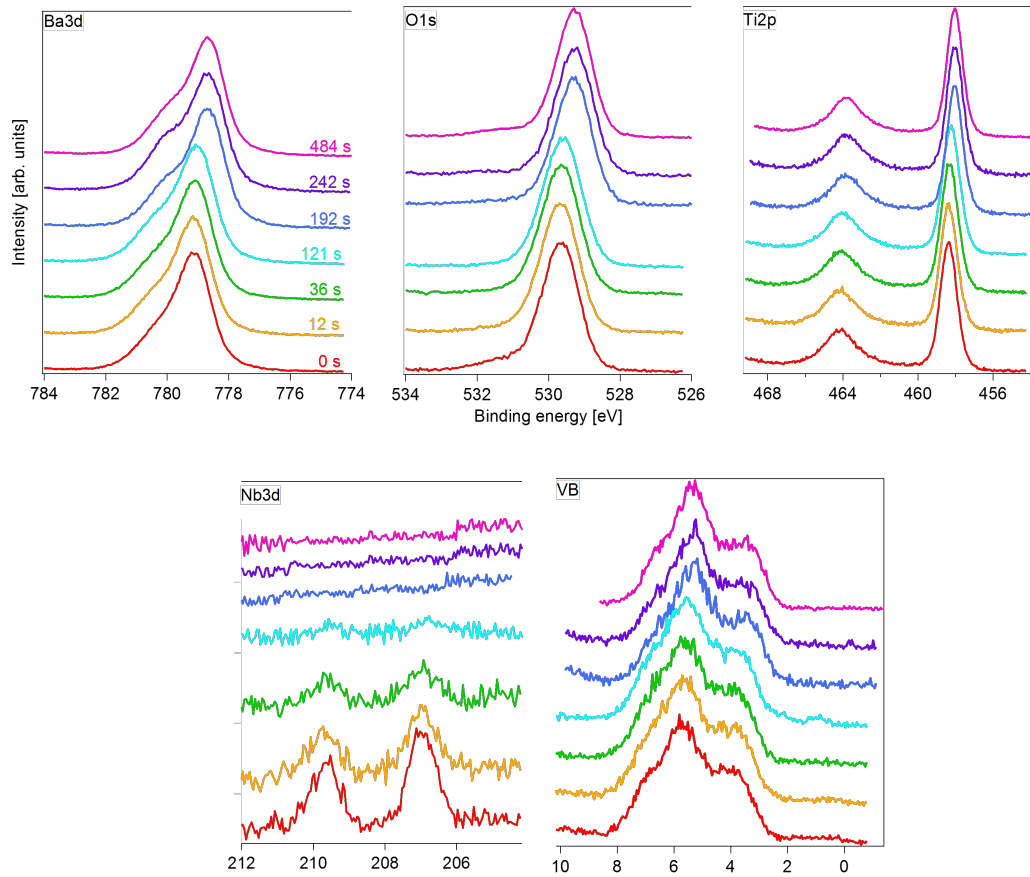


Figure 3.22: Ba $3d$, O $1s$, Ti $2p$, Nb $3d$ core levels and valence band spectra of the interface Nb-doped BaTiO₃ / Mn-doped BaTiO₃. Mn-doped BaTiO₃ deposition times are noted on the Ba $3d$ spectra. For each figure, the computed thickness, assuming a constant deposition rate of 2.5b nm/mn varies from 0.5 nm (bottom) up to 20 nm (top)

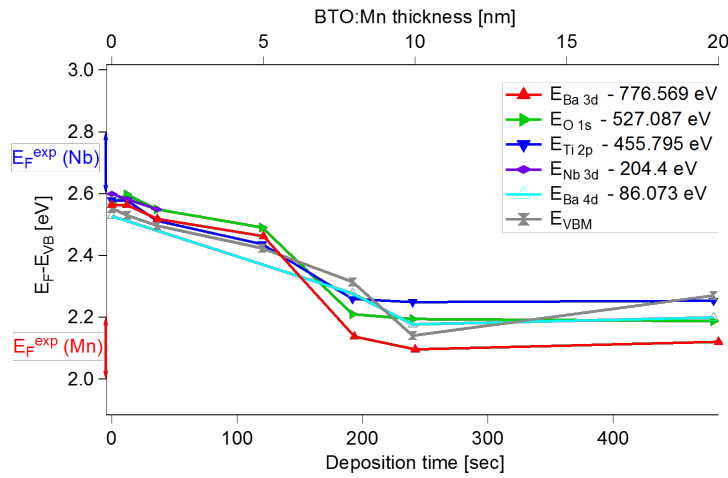


Figure 3.23: Fermi level evolution of Nb -doped BaTiO₃ / Mn-doped BaTiO₃ interface obtained by XPS. Film thickness was determined by using the deposition time and the average deposition rate of Mn-doped BaTiO₃. Experimental Fermi level of single Nb- and Mn-doped samples are included on the y-axis as reference

La/Nb based heterostructures

A base film of 10 nm La-doped BaTiO₃ was deposited in order to reproduce sample LNL10. With the same method as before, the film was analyzed by XPS recording the Ba 3*d*, O 1*s*, Ti 2*p*, Ba 4*d* core levels and the valence band. Following this, a stepwise deposition of Nb-doped BaTiO₃ was carried on, from 0.5 nm until reaching 20nm of this doped material. After each deposition the film was analyzed by XPS. In addition of the core levels mentioned before, the Nb 3*d* peak was recorded and the only valence band for the 2 last steps. Figure 3.24 shows the evolution of the previously mentioned core levels and valence band throughout the Nb-doped BaTiO₃ increasing film thickness.

An initial Fermi level of 2.65 ± 0.05 eV is reached for the La-doped film. After 0.5 nm of Nb-doped BaTiO₃ the Fermi level drops down to 2.35 ± 0.05 eV and then continuously increases to 2.6 eV after reaching 20nm of Nb-doped BaTiO₃. It is worth mentioning that the values of the Fermi level for La-doped and the last step of Nb-doped BaTiO₃ (20nm) are consistent with the values obtained by the corresponding single doped samples.

If we consider a perfect interface between these materials, this drop in Fermi level is not expected as both materials are n-type semiconductors and in both cases the experimental E_F range obtained in this work is 2.7 ± 0.1 eV. Therefore, in order to explain this drop we have to consider the interaction between these 2 doped films, namely an interdiffusion between La and Nb, causing a more insulating interface than the single doped materials (see section 3.7).

As this interdiffusion may occur from both sides, that is to say, Nb diffusing into the La-doped film and vice-versa, we investigated the inverted equivalent of this interface experiment: a Nb-doped BaTiO₃ substrate with a stepwise deposition of a La-doped BaTiO₃ film. The core levels analyzed by XPS were the same as the previous experiment

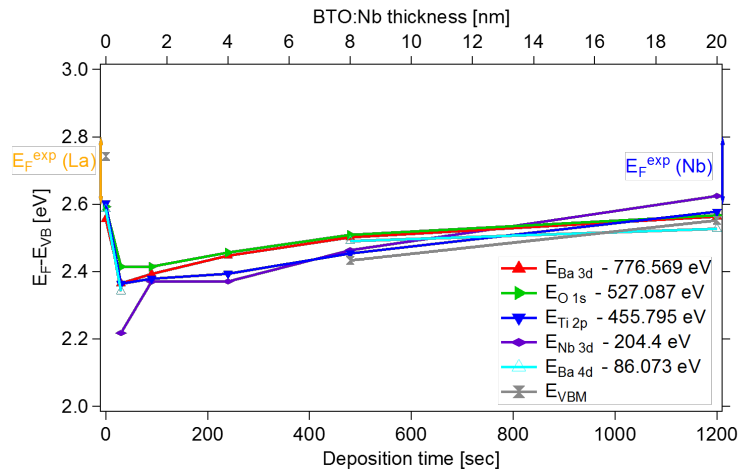


Figure 3.24: Fermi level evolution of La-doped BaTiO₃ / Nb-doped BaTiO₃ interface obtained by XPS. Film thickness was determined by using the deposition time and the average deposition rate of Nb-doped BaTiO₃. Experimental Fermi level of single La- and Nb-doped samples are included on the y-axis as reference

and the step deposition thicknesses were from 0.5 nm up to 8 nm. Figure 3.25 shows the evolution of the core levels and valence band throughout the La-doped BaTiO₃ increasing film thickness.

This time, the Fermi level steadily increases as the La-doped film thickness increases.

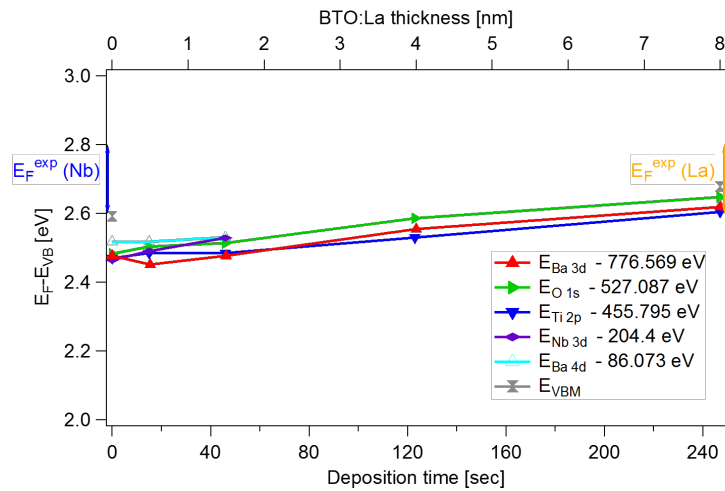


Figure 3.25: Fermi level evolution of Nb-doped BaTiO₃ / La-doped BaTiO₃ interface obtained by XPS. Film thickness was determined by using the deposition time and the average deposition rate of La-doped BaTiO₃. Experimental Fermi level of single Nb- and La-doped samples are included on the y-axis as reference

This suggests that the bottom layer diffusion plays a bigger role than the dopant diffusion that is being deposited onto, as it is the bottom layer which experiences a longer period of heating. With this reasoning, these interface experiments imply that the La diffusion is crucial on the irregular evolution of Fermi level and therefore, the electrical properties.

3.4.4 Summary

We have measured the core level energies of Ba $3d$, O $1s$, Ti $2p$, Ba $4d$ and the valence band spectra of nominally undoped, Mn-, Nb- and La-doped BaTiO₃. By using the Kraut method, we were able to precisely measure the Fermi level position and the surface composition of in-situ and ex-situ thin films. While the Fermi level position of the undoped films can vary, Mn-, La- and Nb-doped BaTiO₃ displayed a $E_F - E_{VB} = 2.2$ eV, 2.7 eV and 2.7 eV correspondingly. These results agree with literature [177, 182, 184, 187, 219, 220]. Additionally, we analysed the band curvatures of Nb/Mn, Nb/La and La/Nb based heterostructures by depositing continuously layers of Mn, La and Nb, correspondingly. While the band bending of the Mn/Nb is continuous with a space charge region of around 10 nm, it is worth mentioning that an unexpected broad band bending arose at the interface La/Nb doped BaTiO₃, where after depositing the first layer of Nb-doped BaTiO₃ the Fermi level dropped on average 0.3 eV. Figure 3.26 displays the general results obtained by XPS; for a given composition, the same marker appears several times because the stoichiometry, XPS emission shape and Fermi level position may vary from one film to the other. This is similar to what was already seen in Figure 3.19 and shows that the deposition conditions matter a lot when looking at the electronic levels in such films and heterostructures. Moreover, the Fermi level positions of La-, Nb-doped and undoped BaTiO₃ films have been lowered by 0.2 eV by O₂ plasma post deposition treatment. This shift of Fermi level was achieved by oxidising our films exposing their surfaces to our oxygen atomic source at room temperature.

In general, a high Fermi level position of a material will induce higher current densities when applying an electric throughout the film. We characterize this by looking at the leakage currents in function of temperature.

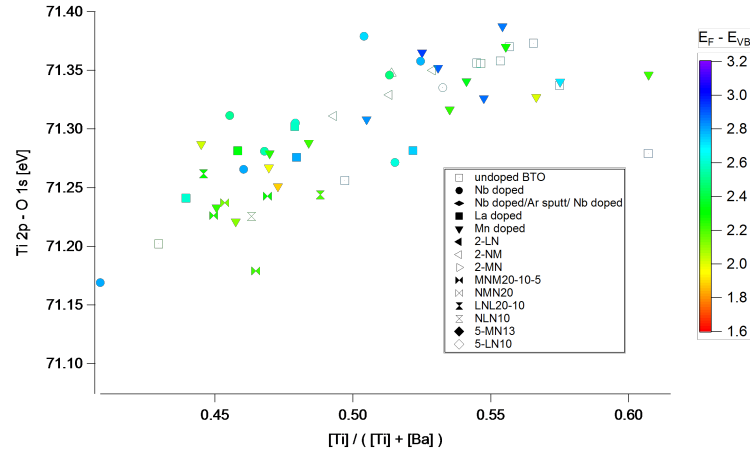


Figure 3.26: Ti $2p$, O $1s$ binding energies difference versus cationic ratio (Ti/[Ba+Ti]). Color of markers corresponds to their Fermi level position $E_F - E_{VB}$. In situ, ex-situ XPS results are shown. Substrates used: Pt, STO:Nb [0.05wt%] single crystal, Ta and Ag

3.5 Leakage Currents

Leakage current analysis of BaTiO $_3$ thin films was carried out on the same series of films characterized by impedance spectroscopy: MIM capacitors of around 300 nm of BaTiO $_3$ and Pt electrodes. The leakage current density was measured at temperatures ranging from room temperature to 200°C. A staircase shaped dc-bias voltage of 0.05 V height and 1 s duration at each step was applied to the top electrode while the bottom electrode was grounded. These parameters were chosen after a study of the time evolution of leakage currents at 100 kV/cm at each temperature investigated (see Annex). For all samples, the measurement was carried on 3 different capacitors of with 300 micron diameter Pt top electrodes.

As these films are polycrystalline and deposited by rf-magnetron sputtering, it is commonly known that this type of films present columnar growth [40] with grain boundaries more likely to shortcut the MIM capacitors at lower electric fields than non-oriented polycrystalline films such as sol-gel films where electric fields up to 800 kV/cm can be applied. For this reason, we opted to limit the maximum electric field to 100 kV/cm to avoid films degradation. Moreover, the columnar grains contribute to the leakage currents of the films, complicating even more the modeling of the curves and therefore making it impossible to fit with the commonly known semi-conductor conduction mechanisms cited in Part 1 (Fundamentals). Consequently, we will not try to fit any of the curves and only compare them among each other's as the fit with the theoretical models would give misleading results as they do not take into account the polycrystallinity nor the geometry of our films. In order to compare all films, we opt to show the leakage current densities at 100°C (373 K) since beyond this temperature the window of time before the film enters the resistance degradation is very short (see section 2.5). To suppress relaxation currents and have consistent measurements [110, 214], we applied at the top electrode 100kV/cm

heated at 100°C for 1000 seconds prior to the measurement.

3.5.1 Single doped BaTiO₃

As stated before, leakage current densities of single doped films were measured at different temperatures. In Figure 3.27, we show an example of the evolution of current density against electric field at different temperatures for a La-doped BaTiO₃.

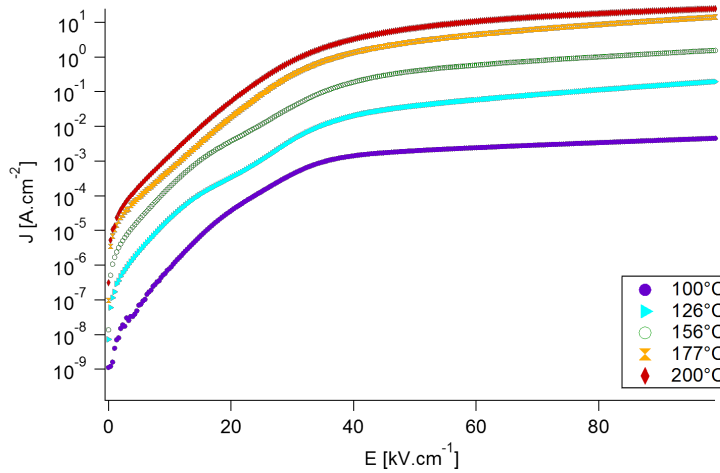


Figure 3.27: Leakage current density in function of electric field of a La-doped BaTiO₃ thin film measured at different temperatures

As expected, the temperature has a significant influence on the current density of our films with an increase for all electric fields at high temperatures. Furthermore, we see a different shape for the 100°C curve, where a change in slope is found around 40 kV/cm. This could mean that an additional conduction mechanism is activated for temperatures above 100°C at around 40 kV/cm. In addition to this, there is a small difference between the current densities of curves measured at 177°C and 200°C. This could be related to a relaxation of the resistance at 200°C as we know that at this temperature (see Annex) we reach J_{\max} in few seconds for the most of our films.

To better observe the influence of doping in BaTiO₃, we plot in Figure 3.28 the evolution of leakage currents in function of electric field at 100°C. We chose this temperature to avoid the resistance degradation and relaxation currents for our 4 single doped films: undoped, Mn-, La- and Nb-doped BaTiO₃.

At 0 kV/cm we found that the leakage current density J_0 is the lowest for the Mn-doped sample, followed by La-doped, then Nb-doped and finally the undoped BaTiO₃. These results are in agreement with the temperature dependent impedance spectroscopy experiment as the dielectric losses at high temperature are related with the conductivity of the material. Indeed, the Mn-doped sample has the lowest dielectric losses at 100°C and the lowest J_0 . The lower leakage current for the Mn-doped film is also consistent with

the lowering of the Fermi level within the band gap for this doping as compared to all other films (Figure 3.17). Furthermore, we found again that the undoped sample presents the highest conductivity as its J_0 is around 10^{-5} A/cm². A peculiar anomaly occurs in the La-doped sample as it displays a lower current density than the Mn-doped sample between 1 and 10 kV/cm, then, as the electric field increases it becomes more conductive even than the Nb-doped sample after 20 kV/cm. Moreover, these results agrees with literature where Mn-doped films exhibit low leakage currents [145, 146, 214] and Nb- [155, 157, 158] and La- [61, 153, 154] doped BaTiO₃ films show higher leakage currents when BaTiO₃ is highly doped.

3.5.2 Heterostructures

As for the single doped samples, all heterostructures were characterized at different temperatures from 100°C to 200°C, and to simplify the comparison, we chose to plot the leakage current density as a function of electric field at 100°C to avoid any relaxation currents and the resistance degradation.

Mn/Nb based heterostructures

In Figure 3.29, the current density versus electric field of trilayer heterostructures MNM5, MNM10 and MNM20, the 5 layer heterostructure 5-MN and both Mn- and Nb-doped BaTiO₃ films are displayed for comparison.

At 0 kV/cm, the J_0 of all heterostructures is lower than the Nb-doped film by at least 1 order of magnitude, reaching as low as 3×10^{-9} A/cm² for MNM10 and MNM20, but they are still more conductive compared to a Mn-doped BaTiO₃ 4×10^{-10} A/cm². At low electric fields (below 18 kV/cm), all heterostructures present lower leakage currents than

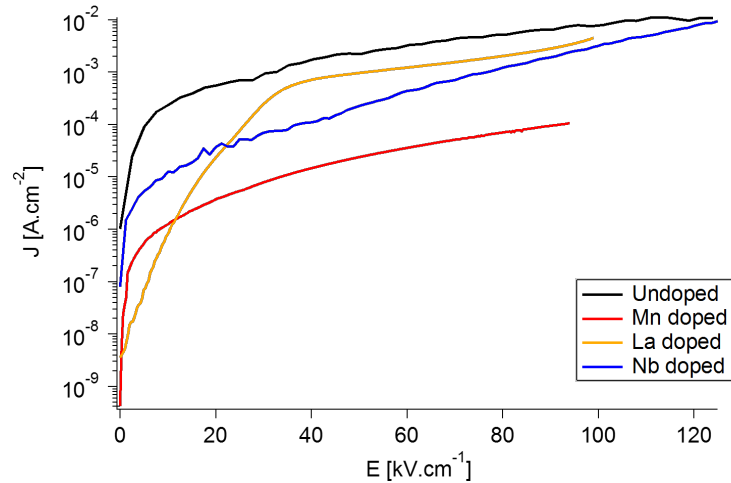


Figure 3.28: Leakage current density in function of electric field of undoped, Mn-, La- and Nb-doped BaTiO₃ thin film measured at 100°C

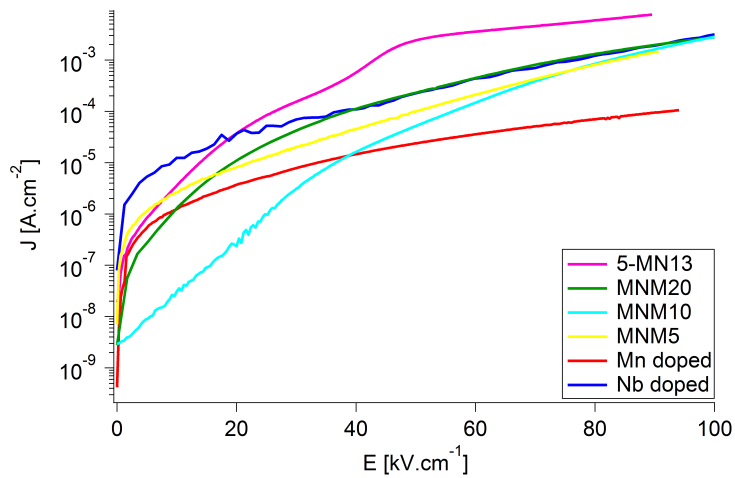


Figure 3.29: Leakage current density in function of electric field of Mn/Nb thin films based heterostructures measured at 100°C. Mn- and Nb-doped BaTiO₃ thin films are plotted as reference

that of a Nb-doped film. In the region 0.5 to 40 kV/cm, we found that MNM10 has the lowest leakage current density among these films, suggesting that the interaction between Nb and 10 nm of Mn in a trilayer heterostructure reduces the leakage currents at very low fields. In the other hand, above 18 kV/cm, the 5 layered heterostructure, which has the same total amount of Mn and Nb as MNM20, displays a higher current density than a Nb-doped film, suggesting that the increment of layers, results in a more conductive film due to the internal interfaces. As the electric field increases, the 3 layered heterostructures follow the same evolution in current density as the Nb-doped film, implying that at low electric fields, the electrode/film interface dictates the leakage current density and at high electric fields the bulk contribution takes over. These results are consistent with other experiments [209] where it is found that at low electric fields we have a higher impact of the electrode/film interface and tunneling conduction (such as Fowler Nordheim tunneling) and at higher electric fields the bulk conduction mechanisms have higher impact on the leakage currents (such as the Poole Frenkel emission).

La/Nb based heterostructures

In Figure 3.30, we show the leakage current density evolution against electric field measured at 100°C of trilayer heterostructures LNL10 and NLN10. Nb- and La-doped BaTiO₃ results are also plotted as reference.

At first sight, it is clear that both heterostructures are more conductive than the single doped constituents. Additionally, the heterostructure NLN10 displays a current density up to 2 orders of magnitude higher than its complementary heterostructure LNL10 and up to 4 orders of magnitude compared to its composing single doped films. This increasing conductivity for both heterostructures at nonzero electric fields may

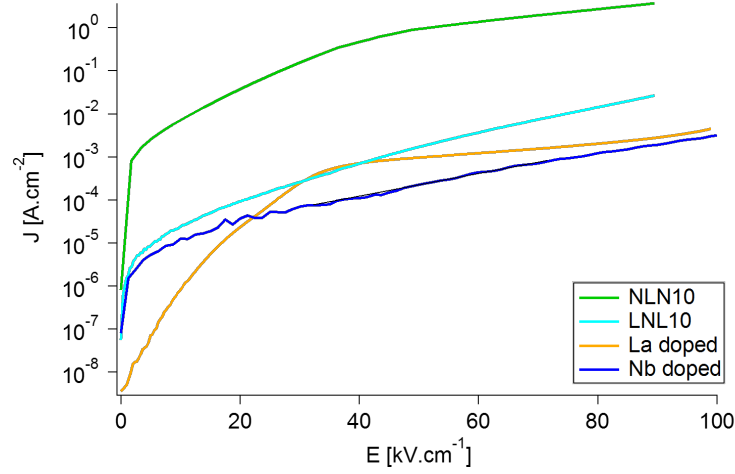


Figure 3.30: Leakage current density in function of electric field of La/Nb thin films based heterostructures measured at 100°C. La- and Nb-doped BaTiO₃ thin films are plotted as reference

come from the interaction of the diffusing dopings, Nb and La, at the internal interfaces. Nevertheless, we found a significant difference in leakage current density between both heterostructures. This difference will be reviewed in the discussion section.

3.5.3 Summary

Leakage current densities of BaTiO₃ thin films have been measured at various temperatures in function of electric field up to 100 kV/cm, in this section, only the J-E plots at 100°C have been shown in the interest of comparison amongst single doped and heterostructures films. We applied low electric fields as the columnar growth of our films does not allow us high voltages in order to reach the Schottky region. Nonetheless, our curves were fitted with all the models presented in section 1.5

Moreover, the breakdown voltage is reduced furthermore with temperature (10 V to less than 5V). As a consequence of this geometry, many phenomena have to be considered to model properly the evolution of leakage currents at nonzero electric field. Nonetheless, we can look at the thermionic emission of films at different temperatures. In Figure 3.31, we display the Arrhenius plot of $J_0/T^2 = f(1/T)$ and extracted the different activation energies from these curves.

Most of these activation energies are related to different ionized defects within the bandgap. For single doped materials, these defects can be easily attributed. This will be discussed in details in the Discussion section, but we can qualitatively summarize the main trends here. It is first very clear that the leakage current activation energy is consistent with the Fermi level position deduced from XPS experiments (Figure 3.17). For the undoped films, unwanted defects raise the Fermi level very close to the conduction band leading to the very small activation energy of 0.3 eV in Figure 3.31. On the opposite,

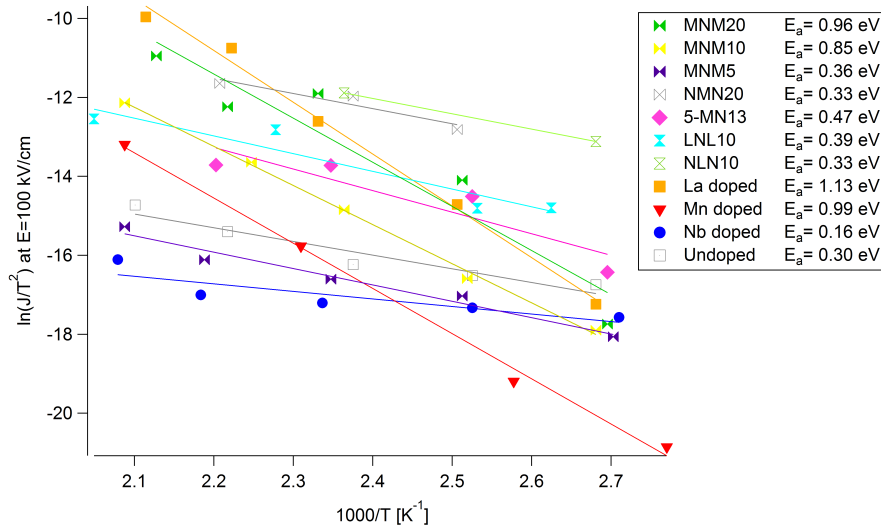


Figure 3.31: Arrhenius plot of the thermionic emission of single doped BaTiO₃ heterostructures. The activation energy obtain from the slopes are reported in the legend

whenever the thickness of Mn-doped layers is higher than 5 nm, the activation energy is increased up to 0.99 eV for the single layer in agreement with the deep trapping of the Fermi level within the band gap. For all other doping and heterostructures, the activation energy lies in between these two extreme cases again in agreement with the Fermi level position in Figure 3.17. Obviously such qualitative assessment is highly questionable in heterostructures for which interfaces have to be taken into account, which is not possible in the dc leakage current experiments. However, we can point out the trend that is shown by the Mn- and Nb-doped BaTiO₃ heterostructures. As seen in figure 3.31, the activation energy is the highest, 0.96 eV, for the sample containing the thicker layers Mn-doped BaTiO₃ (20 nm on each side) and it decreases down to 0.36 eV for the sample containing the thinner layers (5 nm on each side) of Mn-doped BaTiO₃. This is not surprising as the Mn-doped layers create a barrier height for electrons, thus the direct dependence of the activation energy on the thickness of the Mn-doped BaTiO₃ layers. It has to be mentioned that the sample 5-MN13, that is a 5 layered heterostructure of Mn- and Nb-doped BaTiO₃ which has the same total thickness of each dopant as the trilayer MNM20, it presents an activation energy of 0.47 eV which is lower than that of MNM20 (0.96 eV) and also that of MNM10 (0.85 eV), which shows us that the increase of the number of interfaces lowers the activation energy.

In order to get deeper insight in the point defects state of films and multilayers we have performed Electron Paramagnetic Resonance experiments, which are described in the next part. Before that, it should be pointed out that the heterostructures LNL10, which displays the highest effective dielectric permittivity of 1030 (at room temperature and 100 kHz) and moderate losses, has an activation energy for the leakage current which is 0.39 eV indicating a possible contribution of interfaces for the trapping of electronic

charges at interfaces. Moreover, the activation energy for the NLN10 heterostructure is less than 0.3 eV, confirming the inequivalence between the deposition sequence of the stacks LNL and NLN. This will also be discussed further in the Discussion section.

3.6 Electron Paramagnetic Resonance

Electron Paramagnetic Resonance (EPR) measurements were performed using a standard Bruker spectrometer operating at frequency 9.4 GHz (X-band) including a TE 102 rectangular microwave cavity with 100 kHz magnetic field modulation, in a magnetic field measurement range from 5 to 5000 Oe. The samples were introduced in a quartz tube and placed in an Oxford Instruments ESR 900 continuous-flow helium cryostat inside the microwave cavity that allow performing the temperature dependence study.

3.6.1 Powder analysis

The temperature could be varied and controlled over the temperature range 4 to 300 K. EPR measurements were done on BaTiO₃ powders (0.4 mg) and BaTiO₃ thin films deposited onto Si substrates (3x5 mm² and 300 nm thickness). Powders samples were taken from sintered BaTiO₃ samples, which followed the same treatments as for the BaTiO₃ targets used for RF-sputtering. The EPR analysis on BaTiO₃ will allow us to identify certain types of charged defects, such as ion-oxygen vacancies complexes, Ti³⁺ defects, unavoidable Fe and Mn residual defects and free electron densities. With this approach we try to link the dielectric properties (described in section 3.2) and try to explain the band structure and Fermi level position that were deduced from the XPS analysis. The EPR spectra of doped and undoped BaTiO₃ samples are strongly temperature dependent, in fact some paramagnetic ions like Ti³⁺ have short spin-lattice relaxation time, hence these can be only observed at temperatures $T \leq 100K$; for that reason, EPR spectra were measured at low temperatures down to 4K.

Because of the very low detection limit (1 paramagnetic center over 100 billion atoms) of EPR and the unavoidable presence of iron in the nominally pure BaTiO₃, Fe impurity spectra lines are always visible, even on Mn-, Nb- or La-doped samples. This can be explained by the origin of the (un)doped BaTiO₃ powder. In our case, (un)doped BaTiO₃ was fabricated by solid state reaction of BaCO₃ and TiO₂ and the oxide relative of the desired dopant, those were MnO₂, Nb₂O₅ and La₂O₃. In the reactant TiO₂, it is quite common to have Fe impurities, thus, all powders, doped and undoped, will contain the same Fe impurity spectra lines in EPR. Most of the spectra showed an intense resonance (see Figure 3.32) at a gyromagnetic constant (g) of 2.0005 (B = 3350 Oe) due to cubic symmetry Fe³⁺ (Fe³⁺_{cubic}, 3d⁵ ion with an electron spin S=5/2) in the six-fold environment of oxygen associated; this means that no oxygen vacancies (V_O) are next to Fe³⁺ ions in the first coordination sphere, but the valence state of Fe (3+) is revealing oxygen vacancies elsewhere in the sample. The same thing holds for Mn centers which are always present and for which 2+ and 4+ states are EPR active, the former signing the presence of oxygen vacancies.

In Figure 3.32 it is plotted different EPR spectra of sintered BaTiO₃ powders recorded at 4K. Figure 3.32a exhibit EPR resonance lines from a sintered nominally undoped BaTiO₃ powder with 3 different type of resonances, a wide resonance around 2500 Oe with a g value of 2.12 coming from BaCO₃ formed at the surface by aging [179], a large line from

Fe^{3+} ($g=2.002$) and 4 lines from Mn_{cubic}^{2+} ($g=2.001$) indicating that these impurities are not bound directly to oxygen vacancies but the valence state of both impurities ($3+$ and $2+$) imply their presence in the sample. It is worth mentioning that for Mn^{2+} in octahedral environment (cubic symmetry) we expect always 6 lines, 2 of them are not visible on this spectrum because of the overlap with the Fe line. The effect of 1 mol% Mn doping on EPR spectrum in BaTiO_3 are shown in Figure 3.32b.

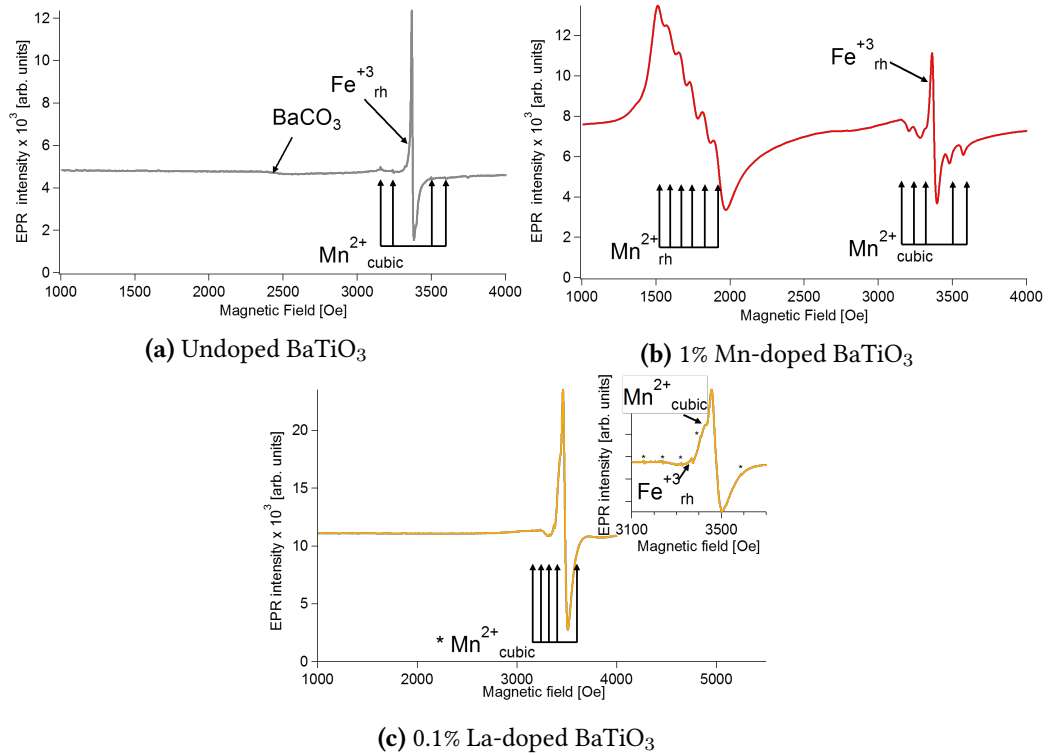


Figure 3.32: EPR spectra recorded at 4K of (un)doped BaTiO_3 sintered powders showing typical Fe^{3+} impurities and resonance lines from Mn^{2+} , the whole sextet is not visible due to typical resonance line around 3400 Oe originated from glass cavity used for measurement.

In addition to the Mn_{cubic}^{2+} and Fe_{cubic}^{3+} lines, we observe a sextet at lower magnetic field attributed to Mn_{rh}^{2+} , meaning that Mn^{2+} is detected in a rhombohedral symmetry, associated to $2V_O$. Due to the high doping concentration, the hyperfine lines are broad and overlapped resulting in a single resonance at $g=4.28$. Mn_{rh}^{2+} signal is too intense that it is not possible to determine whether or not there is Fe_{rh}^{3+} (associated to $\text{Fe}^{3+} - 2V_O$). Lastly, Figure 3.32c ($\text{BaTiO}_3:\text{La}$) displays seemingly a single resonance related to Mn_{cubic}^{2+} , but a short range measurement (inset) shows the typical Fe_{cubic}^{3+} and a small resonance located at around 3440 Oe ($g_{||}=1.943$ and $g_{\perp}=1.964$) assigned to Ti^{3+} , which is expected as the ceramic is donor doped (blue colored powder). This signal has been observed and identified in BaTiO_3 single crystals [225], ceramics [226–228] and thin films [72, 229, 230].

having a wide range of g -values varying from 1.899 to 1.938 and have been assigned to distinct Ti^{3+} paramagnetic defects, such as Ti^{3+} , $Ti^{3+}-V_O$, $Ti^{3+}-V_O-K(Na)$, etc.

3.6.2 Single doped $BaTiO_3$ films

In order to acquire comparable results among all thin films, these were deposited on Si with a thickness of around 300 nm and cleaved on the middle of the substrate to avoid the shadowed corners (sample surface: $3 \times 5\text{mm}^2$). EPR spectra were recorded in a long and short measurement ranges: from 1000 to 4000 Oe, for a general scan, and from 3100 to 3900 Oe in order to highlight the possible Ti^{3+} , Fe and Mn impurities content. In Figure 3.33a the long range (1000-4000 Oe) EPR spectra of undoped and single doped $BaTiO_3$ films is resumed and in 3.33b we plot the short range (3000-4000) measurements in order to determine possible resonances that were too small to be spotted on the long range measurement.

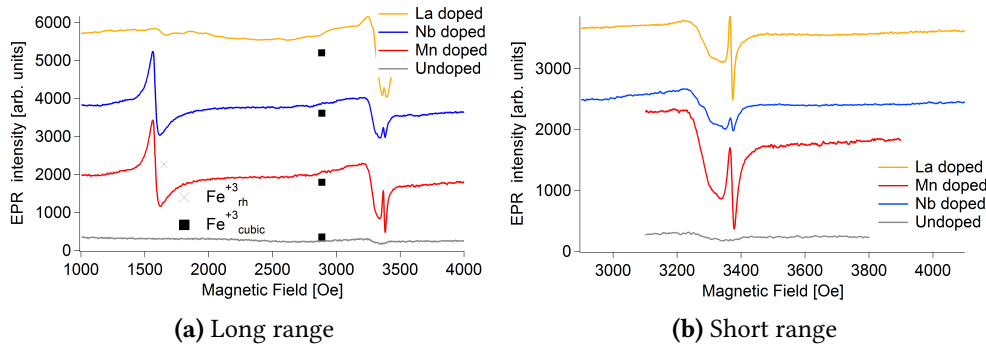
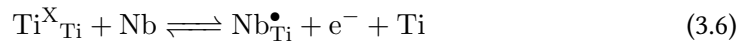
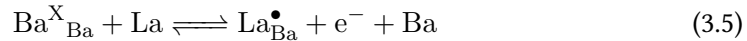


Figure 3.33: EPR spectra taken at 4K of (un)doped films

When comparing both figures, it is evident that the short range measurement did not exhibit any additional resonances in any of the analyzed thin films.

The nominally undoped thin film show a very small Fe_{cubic}^{3+} signal in the low temperature measurement and the presence of $BaCO_3$ at room temperature (not shown), indicating us a low content of V_O . For the La-doped and Nb-doped samples, we only observed a small concentration of Fe_{cubic}^{3+} (low content of V_O) as Nb and La decrease the density of residual oxygen [185, 231]. The extra electrons provided by the introduction of Nb or La in our films are not being compensated by Ti^{3+} and these defects are electronically compensated by the following reactions:



Part of these free electrons may be trapped by the reduction of Mn^{4+} to Mn^{3+} , the latter being EPR silent, and part of these electrons remain untrapped, pulling the Fermi level towards the conduction band, which is consistent with the XPS results (see Figure 3.17).

Lastly for the Mn-doped sample, in comparison with the powder results (see Figure 3.32b) we have detected only Fe_{cubic}^{3+} and Fe_{rh}^{3+} signals, losing the Mn_{rh}^{2+} signal. This can only mean that all the Mn content inside the film is on its form of Mn^{3+} , which is an EPR silent defect. However this is inconsistent with XRD results. This might be corrected by refining the XRD measurements and analysis as XRD measurements on thin films display wider peaks and due to the clamping of the substrate, the calculation of the lattice parameter by this method may be wrong.

3.6.3 Heterostructures

As it has been described in chapter 2 (Fundamentals), each layer of the heterostructures was deposited by the sequential setting of different doped targets in front of the substrate while maintaining the deposition temperature of 650°C . This means that each layer has experienced different annealing times, the bottom layer with the highest time and the top most layer the least. By considering this and the difference of thickness of each layer, it is clear that the internal interfaces are unequal. For instance, in the sample MNM20 (20 nm Mn-doped / 260 nm Nb-doped / 20 nm Mn-doped), the interface created by Mn-doped / Nb-doped layer is different than the one created by Nb-doped / Mn-doped layer. Therefore, in order to identify the defects inside our heterostructures, it is not only needed to compare results with those of the single doped samples but also it is essential to examine and compare both combinations of interfaces.

Mn/Nb based heterostructures

On Figure 3.34a first the EPR spectra obtained at 4K of 2 layers is presented: a sample composed of a bottom layer of 20 nm Mn-doped BaTiO_3 and a top layer of 260 nm Nb-doped BaTiO_3 (20-MN) and another one composed of a bottom layer of 20 nm Nb-doped BaTiO_3 and a top layer of 260 nm Mn-doped BaTiO_3 (20-NM). Even though these

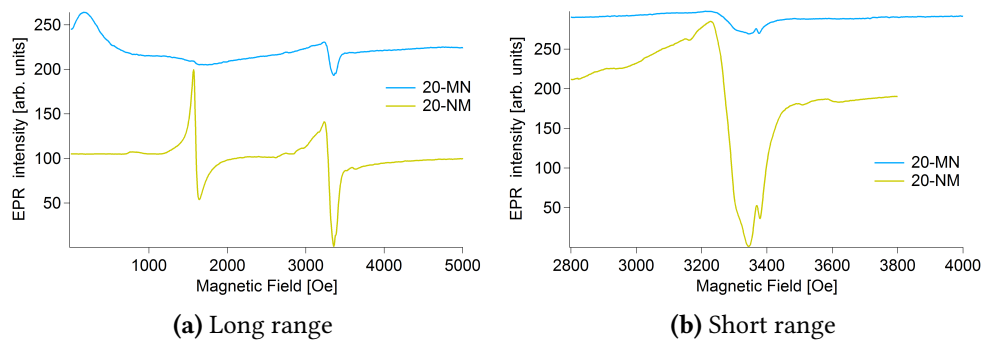


Figure 3.34: EPR spectra recorded at 4K of bilayers 20-MN and 20-NM

two samples contain the same couple of materials, we observe at first glance, that the arrangement of these layers makes a big difference on the EPR spectra, thus different

defects are created at these distinct interfaces. The sample 20-MN shows 3 resonances, 2 low hyperfine lines related to Fe_{cubic}^{3+} and Fe_{rh}^{3+} centers and a low field resonance around 350 Oe that could be related to Fe^{5+} or Fe^{3+} in its high spin state. The most likely from these two is the Fe^{3+} high spin due to its ionic radius (64.5 pm) which is closer to the one of Ti^{4+} (60 pm), but a larger ranged measurement would be necessary to discard one of the two possibilities as a second transition is expected for Fe^{5+} species at 10000 Oe. The sample 20-NM exhibits an intense Fe_{rh}^{3+} and a small Mn_{cubic}^{2+} resonances in the long range spectra. In the short range spectra it was possible to detect some Ti^{3+} centers only for the sample 20-NM (see Figure 3.34b). This means that the Ti^{3+} defects are being created only at the interface between Nb-doped / Mn-doped, as it is not detected on the single Nb-doped BaTiO_3 . This difference may lay on the fact that both materials are being sputtered separately. When the Mn-doped sample is being sputtered on top of Nb-doped BaTiO_3 it is possible that during the first seconds of deposition there is a resputtering of the Nb-doped layer, creating new defects on the interface. On the other hand, when the Nb-doped layer is being sputtered on top of Mn-doped BaTiO_3 , these defects, possibly created in the Mn-doped layer, are being compensated by the multivalent Mn, thus no induction of Ti^{3+} centers.

On Figure 3.35a we can observe the long range EPR spectra of the 3 layer heterostructures constituted of alternating Mn and Nb-doped BaTiO_3 layers. At first glance, by comparing both curves, we clearly see that MNM20 has a higher content of V_O due to the larger Fe_{rh}^{3+} resonance. Moreover, we can also detect the presence of Fe_{cubic}^{3+} on MNM20 and it is worth to point out that no Fe^{5+} is observed as compared to 20-MN. Looking more

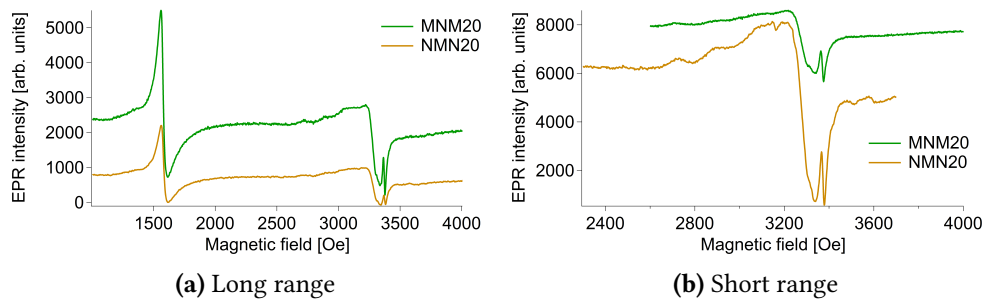


Figure 3.35: EPR spectra recorded at 4K of trilayers MNM20 and NMN20

into detail over a shorter magnetic field range, we note 2 small resonances on the NMN20 spectrum around 2750 Oe attributed to silica coupled to Fe^{3+} , suggesting a diffusion from the substrate towards the film. In addition to this, it is possible to identify two small resonances around 3500 Oe, which marks the presence of Ti^{3+} species ($g_{||}=1.880$, $g_{\perp}=1.931$), similarly to 20-NM. With these observations we can assess that the defects encountered on our trilayer heterostructures are highly dependent on the first 2 layers and the order they are being deposited as we had similar results between trilayers and bilayers having the same first layers and we did not notice additional resonances by the deposition of a third layer.

La/Nb based heterostructures

Following the same approach, we present in Figure 3.36a the bilayer composed of 10nm La-doped BaTiO₃ with a top layer of 280 Nb-doped BaTiO₃. We present here two spectra recorded on the sample with different microwave power to enlighten the high conductivity of this material, as it was necessary to reduce the standard measuring power from 2.5 mW to 0.99 mW in order to stabilize the spectra and reduce the signal to noise ratio. Concerning the resonances detected, we observed a low Fe_{rh}³⁺, Fe_{cubic}³⁺ and Mn_{cubic}²⁺ signals. Figure 3.37 displays the EPR spectra recorded at 4K of heterostructures composed

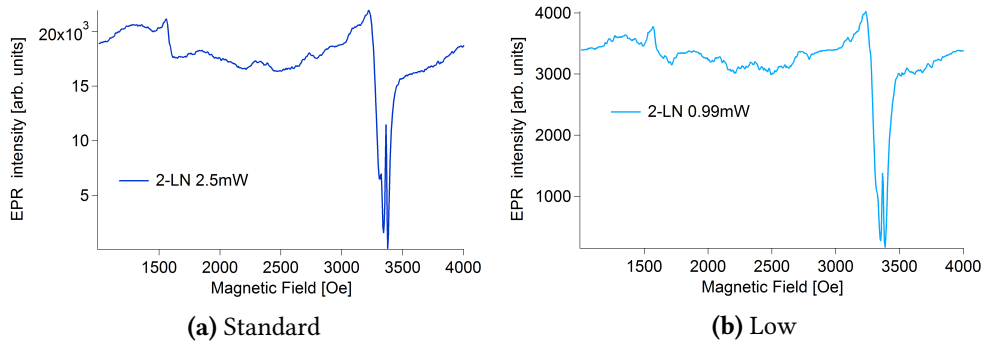


Figure 3.36: EPR spectra recorded at 4K with different microwave power of bilayer 20-LN

of 3 alternating layers of Nb-doped and La-doped BaTiO₃. Sample LNL10 (La 10nm / Nb 280 nm / La 10 nm) shows several resonances already observed before in other thin films: around 1000 Oe, 1500 Oe, 3200 Oe and 3350 Oe related to Fe³⁺ in Si, Fe_{rh}³⁺, Mn_{cubic}²⁺ and Fe_{cubic}³⁺ correspondingly. On the other hand, sample NLN10 only shows resonances coming from Fe_{rh}³⁺ and Fe_{cubic}³⁺. After analysing the spectra of these samples at

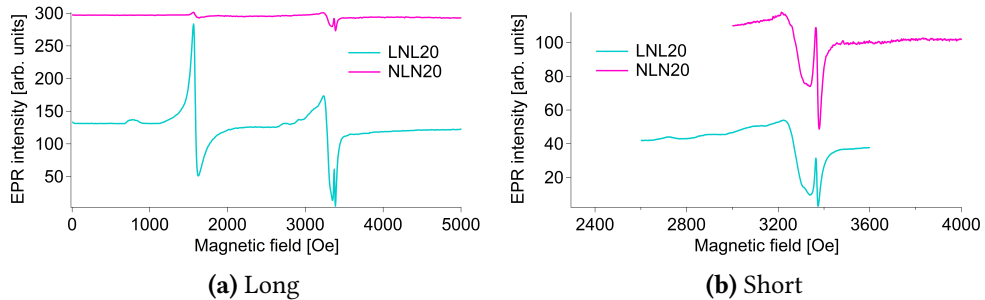


Figure 3.37: EPR spectra recorded at 4K of trilayers LNL10 and NLN10

different temperatures, it can be noticed that there are defects that could not be detected straightaway from the spectra obtained at 4K. Figure 3.38 presents the spectra of LNL10 at 6 different temperatures from 4 K to 195 K.

At 80K it is possible to detect few amounts of Ti³⁺ since this defect stabilizes around 80-90 K. Moreover, there is a resonance that shifts in magnetic field when temperature

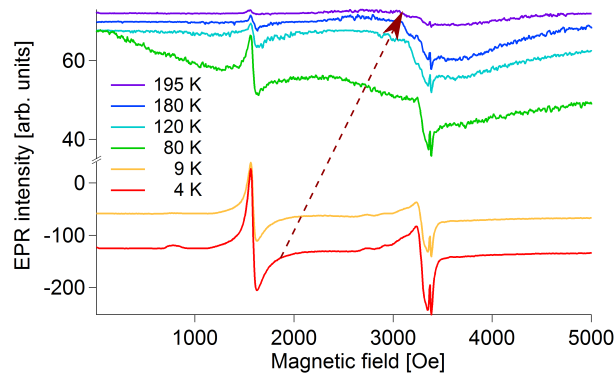


Figure 3.38: EPR spectra of LNL10 recorded at various temperatures

increases from 2000 Oe at 4 K to 3000 Oe at 195 K, suggesting two possible candidates responsible for this : Co_3O_4 or a high electron density inside the material [232-235]. We chose to attribute this temperature dependent resonance to the latter one considering that throughout the whole processing of the thin film, there is no or negligible amounts of Co and its derivatives. Furthermore, if it was the case, this temperature dependent resonance should appear on the EPR spectra of all other thin films. In addition to this, by comparison with sample 20-LN, which appeared to be highly conductive by EPR, it supports the idea that sample LNL10 have a high concentration of electrons within the film. Likewise, we have analyzed the temperature dependence of sample NLN10 (Nb 10nm / La 280 nm / Nb 10 nm) on Figure 3.39. In this case we have not found any Ti^{3+} , Fe^{3+} in Si nor a temperature dependent resonances as in sample LNL10. This means that, as in the case of Mn/Nb doped BaTiO_3 heterostructures, the starting layer of the heterostructure plays a crucial role to the defects formed at these internal interfaces, and in consequence to the overall dielectric and electronic properties of the thin film.

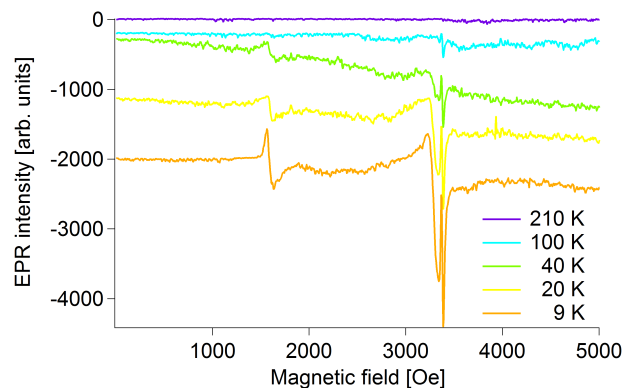


Figure 3.39: EPR spectra of NLN10 recorded at various temperatures

3.6.4 Summary

For the purpose of comparing these results amongst the other techniques, we can summarize the EPR results with the following points:

- Fe hyperfine lines are found in all samples (powders and films) and have a very high intensity due to the unavoidable presence of iron in BaTiO₃ [226] and the high sensibility of iron in EPR. Fe_{cubic}³⁺ reveals the presence of oxygen vacancies V_O in the samples and Fe_{rh}³⁺ centers are associated to two V_O next to Fe³⁺.
- **Single doped samples.** For the nominally undoped, La-doped and Nb-doped BaTiO₃ samples only Fe_{cubic}³⁺ species are observed, implying that the V_O present in the films are being electronically compensated. As for the Mn-doped sample, no Mn²⁺ nor Mn⁴⁺ can be observed, indicating that the compensation for V_O is accomplished by Mn³⁺ species, which are silent in EPR.
- **Bilayer samples.** The Mn/Nb-doped based heterostructures differ on the detection of Ti³⁺ species when the Nb-doped sample is used as a substrate (20-NM) as in the mirror case (20-MN), the Mn-doped sample compensates the defects created by the deposition of the Nb-doped film. Furthermore, for the 20-MN sample, the Fe_{cubic}³⁺ intensity is higher than the Fe_{rh}³⁺ intensity. Concerning the La/Nb bilayer (10-LN), a high conductivity within the material was found, as it was necessary to reduce the standard measuring power to stabilize the spectra. This result agrees with the leakage currents measurements as the samples LNL10 and NLN10 have the highest current density compared to all other samples.
- **Mn/Nb based trilayer samples.** For the trilayer heterostructures, we found the same difference as in the bilayer samples, that is to say, when Nb-doped BaTiO₃ is deposited as the bottom most layer (NMN20), we found Ti³⁺ species and no Ti³⁺ hyperfine lines can be observed in the MNM20 sample. In addition to this, for the 20-MNM sample, both Fe_{cubic}³⁺ and Fe_{rh}³⁺ intensities are comparable (differs from 20-MN), indicating a higher V_O content in the bottom layer since this layer experiences a longer time at high temperature.
- **La/Nb based trilayer samples** Both heterostructures are less conductive than the bilayer sample 10-LN. Nevertheless, we found a temperature dependence hyperfine line on the 10-LNL sample, indicating either Co^{3+/4+} species or a high electron density in the film.

3.7 Discussion

In this section, we will try to link and explain the different results obtained by impedance spectroscopy, EPR, XPS and leakage current measurements. In Table 3.3, we present an overview of the general results of thin films from the techniques previously mentioned.

Table 3.3: General results. Relative permittivity and dielectric losses values are shown for 100kHz, 0V and room temperature. Leakage current densities values are for 0 kV/cm at 100°C. Activation energies results were obtained from a range of temperatures between 100°C and 200°C by considering a thermionic emission model. XPS results are in situ $E_F - E_{VB}$ [eV] values for single doped films and ex situ $E_F - E_{VB}$ [eV] values for heterostructures. EPR signals are as follows: a- Fe_{cubic} , b- $Fe_{rhombohedral}$, c- Ti^{3+} , d- Fe in Si, e- High electron density or $Co^{3+/4+}$

Single doped	ϵ	$\tan(\delta)$ [%]	J_0 [A/cm^2]	E_a [eV]	XPS	EPR
Undoped	350	4	$1 \cdot 10^{-6}$	0.3	2.7	a
Mn-doped	250	1	$4 \cdot 10^{-10}$	1.08	2.2	a,b
La-doped	485	3.2	$3 \cdot 10^{-9}$	0.75	2.8	a
Nb-doped	715	3	$8 \cdot 10^{-8}$	0.53	2.8	a
Heterostructures						
MNM20	430	2	$3 \cdot 10^{-9}$	0.5	2.2	a,b
MNM10	550	3	$3 \cdot 10^{-9}$	0.67	2.2	
MNM5	850	5	$7 \cdot 10^{-9}$	0.13	2.4	
5-MN13	570	4.2	$2 \cdot 10^{-8}$	0.54	2.2	
NMN20	440	2.5	-	0.62	2.1	a,b,c,d
LNL10	1030	3.9	$5 \cdot 10^{-8}$	0.66	2.3	a,b,c,e
NLN10	540	2.3	$8 \cdot 10^{-7}$	0.29	2.3	a,b

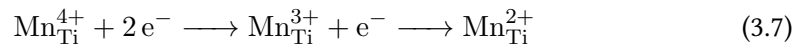
After comparing all results, it is clear that our heterostructures achieved two main objectives: reduce the dielectric losses and leakage currents by using only thin layers of Mn-doped $BaTiO_3$ in contact with the electrodes (MNM20 and MNM10) and more importantly, achieve a high value of relative permittivity stable in temperature (MNM5 and LNL10) without increasing significantly the dielectric losses. In order to understand the different phenomena allowing these enhancements, it is necessary to examine the results from the single doped films

3.7.1 Single doped films

Starting with an undoped $BaTiO_3$ film, we observed that the films of this work possess a rather low relative permittivity and also high dielectric losses, which increase with

temperature. The latter result is consistent with the leakage current measurements, where it is found that these films are the most conductive amongst our single doped films. This result is not unexpected, as XPS results show a Fermi level position close to the conduction band. EPR shows that the only paramagnetic defects found in this film are oxygen vacancies (identified by the presence of Fe^{3+}). By analysing the evolution in temperature of leakage currents at 0 kV/cm, we found an activation energy of 0.3 eV, which is also close to the Fermi level position found by XPS. As no Ti^{3+} could be detected by EPR, we can think that this activation energy (and Fermi level position) is due to oxygen vacancies. Mitra et al [236] found by theoretical models that the most stable state of oxygen vacancies is the doubly charged $\text{V}_\text{O}^{\cdot\cdot}$ with an energy level located 0.28 eV below the conduction band. It has been proven that an annealing at high temperatures ($>800^\circ\text{C}$) in air or high oxygen partial pressure can compensate the oxygen vacancies and therefore, decrease the dielectric losses/leakage currents, but lowers the permittivity as well [40]. It has been also proven that a high oxygen content during magnetron sputtering deposition lowers the Fermi level position [39]), but reduces the crystallinity of the film and induces the emergence of secondary phases [39, 40]

Another strategy to reduce the leakage currents and dielectric losses is to introduce an acceptor dopant in BaTiO_3 . We chose Mn as an acceptor dopant as it has been reported several times in literature to reduce the conductivity and dielectric losses at the expense of reducing the relative permittivity [145–147, 209, 214]. After performing all characterization techniques used in this work, we confirmed that Mn-doped BaTiO_3 reduced the dielectric losses to 1% and leakage currents down to $4 \times 10^{-10} \text{ A/cm}^2$ at 100°C , but also reducing the relative permittivity and tunability. Moreover, we observed a lower Fermi level position from 2.7 eV to 2.2 eV. It is reported in literature that this value corresponds to the transition level of $\text{Mn}^{2+/3+}$ [177, 182]. We confirmed the presence of Mn^{3+} ions in the films, as no Mn^{2+} nor Mn^{4+} was found in EPR. These Mn ions can trap free electrons from the conduction band, reducing effectively the dielectric losses and leakage currents, following the equation:



It is therefore convenient to use this dopant as an interfacial layer next to noble metallic electrodes such as Pt or Au.

To increase the permittivity we opted to dope BaTiO_3 with A site (La) and B site (Nb) donors. The incorporation of donor type dopants in BaTiO_3 compensates and reduces the residual oxygen vacancies which is beneficial for the dielectric response of the material. Moreover, it has been shown multiple times (mostly ceramics) that n-type doped BaTiO_3 exhibit higher permittivity due to the space charge effect characterized by the PTCR effect. It has been documented that the PTCR effect involves a significant change of resistivity with temperature around the Curie temperature T_C [133]. In ceramics, this has been modeled (Heywang-Jonker) with a change in the potential barrier at the grain boundaries [129, 133]. Heywang suggests the existence of electronic states at the grain boundaries acting as electron traps, resulting in a depletion of the grain boundary layer in electrons, increasing effectively the potential barrier. In the case of thin films, it has been shown that

this relative permittivity enhancement due to space charges [237] does not come from grain boundaries (bulk) but from the electrodes interface created by noble metals (Pt). In fact, the Pt/n-type doped BaTiO₃ interface displays bending of the electronic bands, as the bulk show a Fermi level close to the conduction band and a high potential Schottky barrier ϕ_b , creating a space charge region that will act as an additional polarization when applying an oscillating electric field, increasing the overall relative permittivity (Figure 3.40).

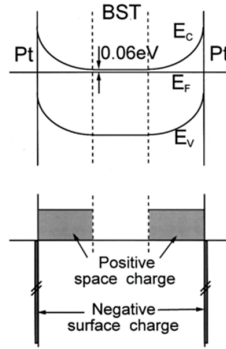


Figure 3.40: Schematic diagram showing band bending, space charge distribution for the Pt/BST/Pt capacitors [237]

This effect is more prominent when we obtain a high Fermi level ($E_{CB} - E_F \approx 0$ eV). We confirmed this by in-situ XPS experiments as both La- and Nb-doped BaTiO₃ display a $E_F - E_{VB} \approx 2.8$ eV. Moreover, it has been observed that the interfaces Pt/Nb-doped BaTiO₃ and Nb-doped BaTiO₃/Pt show band bending and create a Schottky barrier of 1 eV and 0.6 eV, respectively [39]. Furthermore, the presence of defects at the electrode interfaces increase the dielectric losses. Additionally, the geometry (columnar grains, small size grains, polycrystallinity) and the doping content alter the electrical response in temperature giving higher leakage currents and activation energies closer to the conduction band.

3.7.2 Relative permittivity enhancement

As it has been stated before, we opted to create layered heterostructures as to manipulate defects at the internal interfaces in order to create space charges/band bending to increase the dielectric performance of BaTiO₃. To prove that the relative permittivities obtained from these heterostructures are not just the relative permittivities resulting from capacitors connected in series, we show in table 3.4 a comparison between the theoretical ε_{th} value obtained by taking into account the permittivity of each single doped layer with its respective thickness and the experimental ε_{exp} value. The theoretical value ε_{th} of the single doped films has been calculated as the permittivity that we would obtain if we take into account a dead layer of 1 nm and with a permittivity $\varepsilon_D = 5$. This have been achieved by measuring the effective permittivity of the single doped films in function of

thickness. Due to the dead layer effect, the permittivity is typically reduced with reducing film thickness [238]. Moreover, we assume in the model that all layers composing the heterostructures would take the value of the theoretical ϵ_{th} and added to the calculation 2 dead layers with the same characteristics as stated before ($t = 1$ nm and $\epsilon_D = 5$).

Table 3.4: Theoretical relative permittivity of BaTiO₃ layered heterostructures and experimental relative permittivity comparison. Theoretical values were obtained using a simple model of capacitors in series where thickness of the layers and single doped relative permittivities were used.

Sample	Description	Thickness [nm]	ϵ_{th}	ϵ_{exp}
Undoped	-	300	651	350
Mn-doped	-	298	373	250
La-doped	-	289	1465	485
Nb-doped	-	450	1953	715
Heterostructures				
MNM20	20 Mn / 260 Nb / 20 Mn	293	463	436
MNM10	10 Mn / 280 Nb / 10 Mn	250	441	550
MNM5	5 Mn / 290 Nb / 5 Mn	331	564	850
5-MN13	13 Mn / 130 Nb / 13 Mn / 130 Nb / 13 Mn	335	488	570
NMN20	20 Nb / 260 Mn / 20 Nb	310	271	440
LNL10	10 La / 280 Nb / 10 La	341	591	1030
LNL10	10 La / 280 Nb / 10 La	288	523	972
LNL10	10 La / 280 Nb / 10 La	340	590	912
LNL20	20 La / 260 Nb / 20 La	340	586	580
NLN10	10 Nb / 280 La / 10 Nb	288	486	540
5-LN10	10 La / 140 Nb / 10 La / 140 Nb / 10 La	388	643	1060

It is worth noticing that the total thicknesses of the layers were obtained by ellipsometry and are slightly different from the desired 300 nm thickness (sum of the layers' thickness). In order to reduce the uncertainty of calculation and make a better approximation of the theoretical relative permittivity, it is assumed that the thicknesses of the thinner layers (side thin films of the heterostructure) are indeed conserved and the thickness of the thicker layer (core thin film of the heterostructure) was not achieved, therefore, the latter thickness is adjusted to fit the total experimental thickness. This assumption was exerted as it is easier to control in rf-sputtering the thickness of a thin film (< 100 nm) than a thicker one (> 100 nm) [40]. A TOF-SIMS (Time-Of-Flight Secondary Ion Mass Spectroscopy) experiment that confirmed this hypothesis will be shown later in this section. As a reminder, the different thicknesses used in the heterostructures varied to lower and lower values (e.g. MNM heterostructures from 20 nm to 5 nm) as to find a "critical thickness" where effects in relative permittivity and dielectric losses are significantly different from a single doped sample, for instance, MNM heterostructures compared to a single Mn-doped sample.

Taking first into account the MNM heterostructure series, we see that a beneficial effect of interfaces for the dielectric permittivity is achieved only when the thickness of the side films, Mn-doped BaTiO₃, is below 10 nm, as it is seen in the table above, samples with 20 nm bottom and top layers of Mn-doped BaTiO₃ display a lower experimental permittivity than the theoretical one. This shows that, in general, when a low dielectric film is introduced in a series of capacitors, we obtained a much lower dielectric permittivity. The critical value of Mn-doped BaTiO₃ for a dielectric permittivity enhancement is correlated with the band bending created at the interface Nb-doped/ Mn-doped BaTiO₃ (see Figure 3.23). Beyond 10 nm of Mn-doped BaTiO₃, the electronically active defects generated by the Nb-doped film are being compensated by the Mn-doped film and this Mn-doped "dead layer" will have more impact on the permittivity value than an eventual space charge effect created by the band bending of the Nb/Mn doped interface. Below this critical thickness, there are still electronically active defects in the interface Nb/Mn doped BaTiO₃, which will contribute to the permittivity and dielectric losses.

In the case of sample NMN20, we observed a higher permittivity than the modelled one. Two hypothesis could explain this observation: a) the critical thickness of Nb-doped BaTiO₃ for a interface effect with the Mn-doped film is lower than 20 nm and we already see an enhancement of the dielectric permittivity by the space charge effect or b) a band bending at the interface with Pt electrodes is produced by Nb-doped films, enhancing the relative permittivity by the space charge effect. An interface XPS experiment should be done to confirm either of these two hypothesis.

Moreover, it has been proven that introducing a low loss material in a series of capacitors with BaTiO₃ thin films can reduce the overall dielectric loss of the system, but when the number of interfaces increases, the dielectric losses increase as well [239]. We observed this phenomenon in the system MNM (see Table 3.3) in samples MNM20 and 5-MN13 as these films contain roughly the same ratio of Mn-doped and Nb-doped BaTiO₃, but in one case we have 2 interfaces and in 5-MN13 we have 4. Moreover, the dielectric permittivity of 5-MN13 is higher than the theoretical one and the dielectric losses went from 2% to 4.2%. This shows as well that when we increase the number of interfaces, while conserving roughly same total thickness of both dopants (40 nm of Mn-doped BaTiO₃ and 260 nm of Nb-doped BaTiO₃), we achieve higher values of dielectric permittivity.

The case of La- and Nb-doped BaTiO₃ heterostructures is more complex, as we have already stated before. Nonetheless, we observe the same phenomenon as in the Mn- and Nb-doped BaTiO₃ heterostructures, where the thickness of the La-doped BaTiO₃ at the top and bottom layers is critical. Indeed, the samples with 10 nm of La-doped BaTiO₃ at the top and bottom layers of the heterostructures display a very high permittivity, in the other hand, samples with 20 nm of the LNL heterostructure display a quite low permittivity. The same reasoning as with sample 5-MN13 is applied to the LNL heterostructures. The total thickness of La-doped BaTiO₃ increased from 20 to 30 in 5-LN10, but the number of interfaces was increased from 2 to 4. Even if the total thickness of La-doped BaTiO₃ was increased we still observed a very high permittivity, confirming the hypothesis stated before where the introduction of more interfaces is beneficial for the relative permittivity.

All of these results are stunning, and most of them are hypothesized to the cross diffusion of dopants in the heterostructures, as clean interfaces should not show the electronic properties that we observed with XPS, such as sharp Fermi level drop (for La- and Nb-doped BaTiO₃) and large band bending.

3.8 TOF-SIMS analysis

To confirm the previous hypothesis, we performed Time-Of-Flight Secondary Ion Mass Spectroscopy (TOF-SIMS) experiments on a couple of heterostructures, in collaboration with Dr. Jean-Paul Salvétat (PLACAMAT, CNRS). TOF-SIMS experiments have been done using 1 keV Cs pulsed beam to sputter the elements from the surface ($300 \times 300 \mu\text{m}^2$) of the samples and analyzed by 30 keV Bi ions ($100 \times 100 \mu\text{m}^2$). Thanks to the low detection limit and the mass difference between ions, it is possible to detect by TOF-SIMS traces of elements such as La, Nb and Mn, that are undetectable (except for Nb) in XPS as dopants in BaTiO_3 . A more detailed principle can be found in section [2.7](#).

Moreover, this technique allows us to determine the diffusion length of dopants in our heterostructures as it is possible to control the Cs sputtering rate and the highly surface sensitivity of SIMS (usually 1-2 monolayers). Nonetheless, one has to look out for the different sources of error affecting the information depth such as the quality of the surface (roughness) and the energy of sputtering particles inducing surface mixing. These effects will increase artificially the depth of detection of the different elements throughout the sample, typically 2-3 nm.

In TOF-SIMS analysis we have the option to analyse the negative or positive sputtered ions coming from the sample. We chose to analyse the negative ions (TiO^- , $^{18}\text{O}^-$, NbO_2^- , BaO_2^- , MnO^-) as they provided the best signal to noise ratio.

In Figure [3.41](#) we show a Cs sputtering (3D) TOF-SIMS experiment on a bilayer constituted of 5 nm Mn-doped BaTiO_3 top layer and a 20 nm Nb-doped BaTiO_3 bottom layer deposited on a Pt-Si substrate to observe the diffusion length of Nb in Mn-doped films and vice-versa.

Looking at the MnO^- and NbO_2^- lines, it is evident that at the top interface there is a region where there is a coexistence of Nb and Mn impurities, a region for which only Mn impurities were intended to be present. This induces a slow change in Fermi level position and explains the critical thickness (around 10 nm) needed to reach the Fermi level position of a single Mn-doped BaTiO_3 (experimental value obtained in this work).

Looking at the dielectric performance of the LN heterostructure series, there are 3 relevant results. Firstly, the enhancement of the relative permittivity using LNL10 heterostructures is reproducible as long as the 10 nm of La-doped BaTiO_3 is respected. Secondly, this enhancement is not as important for samples with the structure NLN, implying a discrepancy of diffusion between La and Nb causing this difference. And lastly, increasing the number of layers from 3 to 5 on the LNL heterostructure increases slightly the relative permittivity but increases even more the dielectric losses.

As it has been stated in previous sections, this relative permittivity enhancement comes from space charged regions created at the interfaces between 2 doped layers. The nature and thickness of each layer is crucial to effectively increase the relative permittivity without increasing significantly the dielectric losses. Sample LNL20 is a proof of this hypothesis as its relative permittivity is significantly lower than the dielectric permittivity obtained in LNL10 samples.

In order to better understand the difference between NLN and LNL dielectric per-

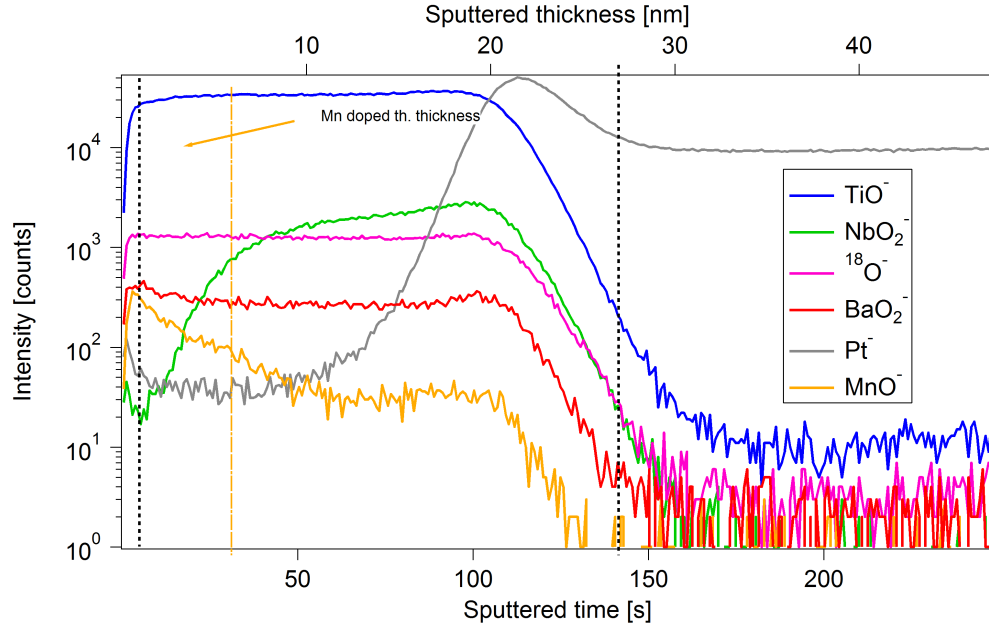


Figure 3.41: TOF-SIMS Cs sputtering (3D) analysis on bilayer Mn-doped BaTiO₃ 5 nm/ Nb-doped BaTiO₃ 20 nm/Pt-Si substrate. Sputter parameters : Cs⁺ species, 1keV, 300x300 μm². Analysis parameters : Negative polarity, Bi⁺, 30 keV, 100x100 μm²

formances, it is critical to understand the diffusion lengths of Nb and La as dopants in BaTiO₃ heterostructures and their impact in the electronic properties. We show in Figure 3.42 a Cs sputtering TOF-SIMS experiment on the trilayer LNL10 (bottom graph), combined with the 2 XPS in situ interface experiments (shown previously in Figure 3.24 and Figure 3.25): Nb-doped BaTiO₃ growing on La-doped BaTiO₃ (top right figure) and La-doped BaTiO₃ growing on Nb-doped BaTiO₃ (top left figure). It is worth mentioning that the very first points of the XPS interface experiments are at the most right of the figure and they correspond to the Fermi level position of a single doped layer, La-doped BaTiO₃ for the top right figure and Nb-doped BaTiO₃ for the bottom right figure. To be completely clear for the reader, the left side of the figure corresponds to the top most interface and the right side of the figure corresponds to the bottom most interface of the sample LNL10 (see Figure 3.42).

If we look at the diffusion profiles of La and Nb in BaTiO₃ at the bottom and top interfaces, it is evident that they are not symmetric. This discrepancy has a significant effect on the Fermi level position. Starting from the top of the heterostructure, the interface from the La-doped layer towards the Nb-doped one is as sharp as expected from the depth resolution of TOF-SIMS [205-207]. Meanwhile, the Nb signal is very small in the La-doped layer, which shows that interdiffusion of dopants did not occur. This is slightly different for the bottom interface close to the Si/Pt substrate. The intensity of the Gaussian-like LaO₂⁻ peak remains below that of the outer La-doped layer, whereas the intensity of the NbO₂⁻ peak does not decay as fast as expected without interdiffusion ($=I_{max}/3$ in

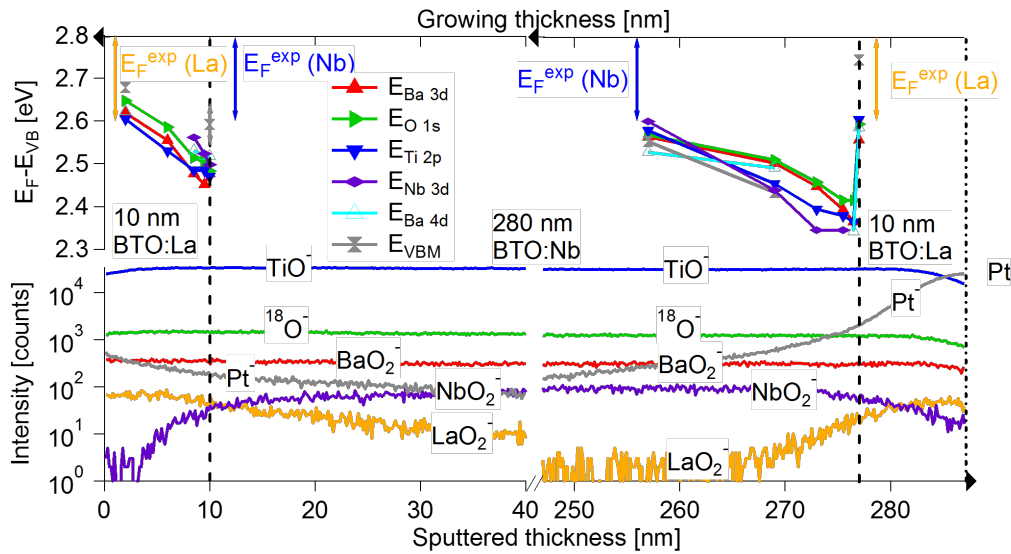


Figure 3.42: Top. In situ XPS stepwise interface experiments of 10 nm thick BTO:La layer on a BTO:Nb layer (left) and a 10 nm thick BTO:Nb layer on a BTO:La substrate (right). First points (starting from dashed lines) corresponds to a single doped layer. For reference, the range Fermi level position with respect to the valence band of single doped films obtained by XPS in situ is plotted. As $E_{CL} - E_{VBM}$ is a material constant, the values of core level positions of each element is obtained by subtracting: 776.57 eV for Ba 3d, 527.09 eV for O 1s, 455.79 eV for Ti 2p, 204.40 eV for Nb 3d and 86.07 for Ba 4d (values obtained by averaging over 100 samples). Error on these values is ± 0.05 eV. Bottom. TOF-SIMS depth profiling of sample LNL10. Analyzed ion species are written over their corresponding line.

the middle of the layer). Long range interdiffusion between the dopant ions was thus much more efficient at the bottom Nb/La interface as compared to the top La/Nb one. In agreement with the XPS analysis, the Nb content near the bottom interface was also larger than at the top contact. Such interface contrast between bottom and top interfaces has been observed by in-situ XPS in metal/ferroelectric/metal structures and explained in terms of a different thermal budget. The bottom interface was exposed to the growth temperature of 650 °C for several hours, while the top interface was only exposed for a few minutes. We therefore ascribed the strong disparity in the La/Nb/La heterostructures to the thermal history of the sample and the diffusion coefficients difference of La and Nb in $BaTiO_3$. This allows to the Nb and La to diffuse from one layer to the other, resulting in this coexistence and erasing/eliminating the La-doped layer at the bottom as it was intended. On the other hand, the top interface had only the time to diffuse as much as the deposition time of the La-doped layer and the cooling down time of the sample, resulting in this incomplete diffusion of the Nb species on the La-doped top most layer.

To better understand these interface experiments, Figure 3.43 displays the corresponding band energy diagram of sample LNL10.

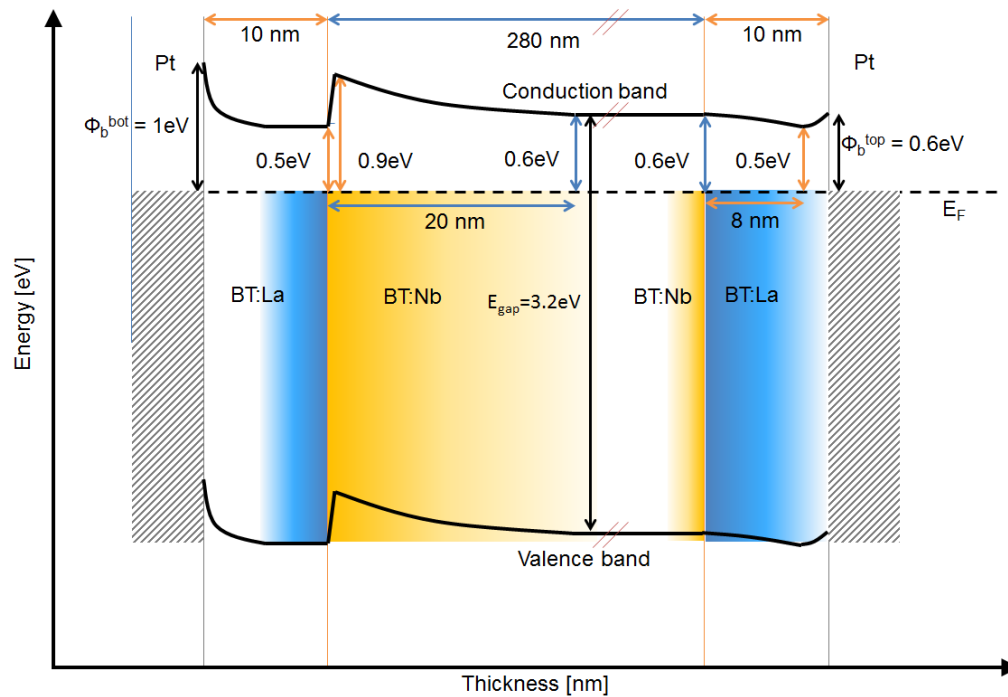


Figure 3.43: Energy band diagram of sample LNL10 capacitor with Pt barrier heights derived from the results of E. Arveux [39]

A sharp immediate drop in Fermi level (0.25 eV) and a change of band position over about 20 nm was observed for Nb growing on La (right) while less pronounced effects (0.1 eV, 8 nm) are observed for the reverse deposition (left). The sharp drop in Fermi level after the initial deposition of Nb-doped BaTiO₃ onto the La-doped substrate is not expected as donor type dopants are present in both films. However, the abrupt lowering of E_F comes along with unexpectedly high Nb signal, which suggests an enhanced Nb concentration at this particular interface. This might be the origin for the depletion layer and the enhanced permittivity. Nb is a donor in BaTiO₃ and lightly doped polycrystalline samples show resistivities of $\sim 10 \text{ Ohm} \cdot \text{cm}$ and a pronounced PTCR effect [131, 133, 134]. When the Nb concentration is increased above 0.1 wt%, the samples become insulating again. This behaviour is likely related to insulating grain boundaries induced by Nb segregation, as it is not expected that the grains themselves become insulating with increasing donor concentration. Moreover, what is new here, and obviously not observed in metal/ferroelectric interfaces, is that cross diffusion of dopants through oxide/oxide interfaces is possible because of the crystalline continuity at the interface and column-like grains. This is why we linked the specific band bending at the bottom Nb/La interface observed by in-situ XPS to the interdiffusion observed by TOF-SIMS.

3.9 Fermi level engineering, case of Mn-doped BaTiO₃ thin films

One of the crucial properties that allow BaTiO₃ thin films to be integrated in Si technologies as tunable radiofrequency capacitors is to reach a Fermi level position as close to its midgap (1.6 eV) in order to reduce the dielectric losses and leakage currents. During this Ph.D. work, we chose to use Mn doping as it is well known to reduce both leakage currents and dielectric losses in ceramics [178–181]. As for thin films, while using Pt electrodes, we achieved a $E_F - E_{VB}$ around 2.2 eV (see section 3.4) and found out that the Mn found in our films was incorporated as Mn³⁺ (see EPR section), indicating that a lower $E_F - E_{VB}$ could be achieved if we were able to incorporate Mn in valence state of 4+. We started with trying out different substrates, then oxydizing our BaTiO₃/Pt samples with an atomic oxygen source and lastly using an atomic oxygen source as oxygen ion supplier during the thin film growth (reactive sputtering).

Substrate dependence

In this work, we deposit BaTiO₃ on 4 different substrates to test the Fermi level position: Ta foil, STO:Nb [111] 0.05%wt., Ag and Pt layers on Si substrates. To reduce the uncertainty of deposition conditions prior to XPS in-situ measurements, we placed our substrates in the same substrate holder and deposit BaTiO₃ using the same conditions described before (2.5 W/cm², 5 Pa, 1% O₂ content, 650°C and 8 cm target to substrate distance).

In a first approach, we should look at the components as well as the quality of our films by XRD, shown in Figure 3.44.

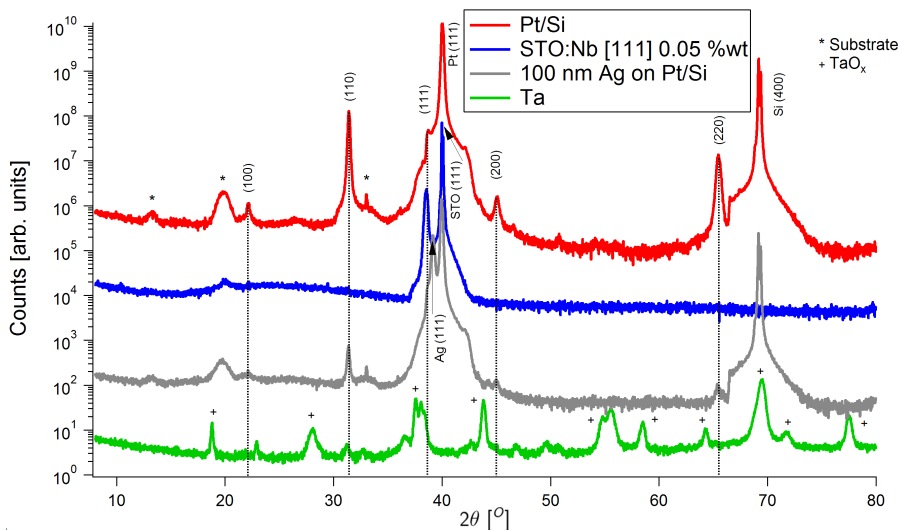


Figure 3.44: Routine XRD 2theta scan of Mn-doped BaTiO₃ deposited on different substrates

For samples deposited on Pt/Si and Ag/Pt/Si we do not see a difference as the sample is polycrystalline in both cases. In the case of the sample deposited on STO:Nb, the sample has a preferential growth on the same direction as the crystal substrate ([111] in this case). Finally, the film deposited on Ta foil is polycrystalline but there are 2 phases of tantalum oxide, Ta_2O_5 and TaO_x , the latter one could be formed during the heating process prior to deposition and/or during the first instants of $BaTiO_3$ deposition.

Figure 3.45 resumes the Fermi level position found in 1 at.% Mn-doped $BaTiO_3$ on these 4 different substrates.

It is evident that Mn-doped $BaTiO_3$ show clearly a difference in Fermi level position depending on the substrate it is being deposited. Nonetheless, far from the substrate, our material should display the same E_F for all substrates as the E_F should reach its bulk value which it is independent of the substrate. Nevertheless, this is not the case as all films are thicker than 150 nm, which is considered thick enough for the bulk value to be established.

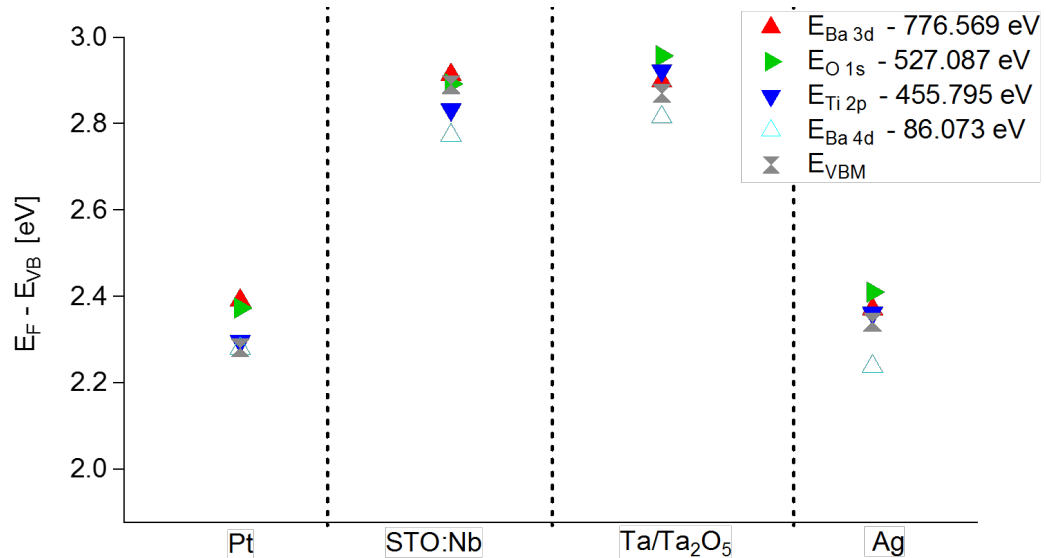


Figure 3.45: Fermi level position with respect to the Valence band of Mn-doped samples deposited on different substrates

It is clear that for samples deposited on noble metals (Ag, Pt) the Fermi level stays around 2.2 eV, but for Ta and STO:Nb, the Fermi level rises upto 2.9 eV, even if our $BaTiO_3$ is heavily doped with 1at.% Mn. From XRD, we learned that the Ta foil forms a thin oxide layer, which creates an insulator layer between our metallic foil and our sample, charging our surface during the XPS experiment and therefore displaying a high Fermi level position. In order to verify that our sample's surface is not insulating, we used the neutralizer as to compensate for the charges at the surface, which would induce a shift towards lower binding energies for all core levels. After switching on the neutralizer, no

shift was detected, indicating that our sample's surface was being grounded correctly and the high Fermi level was most likely being caused by the insulating interface (Ta_2O_5) between BaTiO_3 and the grounded Ta foil. To verify this, we deposited a 3 nm thin film of BaTiO_3 on Ta foil with the purpose of measuring both the thin film and the substrate during the XPS experiment. Once the film was deposited, we analysed the core levels of BaTiO_3 and Ta without neutralizer (w/o-N), with neutralizer (N), with neutralizer and applying a positive bias to the ground (+4N) and with neutralizer and applying a negative bias to the ground (-4N), as shown in Figure 3.46. If such hypothesis is true the shift in binding energy of the core levels should be zero.

As shown in Figure 3.46, neither the core levels of BaTiO_3 nor those of Ta follow the bias applied, indicating that the Ta_2O_5 insulating layer between our film and the substrate charges during the XPS experiment, causing to alter the measurement and "artificially rise" the Fermi level of our film. As the Ta peak shifts in parallel with the BTO peaks, it is nevertheless clear that a "charging" of the Ta_2O_5 capacitor occurs, which would mean that the binding energy of the BaTiO_3 film deposited on Ta foil do not reflect the real Fermi energy in the BaTiO_3 .

In the case of the sample $\text{STO:Nb/BaTiO}_3\text{:Mn}$, as the interface between these two materials is nearly epitaxial, no charging is being induced by the substrate, that is to say, during XPS core level intensity calibration of the sample, the neutralizer did not shift the Ba 3d core level, implying that the substrate is conductive enough. Nevertheless, we observe a Fermi level close to the conduction band far from the interface between the substrate and the film even if our doping has clearly shown a Fermi level position around 2.2 eV.

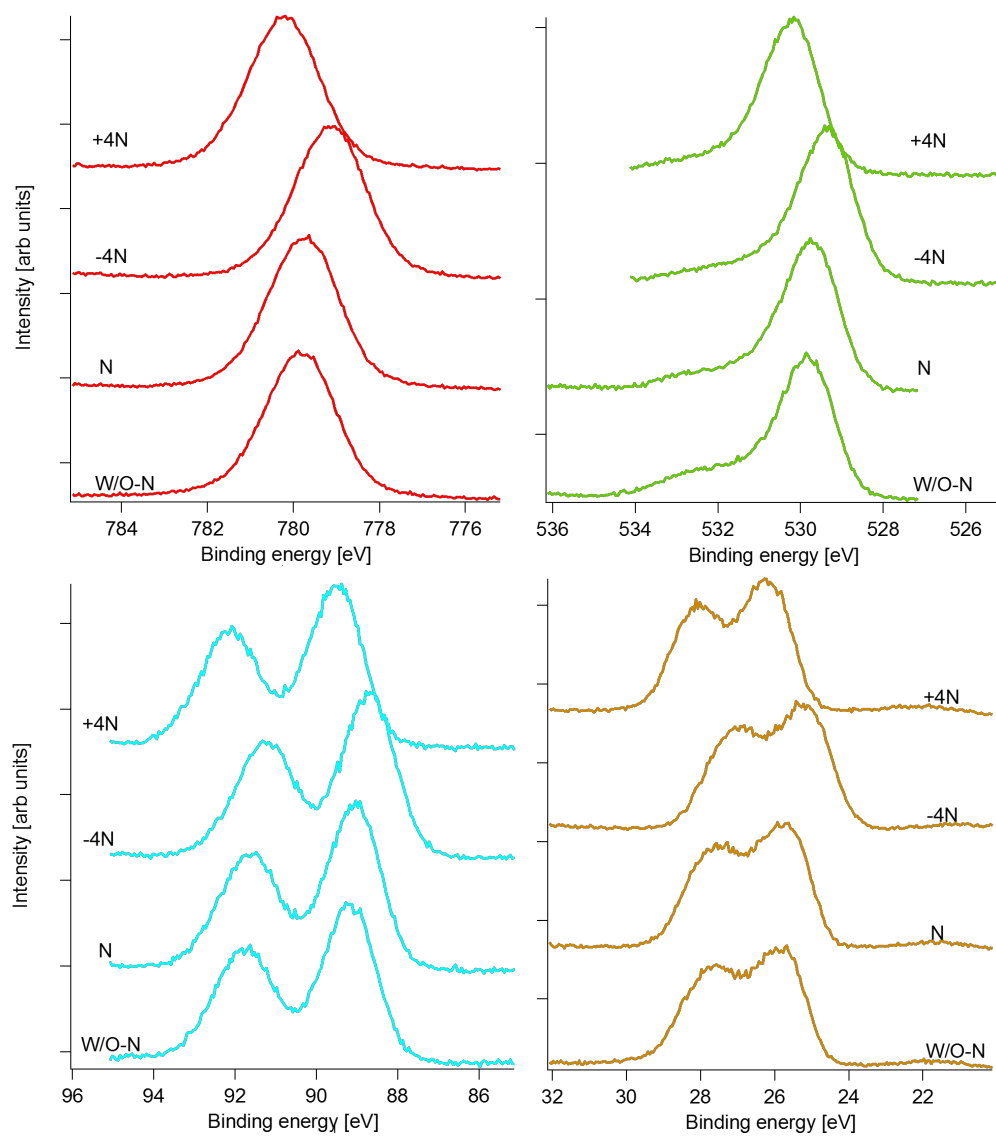


Figure 3.46: Ba 3*d*, O 1*s*, Ba 4*d* and Ta 4*f* core level positions analyzed by XPS without neutralizer (w/o-N), with neutralizer (N), with neutralizer and applying +4 volts bias (+4N) and with neutralizer and applying -4 volts bias (-4N)

To better understand this result, we performed a XPS interface experiment depositing in a step-wise manner Mn-doped BaTiO₃ on top of a single crystal STO:Nb substrate. Figure 3.47 shows the evolution of Fermi level position at each step of the film deposition.

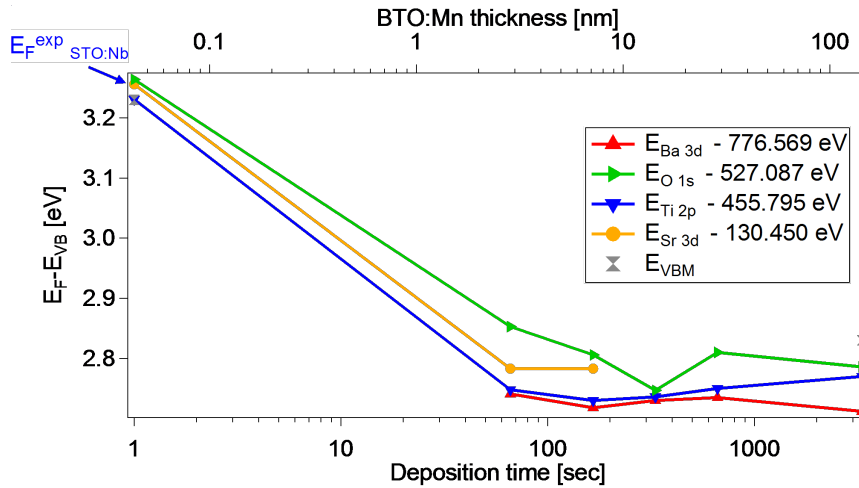


Figure 3.47: Fermi level evolution of Nb-doped SrTiO₃ (STO:Nb) / Mn-doped BaTiO₃ interface obtained by XPS. The film thickness was determined by using the deposition time and the average deposition rate of Mn-doped BaTiO₃. Experimental Fermi level of STO:Nb single crystal is included on the graph as the starting point

We observe that after the first deposition of Mn-doped BaTiO₃ (around 2 nm thick) the Fermi level drops to 2.8 ± 0.1 eV. Moreover, even after the substrate core level is no longer visible (> 10 nm) this value stays constant during further deposition. This means that the Fermi level position of our film is being shifted "artificially" to higher values since the Fermi level position of our film must be 2.2 eV when measured far from the substrate (as our single doped films measured in section 3.4), that is to say, when the substrate is no longer visible on XPS (> 10 nm).

As the substrate is not a perfect electronic conductor, one could think that depositing an insulating material would induce a surface photovoltage (SPV) at the surface during measurement as in the case of SrTiO₃:Nb/Pt [198].

To better understand the following results, we shall explain briefly the basic physical principle of SPV, considering as an example a n-type semiconductor surface on which electronic surface states are present in its bandgap, as shown in Figure 3.48. It is well known that thermal equilibrium is characterized by a constant Fermi level throughout the whole material, but in the case where surface states are present, it can only be established by a charge transfer between surface and bulk. Therefore, the surface carries a charge that is balanced by a space charge located in the bulk, which depletes the layer below the surface of majority carriers. As stated in Poisson's equation, such charge distribution results in a built-in electric field displaying a band bending. Irradiation with a photon energy greater than the band gap generates electron-hole pairs. Those excess carriers are separated by the built-in electric field. Consequently, again a charge

redistribution takes place along with a change of the total band bending. The shift of the band bending compared with the equilibrium value is denoted as the surface photovoltage [198, 240, 241].

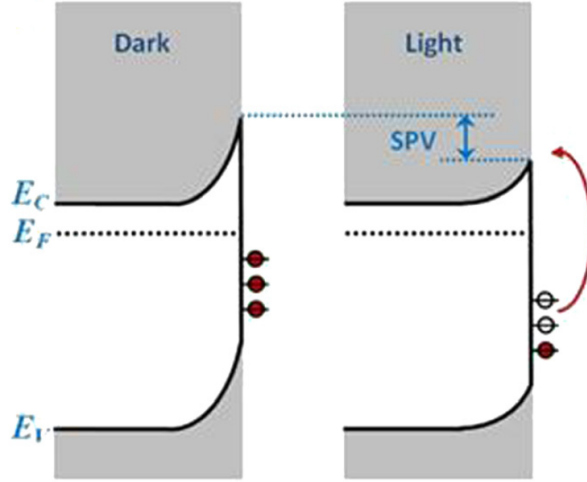


Figure 3.48: Schematic band diagram showing a surface photovoltage of a n-type semiconductor, which is the ionization of deep surface acceptors giving rise to a reduction of the surface band bending.

Such photovoltage would raise the Fermi level without charging the surface, so using a neutralizer would not shift the binding energies of the measured core levels. Nonetheless, one way to detect this photovoltage is by grounding our surface with a metallic film. On the other hand, depositing a metal on the surface of the material would heavily decrease the intensity of BaTiO₃ core levels, and would be impossible to verify the photovoltage. In our case, it has been observed that a very thin layer of Pt deposited on BaTiO₃ can form islands after a thermal treatment. This would ground our sample and the binding energy of the Pt formation reveal Fermi energy at the surface of BaTiO₃. To verify the photovoltage generated by the substrate, we need to verify that the core level of Pt and the valence band are shifting towards higher binding energies once the BaTiO₃ film is revealed. Such experiment is shown in Figure 3.49. In Figure 3.49 the evolution of core levels Ba 3*d*, Ti 2*p*, O 1*s*, Pt 4*f* and valence band of 20 nm of Mn-doped BaTiO₃ as deposited on single crystal STO:Nb are displayed.

The photovoltage induced by the X-ray source can be calculated as: $U_{ph} = k_B \times T/q \times \ln(j_{ph}/j_0 + 1)$, where j_{ph} is the current density induced by the X-ray source.

The photon flux of the monochromated X-ray source ($h\nu = 1486.6$ eV) is 10^{11} photons/s [198] and the illuminated area is estimated as $2\text{-}4$ mm². Assuming that the energy required for the creation of electron-hole pair is on average $3 \times E_g$, the photocurrent density j_{ph} is calculated as 1 mA/cm² [198]. With a measured difference of Fermi energy of STO:Nb and BTO:Mn of $\Phi_b = 1$ eV, the photovoltage results of $U_{ph} = 0.4$ eV. This agrees approximatively with the difference of the Fermi energy measured at the BTO:Mn films

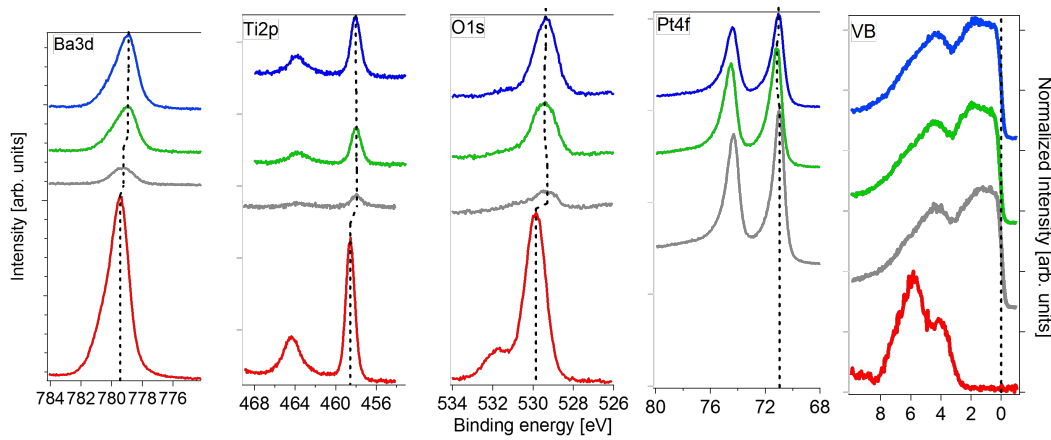


Figure 3.49: Ba $3d$, O $1s$, Ti $2p$, Pt $4f$ core level positions and valence band analyzed by XPS. The intensities of the valence band spectra are normalized for better comparison. (A) XPS core levels band valence band spectra of 20 nm Mn-doped BaTiO₃ film deposited on a STO:Nb crystal, (B) deposition of 2 nm Pt film, (C) Pt island formation by annealing in oxygen atmosphere (1 sccm O₂, 0.05 Pa, 450°C for 30 min). Notice the increasing intensity of Ba $3d$ and Ti $2p$ core levels, confirming that the surface of BaTiO₃ is being exposed as the Pt is forming islands. Last step (D) is the reduction of the surface by heating in vacuum (5×10^{-7} Pa, 450°C for 30 min).

on STO:Nb and Pt. The difference observed between the calculation and our experiment may come from the underestimation of the band bending in the STO:Nb substrate induced by the deposition of the Mn-doped BaTiO₃ due to Nb surface segregation.

Post-deposition atomic oxygen source treatment

As seen in section 3.4.2, after exposing our samples through an oxygen atomic source, it is possible to decrease the Fermi level position. In Figure 3.50, we show the Fermi level position of single doped samples before and after oxygen plasma treatment determined by the position of the valence band and the core level binding energies using the Kraut method.

In general, the oxygen plasma treatment decreased effectively the Fermi level position of our films by about 0.2 eV. In the case of Mn doping, this shift was only about 0.1 eV.

The Fermi level shift seen in the undoped BaTiO₃ can be explained by the reduction of oxygen vacancies at the surface. Indeed, as seen in section 3.4.1, the Fermi level obtained on these layers are mostly due to the doubly charged oxygen vacancy energy level in BaTiO₃. In the case of the Nb- and La-doped samples, where oxygen vacancies are expected to be lower than in an undoped BaTiO₃ sample, an oxidation occurs after the oxygen plasma treatment, resulting in a lowering of the Fermi energy.

In the case of Mn doping, the oxidation by O₂ plasma was not sufficient to induce a change of valency, (and therefore a lower Fermi Level position) that is to say, from

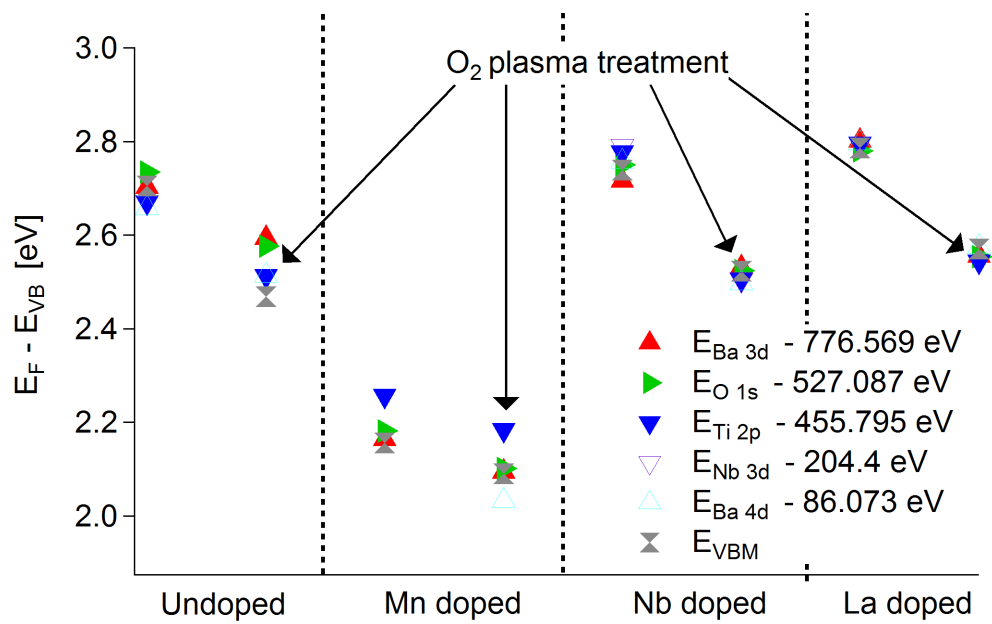


Figure 3.50: Fermi level position with respect to the valence band of single doped samples. O₂ plasma post-deposition treated samples are indicated with an arrow

Mn^{2+/3+} to Mn^{3+/4+}. To achieve this, we tried different configurations as to reach lower Fermi level positions in Mn-doped BaTiO₃. We annealed samples during O₂ plasma treatment as to increase the oxidation of the sample and thus achieve our goal mentioned before. The ramping up and down of temperature was done without sample. Because of the nature of the heater (lamp), the temperatures were restricted up to 400°C. Lastly, we annealed a Mn doped sample at 700°C in 2sccm of O₂ with a pressure of 0.5 Pa for 2h. Figure [3.51](#) displays the Fermi level position of different treated Mn-doped BaTiO₃ films.

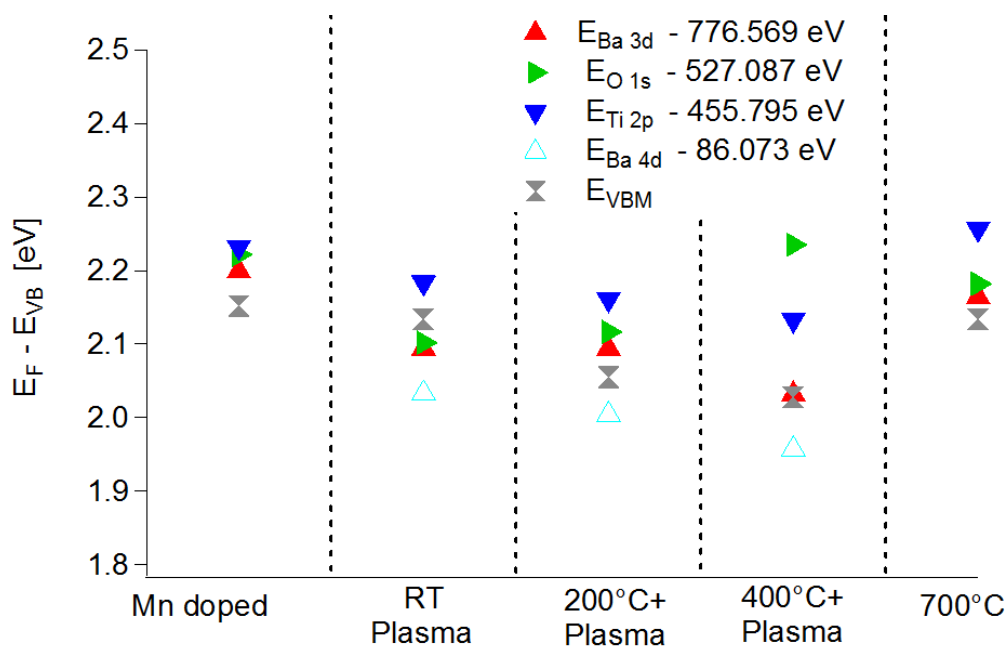


Figure 3.51: Fermi level position with respect to the valence band of Mn-doped samples. O_2 plasma post-deposition treated samples are indicated with the label "Plasma". Temperatures used during plasma treatment are indicated.

Atomic oxygen source co-sputtering

As stated in the section before, the atomic source can also be used as a reactive ion supplier during sputtering. In this case, we used another instrument (homemade, photo in Figure 3.52). The system was adjusted as to the oxygen input passed through the atomic source and the argon input passed through a second gas line. Nevertheless, with this setup it is impossible to insure 100% pure O_2 through the atomic source as the whole system is pressured to 5 Pa. With this system, it low reflected power is necessary to



Figure 3.52: Homemade plasma oxygen source co-sputtering set up. A: Vacuum chamber for thin film deposition. B: Quartz tube for plasma generation

maintain the plasma ignition throughout the thin film deposition. Therefore, the window of working power is very short (100 W to 130 W). All things considered, we tested 3 working powers for the atomic source: 100 W, 115 W and 130 W. In Figure 3.53, we show the routine diffractograms of 130 W Mn-doped BaTiO₃ film deposited with the O₂ atomic source and single doped films for comparison.

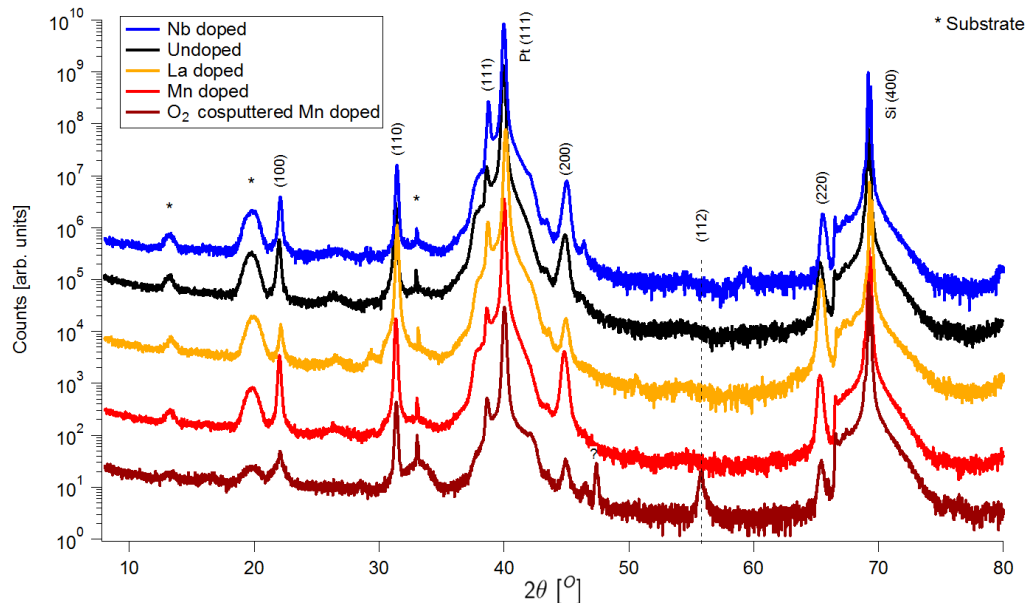


Figure 3.53: Diffractograms of undoped, Mn-, La- and Nb-doped BaTiO₃ thin films cosputtered with O₂ plasma deposited on Si platinized (111) substrates

The addition of O₂ plasma on the sputtering process may have introduced another phase at 47.37°. However, this is most likely a surface contamination since it is a very low intensity peak. Moreover, the reflection (112) of BaTiO₃ can now be observed indicating a more crystalline film. Furthermore, when measuring the thickness by ellipsometry (see Annex), all films had the same thickness, indicating us that the introduction of O₂ plasma to the sputtering process did not affect the deposition rate of the films since all films had the same time of deposition.

Next, we tested the dielectric properties in frequency (Figure 3.54) and electric field (Figure 3.55) of these films at room temperature.

As seen in Figure 3.54, the presence of O₂ plasma during deposition increased the permittivity of all Mn-doped films. This is probably due to an increasing of crystallinity of the film as more crystalline films tend to have better dielectric properties [40, 214, 215]. Moreover, increasing power of O₂ plasma during deposition decrease the dielectric losses upto values lower than the untreated Mn-doped sample (1.1% compared to 1.8%). This is probably due to an increasing Mn³⁺ concentration in the film causing more electron trap sites and therefore decreasing the dielectric losses. Moreover, for the sample 130 W, we can observe an increasing dielectric loss, which would be seen as increasing density

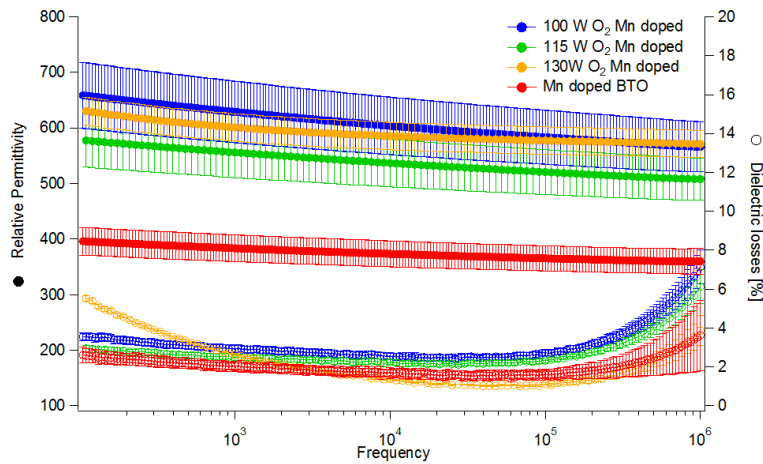


Figure 3.54: Dielectric permittivity and losses of 100 W, 115 W and 130 W O_2 plasma cosputtered Mn-doped $BaTiO_3$ films in function of frequency at room temperature. Untreated Mn-doped $BaTiO_3$ sample is for reference.

currents in the leakage currents measurements.

To verify these hypothesis, we measured the I-V characteristic, displayed in Figure [3.56](#)

The effect of O_2 plasma in the J-E characteristics is clear: at low fields, that is, lower than 20 kV/cm , the leakage currents are lower for 100 W and even lower for 115 W. However, the 130 W sample leakage currents increased compared to the other 2 treated samples, which was expected from the dielectric measurements. This can be explained as the sample 130 W has better crystallinity, which increases also the leakage currents as the films have columnar growth, which facilitates the passage of electric current through

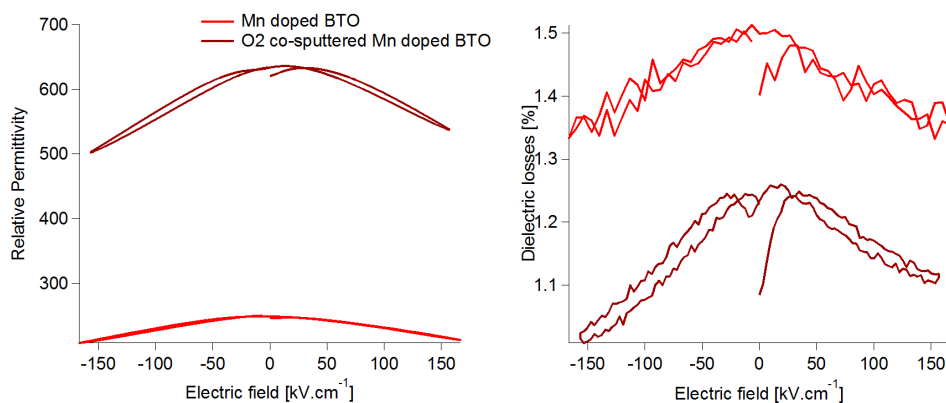


Figure 3.55: Dielectric permittivity and losses of 130 W O_2 plasma cosputtered Mn-doped $BaTiO_3$ in function of electric field at 100kHz at room temperature. Untreated Mn-doped $BaTiO_3$ sample is for reference.

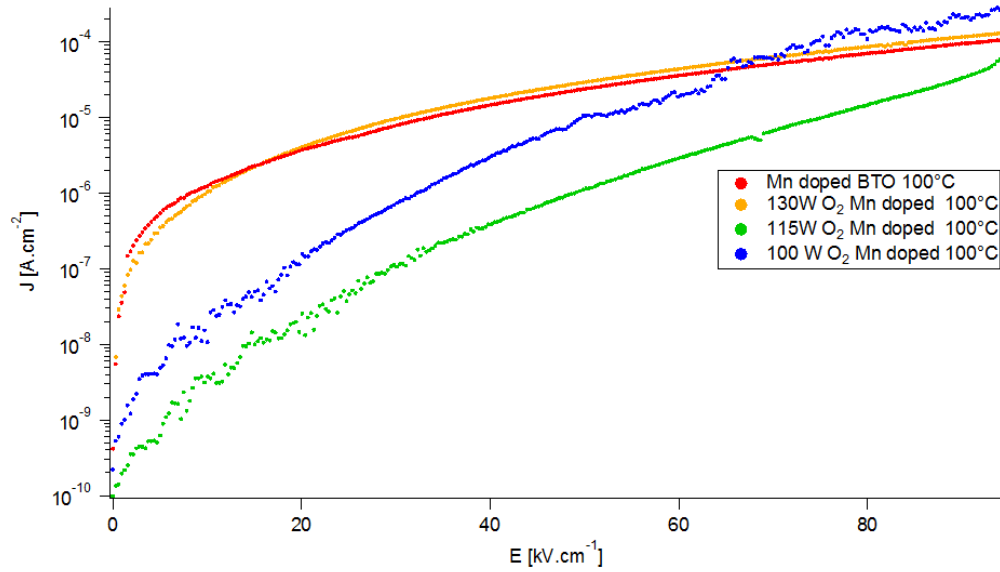


Figure 3.56: Valence band of different Mn-doped BaTiO₃ thin films

the vertical grain boundaries.

Finally, we performed *ex-situ* XPS measurements of the sample prepared with 130 W (other films to be tested) shown in Figure 3.57. To better grasp the effects of oxygen plasma, we displayed on the same figure all treatments that were performed on Mn-doped BaTiO₃. These were executed on the oxygen atomic source at DAISY-MAT as in section 3.9.

It is worth noticing that all peaks of the core levels display the same shape and the binding energies stay the same after treatment with O₂ plasma. Moreover, the valence band maximum shape also stays the same but only the sample with O₂ plasma co-sputtering has not only the lower Fermi level position but also there are some states between 1.5 eV and 2 eV as shown in Figure 3.57.

Looking at all results coming from the different techniques, in general, O₂ plasma co-sputtering increased the crystallinity of the film, increasing the dielectric permittivity. Moreover, the 130 W sample slightly decreased the dielectric losses and lower powers (i.e. 100 W and 115 W) decreased the leakage currents at low electric fields ($E < 100$ kV/cm), putting in evidence a possible shift of the Mn transition level from 4+/3+ to 3+/2+. Furthermore, none of the post-deposition treatments shifted the Fermi level position. Only the O₂ plasma co-sputtering was able to create some states lower than 2 eV, confirming our hypothesis of the shift of the transition level of Mn as the transition level Mn^{2+/3+} has a lower Fermi level position in BaTiO₃ [177] [182].

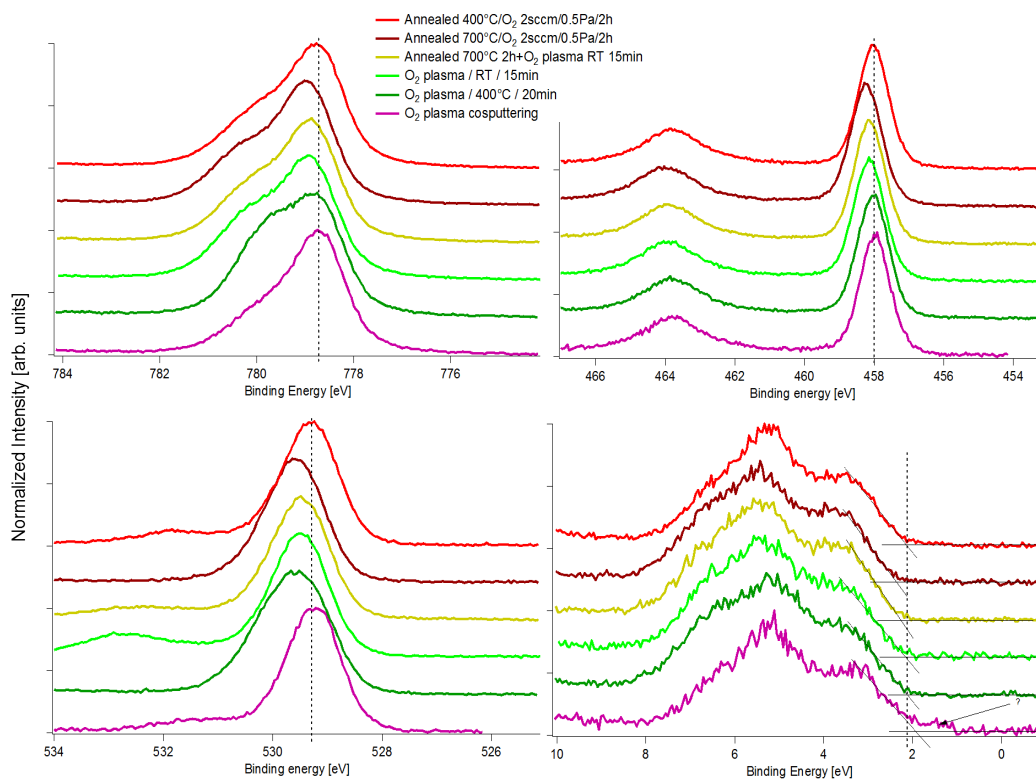


Figure 3.57: Valence band of different Mn-doped BaTiO₃ thin films

Chapter 4

General conclusion and perspectives

This work was dedicated to the development and characterization of single doped and multilayered doped BaTiO₃ thin films, in order to better understand the dielectric and electronic properties of this ferroelectric oxide as well as its internal interfaces. Dielectric measurements were performed at the ICMCB in Bordeaux, France, whereas in situ photoemission spectroscopy has been carried out in the surface science division at TU-Darmstadt, Germany.

The magnetron sputtering technique in reactive mode was chosen during this study to deposit all of our films, for reasons of availability and because it is the most widespread in industrial environment for the deposition of thin layers. We have then chosen 3 dopants, La, Mn and Nb, since they have been the most studied in literature and due to our own specifications, such as high values of permittivity and/or low leakage currents. We then have done systematic measurements on all of our films, impedance analysis in temperature and electric field, leakage currents in temperature and in and ex-situ XPS measurements. We confirmed that Nb-doped BaTiO₃ has the highest value of permittivity, highest leakage currents and a Fermi level position close to the conduction band. Moreover, Mn-doped films presented lower values of permittivity but also the lowest values of dielectric losses and leakage currents and a Fermi level position closer to the bandgap ($E_F - E_{VB} = 2.0$ eV). Thanks to EPR, we were able to identify the oxidation state of Mn in BaTiO₃. The oxidation state of Mn in BaTiO₃ has been attributed to 3+ as this impurity is "silent" and no Mn²⁺ nor Mn⁴⁺ were detected by the EPR analysis. As a perspective, it would be nice to confirm the presence of all dopants in the BaTiO₃ lattice. RBS can be performed for Mn and La-doped films as they can be distinguished from the Ba peak (Nb is very difficult to detect due to its proximity to Ba in RBS spectrum).

Due to the polycrystallinity of films and their columnar growth, leakage currents are very restrained in applied electric fields. However, we were able to qualitatively characterise the effect of the different chosen dopants in BaTiO₃. It would be helpful to perform this analysis on films deposited with other less energetic techniques such as sol-gel.

Our main case of study were the heterostructures of layered BaTiO₃ based films. We have explored mainly the trilayers of 4 stacks: Mn/Nb/Mn, Nb/Mn/Nb, La/Nb/La and Nb/La/Nb. In order to maintain the same thickness as the other single doped films, we varied the thickness of the outer layers and then we adjusted the thickness of the core stack as to always get 300 nm. The effect of the interfaces created at the contact of each layer was clear, the space charges created at the interfaces increases artificially the dielectric permittivity. This effect can be seen when we calculate a "theoretical" value of these multilayers, 3 separate capacitors in series of each dopant have a lower value of permittivity than the measured value of these heterostructures. An extensive study of the bilayers is expected to better understand the effect of each dopant on these multilayers.

Furthermore, we have achieved large and temperature-stable dielectric permittivity by the three-layer stack of La-doped and Nb-doped BaTiO₃ thin films(LNL10) (see Table 4.1). Using XPS, we could link these features to interface localization of space charges resulting in large band bending over more than a thickness of 10 nm. TOF-SIMS experiments suggest that this band bending results from cross diffusion of dopants at the internal interface.

A more detailed XPS investigation of Mn-doped BaTiO₃ has been performed. Different treatments have been implemented as to change the valency of Mn in BaTiO₃ from the transition level of 4+/3+ to 3+/2+ and reach lower values of Fermi level position. We have determined that the high values of Fermi level obtained on Mn-doped films deposited on Ta foils and Nb-doped SrTiO₃ are not intrinsic. The first one is most likely due to a tantalum oxide formed between the BaTiO₃ film and the metallic Ta foil creating thus an insulating barrier, inducing a charge that increases measured Fermi level position at the surface. In the second case we attributed this effect to a surface photovoltage created by the Nb:STO substrate. On the other hand, none of the post-deposition treatments performed on Mn-doped films were successful on lowering the Fermi level position. This is mostly due to the choice of the substrate and it would be interesting to measure the Fermi level position of Mn-doped films deposited on conducting oxides such as SrRuO₃. Moreover, the atomic oxygen co-sputtering during deposition had conclusive effects on the permittivity and leakage currents. These films had higher values of dielectric permittivity and lower leakage currents at low electric field values. Moreover, XPS analysis revealed that the valence band of the 130 W Mn-doped BaTiO₃ sample had some states located close to the valence band maximum, indicating a possible shift of the transition level of Mn from 4+/3+ to 3+/2+. This experiment should be recreated and all remaining samples need to be measured to confirm this hypothesis. Moreover, it would be nice to observe the effect of this co-sputtering on all the remaining dopants, including a nominally undoped BaTiO₃. Moreover, EPR measurements would be interesting in films cosputtered with oxygen plasma specially on Mn-doped films as we detect some states at the valence band, indicating some Mn²⁺ states in the lattice lowering the Fermi level, which would be detectable on EPR.

In conclusion, the major achievement of this thesis is based on the study of BaTiO₃ based multilayers with several analysing methods via a collaboration of ICMCB and TU-Darmstadt. The in-depth understanding of the mechanisms for improving (di)electric

and electronic properties, using numerous systematic characterizations of the material, enabled us to propose a novel heterostructure. This deposition architecture offers new perspectives for making tunable capacitors and may be useful to model the so-called giant permittivity in isotropic polycrystalline samples.

In table 4.1 we resume the general results obtained in this thesis.

Table 4.1: General results of (un)doped BaTiO₃ thin films deposited on platinized Si substrates. Dielectric permittivity and loss values are given for 100 kHz at room temperature. Leakage currents are given for 0 kV/cm at room temperature

Single doped films				
Sample	ε	$\tan(\delta)$ [%]	J_0 [A/cm ²]	XPS[eV]
Undoped	350	4	$1 \cdot 10^{-6}$	2.7
Mn-doped	250	2	$4 \cdot 10^{-10}$	2.2
La-doped	485	3.2	$3 \cdot 10^{-9}$	2.8
Nb-doped	715	3	$8 \cdot 10^{-8}$	2.8

Heterostructures				
Sample	ε	$\tan(\delta)$ [%]	J_0 [A/cm ²]	XPS[eV]
MNM20	430	2	$3 \cdot 10^{-9}$	2.2
MNM10	550	3	$3 \cdot 10^{-9}$	2.2
MNM5	850	5	$7 \cdot 10^{-9}$	2.4
NMN20	440	2.5	-	2.1
LNL10	1030	3.9	$5 \cdot 10^{-8}$	2.3
NLN10	540	2.3	$8 \cdot 10^{-7}$	2.3

Bibliography

- [1] J. Valasek, "Piezo-electric and allied phenomena in Rochelle salt," *Physical Review*, vol. 17, no. 4, pp. 475–481, 1921.
- [2] L. E. Cross and R. E. Newnham, "History of Ferroelectrics," *Ceramics and Civilization*, vol. III, pp. 289–305, 1987.
- [3] J. F. Scott, "Applications of modern ferroelectrics," *Science*, vol. 315, no. 5814, pp. 954–959, 2007.
- [4] J. M. Gregg, "Ferroelectrics at the nanoscale," *Physica Status Solidi (A) Applications and Materials Science*, vol. 206, no. 4, pp. 577–587, 2009.
- [5] V. Reymond, "Nouvelles couches minces et multicouches dérivées de BaTiO₃: optimisation des propriétés diélectriques," Ph.D. dissertation, Université de Bordeaux, 2004.
- [6] F. A. Miranda, F. W. Van Keuls, R. R. Romanofsky, C. H. Mueller, S. Alterovitz, and G. Subramanyam, "Ferroelectric thin films-based technology for frequency- and phase-agile microwave communication applications," *Integrated Ferroelectrics*, vol. 42, no. October 2014, pp. 131–149, 2002.
- [7] A. K. Tagantsev, V. O. Sherman, K. F. Astafiev, J. Venkatesh, and N. Setter, "Ferroelectric materials for microwave tunable applications," *Journal of Electroceramics*, vol. 11, no. 1-2, pp. 5–66, 2003.
- [8] C. Hubert, "Synthese et caracterisation de nouveaux materiaux ferroelectriques accordables pour applications hyperfrequences." Ph.D. dissertation, Universite Bordeaux 1, 2003.
- [9] B. Guigues, B. Guigues, and E. De, "Elaboration de capacites variables ferroelectriques a base de (Ba , Sr) TiO₃ pour applications radiofrequences," Ph.D. dissertation, Ecole Central Paris, 2009.
- [10] A. Islam Khan, D. Bhowmik, P. Yu, S. Joo Kim, X. Pan, R. Ramesh, and S. Salahuddin, "Experimental evidence of ferroelectric negative capacitance in nanoscale heterostructures," *Applied Physics Letters*, vol. 99, no. 11, pp. 0–3, 2011.

- [11] P. Bao, T. J. Jackson, X. Wang, and M. J. Lancaster, "Barium strontium titanate thin film varactors for room-temperature microwave device applications," *Journal of Physics D: Applied Physics*, vol. 41, no. 6, 2008.
- [12] G. Busch and P. Scherrer, "Ferroelectrics A new seignette-electric substance," *Naturwiss.*, vol. 23, p. 737, 1935.
- [13] C. A. Mead, "Anomalous capacitance of thin dielectric films," *Physical Review Letters*, vol. 6, no. 10, pp. 5–6, 1961.
- [14] C. Basceri, S. K. Streiffer, A. I. Kingon, and R. Waser, "The dielectric response as a function of temperature and film thickness of fiber-textured (Ba,Sr)TiO₃ thin films grown by chemical vapor deposition," *Journal of Applied Physics*, vol. 82, no. 5, pp. 2497–2504, 1997.
- [15] C. B. Parker, J. P. Maria, and A. I. Kingon, "Temperature and thickness dependent permittivity of (Ba,Sr)TiO₃ thin films," *Applied Physics Letters*, vol. 81, no. 2, pp. 340–342, 2002.
- [16] S. K. Streiffer, C. Basceri, C. B. Parker, S. E. Lash, and A. I. Kingon, "Ferroelectricity in thin films: The dielectric response of fiber-textured (Ba_xSr_{1-x})Ti_{1+y}O_{3+z} thin films grown by chemical vapor deposition," *Journal of Applied Physics*, vol. 86, no. 8, pp. 4565–4575, 1999.
- [17] C. Lichtensteiger and M. Dawber, "Appendix B – Material–Substrate Combinations Tables," *Physics of Ferroelectrics*, vol. 3, pp. 373–384, 2007.
- [18] D. Damjanovic, "Ferroelectric, dielectric and piezoelectric properties of ferroelectric thin films and ceramics - Abstract - Reports on Progress in Physics," *Reports on Progress in Physics*, vol. 61, no. dc, p. 1267, 1998.
- [19] M. E. Lines and A. M. Glass, *Principles and Applications of Ferroelectrics and Related Materials*, Bell Laboratories, Ed. Oxford University Press, 1977.
- [20] R. Coelho. Amsterdam: Elsevier Scientific Publishing Company, 1978.
- [21] E. Schlömann, "Dielectric losses in ionic crystals with disordered charge distributions," *Phys. Rev.*, vol. 135, p. A413–A419, 1964.
- [22] P. Vendik, O. and L.M., "Effect of charged lattice imperfections on the dielectric properties of materials." *Sov. Phys. Solid State*, vol. 13, p. 1353–1359, 1971.
- [23] B. M. Garin, "One phonon dielectric losses by excitation of sound," *Sov. Phys. Solid State*, vol. 32, p. 1917, 1990.
- [24] C. Borderon, R. Renoud, K. Nadaud, and H. Gundel, "Dielectric losses due to domain walls in ferroelectric materials," in *ECAPD*, Vilnius, Lithuania, Jul. 2014.

- [25] M. D. Coulibaly, C. Borderon, R. Renoud, and H. W. Gundel, "Effect of ferroelectric domain walls on the dielectric properties of PbZrO₃ thin films," *Applied Physics Letters*, vol. 117, no. 14, Oct. 2020.
- [26] B. Wul and I. Goldman, *C.R. Acad. Sci. URSS*, vol. 46, p. 139, 1945.
- [27] A. V. Hippel, R. Breckenridge, and F. Chesley, *Ind. Eng. Chem.*, vol. 38, p. 1097, 1946.
- [28] A. Devonshire, "Theory of barium titanate," *Phil. Mag.*, vol. 40, pp. 1040–1063, 1949.
- [29] N. Xu, H. Zhao, X. Zhou, W. Wei, X. Lu *et al.*, "Dependence of critical radius of the cubic perovskite ABO₃ oxides on the radius of a- and b-site cations," *International Journal of Hydrogen Energy*, vol. 35, p. 7295 – 7301, 2010.
- [30] W. Merz, "The Electric and Optical Behavior of BaTiO₃ Single-Domain Crystals," *Phys. Rev.*, vol. 76, pp. 1221–1225, 1949.
- [31] M. N. R. Ashfold, F. Claeysens, G. M. Fuge, and S. J. Henley, "Pulsed laser ablation and deposition of thin films," *Chem. Soc. Rev.*, vol. 33, pp. 23–31, 2004. [Online]. Available: <http://dx.doi.org/10.1039/B207644F>
- [32] H. Tabata, H. Tanaka, and T. Kawai, "Formation of artificial BaTiO₃/SrTiO₃ superlattices using pulsed laser deposition and their dielectric properties," *Applied Physics Letters*, vol. 65, no. 15, pp. 1970–1972, 1994.
- [33] A. Y. Fasasi, R. Bucher, B. D. Ngom, U. Buttner, M. Maaza, C. Theron, and E. G. Rohwer, "Structural and optical properties of annealed W-doped BaTiO₃ thin films prepared by pulsed laser deposition," *Journal of Physics Condensed Matter*, vol. 19, no. 46, 2007.
- [34] A. Y. Fasasi, B. D. Ngom, J. B. Kana-Kana, R. Bucher, M. Maaza, C. Theron, and U. Buttner, "Synthesis and characterisation of Gd-doped BaTiO₃ thin films prepared by laser ablation for optoelectronic applications," *Journal of Physics and Chemistry of Solids*, vol. 70, no. 10, pp. 1322–1329, 2009.
- [35] J. S. Horwitz, W. Chang, W. Kim, S. B. Qadri, J. M. Pond, S. W. Kirchoefer, and D. B. Chrisey, "Effect of stress on the microwave dielectric properties of Ba_{0.5}Sr_{0.5}TiO₃ thin films," *Journal of Electroceramics*, vol. 4, no. 2, pp. 357–363, 2000.
- [36] Y. Liu, Z. Chen, C. Li, D. Cui, Y. Zhou, G. Yang, and Y. Zhu, "Electrical and electro-optical properties of Ce-doped barium titanate thin films prepared by pulsed laser deposition," *Journal of Applied Physics*, vol. 81, no. 9, pp. 6328–6331, 1997.
- [37] C. Eom *et al.*, *Appl. Phys. Lett.*, vol. 55, p. 595, 1989.
- [38] J. Triscone *et al.*, *J. Appl. Phys.*, vol. 79, p. 4298, 1996.

- [39] E. Arveux, "Surface and interface properties of BaTiO₃ ferroelectric thin films studied by in-situ photoemission spectroscopy," Ph.D. dissertation, Université de Bordeaux, 2009.
- [40] V. Reymond, D. Michau, S. Payan, and M. Maglione, "Substantial reduction of the dielectric losses of Ba_{0.6}Sr_{0.4}TiO₃ thin films using a SiO₂ barrier layer," *Journal of Physics Condensed Matter*, vol. 16, no. 50, pp. 9155–9162, 2004.
- [41] W. Zhang, M. Yuan, X. Wang, W. Pan, C. M. Wang, and J. Ouyang, "Design and preparation of stress-free epitaxial BaTiO₃ polydomain films by RF magnetron sputtering." *Science and technology of advanced materials*, vol. 13, p. 035006, 2012.
- [42] B. Wagué, J.-B. Brubach, G. Niu, G. Dong, L. Dai, P. Roy, G. Saint-Girons, P. Rojo-Romeo, Y. Robach, and B. Vilquin, "Structural studies of epitaxial BaTiO₃ thin film on silicon," *Thin Solid Films*, vol. 693, p. 137636, 2020.
- [43] N.-Y. Lee, T. Sekine, Y. Ito, and K. Uchino, "Deposition Profile of RF-Magnetron-Sputtered BaTiO₃ Thin Films," *Japanese Journal of Applied Physics*, vol. 33, pp. 1484–1488, 1994.
- [44] E. Evangelou, N. Konofaos, and C. B. Thomas, "Properties of barium titanate (BaTiO₃) thin films grown on silicon by rf magnetron sputtering," *Philosophical Magazine B*, vol. 80, pp. 395–407, 2000.
- [45] N. Setter, D. Damjanovic, L. Eng, G. Fox, S. Gevorgian, S. Hong, A. Kingon, H. Kohlstedt, N. Y. Park, G. B. Stephenson, I. Stolitchnov, A. K. Taganstev, D. V. Taylor, T. Yamada, and S. Streiffer, "Ferroelectric thin films: Review of materials, properties, and applications," *Journal of Applied Physics*, vol. 100, no. 5, pp. 0–46, 2006.
- [46] J. Puebla, "Spin phenomena in semiconductor quantum dots," Ph.D. dissertation, 10 2012.
- [47] C. Dubourdieu, J. Bruley, T. M. Arruda, A. Posadas, J. Jordan-Sweet, M. M. Frank, E. Cartier, D. J. Frank, S. V. Kalinin, A. A. Demkov, and V. Narayanan, "Switching of ferroelectric polarization in epitaxial BaTiO₃ films on silicon without a conducting bottom electrode," *Nature Nanotechnology*, vol. 8, no. 10, pp. 748–754, 2013.
- [48] H. Shigetani, M. Fujimoto, W. Sugimura, Y. Matsui, and J. Tanaka, "BaTiO₃/SrTiO₃ thin films grown by an MBE method using oxygen radicals," *Materials Science and Engineering B*, vol. 41, no. 1, pp. 148–151, 1996.
- [49] T. Tsurumi, T. Miyasou, Y. Ishibashi, and N. Ohashi, "Dielectric property of BaTiO₃-SrTiO₃ artificially modulated structure made by MBE," *IEEE International Symposium on Applications of Ferroelectrics*, pp. 47–50, 1998.
- [50] R. McKee, F. Walker, E. Specht, and K. Alexander, *Mat. Res. Soc. Symp. Proc.*, vol. 341, p. 309, 1994.

- [51] B. Kwak, E. Boyd, and A. Erbil, "Metalorganic chemical vapor deposition of PbTiO_3 thin films," *Appl. Phys. Lett.*, vol. 53 (18), pp. 1702–1704, 1988.
- [52] P. Van-Buskirk, R. Gardiner, and P. Kirlin, "Plasma-enhanced metalorganic chemical vapor deposition of BaTiO_3 films," *J. Vac. Sci. Technol.*, vol. 4, pp. 1578–1583, 1992.
- [53] T. Chiba, K. Itoh, and O. Matsumoto, "Deposition of BaTiO_3 thin films by plasma MOCVD," *Thin Solid Films*, vol. 300, pp. 6–10, 1997.
- [54] T. Hatanpää, M. Vehkamäki, I. Mutikainen, J. Kansikas, M. Ritala, and M. Leskelä, "Synthesis and characterisation of cyclopentadienyl complexes of barium: Precursors for atomic layer deposition of BaTiO_3 ," *Dalton Transactions*, no. 8, pp. 1181–1188, 2004.
- [55] J. H. Shim, H. J. Choi, Y. Kim, J. Torgersen, J. An, M. H. Lee, and F. B. Prinz, "Process-property relationship in high- κ ALD SrTiO_3 and BaTiO_3 : A review," *Journal of Materials Chemistry C*, vol. 5, no. 32, pp. 8000–8013, 2017.
- [56] T. U. J. An, M. Logar, J. Park, D. Thian, S. Kim, K. Kim, and F. B. Prinz, *ACS Appl. Mater. Interfaces*, vol. 6, p. 10656, 2014.
- [57] P. Schlindler, Y. Kim, D. Thian, A. Jihwan, and F. B. Prinz, "Plasma enhanced atomic layer deposition of BaTiO_3 ," vol. 111, no. 1, pp. 51–60, 2016.
- [58] S. Harrison, "Exploring and exploiting charge-carrier confinement in semiconductor nanostructures," Ph.D. dissertation, 11 2016.
- [59] S. Regnery, Y. Ding, P. Ehrhart, C. L. Jia, K. Szot, R. Thomas, and R. Waser, "Metalorganic chemical-vapor deposition of $(\text{Ba,Sr})\text{TiO}_3$: Nucleation and growth on Pt-(111)," *Journal of Applied Physics*, vol. 98, no. 8, 2005.
- [60] P. Ehrhart and R. Thomas, "Electrical properties of $(\text{Ba,Sr})\text{TiO}_3$ thin films revisited: The case of chemical vapor deposited films on Pt electrodes," *Journal of Applied Physics*, vol. 99, no. 11, 2006.
- [61] S. R. Gilbert, L. A. Wills, B. W. Wessels, J. L. Schindler, J. A. Thomas, and C. R. Kannewurf, "Electrical transport properties of epitaxial BaTiO_3 thin films," *Journal of Applied Physics*, vol. 80, no. 2, pp. 969–977, 1996.
- [62] G. W. Dietz and R. Waser, "Charge injection in SrTiO_3 thin films," *Thin Solid Films*, vol. 299, no. 1-2, pp. 53–58, 1997.
- [63] A. Yahia, A. Attaf, H. Saidi, M. Dahnoun, C. Khelifi, A. Bouhdjer, A. Saadi, and H. Ezzaouia, "Structural, optical, morphological and electrical properties of indium oxide thin films prepared by sol gel spin coating process," *Surfaces and Interfaces*, vol. 14, pp. 158–165, 2019. [Online]. Available: <https://www.sciencedirect.com/science/article/pii/S2468023018305091>

- [64] M. W. Cole, W. D. Nothwang, C. Hubbard, E. Ngo, and M. Ervin, "Low dielectric loss and enhanced tunability of $\text{Ba}_{0.6}\text{Sr}_{0.4}\text{TiO}_3$ based thin films via material compositional design and optimized film processing methods," *Journal of Applied Physics*, vol. 93, no. 11, pp. 9218–9225, 2003.
- [65] M. B. Okatan, M. W. Cole, and S. P. Alpay, "Dielectric tunability of graded barium strontium titanate multilayers: Effect of thermal strains," *Journal of Applied Physics*, vol. 104, no. 10, pp. 1–7, 2008.
- [66] A. Li, D. Wu, Z. Liu, H. Ling, C. Z. Ge, X. Liu, H. Wang, M. Wang, P. Lü, and N. Ming, "Fabrication and electrical properties of sol-gel derived $(\text{BaSr})\text{TiO}_3$ thin films with metallic LaNiO_3 electrode," *Thin Solid Films*, vol. 336, no. 1-2, pp. 172–175, 1998.
- [67] B. Bajac, J. Vukmirović, D. Tripković, E. Djurdjić, J. Stanojev, Ž. Cvejić, B. Škorić, and V. V. Srdić, "Structural characterization and dielectric properties of BaTiO_3 thin films obtained by spin coating," *Processing and Application of Ceramics*, vol. 8, no. 4, pp. 219–224, 2014.
- [68] A. Khanfekr, M. Tamizifar, and R. Naghizadeh, "Microwave-Hydrothermal Synthesis of Nb-doped BaTiO_3 Nanoparticles under Various Conditions," vol. 51, no. 5, pp. 23–28, 2015.
- [69] R. R. Bacsa, J. P. Dougherty, and L. J. Pilione, "Low-temperature synthesis of BaTiO_3 thin films on silicon substrates by hydrothermal reaction," *Applied Physics Letters*, vol. 63, no. 8, pp. 1053–1055, 1993.
- [70] K. W. Seo and H. G. Kong, "Hydrothermal Preparation of BaTiO_3 Thin Films," *Korean Journal of Chemical Engineering*, vol. 17, no. 4, pp. 428–432, 2000.
- [71] H. Akyildiz, M. D. Casper, S. M. Aygün, P. G. Lam, and J. P. Maria, "Hydrothermal BaTiO_3 thin films from nanostructured Ti templates," *Journal of Materials Research*, vol. 26, no. 4, pp. 592–599, 2011.
- [72] L. Qiao and X. Bi, "Microstructural orientation, strain state and diffusive phase transition of pure argon sputtered BaTiO_3 film," *J. Phys. D: Appl. Phys.*, vol. 42, p. 175508, 2009.
- [73] L.-W. Chang, M. Alexe, J. F. Scott, and J. M. Gregg, "Settling the "Dead Layer" Debate in Nanoscale Capacitors," *Advanced Materials*, vol. 21, p. 4911–4914, 2009.
- [74] T. Takeuchi, K. Ado, T. Asai, H. Kageyama, Y. Saito, C. Masquelier, and O. Nakamura., *J. Am. Ceram. Soc.*, vol. 77, p. 1665, 1994.
- [75] M. Tanaka and Y. Makino., *Ferroelec. Lett.*, vol. 24, p. 13, 1998.
- [76] M. Anliker, H. Brugger, and W. Kanzig., *Helv. Phys. Acta.*, vol. 27, p. 99, 1954.

- [77] W. Kanzig, "Intrinsic dead layer effect and the performance of ferroelectric thin film capacitors.," *Phys. Rev.* 98, vol. 98, p. 549, 1955.
- [78] F. Tsai and J. Cowley., *Appl. Phys. Lett.*, vol. 65, p. 1906, 1994.
- [79] J. Padilla and D. Vanderbilt., *Phys. Rev. B.*, vol. 56, p. 1625, 1997.
- [80] C. Bungaro and K. Rabe., *Phys. Rev. B.*, vol. 71, p. 35420, 2005.
- [81] R. I. Eglitis, E. A. Kotomin, and G. Borstel, "Large scale computer modelling of point defects in ABO_3 perovskites," *Physica Status Solidi C: Conferences*, vol. 2, no. 1, pp. 113–119, 2005.
- [82] C. Zhou and D. M. Newns, "Intrinsic dead layer effect and the performance of ferroelectric thin film capacitors.," *J. Appl. Phys.*, vol. 82, p. 3081–3088, 1997.
- [83] K. Natori, D. Otani, and N. Sano, "Thickness dependence of the effective dielectric constant in a thin film capacitor.," *Appl. Phys. Lett.*, vol. 73, p. 632–634, 1998.
- [84] O. G. Vendik, S. P. Zubko, and L. T. Ter-Martirosyan, "Experimental evidence of the size effect in thin ferroelectric films.," *Appl. Phys. Lett.*, vol. 73, p. 37–39, 1998.
- [85] M. Tyunina and J. Levoska, "Application of the interface capacitance model to thin-film relaxors and ferroelectrics.," *Appl. Phys. Lett.*, vol. 88, p. 262904, 2006.
- [86] G. Gerra, A. K. Tagantsev, N. Setter, and K. Parlinski, "Ionic polarizability of conductive metal oxides and critical thickness for ferroelectricity in $BaTiO_3$." *Phys. Rev. Lett.*, vol. 96, p. 107603, 2006.
- [87] R. Dittmann, R. Plonka, N. P. E. Vasco, J. He, C. Jia, S. Hoffmann-Eifert, and R. Waser., *J. Appl. Phys.*, vol. 83, p. 5011, 2003.
- [88] J. Berge, A. Vorobiev, and S. Gevorgian., *Thin Solid Films.*, vol. 515, p. 6302, 2007.
- [89] M. Stengel and N. Spaldin, "Origin of the dielectric dead layer in nanoscale capacitors," *Nature*, vol. 443, p. 679, 2006.
- [90] J. W. Liou and B. S. Chiou, "Dielectric tunability of barium strontium titanate/silicone-rubber composite." *J. Phys.: Condens. Matter*, vol. 10, p. 2773, 1998.
- [91] L. J. Sinnamon, M. M. Saad, R. M. Bowman, and J. M. Gregg, "Exploring grain size as a cause for "dead-layer" effects in thin film capacitors." *Appl. Phys. Lett.*, vol. 81, p. 703–705, 2002.
- [92] J. H. Haeni, P. Irvin, W. Chang, R. Uecker, P. Reiche *et al.*, "Room-temperature ferroelectricity in strained $SrTiO_3$." *Letters to Nature*, vol. 430, p. 758–761, 2004.

- [93] T. M. Shaw, Z. Suo, M. Huang, E. Liniger, R. B. Laibowitz *et al.*, "The effect of stress on the dielectric properties of barium strontium titanate thin films." *Appl. Phys. Lett.*, vol. 75, p. 2129–2131, 1999.
- [94] J. S. Chang, W. and Horwitz, A. C. Carter, S. W. Pond, J. M. and Kirchoefer *et al.*, "The effect of annealing on the microwave properties of Ba_{0.5}Sr_{0.5}TiO₃ thin films." *Appl. Phys. Lett.*, vol. 74, p. 1033–1035, 1999.
- [95] C. J. Brennan, "Defect chemistry model of the ferroelectric electrode interface." *Integrated Ferroelectrics* 7, vol. 93–109, pp. –1995, 1999.
- [96] T. Hirano, M. Ueda, K. ichi Matsui, T. Fujii, K. Sakuta *et al.*, "Dielectric properties of SrTiO₃ epitaxial film and their application to measurement of work function of YBa₂Cu₃O_y epitaxial film." *Japanese Journal of Applied Physics*, vol. 31, p. L1345–L1347, 1992.
- [97] A. K. Tagantsev, C. Pawlaczyk, K. Brooks, and N. Setter, "Built-in electric field assisted nucleation and coercive fields in ferroelectric thin films." *Integrated Ferroelectrics*, vol. 4, p. 1–12, 1994.
- [98] A. P. Bratkovsky, A. M. and Levanyuk, "Ferroelectric phase transitions in films with depletion charge." *Phys. Rev. B*, vol. 61, p. 15042–15050, 2000.
- [99] F. M. Pontes, E. R. Leite, E. Longo, J. A. Varela, E. B. Araujo *et al.*, "Effects of the postannealing atmosphere on the dielectric properties of (BaSr)TiO₃ capacitors: Evidence of an interfacial space charge layer." *Appl. Phys. Lett.*, vol. 76, p. 2433–2435, 2000.
- [100] B. R. M. A. Subramanian, D. Li and N. Duan and A. Sleight., "High Dielectric Constant in ACu₃Ti₄O₁₂ and ACu₃Ti₃FeO₁₂ Phases," *J. Solid. State Chem.*, vol. 151, p. 323, 2000.
- [101] O. Trithaveesak, J. Schubert, and C. Buchal, "Ferroelectric properties of epitaxial BaTiO₃ thin films and heterostructures on different substrates," *Journal of Applied Physics*, vol. 98, no. 11, 2005.
- [102] S. M. Sze, *Semiconductor Devices—Physics and Technology*, 2nd ed., Wiley, Ed., New York, 1986, vol. 23.
- [103] H. Salehi, N. Shahtahmasebi, and S. M. Hosseini, "Band structure of tetragonal BaTiO₃," *European Physical Journal B*, vol. 32, no. 2, pp. 177–180, 2003.
- [104] A. M. Cowley and S. M. Sze, "Surface states and barrier height of metal-semiconductor systems," *Journal of Applied Physics*, vol. 36, no. 10, pp. 3212–3220, 1965.

- [105] S. G. Louie, J. R. Chelikowsky, and M. L. Cohen, "Tonicity and the theory of Schottky barriers," *Phys. Rev. B*, vol. 15, p. 2154–2162, 1977.
- [106] S. Kurtin, T. McGill, and C. Mead, "Fundamental transition in the electronic nature of solids," *Phys. Rev. Lett.*, vol. 22, p. 1433, 1969.
- [107] J. F. Scott, B. M. Melnick, C. A. Araujo, and R. McMillan, L. D. and Zuleeg, "D.C. leakage currents in ferroelectric memories." *Integrated Ferroelectrics*, vol. 1, p. 323–331, 1992.
- [108] J. F. Scott, "Dielectric breakdown in high-epsilon films for ULSI DRAMs: III. Leakage current precursors and electrodes." *Integrated Ferroelectrics*, vol. 9, p. 1–12, 1995.
- [109] G. W. Dietz, W. Antpöhler, M. Klee, and R. Waser, "Electrode influence on the charge transport through SrTiO₃ thin films." *J. Appl. Phys.*, vol. 78, p. 6113–6121, 1995.
- [110] E. Bouyssou, R. Jérisian, N. Cézac, P. Leduc, G. Guégan, and C. Anceau, "Wafer level reliability and leakage current modeling of PZT capacitors," *Materials Science and Engineering B: Solid-State Materials for Advanced Technology*, vol. 118, no. 1-3, pp. 28–33, 2005.
- [111] T.-M. Li, P. and Lu, "Conduction mechanisms in BaTiO₃ thin films." *Phys. Rev. B*, vol. 43, p. 14261–14264, 1991.
- [112] H. Mihara, T. and Watanabe, "Electronic conduction characteristics of sol-gel ferroelectric Pb(Zr_{0.4}Ti_{0.6})O₃ thin-film capacitors: Part I." *Japanese Journal of Applied Physics*, vol. 34, p. 5664, 1995.
- [113] T. Mihara and H. Watanabe, "Electronic conduction characteristics of sol-gel ferroelectric Pb(Zr_{0.4}Ti_{0.6})O₃ thin-film capacitors: Part II," *Japanese Journal of Applied Physics*, vol. 34, p. 5674, 1995.
- [114] J. G. Simmons, "Richardson-schottky effect in solids," *Physical Review Letters*, vol. 15, no. 25, pp. 967–968, 1965.
- [115] S. Sengupta, L. C. and Sengupta, "Novel ferroelectric materials for phased array antennas." *Ultrasonics Ferroelectrics and Frequency Control IEEE Transactions*, vol. 44, p. 792–797, 1997.
- [116] L. C. Sengupta and S. Sengupta, "Breakthrough advances in low loss, tunable dielectric materials," *Materials Research Innovations*, vol. 2, no. 5, pp. 278–282, 1999.
- [117] Q. X. Jia, B. H. Park, B. J. Gibbons, J. Y. Huang, and P. Lu, "Dielectric response and structural properties of TiO₂-doped Ba_{0.6}Sr_{0.4}TiO₃ films." *Appl. Phys. Lett.*, vol. 81, p. 114–116, 2002.

- [118] D.-S. Lee, S.-G. and Kang, "Dielectric properties of ZrO₂-doped (Ba-Sr-Ca)TiO₃ ceramics for tunable microwave device applications." *Materials Letters*, vol. 57, p. 1629 – 1634, 2003.
- [119] K. B. Chong, L. B. Kong, L. Chen, L. Yan, C. Y. Tan, T. Yang, C. K. Ong, and T. Osipowicz, "Improvement of dielectric loss tangent of Al₂O₃ doped Ba_{0.5}Sr_{0.5}TiO₃ thin films for tunable microwave devices," *Journal of Applied Physics*, vol. 95, no. 3, pp. 1416–1419, 2004.
- [120] V. Reymond, D. Michau, S. Payan, and M. Maglione, "Substantial reduction of the dielectric losses of Ba_{0.6}Sr_{0.4}TiO₃ thin films using a SiO₂ barrier layer." *J. Phys.: Condens. Matter*, vol. 16, p. 9155, 2004.
- [121] W. Zhu, J. Cheng, S. Yu, J. Gong, and Z. Meng, "Enhanced tunable properties of Ba_{0.6}Sr_{0.4}TiO₃ thin films grown on Pt/Ti/SiO₂/Si substrates using MgO buffer layers." *Appl. Phys. Lett.*, vol. 90, p. 32907, 2007.
- [122] H. S. Kim, H. G. Kim, I. D. Kim, K. B. Kim, and J. C. Lee, "High-tunability and low-microwave-loss Ba_{0.6}Sr_{0.4}TiO₃ thin films grown on high-resistivity Si substrates using TiO₂ buffer layers," *Applied Physics Letters*, vol. 87, no. 21, pp. 1–3, 2005.
- [123] R. Ott, R. and Wördenweber, "A new design of tunable ferroelectric capacitors in RF applications." *Physica C: Superconductivity*, vol. Part 1, p. 540 – 542, 2002.
- [124] M. W. Cole, P. C. Joshi, M. Ervin, M. Wood, and R. L. Pfeffer, "Evaluation of Ta₂O₅ as a buffer layer film for integration of microwave tunable Ba_{1-x}Sr_xTiO₃ based thin films with silicon substrates." *J. Appl. Phys.*, vol. 92, p. 3967–3973, 2002.
- [125] I.-D. Kim, H. L. Tuller, H.-S. Kim, and J.-S. Park, "High tunability (Ba-Sr)TiO₃ thin films grown on atomic layer deposited TiO₂ and Ta₂O₅ buffer layers." *Appl. Phys. Lett.*, vol. 85, p. 4705–4707, 2004.
- [126] F. Kroger and H. Vink., "Relations between the concentrations of imperfections in crystalline solids," *Solid State Phys.*, vol. 3, p. 307–435, 1956.
- [127] N. Chan, R. Sharma, and D. Smyth, "Nonstoichiometry in Undoped BaTiO₃," *J. Am. Ceram. Soc.*, vol. 64, p. 556, 1981.
- [128] F. D. Morrison, A. M. Coats, D. C. Sinclair, and A. R. West, "Charge compensation mechanisms in La-doped BaTiO₃," *Journal of Electroceramics*, vol. 6, no. 3, pp. 219–232, 2001.
- [129] G. H. Jonker, "Some aspects of semiconducting barium titanate," *Solid State Electronics*, vol. 7, no. 12, pp. 895–903, 1964.
- [130] D. Smyth, *J. Electroceram.*, vol. 9, p. 179, 2002.

- [131] W. Heywang, "Semiconducting barium titanate," *Journal of Materials Science*, vol. 6, no. 9, pp. 1214–1224, 1971.
- [132] N. Chan and D. Smyth, *J. Am. Ceram. Soc.*, vol. 67, p. 285, 1984.
- [133] W. Heywang, "Resistivity anomaly in doped barium titanate," *J. Am. Ceram. Soc.*, vol. 47, no. 10, pp. 484–490, 1964.
- [134] H. Sauer and S. Flaschen, *Proceedings of Seventh Electronics Symposium, Washington*, p. 41–46, 1956.
- [135] M. W. Cole, P. C. Joshi, and M. H. Ervin, "La doped Ba_{1-x}Sr_xTiO₃ thin films for tunable device applications," *Journal of Applied Physics*, vol. 89, no. 11 I, pp. 6336–6340, 2001.
- [136] S. F. Wang, J. P. Chu, C. C. Lin, and T. Mahalingam, "Dielectric properties and microstructure of nano-MgO dispersed Ba_{0.3}Sr_{0.7}TiO₃ thin films prepared by sputter deposition," *Journal of Applied Physics*, vol. 98, no. 1, pp. 1–5, 2005.
- [137] W. Hofman, S. Hoffmann, and R. Waser, "Dopant influence on dielectric losses leakage behaviour and resistance degradation of SrTiO₃ thin films." *Thin Solid Films*, vol. 305, p. 66 – 73, 1997.
- [138] X. Sun, B. Zhu, T. Liu, M. Li, X. Z. Zhao, D. Wang, C. Sun, and H. L. Chan, "Dielectric and tunable properties of K-doped Ba_{0.6} Sr_{0.4} Ti O₃ thin films fabricated by sol-gel method," *Journal of Applied Physics*, vol. 99, no. 8, pp. 1–6, 2006.
- [139] K. P. Jayadevan, C. Y. Liu, and T. Y. Tseng, "Dielectric characteristics of nanocrystalline Ag–Ba_{0.5}Sr_{0.5}TiO₃ composite thin films." *Appl. Phys. Lett.*, vol. 85, p. 1211–1213, 2004.
- [140] S. Y. Wang, B. L. Cheng, C. Wang, S. Y. Dai, H. B. Lu, Y. L. Zhou, Z. H. Chen, and G. Z. Yang, "Reduction of leakage current by Co doping in Pt/Ba_{0.5}Sr_{0.5}TiO₃/Nb–SrTiO₃ capacitor," *Applied Physics Letters*, vol. 84, no. 20, pp. 4116–4118, 2004.
- [141] J. Zhang, J. Zhai, H. Jiang, and X. Yao, "Raman and dielectric study of Ba_{0.4} Sr_{0.6} TiO₃ - MgAl₂ O₄ tunable microwave composite," *Journal of Applied Physics*, vol. 104, no. 8, pp. 1–6, 2008.
- [142] T. Gon, S. Su, and J. Kuk, "Cu-doping effects on the dielectric and insulating properties of sol-gel derived Ba_{0.7}Sr_{0.3}TiO₃ thin films." *Journal of the Korean Physical Society*, vol. 49, p. 1, 2006.
- [143] T.-G. In, S. Baik, and S. S. Kim, "Leakage current of Al- or Nb-doped Ba_{0.5}Sr_{0.5}TiO₃ thin films by rf magnetron sputtering," *Journal of Materials Research*, vol. 235, no. 4784, p. 9, 1998.

- [144] R. Roy, "Multiple ion substitution in the perovskite lattice," *Journal of the American Ceramic Society*, vol. 37, no. 12, pp. 581–588, 1954.
- [145] Y. Shuai, S. Zhou, D. Bürger, H. Reuther, I. Skorupa, V. John, M. Helm, and H. Schmidt, "Decisive role of oxygen vacancy in ferroelectric versus ferromagnetic Mn-doped BaTiO₃ thin films," *Journal of Applied Physics*, vol. 109, no. 8, p. 084105, 2011.
- [146] J. P. Chu, T. Mahalingam, C. F. Liu, and S. F. Wang, "Preparation and characterization of Mn-doped BaTiO₃ thin films by magnetron sputtering," *Journal of Materials Science*, vol. 42, no. 1, pp. 346–351, 2007.
- [147] Y. Takezawa, K. Kobayashi, F. Nakasone, T. Suzuki, Y. Mizuno, and H. Imai, "Mn-doped BaTiO₃ thin film sintered using nanocrystals and its dielectric properties," *Japanese Journal of Applied Physics*, vol. 48, no. 11, 2009.
- [148] D. Levasseur, E. Bouyssou, R. De Paolis, A. Rousseau, F. Coccetti, G. Guegan, S. Payan, and M. Maglione, "Systematic tuning of the conduction mechanisms in ferroelectric thin films," *Journal of Physics Condensed Matter*, vol. 25, no. 49, 2013.
- [149] P. Dobal, A. Dixit, and R. S. Katiyar, "Effect of lanthanum substitution on the Raman spectra of barium titanate thin films," *Journal of Raman Spectroscopy*, vol. 38, no. April, pp. 1538–1553, 2007.
- [150] A. I. Ali, K. Park, A. Ullah, R. Huh, and Y. S. Kim, "Ferroelectric enhancement of La-doped BaTiO₃ thin films using SrTiO₃ buffer layer," *Thin Solid Films*, vol. 551, pp. 127–130, 2014.
- [151] D. Nagano, M. Sugiura, N. Wakiya, H. Funakubo, K. Shinozaki, and N. Mizutani, "Conduction mechanism of La-, Nb-doped BaTiO₃ thin films by doping MOCVD," *Key Engineering Materials*, vol. 216, pp. 87–91, 2002.
- [152] M. Cernea, I. N. Mihailescu, C. Martin, C. Ristoscu, and M. Iliescu, "La₂O₃-doped BaTiO₃ thin films obtained by pulsed laser deposition," *Journal of Modern Optics*, vol. 48, no. 15, pp. 2185–2189, 2001.
- [153] C. H. Wu, J. P. Chu, S. F. Wang, T. N. Lin, W. Z. Chang, and V. S. John, "Effects of post annealing on the material characteristics and electrical properties of La doped BaTiO₃ sputtered films," *Surface and Coatings Technology*, vol. 202, no. 22-23, pp. 5448–5451, 2008.
- [154] A. Zhang, Q. Li, D. Gao, M. Guo, J. Feng, Z. Fan, D. Chen, M. Zeng, X. Gao, G. Zhou, X. Lu, and J. M. Liu, "Conductivity, charge transport, and ferroelectricity of La-doped BaTiO₃ epitaxial thin films," *Journal of Physics D: Applied Physics*, vol. 53, no. 2, p. 025301, 2020.

- [155] M. Sedlar, V. Chivukula, and M. Sayer, "Characterization of Doped BST Thin Films Prepared by a Modified Sol Gel Method," *Integrated Ferroelectrics*, vol. 10, no. 1-4, pp. 113–121, 1995.
- [156] E. Arveux, S. Payan, M. Maglione, and A. Klein, "Surface segregation in Nb-doped BaTiO₃ films," *Applied Surface Science*, vol. 256, no. 21, pp. 6228–6232, 2010.
- [157] L. Yan, L. Hui-Bin, Z.-H. Chen, S. Dai, G.-T. Tan, and G.-Z. Yang, "Highly Conductive Nb-doped BaTiO₃ epitaxial thin films grown by Laser Molecular Beam Epitaxy," *Chinese Journal of Physics*, vol. 18, no. 11, pp. 1513–1515, 2001.
- [158] D. Nagano, H. Funakubo, K. Shinozaki, and N. Mizutani, "Electrical properties of semiconductive Nb- doped thin films prepared by metal – organic chemical-vapor deposition," *Appl. Phys. Lett.*, vol. 2017, no. 1998, pp. 1996–1999, 2017.
- [159] Z. Liu, Z. Zhang, G. Sheng, P. Yang, and J. Chu, "The electrical and optical properties of doped BTO thin films," *Photonics and Optoelectronics Meetings (POEM) 2009: Solar Cells, Solid State Lighting, and Information Display Technologies*, vol. 7518, p. 751812, 2009.
- [160] Z. Liu, H. Deng, P. Yang, and J. Chu, "Enhanced ferroelectric properties of Fe-doped BaTiO₃ thin film deposited on LaNiO₃/Si substrate by sol-gel technique," *Materials Letters*, vol. 63, no. 30, pp. 2622–2624, 2009.
- [161] R. Maier, J. L. Cohn, J. J. Neumeier, and L. A. Bendersky, "New magnetic and ferroelectric cubic phase of thin-film Fe-DOPED BaTiO₃," *Materials Research Society Symposium-Proceedings*, vol. 602, no. 45, pp. 29–33, 2000.
- [162] N. Masó, H. Beltrán, E. Cordoncillo, P. Escribano, and A. R. West, "Electrical properties of Fe-doped BaTiO₃," *Journal of Materials Chemistry*, vol. 16, no. 17, pp. 1626–1633, 2006.
- [163] A. Jana, T. K. Kundu, S. K. Pradhan, and D. Chakravorty, "Dielectric behavior of Fe-ion-doped BaTiO₃ nanoparticles," *Journal of Applied Physics*, vol. 97, no. 4, 2005.
- [164] W.-Y. Choi, Y. Tsur, C. A. Randall, and S. Trolier-Mckinstry, "Effect of Y-doping on the dielectric properties of BaTiO₃ films deposited in reducing atmospheres using pulsed laser deposition," *Materials Research Society Symposium - Proceedings*, vol. 596, pp. 487–492, 2000.
- [165] W. Y. Choi and S. T. McKinstry, "Preparation and characterization of dielectric (Y-doped BaTiO₃) and resistive (TaN) films for distributed rc network," *Integrated Ferroelectrics*, vol. 37, no. 1-4, pp. 83–93, 2001.
- [166] A. Jana and T. K. Kundu, "Microstructure and dielectric characteristics of Ni ion doped BaTiO₃ nanoparticles," *Materials Letters*, vol. 61, no. 7, pp. 1544–1548, 2007.

- [167] S. Liu, H. Zhang, L. Sviridov, L. Huang, X. Liu, J. Samson, D. Akins, J. Li, and S. O'Brien, "Comprehensive dielectric performance of bismuth acceptor doped BaTiO₃ based nanocrystal thin film capacitors," *Journal of Materials Chemistry*, vol. 22, no. 41, pp. 21 862–21 870, 2012.
- [168] A. Sadeghzadeh Attar, E. Salehi Sichani, and S. Sharafi, "Structural and dielectric properties of Bi-doped barium strontium titanate nanopowders synthesized by sol-gel method," *Journal of Materials Research and Technology*, vol. 6, no. 2, pp. 108–115, 2017.
- [169] H. Sharma and N. S. Negi, "Structural, microstructural and ferroelectric properties of lead-free Ca-doped BaTiO₃ thin films," *Ferroelectrics*, vol. 518, no. 1, pp. 118–123, 2017.
- [170] L. N. Gao, X. J. Yang, L. Y. Zhang, and X. Yao, "Structure and dielectric properties of Ca-doped (Ba_{0.7}Sr_{0.3})TiO₃ thin films fabricated by sol-gel method," *Journal of Electroceramics*, vol. 21, no. 1-4 SPEC. ISS., pp. 645–648, 2008.
- [171] F. Khatkhatay, A. Chen, J. H. Lee, W. Zhang, H. Abdel-Raziq, and H. Wang, "Ferroelectric properties of vertically aligned nanostructured BaTiO₃-CeO₂ thin films and their integration on silicon," *ACS Applied Materials and Interfaces*, vol. 5, no. 23, pp. 12 541–12 547, 2013.
- [172] L. Xiao, K. L. Choy, and I. Harrison, "Co-doped BST thin films for tunable microwave applications," *Surface and Coatings Technology*, vol. 205, no. 8-9, pp. 2989–2993, 2011.
- [173] L. Gao, J. Zhai, and X. Yao, "The influence of Co doping on the dielectric, ferroelectric and ferromagnetic properties of Ba_{0.70}Sr_{0.30}TiO₃ thin films," *Applied Surface Science*, vol. 255, no. 8, pp. 4521–4525, 2009.
- [174] C. Chen, A. Wei, Y. Li, K. Zhou, and D. Zhang, "Improved tunable properties of Co doped Ba_{0.8}Sr_{0.2}TiO₃ thin films prepared by sol-gel method," *Journal of Alloys and Compounds*, vol. 692, pp. 204–211, 2017.
- [175] P. Jullien, P. Mathey, P. Lompre, A. Novikov, and S. Odoulov, "Polarization backward-wave four-wave mixing in BaTiO₃:Fe using the photovoltaic effect," *Journal of the Optical Society of America B*, vol. 14, no. 7, p. 1735, 1997.
- [176] B. Deka, S. Ravi, A. Perumal, and D. Pamu, "Ferromagnetism and ferroelectricity in Fe doped BaTiO₃," *Physica B: Condensed Matter*, vol. 448, no. 1, pp. 204–206, 2014.
- [177] H. J. Hagemann and H. Ihrig, "Valence change and phase stability of 3d-doped BaTiO₃ annealed in oxygen and hydrogen," *Physical Review B*, vol. 20, no. 9, pp. 3871–3878, 1979.

- [178] H. J. Hagemann, "Loss mechanisms and domain stabilisation in doped BaTiO₃," *Journal of Physics C: Solid State Physics*, vol. 11, no. 15, pp. 3333–3344, 1978.
- [179] J. Jeong and Y. H. Han, "Electrical properties of acceptor doped BaTiO₃," *Journal of Electroceramics*, vol. 13, no. 1-3, pp. 549–553, 2004.
- [180] Y. Y. Yeoh, H. Jang, and H. I. Yoo, "Defect structure and Fermi-level pinning of BaTiO₃ co-doped with a variable-valence acceptor (Mn) and a fixed-valence donor (Y)," *Physical Chemistry Chemical Physics*, vol. 14, no. 5, pp. 1642–1648, 2012.
- [181] R. A. Maier, C. A. Randall, and J. Stevenson, "Low Temperature Ionic Conductivity of an Acceptor-Doped Perovskite: II. Impedance of Single-Crystal BaTiO₃," *Journal of the American Ceramic Society*, vol. 99, no. 10, pp. 3360–3366, 2016.
- [182] P. Moretti and F. M. Michel-Calendini, "Impurity energy levels and stability of CR and MN ions in cubic BaTiO₃," *Physical Review B*, vol. 36, no. 7, pp. 3522–3527, 1987.
- [183] C. Castro-Chavarria, S. Payan, J.-P. Salvetat, M. Maglione, and A. Klein, "Fermi level engineering for large permittivity in BaTiO₃-based multilayers," *Surfaces*, vol. 3, pp. 567–578, 2021.
- [184] H. Pinto, A. Stashans, and P. Sanchez, *Theoretical Studies of Impurity Doped and Undoped BaTiO₃ and SrTiO₃ Crystals*. Dordrecht: Springer Netherlands, 2000, pp. 67–72.
- [185] M. Maglione, "Free charge localization and effective dielectric permittivity in oxides," *Journal of Advanced Dielectrics*, vol. 6, no. 2, pp. 1–13, 2010.
- [186] C. Gillot and J. Michenaud, "DC electrical resistivity of Nb-doped BaTiO₃ and EPR measurements," *Solid State Communications*, vol. 84, no. September, pp. 1033–1038, 1992.
- [187] M. Actis and F. Michel-Calendini, "Impurity levels and nonlinear optical properties of doped BaTiO₃ from extended cluster LDA calculations," *International Journal of Quantum Chemistry*, vol. 61, no. 4, pp. 657–664, 1997.
- [188] N. Lemée, C. Dubourdieu, G. Delabouglise, J. P. Sénateur, and F. Laroudie, "Semiconductive Nb-doped BaTiO₃ films grown by pulsed injection metalorganic chemical vapor deposition," *Journal of Crystal Growth*, vol. 235, no. 1-4, pp. 347–351, 2002.
- [189] D. Phuyal, S. Mukherjee, S. Jana, F. Denoel, M. V. Kamalakar, S. M. Butorin, A. Kalaboukhov, H. Rensmo, and O. Karis, "Ferroelectric properties of BaTiO₃ thin films co-doped with Mn and Nb," *AIP Advances*, vol. 9, no. 9, 2019.

- [190] Y. L. Chen and S. F. Yang, "PTCR effect in donor doped barium titanate: Review of compositions, microstructures, processing and properties," *Advances in Applied Ceramics*, vol. 110, no. 5, pp. 257–269, 2011.
- [191] A. Klein, T. Mayer, A. Thissen, and W. Jaegermann, "Photoelectron Spectroscopy in Materials Science and Physical Chemistry: Analysis of Composition, Chemical Bonding and Electronic Structure of Surfaces and Interfaces," in *Methods in Physical Chemistry*, R. Schäfer and P. C. Schmidt, Eds. Weinheim: Wiley-VCH, 2012, vol. 2, pp. 477–512.
- [192] J. F. Moulder, W. F. Stickle, P. E. Sobol, and K. D. Bomben, *Handbook of XPS.pdf*, 1995.
- [193] R. Schafranek and A. Klein, *Solid. Stat. Ionics.*, vol. 177, p. 1659, 2006.
- [194] L. T. Hudson, R. L. Kurtz, S. W. Robey, D. Temple, and R. L. Stockbauer, "Photoelectron spectroscopic study of the valence and core-level electronic structure of BaTiO₃," *Physical Review B*, vol. 47, no. 3, pp. 1174–1180, 1993.
- [195] B. Cord and R. Courths, *Surf. Sci.*, vol. 152, p. 1141, 1985.
- [196] P. Pertosa and F. M. Michel-Calendini, "X-ray photoelectron spectra, theoretical band structures, and densities of states for batio₃ and knbo₃," *Phys. Rev. B*, vol. 17, pp. 2011–2020, Feb 1978.
- [197] M. Copel, P. Ducombe, D. Neumayer, T. Shaw, and R. Tromp, *Appl. Phys. Lett.*, vol. 70, p. 3227, 1998.
- [198] R. Schafranek, S. Payan, M. Maglione, and A. Klein, "Barrier height at (Ba,Sr)TiO₃/Pt interfaces studied by photoemission," *Phys. Rev. B*, vol. 77, no. 19, pp. 30–33, 2008.
- [199] J. Baniecki, M. Ishii, K. Kurihara, K. Yamanaka, T. Yano, K. Shinozaki, T. Imda, K. Nozaki, and N. Kin, *Phys. Rev. B.*, vol. 78, p. 195414, 2008.
- [200] V. Henrich, *Phys. Rev. B.*, vol. 17, p. 4908, 1978.
- [201] H. Thomann, *Ferroel.*, vol. 73, p. 183, 1987.
- [202] M. Cardona, "Optical properties and band structure of SrTiO₃ and BaTiO₃," *Physical Review*, vol. 140, no. 2A, 1965.
- [203] A. Klein, "Energy band alignment at interfaces of semiconducting oxides: A review of experimental determination using photoelectron spectroscopy and comparison with theoretical predictions by the electron affinity rule, charge neutrality levels, and the common anion," *Thin Solid Films*, vol. 520, no. 10, pp. 3721–3728, 2012.

- [204] A. Artemenko, "INTRODUCTION TO ELECTRON RESONANCE."
- [205] A. Benninghoven, "Chemical Analysis of INorganic and Organic Surfaces and Thin Films by Static Time-of-Flight Secondary Ion Mass Spectrometry (ToF-SIMS)," *Angewandte Chemie International*, vol. 33, pp. 1023–1043., 1994.
- [206] L. VanVaeck, A. Adriaens, and R. Gijbels, "Static Secondary Ion Mass Spectrometry: (S-SIMS) Part 1. Methodology and Structural Interpretation," *Mass Spectrometry Reviews*, vol. 18, pp. 1–47, 1999.
- [207] A. Adriaens, L. VanVaeck, and F. Adams, "Static Secondary Ion Mass Spectrometry (S-SIMS) Part 2: Material Science Applications," *Mass Spectrometry Reviews*, vol. 18, pp. 48–81, 1999.
- [208] A. I. Ali, V. Senthikuma, I. W. Kim, and Y. S. Kim, "The influence of SrTiO₃ buffer layer on ferroelectric properties of Al-doped BaTiO₃ thin films," *Journal of Electroceramics*, vol. 33, no. 1-2, pp. 47–52, 2014.
- [209] D. Levasseur, "Nouvelle génération de capacités intégrées : influence des matériaux sur les performances diélectriques des capacités en couches minces," Ph.D. dissertation, Université de Bordeaux, 2015.
- [210] B. Su and T. W. Button, "Microstructure and dielectric properties of Mg-doped barium strontium titanate ceramics," *Journal of Applied Physics*, vol. 95, no. 3, pp. 1382–1385, 2004.
- [211] W. Cai, C. L. Fu, J. C. Gao, and C. X. Zhao, "Dielectric properties and microstructure of Mg doped barium titanate ceramics," *Advances in Applied Ceramics*, vol. 110, no. 3, pp. 181–185, 2011.
- [212] M. Dawber, "I-9 Standar Pembiayaan Pembelajaran FEB," vol. 77, no. October, pp. 1083–1130, 2005.
- [213] A. Klein, "Interface Properties of Dielectric Oxides," *Journal of the American Ceramic Society*, vol. 99, no. 2, pp. 369–387, 2016.
- [214] D. Levasseur, H. B. El-Shaarawi, S. Pacchini, A. Rousseau, S. Payan, G. Guegan, and M. Maglione, "Systematic investigation of the annealing temperature and composition effects on the dielectric properties of sol-gel BaxSr1-xTiO₃ thin films," *Journal of the European Ceramic Society*, vol. 33, no. 1, pp. 139–146, 2013.
- [215] M. Tsai, S. C. Sun, and T. Y. Tseng, *J. Appl. Phys.*, vol. 87, no. 7, p. 3482, 1997.
- [216] D. M. Smyth, "Effects of dopants on the properties of metal oxides," *Solid State Ionics*, vol. 129, no. 1, pp. 5–12, 2000.

- [217] D. Smyth, "Comments on the defect chemistry of undoped and acceptor-doped BaTiO₃," *Journal of Electroceramics*, vol. 11, no. 1-2, pp. 89–100, 2003.
- [218] M. Maglione, G. Philippot, D. Levasseur, S. Payan, C. Aymonier, and C. Elissalde, "Defect chemistry in ferroelectric perovskites: long standing issues and recent advances," *Dalton Transactions*, vol. 44, no. 30, pp. 13 411–13 418, 2015.
- [219] C. Mitra, C. Lin, J. Robertson, and A. A. Demkov, "Electronic structure of oxygen vacancies in SrTiO₃ and LaAlO₃," *Phys. Rev. B*, vol. 86, p. 155105, 2012.
- [220] R. K. Astala and P. D. Bristowe, "Ab initio calculations of doping mechanisms in SrTiO₃," *Modelling and Simulation in Materials Science and Engineering*, vol. 12, no. 1, pp. 79–90, 2004.
- [221] B. A. Wechsler and M. B. Klein, "Thermodynamic point defect model of barium titanate and application to the photorefractive effect," *Journal of the Optical Society of America B*, vol. 5, no. 8, p. 1711, 1988.
- [222] P. Sigmund, "Theory of Sputtering. I. Sputtering of amorphous and polycrystalline targets." *Phys. Rev.*, vol. 184, pp. 383–416, 1969.
- [223] H. F. Wardenga, "Surface potentials of ceria and their influence on the surface exchange of oxygen," Ph.D. dissertation, Technische Universität Darmstadt, 2019.
- [224] E. A. Kraut, R. Grant, J. Waldrop, and S. Kowalczyk, "Precise Determination of the Valence-Band Edge in X Ray Photoemission Spectra," *Physical Review Letters*, vol. 44, no. 24, p. 1620, 1980.
- [225] R. A. Theerthan, A. Artemenko, and M. Maglione, "Magnetic field tuning of polaron losses in Fe doped BaTiO₃ single crystals," *Journal of Physics Condensed Matter*, vol. 24, no. 40, 2012.
- [226] A. M. Slipenyuk, M. D. Glinchuk, V. V. Laguta, I. P. Bykov, A. G. Bilous, and O. I. V'yunov, "Impurity and intrinsic defects in barium titanate ceramics and their influence on PTCR effect," *Ferroelectrics*, vol. 288, no. November 2014, pp. 243–251, 2003.
- [227] Slipenyuk, Glinchuk, Bykov, Yurchenko, Mikheev, Frenkel, Tkachenko, and Garmash, "Study of Batio_3 Ceramics Doped With Mn and Ce or Nb and Sr," *Condensed Matter Physics*, vol. 6, no. 2, p. 237, 2003.
- [228] C. Elissalde, U. C. Chung, A. Artemenko, C. Estournès, R. Costes, M. Paté, J. P. Ganne, S. Waechter, and M. Maglione, "Stoichiometry and grain boundaries control by spark plasma sintering in Ba_{0.6}Sr_{0.4} TiO₃: Mn / MgO composites," *Journal of the American Ceramic Society*, vol. 95, no. 10, pp. 3239–3245, 2012.

- [229] V. V. Laguta, A. M. Slipenyuk, I. P. Bykov, M. D. Glinchuk, M. Maglione, D. Michau, J. Rosa, and L. Jastrabik, "Electron spin resonance investigation of oxygen-vacancy-related defects in BaTiO₃ thin films," *Applied Physics Letters*, vol. 87, no. 2, pp. 2–4, 2005.
- [230] A. Artemenko, S. Payan, A. Rousseau, D. Levasseur, E. Arveux, G. Guegan, and M. Maglione, "Low temperature dielectric relaxation and charged defects in ferroelectric thin films," *AIP Advances*, vol. 3, no. 4, pp. 0–8, 2013.
- [231] J. Nowotny and M. Rekas, "Positive temperature coefficient of resistivity for BaTiO₃-based materials," *Ceramics International*, vol. 17, no. 4, pp. 227–241, 1991.
- [232] G. Dong, H. Hu, X. Huang, Y. Zhang, and Y. Bi, "Rapid activation of Co₃O₄ cocatalysts with oxygen vacancies on TiO₂ photoanodes for efficient water splitting," *J. Mater. Chem. A*, vol. 6, pp. 21 003–21 009, 2018.
- [233] C. Poole, *Electron spin resonance*. New York: John Wiley & Sons, 1962.
- [234] B. Prabhananda, "Electron Spin Resonance in Paramagnetic Systems," Ph.D. dissertation, University of Bombay, 1970.
- [235] R. N. Schwartz and B. A. Wechsler, "Electron-paramagnetic-resonance study of transition-metal-doped BaTiO₃: Effect of material processing on Fermi-level position," *Physical Review B*, vol. 48, no. 10, pp. 7057–7069, 1993.
- [236] S. Maitra, M. Banerjee, S. Mukherjee, and P. K. Singh, "Synthesis and characterization of cobalt oxide doped barium strontium titanate," *Journal of the Australian Ceramic Society*, vol. 49, no. 1, pp. 79–83, 2013.
- [237] C. S. Hwang, B. T. Lee, C. S. Kang, J. W. Kim, K. H. Lee, H. J. Cho, H. Horii, W. D. Kim, S. I. Lee, Y. B. Roh, and M. Y. Lee, "A comparative study on the electrical conduction mechanisms of (Ba_{0.5}Sr_{0.5})TiO₃ thin films on Pt and IrO₂ electrodes," *Journal of Applied Physics*, vol. 83, no. 7, pp. 3703–3713, 1998.
- [238] A. Selmi, M. Mascot, F. Jomni, and J. C. Carru, "Investigation of interfacial dead layers parameters in Au/ Ba_{0.85}Sr_{0.15}TiO₃/Pt capacitor devices," *Journal of Alloys and Compounds*, vol. 8, p. 154048, 2020.
- [239] V. Reymond, S. Payan, D. Michau, J. P. Manaud, and M. Maglione, "Structural and electrical properties of BaTi_{1-x}Zr_xO₃ sputtered thin films: Effect of the sputtering conditions," *Thin Solid Films*, vol. 467, no. 1-2, pp. 54–58, 2004.
- [240] M. Alonso, R. Cimino, and K. Horn, "Surface photovoltage effects in photoemission from metal-GaP(110) interfaces: Importance for band bending evaluation," *Phys. Rev. Lett.*, vol. 64, p. 1947, 1990.

- [241] L. Kronik and Y. Shapira, "Surface photovoltage phenomena : theory , experiment , and applications," *Surface Science Reports*, vol. 37, pp. 1–206, 1999.
- [242] F. Bernoux, J.-P. Piel, B. Castellon, C. Defranoux, J.-H. Lecat, P. Boher, and J.-L. Stehlé, "Ellipsométrie théorie," *Techniques de l'ingénieur Métrologie optique et photonique*, no. r6490, 2003.
- [243] F. Tcheliébou, H. Ryu, C. Hong, W. Park, and S. Baik, "On the microstructure and optical properties of Ba_{0.5}Sr_{0.5}TiO₃ films," *Thin Solid Films*, vol. 299, p. 14 – 17, 1997.
- [244] B. Panda, A. Dhar, G. Nigam, D. Bhattacharya, and S. Ray, "Optical properties of RF sputtered strontium substituted barium titanate thin films," *Thin Solid Films*, vol. 332, pp. 46–49, 1998.
- [245] V. Zelezný, D. Chvostová, L. Pajasová, M. Jelínek, and T. Kocourek, "Optical study of BST films combining ellipsometry and reflectivity," *Applied Surface Science*, vol. 255, p. 5280 – 5283, 2009.
- [246] D. Bruzzese, K. J. Fahnstock, C. L. Schauer, J. E. Spanier, and C. V. Weiss, "The optical dielectric function in monolithic Ba_xSr_{1-x}TiO₃," *Integrated Ferroelectrics*, vol. 111, p. 27–36, 2010.

Annex

4.1 Annex 1: Literature

This section contains a more detailed literature of bulk BaTiO₃.

Table 4.2: Literature. ϵ_r : Relative permittivity at room temperature. Dielectric losses $\tan(\delta)$ at room temperature. Leakage currents J [$\mu\text{A}/\text{cm}^2$]. Tunability and leakage currents displayed values are for an indicated value of electric field.

Dopant	Doping conc.	Freq.	ϵ_r	Losses	Tunability (E)	J (E)
Ni						
Fukami2001						
Jeon2001	3 à 12 at. %					
Seo2002						
Oh2003						
Kim2003						
Kim2004	0, 1, 5 at. %					
Lim2004	0, 1, 2, 5 at. %					
Zhang2005	1-10 %					
Shihua2009						
Shihua2010						
Seo2010	1 at. %					
Qian2011						
Zhou2010						
Banerjee2012	0,25, 0,5 , 1 wt. %					
Liao2009	0-0,3 at. %					
Ding2009	0-10 at. %					
Kim2009	0 -1 at. %					
Ahn2002	0-0,5 at. %					
Ponchel2011	1, 3, 5 at. %					
Co						
Xiao2011	0, 0,25; 0,5; 1 at. %	12 GHz	200	0.04	12% (30 kV/cm)	
Gao2009	0; 2; 5; 10 at. %	100 kHz	230	0.013	45% (500 kV/cm)	0,369 (280 kV/cm)
Zhang2009	0,25-0,5 at. %	10 kHz				

Delprat2007 Zhan2009 Zheng2006 Liang2003 Saha2001 In1998 Kao2008 Oh2009 Chen2005 Kim1999 Liang2004 Cole2006 Wu2000	0-25 (Al) at% 2; 9; 14 at.% 0.03 5 at. % 0,5 at.% various 0,5-20 w. %	1 MHz				13% (10 kV/cm)	0,01 (125 kV/cm)
Fe							
Menesklou2011 Nur2012 Gong2007 Imai2002 Yonezawa2002 Seong1998 Ye2009 Zhou2010 Stemme2012 Liang2004 Paul2008 Chang1999 Huang2008 Dahrul2010 Radhapiyari2003 Radhapiyari2005 Li2001 Zhang2012 Herner1993 Lorenz2003 Laishram2013 Stemme2013 Guo2013 xu2009	0,1-1 at.% 0,1-6 at.% 0-0,3 at. % 1; 2 at.% various 0,1 at.% 0,1 at.% 0-0,611 at. % 0-5 wt. % 5at%	1 MHz 10 kHz 1 MHz 10 GHz 1MHz	350 177 2200 249 500	0.008 0.0159 0.002 0.058 0.25		44% (300 kV/cm) 45,5% (400 kV/cm)) 20% (10 kV/cm) 20,6% (58 kV/cm)	2 (100 kV/cm) 2 (100 kV/cm) 2 (100 kV/cm)
W							
Navi2002 Navi2003	1 at.% 1 at.%	2 GHz 2 GHz					

Mg						
Liang2004 Ponchel2011	various 1, 3, 5 at.%					
Ce						
Cernea2001 Lu2009 Hwang2001	0.03 2at.%		3500 2000			0.1
Undoped						
Jia2001 Jin1998 Butler2015 wang2012 chen2013 Heywang(1971).						
Nd						
Hashinshin2011 Liu2018	.25 to .45% 2 to 6%					

4.2 Annex 2: Leakage currents

Obtaining the "real" leakage current turns out to be complex, requiring the prior establishment of a suitable acquisition procedure. Indeed, the results of $I(V)$ measurements may vary depending on the acquisition conditions, due to the temporal dependence of the leakage currents [110]. The study of the evolution of the current as a function of time is therefore necessary first. Several physical phenomena can occur in the material in response to the application of a constant electric field. These different behaviors, also dependent on temperature, each induce a characteristic signature on the measurements of leakage currents as a function of time, and will be differentiated into several regions on the curves. Figure 4.1 shows a typical example of the time course of the leakage current of ferroelectric titanates.

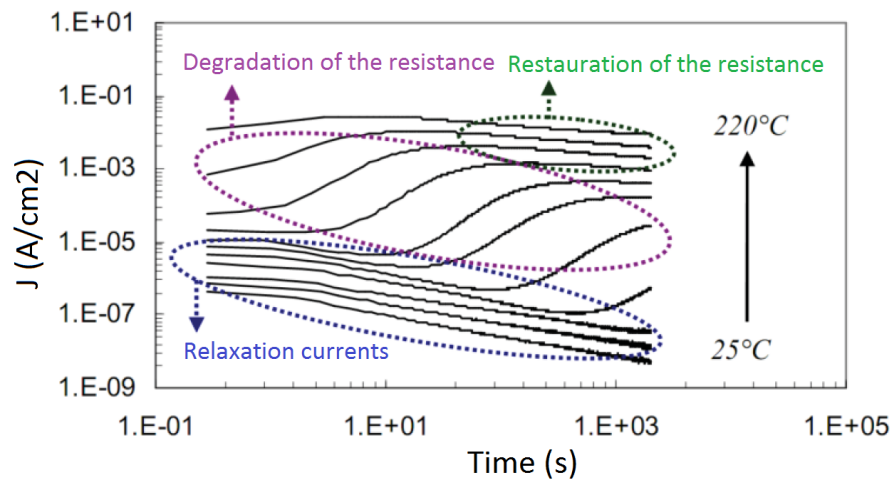


Figure 4.1: Example of the temporal evolution of the leakage current of a capacitor based on $(\text{Pb}, \text{Zr})\text{TiO}_3$ for different temperatures. [110]

The measurement of the leakage current as a function of the electric field can be carried out according to various procedures. The most common are the Staircase mode for which the voltage is increased in steps, and the Pulse mode for which successive voltage steps are applied, separated by short-circuiting intervals. For each step, voltage is applied for a certain time before taking the measurement.

To obtain stable $I(V)$ curves, it is necessary to avoid measuring the relaxation currents or the phenomenon of resistance degradation, which will disturb the measurement of the "real" leakage current as illustrated by the example in figure 4.2.

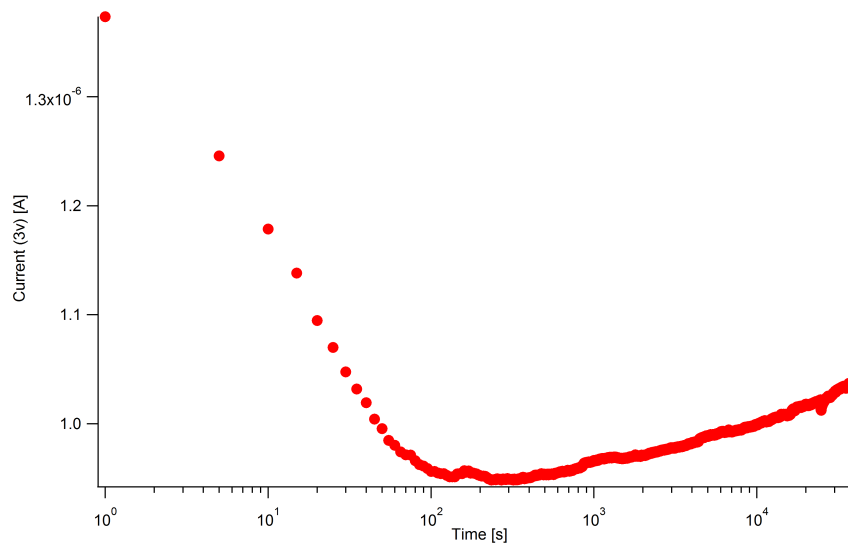


Figure 4.2: Example of the temporal evolution of the leakage current of a Mn-doped BaTiO₃ thin film at room temperature

4.3 Annex 3: Ellipsometry

4.3.1 Principle

Spectroscopic ellipsometry is an optical non-destructive surface analysis technique based on measuring the change in the polarization state of light after reflection from a flat surface. The particularity of this analysis technique is that it is indirect. Indeed, a modeling step is required to obtain the characteristic physical quantities of the material, in general the optical indices and the thickness [242].

The principle is as it follows: a plane wave is sent over the plane sample, part of the wave is transmitted or absorbed through the surface, another part is reflected as shown in Figure 4.3. The modification of the electric field of the incident wave \vec{E}_i can be broken down along two axes: \vec{E}_{pi} : parallel to the plane of incidence \vec{E}_{si} : perpendicular to the plane of incidence

The modification of the electric field after reflection \vec{E}_r is then represented by two reflection coefficients r_p and r_s . - the reflection coefficient for a polarization parallel to the plane of incidence:

$$r_p = \frac{E_{pr}}{E_{pi}} = |r_p| \exp(j\delta_p)$$

- the reflection coefficient for a polarization perpendicular to the plane of incidence

$$r_s = \frac{E_{sr}}{E_{si}} = |r_s| \exp(j\delta_s)$$

The two coefficients r_p and r_s are complex. Their module $|r_p|$, $|r_s|$ represents the modification made to the amplitude of the field component, and their phase, δ_p and δ_s , the delay introduced through reflection. In practice, the measured quantity is the ratio of these two coefficients, and is expressed in the form:

$$\frac{r_p}{r_s} = \tan\Psi \cdot \exp(j\Delta) = \rho$$

These geometric quantities Ψ and Δ reflect the state of elliptical polarization of the light wave after reflection. The measurement of ρ therefore leads to the identification of the two quantities $\tan\Psi$ and $\cos\Delta$ over a continuous range of wavelength or energy, thus providing a characteristic signature of the material. These parameters are displayed in figure 4.3

with \vec{E}_{pi} component of the incident electric field in the plane of incidence, \vec{E}_{si} component of the incident electric field perpendicular to the plane incidence, \vec{E}_{pr} component of the electric field reflected in the plane of incidence, \vec{E}_{sr} component of the reflected electric field perpendicular to the plane of incidence and Φ_0 angle of incidence.

4.3.2 Main results

The equipment used for this study is a Nanofilm's EP3 Imaging model spectroscopic ellipsometer. The Δ and Ψ data were recorded in the visible domain, from 350nm to

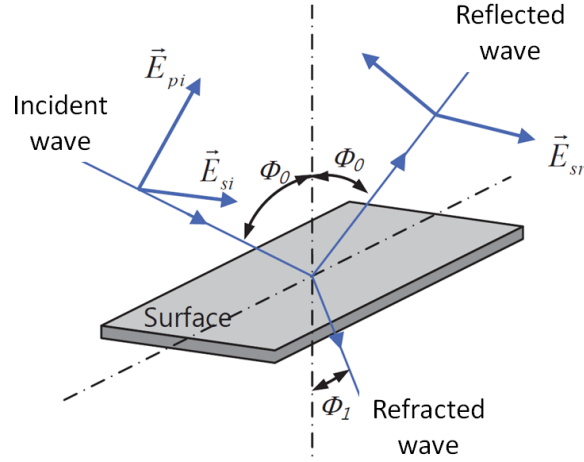


Figure 4.3: Principle of spectroscopic ellipsometry

800nm. These measurement parameters were used to obtain the optical index of the films using the EP4Model software.

Since the measurement is indirect, a data analysis step is inseparable from that of the measurement in order to be able to access the physical quantities. The use of the results consists in analyzing the spectra obtained and comparing them with a theoretical model, in order to adjust the model parameters by regression and go back to the actual values of thickness and optical indices. It is essential to know as much information as possible about the nature of the layer studied in order to develop the theoretical model.

The layer to be studied is defined by a law of dispersion. It is a mathematical model that makes it possible to simulate optical indices n and k as a function of wavelength. Among the many existing models, Cauchy's law was used for this study, very commonly applied to BaTiO₃ in the visible domain [243-246]:

$$n(\lambda) = A_n + \frac{B_n}{\lambda^2} + \frac{C_n}{\lambda^4}$$

$$K(\lambda) = A_K + \frac{B_K}{\lambda^2} + \frac{C_K}{\lambda^4}$$

where A , B , and C are fit parameters, and λ is the wavelength. This purely phenomenological model without a physical basis allows us to obtain a good description of the shape of the curves of $n(\lambda)$ and $k(\lambda)$.

The structure, once defined, will make it possible to reconstruct curves $\Delta(\lambda)$ and $\Psi(\lambda)$, which will be compared to the experimental curves during the regression using a mathematical algorithm. The results obtained are considered relevant when the RMSE (Root Mean Square Error) regression parameter is as low as possible. The refraction index of all films was calculated to be 2.26 ± 0.07 at 630 nm and the thickness of all samples are displayed in Table 4.3

Table 4.3: BaTiO₃ thin films thicknesses measured by ellipsometry.

Sample name	Doping	Thickness [nm]	Sample name	Doping	Thickness [nm]
CCT01	Undoped	35	ccb12p	Mn/Nb/Mn	331
CCT02	Undoped	432	ccb12	Mn/Nb/Mn	250
CCT03	Undoped	128	CCB20	La/Nb/La	288
CCT04	Undoped	234	CCB21	Nb/La/Nb	288
CCT05	Undoped	286	CCB22	5-LN	388
CCT06	Mn	81	CCB19	Undoped	203
CCT07	Mn	143	CCB19-2	Undoped	362
CCT08	Mn	159	CCB24	Nb/Ar/Nb	365
CCT09	Mn	156	CCB25	Nb / Mn	266
CCT10	Mn	161	CCB26	La / Mn	238
CCT10	Mn	161	CCB32	Mn / Nb	265
CCT11	Mn	156	CCB32	Mn / Nb	265
CCT12	Mn	34	CCB32	Mn / Nb	265
CCT13	Mn	152	CCB34	La	304
CCT19	Mn	970	CCB35	Nb	280
CCB01	Nb	82	CCB36	Nb/Ar/Nb	233
CCB03	Nb	450	CCB37	La/Nb/La	340
CCB03-2	Nb	420	CCB38	Mn	318
CCB04	Mn	298	CCB39	Mn	319
CCB05	Undoped	342	CCB42	La/Nb/La	340
CCB06	Mn/Nb/ Mn	293	CCB44	Mn	319
CCB07	Undoped	178	CCB40	Mn	319
CCB09	Mn	300	CCB43	La	311
CCB10	Mn	300	CCBS01	Nb	25
CCB11	5-MN	335	CCBS01	Nb	25
CCB14	Nb/Mn/Nb	310	CCBS04	Mn	21
CCB15	La	289	CCBS06	Mn	338
CCB16	Nb	307	CCBS06	Mn	338
CCB17	La/Nb/La	341			

Résumé

Christopher Castro Chavarría

christopher.castro.chavarria@gmail.com · +33 6 49 59 06 03

Citizenship: Mexican

Education

- 2015 – Present **Doctoral studies**– Darmstadt, Germany and Bordeaux, France
Technische Universität Darmstadt, Surface Science Division and Institut de la Matière Condensée, Groupe 1
Title of Thesis: "Charged defects in BaTiO₃ thin films"
- 2014 – 2015 **Master's degree Nanoscale Engineering** – Lyon, France
Université de Lyon 1 and INSA de Lyon
Degree: Master of Science
Title of thesis: "Chalcogenide materials thin films deposited onto silicon to develop innovative ultra-nonlinear integrated photonics devices in the MIR"
- 2010 – 2015 **Bachelor of Engineering's degree Materials Science** – Lyon, France
INSA de Lyon
Title of thesis: "Molybdenum disulphide (MoS₂), the innovative material for the electronics and optoelectronics of the future."

Professional Experience

- 2015 – Present **Research Assistant**– Darmstadt, Germany and Bordeaux, France
Technische Universität Darmstadt, Surface Science Division and Institut de la Matière Condensée, Groupe 1

List of publications

- 2020 **Fermi Level Engineering for Large Permittivity in BaTiO₃-Based Multilayers**
C. Castro Chavarría, S. Payan, J-P. Salvetat, M. Maglione and A. Klein.
Surfaces, 3(4), 567-57 (2020)
- 2020 **Ge–Sb–S–Se–Te amorphous chalcogenide thin films towards on-chip nonlinear photonic devices**
J.-B. Dory, C. Castro Chavarría, A. Verdy, J.-B. Jager, M. Bernard, C. Sabbione, M. Tessaire, J.-M. Fédéli, A. Coillet, B. Cluzel and P. Noé
Scientific reports, 10, 11894 (2020).
- 2017 **Simple synthesis and characterization of vertically aligned Ba_{0.7}Sr_{0.3}TiO₃-CoFe₂O₄ multiferroic nanocomposites from CoFe₂ nanopillar arrays**
S. Basov, C. Elissalde, Q. Simon, M. Maglione, C. Castro-Chavarría, T.H. de Beauvoir, S. Payan, K. Temst, V. Lazenka, V. Andrei Antohe, P.M.P de Sá, D. Sallagoity, L. Piraux
Nanotechnology, 28(47), 475707 (2017)